eman ta zabal zazu

Universidad del País Vasco

Euskal Herriko Unibertsitatea

TOWARDS CO-SINTERING OF OXIDE-BASED INORGANIC SOLID-STATE BATTERIES.

UNDERSTANDING AND OVERCOMING THE TEMPERATURE BARRIERS.

Sona Valiyaveettil SobhanRaj

A dissertation presented for the Doctoral degree in
Physics with an 'International Doctor' mention
Leioa, March 2023

eman ta zabal zazu

Universidad del País Vasco

Euskal Herriko Unibertsitatea

CIC energiGUNE

MEMBER OF BASQUE RESEARCH & TECHNOLOGY ALLIANCE

Towards co-sintering of oxide-based inorganic solid-state batteries: **Understanding and overcoming the temperature barriers.**

by

Sona Valiyaveettil SobhanRaj

Directed by

Dr. Montserrat Casas-Cabanas

Dr. Gabriel Alejandro López

A dissertation presented for the Doctoral degree in Physics with an 'International Doctor' mention

Leioa, March 2023

To the lovable memories of my Didi, Ammachan & Maman·

And for you, my unborn angel, Tania!

☺

ACKNOWLEDGEMENT

The journey that I have dreamt of and fought for since 2015, started officially on the 11th of June 2018, finally reaching its destination. I am grateful to all those who were with me during this period and content for the personal and professional experiences I could earn.

It is my greatest pleasure to acknowledge my supervisor, Dr. Montserrat Casas-Cabanas for her immense support during my research period. She has been a great mentor academically, professionally as well as personally. I thank her for the knowledge and time she shared with me during this period and admire her patience in those crucial moments. And I thankfully remember her moral support during my hardships.

A sincere gratitude to my supervisor, Dr. Gabriel Alejandro López, and the director, Prof. Alberto Oleaga Paramo from UPV/EHU for their immense support in the organization of my doctoral thesis.

I am profoundly grateful to Dr. Frederic Aguesse, Dr. Rosalia Cid, Dr. Marina Enterría, Dr. Pedro López, Dr. Ramakumar Sampathkumar, Dr. Damien Saurel, Dr. Francisco Bonilla, Dr. Gene Medard Nolis, Dr. Nicola Boaretto, Dr. Iñigo Garbayo, Amaia Quintela and Dr. Chunmei Li for their scientific discussion, constructive suggestions, and support to develop various experiments. I am happy to say that I was working closely with them and it was a great opportunity to learn from them about various research skills. With their immeasurable support, this thesis is organized well and deeply covers the different aspects.

I would like to thank María Jauregui, María Echeverría, and Yagmur Polat for their support in using the research equipment and Elena Vozmediano for her great assistance during my PhD work period. My special thanks to Umicore for the sponsorship and CIC energiGUNE for offering the platform to carry out my

PhD research. Thanks to Asier Urzelai and Estibaliz Martínez for their support and all CIC energiGUNE members for the wonderful time we spent together.

I would like to thank Umicore for hosting me for my PhD internship, and Dr. Travis Thompson, Dr. Florencia Marchini, Dr. Jérémie Auvergniot, and Sophia Verbrugghe for their support and scientific discussions during my stay.

Very special gratitude to Prof. Murugan Ramaswamy for introducing me to battery investigations and providing me with opportunities to establish my research career as a master's student and later as a research assistant with him at Pondicherry University. It was a milestone in my research career.

Special thanks to my brother, Soju, for his graphic design skills on my thesis formatting.

My deep thanks to my well-wishers Silvia, Esti, Aga, Yagmur, Marina, Elena, Dhruba, Tandra, Roshan, Mohana, Nithi, Geetha, and Bavya. Thankfully, I remember my besties with whom I shared the apartment and a lot of memorable moments- Imane, Agin, Natalia, and Maria.

Last but not least, I thank my family, Achan, Amma, and Soju for giving me the freedom, motivation, and trust despite all the pressures they had from a conservative society. I thankfully remember my Didi, who molded me as a person, and without her, I wouldn’t have reached where I am now. Loads of love to Ammachan, Ammamma, and all the other family members for their love and support. Finally, my husband Sergio, Papá, Ama and my unborn little princess, Tania for their love, support, and sacrifice. Without them I wouldn’t be able to finish this journey.

ABSTRACT

All inorganic solid-state batteries (SSBs) are considered the batteries of the future because of their superior energy density and safety. Their commercialization is in its infancy since further understanding of the materials and processing aspects is still required. Here we propose an oxide-based SSB model comprising NMC+LATP+carbon composite cathode, LATP solid electrolyte, and Li metal anode able to potentially convey an energy density of >300 Wh/kg and >700 Wh/l. A review of existing processing techniques of the selected materials indicates the necessity of very high densification temperatures to assure sufficient ionic conductivity and mechanical stability. The electrode and electrolyte need to be co-densified to avoid interfacial contact resistance, but the components of the composite cathode react at these elevated temperatures. In this work, the composite cathode thermal compatibility is first studied to determine the tolerance of the system under temperature, considering also the heating atmosphere and the decomposition reaction mechanism. In a second step, mitigation strategies to overcome the threshold limits identified have been examined, such as the selection of the carbon conducting additive and the impact of other additives. On the other hand, the realization that the threshold temperature is much lower than the conventional processing temperature requires the exploration of alternative low-temperature densification techniques. Hence a high-pressure low-temperature (HPLT) technique has been identified and initially investigated for oxide-based ceramic solid electrolyte densification. Our results show that this technique enables a significant reduction of the processing temperature and time compared to conventional sintering. Finally, preliminary investigations indicate that with further exploration of the HPLT technique, the realization of the proposed SSB model should be possible, resulting in significant gains of processing consumed energy.

RESUMEN

Las baterías inorgánicas de estado sólido (SSB, por sus siglas en inglés) se consideran las baterías del futuro debido a su densidad de energía superior y seguridad. Su comercialización está en sus inicios, ya que todavía se requiere una mayor comprensión de los aspectos de materiales y procesado. El sistema en el que se enfoca este trabajo consiste en un cátodo compuesto de NMC+LATP+carbono, electrolito sólido LATP y ánodo de Li metal, capaz de acumular, potencialmente, una densidad de energía de >300 Wh/kg y >700 Wh/l. Una revisión de las técnicas de procesado existentes de los materiales seleccionados indica la necesidad de temperaturas de densificación muy altas para garantizar una conductividad iónica y estabilidad mecánica suficientes. El electrodo y el electrolito necesitan ser densificados juntos para evitar la resistencia de contacto interfacial, pero los componentes del cátodo compuesto reaccionan a estas temperaturas elevadas. En esta tesis, la compatibilidad térmica del cátodo compuesto se estudia primero para determinar la tolerancia del sistema bajo temperatura, considerando también la atmósfera de calentamiento y el mecanismo de reacción de descomposición. En una segunda etapa, se han examinado estrategias de mitigación para superar los límites de umbral identificados, como la selección del aditivo conductor de carbono y el impacto de otros aditivos. Por otro lado, puesto que la temperatura umbral identificada es mucho menor que la temperatura de procesamiento convencional, se hace necesaria la exploración de técnicas alternativas de densificación a baja temperatura. En este contexto, la técnica de baja temperatura de alta presión (HPLT, por sus siglas en inglés) se ha identificado e investigado inicialmente para la densificación de electrolitos sólidos de cerámica a base de óxido. Nuestros resultados muestran que esta técnica permite una reducción significativa de la temperatura y el tiempo de procesado en comparación con la sinterización convencional. Por último, investigaciones preliminares indican que con una mayor exploración de la técnica de HPLT, la

realización de multicapas cátodo/electrolito debería ser posible, lo que resultaría en ganancias significativas de energía consumida en el procesado de SSBs.

TABLE OF CONTENTS

GENERAL INTRODUCTION

Li-ion battery is the most advanced and implemented energy storage technology for transport and stationary markets. However, the flammable and volatile liquid electrolytes cause major safety concerns. Replacing the organic liquid with a safe inorganic solid electrolyte is foreseen as a realistic strategy to reduce safety hazards while maintaining (or even increasing) high energy and power densities. The development of all-inorganic solid batteries is still in its infancy, as they present various challenges related to the interfacial and mechanical properties, and processing of the battery materials. Among the most prominent solid-state electrolyte chemistries, oxide-based ceramic electrolytes show high ionic conductivity, intrinsic safety, and a wide electrochemical stability window. But the high processing temperatures required to densify these materials lead to chemical reactions that are detrimental to the battery's performance.

In this thesis, we propose an all-inorganic solid-state battery model composed of a composite cathode, ceramic oxide electrolyte ($Li_{1+x}Al_xTi_{2-x}P_3O_{12}$ - LATP), and lithium metal anode (Figure 0. 1) that conveys an energy density of >300 Wh/kg and >700 Wh/l. The composite cathode is composed of active material ($LiNi_{0.6}Co_{0.2}Mn_{0.2}O_2$ - NMC), ionic conductive filler (LATP), and electronic conductive filler (Carbon). But the practical realization of this model has many challenges since a densely packed system is necessary to achieve conductivity, and the electrode and electrolyte components need to be co-densified to avoid resistive solid interfaces. A temperature of more than 1000˚C is necessary for the processing of LATP, and composite cathode components will be reactive at this temperature range.

Our work is focused on the systematic and step-by-step evaluation of the relevant factors involved in these temperature barriers, and strategies to overcome them (Figure 0. 1). First, the thermal stability limits of the composite cathode need to be identified. Next, the careful selection of additives is proposed

to elevate this threshold limit. Finally, we identify and explore the High-Pressure Low-Temperature (HPLT) densification technique to enable the densification of LATP at lower temperatures (see the conceptual summary of this work in Figure 0. 1).

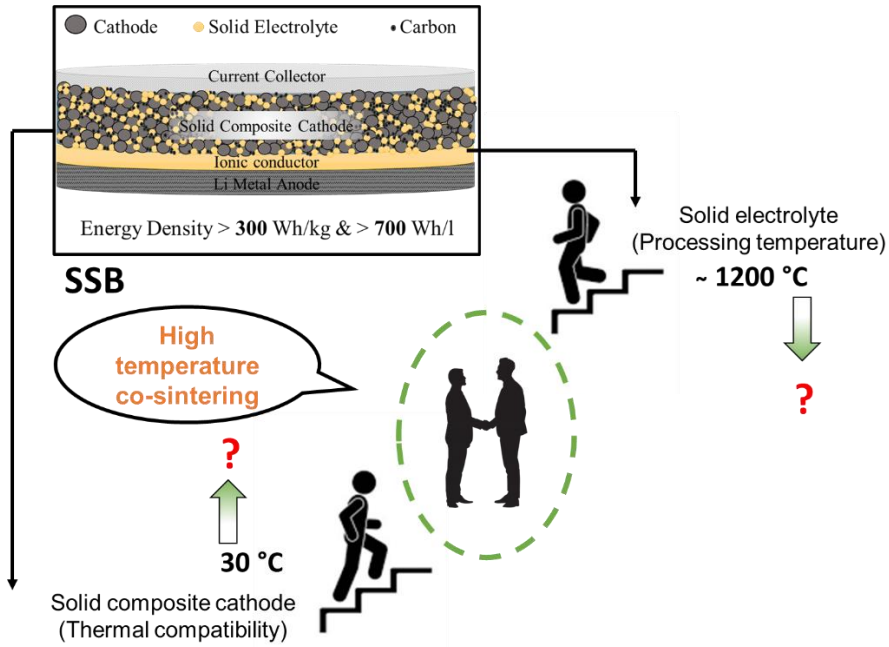

Figure 0. 1: A schematic illustration of the proposed SSB model and the methodologies followed in the thesis for addressing and overcoming the temperature barriers in realizing this battery model. The SSB is composed of the aluminum current collector, thick composite cathode (>1mm) with 65% of active loading, thin solid electrolyte separator (<50µm), and thin lithium metal anode (<100µm). The composite cathode consists of NMC, LATP, and carbon in the weight ratio of 65:30:05 respectively. The temperature barriers are bifold which needs attention on the composite cathode as well as on the solid electrolyte.

In Chapter 1,we summarize the state of the art of lithium solid-state batteries and the challenges related to the processing of all-inorganic SSBs. Different types of materials and processing techniques are described in detail together with the resulting interfacial compatibility of materials and components.

Chapter 2 focuses on the thermal compatibility of the composite components of the system chosen for this work (NMC, LATP, and carbon) to define the

threshold processing conditions such as heating atmosphere and temperature up to which the composite remains stable. The reaction mechanism of the composite components after the threshold values has been thoroughly investigated to propose strategies for the co-sintering of the proposed all-inorganic solid-state battery model.

A strategy has been introduced in Chapter 3 to enhance composite electrochemical performance at the threshold limits. The approach consists of the addition of Lithium fluoride (LiF) to the composite, which was found to favor the electrochemical performance of composites with and without heat treatments.

In Chapter 4 we investigate the importance of choosing carbon conductive additives for NMC-LATP composite cathodes and their impact on composite thermal stability. Different types of carbons were evaluated based on their physical, chemical, and morphological properties and our results show that the carbon choice can increase the threshold processing temperature.

On the other hand, in Chapter 5 a high-pressure and low-temperature sintering technique has been explored to reduce the sintering temperature of LATP below the temperature threshold of the composite cathode. The processing parameters such as temperature, pressure, and time have been optimized. The effect of low-temperature post-heat treatments and LATP particle size on the conductivity of the processed samples has also been analyzed. As a result, a substantial decrement in the processing temperature of LATP has been achieved and therefore this technique is proposed as an interesting approach worth exploring further for the fabrication of inorganic SSBs. Preliminary results of the processing of composite cathodes are also presented.

Finally, a general conclusion sums up the results obtained compared to the aims of the study and future perspectives are proposed to realize the fabrication of the proposed SSB model.

CHAPTER 1: LITHIUM SOLID-STATE BATTERIES STATE-OF-THE-ART AND CHALLENGES FOR MATERIAL, INTERFACES, AND PROCESSING

1.1 Introduction

Modern society is demanding, more than ever, solutions for advanced energy storage systems that require higher energy and/or power densities, better safety, and improved sustainability. This is mainly due to the increasing demand for electric vehicles, the main driving force of energy storage solutions, and the technological push for other applications such as drones, portable electronic devices, or stationary applications.[1] Climatic and environment considerations are other factors that urgently need advanced energy storage solutions. Among rechargeable technologies, lithium-ion batteries (LIBs) are the most mature technology, currently leading as the power and energy supplier for technological applications due to their comparatively superior performance in most aspects. [2], [3] Figure 1. 1 briefly visualizes the evolution of energy storage demands, current technology, and future alternatives along with their pros and cons.

State-of-the-art (SoA) LIB technology, which is based on liquid, organic electrolytes, is generally believed to be close to reaching its theoretical maximum energy density (250 $Wh \cdot kg^{-1}$ and 600 $Wh \cdot L^{-1}$). [4] However, this does not meet the emerging energy requirements of new applications. Also, the safety of SoA LIBs faces challenges associated with the use of toxic and flammable liquid electrolytes.[5]–[7] The solid-state battery approach, which replaces the liquid electrolyte with a solid-state counterpart, is considered a major contender to LIBs as it shows a promising way to satisfy the requirements for energy storage systems more safely. Solid Electrolytes (SEs) can be coupled with lithium metal anodes resulting in an increased cell energy density, with low or nearly no risk of thermal runaway.[8], [9] Further increase of the energy density

up to 400 $Wh \cdot kg^{-1}$ and 900 $Wh \cdot L^{-1}$ is thus possible with the use of high capacity and high voltage cathode active materials.[10], [11] Nonetheless, the maximum thickness of the electrolyte and its loading in the cathode should be precisely assessed, depending on the density of each material, to obtain full cells with competitive and desired energy density.

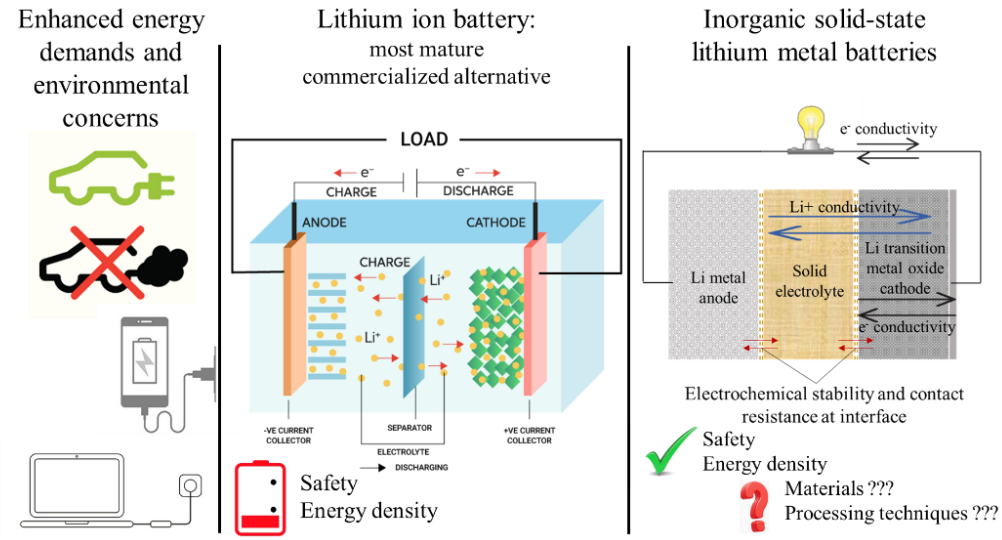

Figure 1. 1: Schematic illustration that represents the increasing energy demands, current commercialized energy storage options[12], their demerits, future alternatives, and their challenges.

SEs fulfill a dual role in solid-state batteries (SSBs), *viz.* i) being an ionic conductor they ensure the transport of Li-ions between electrodes and ii) being an electronic insulator they act as a physical barrier (separator) between the electrodes, thus avoiding the shorting of the cell. Over the past few decades, remarkable efforts were dedicated to the development of SEs, and the most relevant results have been summarized in several reviews.[10], [13]–[16] SEs are typically comprised of polymer materials (famous for their integration in the Blue Car® [17], the first industrially developed electric vehicle based on solid-state technology), and ceramic materials.[18] Recently, new high-performing inorganic SEs [19], [20]have been proposed and attracted a lot of attention. However, the development of SSBs is not only limited to the

development of new SEs, as the replacement of the liquid component by a solid one represents a challenge for current cell production processes, whose steps need to be adapted and even redesigned. Over the last few years, research activities have also been oriented toward the adaptation of novel cell processing routes and the integration of components from these new routes towards the production of solid-state technology.[21] The processing of SSBs includes the development of the SE, the solid cathode and anode and their integration. The utilization of ultra-thin electrolyte separators[22], and the increase of the packing density of the positive electrode[23] will further push the limits of the energy density towards high values. It is thus highly possible that the processing route of SSBs will be different from the current ones applied to LIB production. Processing of the different components should thus be revisited to ensure efficient cell fabrication in terms of performance, production speed, and sustainability.

Another challenge is related to the potential current density limits because of the lower conductivity of solid-state electrolytes to that of the liquid counterparts, and due to the presence of highly resistive solid-solid internal interfaces. Thus, the development of highly conducting electrolytes and of low and stable resistive interfaces is one of the most important challenges facing SSBs.[24] Mechanical, chemical and electrochemical instability upon cycling, result in the formation of undesired reactions at the interfaces.[25]–[27] These, besides consuming part of the lithium inventory, are also translated into large internal resistances and mechanical failures derived from volume changes or interfacial stresses.[28]

Below, SoA materials, most promising processing techniques, and the main challenges to overcome concerning their integration in functional SSBs are briefly summarized.

1.2 Materials for Inorganic solid-state batteries

1.2.1 Positive and negative electroactive materials

Overall, the most studied cathode active materials (CAMs) for SSBs are the same as those currently used in commercial LIBs, since they are the most promising to reach high energy and power densities. They include layered oxides $LiCoO_2$ (LCO), $LiNi_{1-x-y}Co_xAl_yO_2$ (NCA), and $LiNi_{1—x—y}Co_xMn_yO_2$ (NMC); spinel $LiMn_2O_4$ (LMO) and polyanionic $LiFePO_4$ (LFP) [29].

Layered oxides crystallize in a hexagonal layered structure ($\alpha NaFeO_2$-type structure) where transition metal atoms and lithium alternate between oxygen layers, resulting in a 2-D diffusion path for lithium atoms. LCO remains the best cathode material for portable electronic domains owing to its superior packing density (~4.3 g cm^{-3}), high initial coulombic efficiency, excellent cycle stability, high-voltage plateau, and stable charge/discharge voltage. The upper cutoff voltage of LCO has been gradually increased from 4.2 to 4.45 V since 1991 via surface modification, with a concomitant increase in capacity from 137 to 180 $mAh \cdot g^{-1}$ [30], still being far from the theoretical capacity (274 $mAh \cdot g^{-1}$). Poor structural stability and interface issues have prevented the use of LCO at higher voltages.

The high cost and supply risks of cobalt, coupled with the high voltage required by LCO, make $LiNi_{1-x-y}Co_xAl_yO_2$ (NCA) and $LiNi_{1-x-y}Co_xMn_yO_2$ (NMC) better options for commercial Li-ion batteries. Both were developed from $LiNiO_2$ by partially substituting Ni with Co, Mn, and Al, and both have been successfully commercialized. In $LiNi_{1-x-y}Co_xAl_yO_2$ (NCA, with typically x= 0.15 and y= 0.05) [31], Ni is partially replaced by Co to suppress phase transitions driven by lithium ordering [32] (considered detrimental for capacity retention) and eliminate Ni/Li cation mixing [33] (which limits the capacity of the material); while Al improves the thermal stability of Ni-rich oxides [34], [35]. Indeed, delithiated Ni-rich layered oxides undergo thermally-induced

phase transitions to spinel and rock-salt structures, which are accompanied by oxygen release. Such transformations are highly exothermic and can lead to thermal runaway of the battery [31]. NCA electrodes yield capacities of ~200 $mAh \cdot g^{-1}$ in the range of 3.0–4.2 V [36]. Several NMC compositions starting from NMC111 (x=y=1/3, with better safety properties compared to LCO and NCA) have been commercialized. In these, increasing the Co content substantially re duces the capacity loss during cycling, while electrochemically inactive Mn dominates the thermal stability [37]. In delithiated NMC, the more Ni, the lower the onset temperature of the phase transitions and the larger the amount of oxygen released [38]. Efforts have been directed towards increasing Ni content to reach higher capacities without compromising safety, with compositional gradient strategies as the most promising technical solutions (*i.e.*, an Mn-rich shell region to reduce the amount of highly reactive Ni^{4+} at the surface and/or impede the reactivity towards the electrolyte) [39], [40]. Following such approaches, prospects of NMC811 commercialization (~200 $mAh \cdot g^{-1}$ in the range 3.0–4.3 V) [37] have been announced [41]. Later, BMW unveiled its new electric car, that includes a NMC811 battery made with 188 prismatic cells from CATL.[42]

$LiFePO_4$ (LFP) and $LiMn_2O_4$ (LMO), with 1D and 3D lithium diffusion processes respectively, represent safer alternatives to layered oxides at the expense of limited energy density. LFP crystallizes in the olivine structure from which Li-ions can be reversibly extracted yielding a capacity of 170 $mAh \cdot g^{-1}$ and exhibiting a potential plateau at 3.5 V vs. Li^+/ Li^0 [43]. Despite the intrinsic advantages of such a low cell voltage in terms of safety, it limits the energy density and is considered the main drawback of LFP together with its low electronic conductivity.

$LiMn_2O_4$ (LMO) spinel is another well-established cathode. Removal of lithium to form $Li_{1-x}MnO_2$ occurs at 4 V vs. Li^+/Li^0, with a capacity of about

120 mAh·g^{-1} considering the extraction/insertion of 0.8 Li^+ per formula unit. This material exhibits an excellent power capability thanks to the 3D diffusion of Li-ions within the structure and better thermal stability compared to layered oxides. Additionally, manganese is inexpensive and environmentally benign. However, this material is prone to Mn^{2+} dissolution (resulting from Mn^{3+} disproportionation into Mn^{2+} and Mn^{4+}) in liquid electrolyte cells [44]. Manganese dissolution might be mitigated with SEs, possibly enabling the use of LMO in SSBs [45]–[48].

Similarly, to CAMs, the options for negative electrode materials for SSBs can be directly extrapolated from those already developed (and commercialized) for LiBs [49]. Still, graphite is the anode found in most Li-ion batteries since the first LCO/C rocking-chair cells were first commercialized in 1991 [50]. Graphite intercalates Li-ions at about 0.15 V vs Li^+/Li up to a final nominal composition LiC_6 (resulting from avoiding lithium occupation in the nearest neighbor positions, leading to a hexagonal ring) delivering a capacity of 372 mAh·g^{-1} [51]. The replacement of graphite anodes with silicon has been an active field of research. Pure silicon-based anode materials can theoretically deliver a capacity of an order of magnitude higher (3600 mAh·g^{-1}) than the currently applied graphite anode. However, the large volume changes that alloy-type anodes undergo (~400% for Si, compared to 10% for graphite) represent a major obstacle to their commercialization, and therefore must be contained in a composite design [52]. Opposite to silicon, $Li_4Ti_5O_{12}$ defect spinel (also written as $Li[Li_{1/3}Ti_{5/3}]O_4$, LTO) can reversibly intercalate lithium to yield the rock-salt type phase $Li_2[Li_{1/3}Ti_{5/3}]O_4$, with nearly no volume change [53]. This makes it a competitive commercial alternative to graphite for high-rate designs despite limited capacity (175 mAh·g^{-1}) and voltage (1.55 V vs. Li/Li^+). Although Li-ion intercalation occurs above the HOMO of the electrolyte, continuous interfacial reactions with the electrolyte still occur, leading to gas

evolution, which can be mitigated via surface modification [54].

Metallic lithium combines a very negative redox potential (3.04 V vs standard hydrogen electrode) with a low density (0.534 g cm^{-3}), which results in the highest theoretical capacity (3860 $mAh \cdot g^{-1}$). These appealing qualities resulted in a first commercialization attempt in the late 80s by Moli Energy, although all the commercialized cells (in which Li was paired to a MoS_2 cathode) were recalled owing to frequent accidents caused by Li-dendrite formation [55]. Cyclability is also a key issue as low coulombic efficiency leads to capacity fading. The low coulombic efficiency stems partially from the continuous loss of active Li in the SEI (solid electrolyte interface), but mostly from the fact that the SEI wraps plated lithium deposits, isolating them from the conductive network (inactive Li) [56]. The stringent demand for higher energy densities has motivated a revival of Li metal anodes, which are critical to overcoming the energy-density limit of Li-ion cells [30].

1.2.2 Solid electrolyte materials

This section reviews the most relevant inorganic solid electrolyte (SE) materials for SSBs. A simple classification based on chemical composition is followed. Most relevant parameters are briefly discussed, including ionic conductivity, thermal stability, and electrochemical stability window. Table 1. 1 summarizes the main characteristics of all the discussed compositions.

1.2.2.1 Oxide and polyanionic compounds

Lithium Superionic Conductors (LISICONs) were first reported by the composition $Li_{14}Zn(GeO_4)_4$, giving an ionic conductivity of 0.13 S cm^{-1} at 300 °C.[57] An interesting material within this family is the (1-x) Li_4SiO_4-(x) Li_3PO_4 solid solution. A wide range of compositions was explored by varying the value of x: $0 < x < 1$ and appreciable ionic conductivities were reported for x 0.25, 0.5, and 0.75 [58] as well as adding different dopants to the structure such as Al, Ge, As and V.[59], [60] LISICONs are stable against

water and their thermal stability and near-zero vapor pressure make them operational at high temperatures. The main drawback is typically associated with a low ionic conductivity at room temperature (*ca.* 10^{-7} S cm^{-1})[57], although enhanced Li-ion conduction could be achieved by strategic substitution (recently, Deng et al. proved by molecular dynamics simulations a conductivity of $9 \cdot 10^{-4}$ S cm^{-1} at room temperature for $Li_4Al_{1/3}Si_{1/6}Ge_{1/6}P_{1/3}O_4$ [58]). Still, LISICONs are highly reactive with lithium metal and atmospheric CO_2 [18] and their electrochemical stability window is limited within the range of 1.4 V and 4 V.[61]

Sodium Superionic Conductors (NASICONs) were first reported in 1976, by partial substitution of P by Si in the $NaM_2(PO_4)_3$ (M=Ge, Ti, Zr) structure.[18] Later on, the substitution of Na by Li was explored aiming to develop advanced Li-ion conductors. Partial substitutions were experimentally realized with different elements and valences to boost the ionic conductivity. In particular, trivalent Al is preferable for partial substitution thanks to its smaller ionic radius and the compositions made with M = Ti, Ge with partial substitution of Al ($Li_{1+x}Al_xTi_{2-x}(PO_4)_3$ – LATP and $Li_{1+x}Al_xGe_{2-x}(PO_4)_3$ – LAGP, respectively) were reported showing higher ionic conductivity than the corresponding parent compounds [62], [63]. The highest reported conductivities of LATP and LAGP are $1.09 \cdot 10^{-3}$ S cm^{-1} [64] and $6.18 \cdot 10^{-3}$ S cm^{-1} [65], respectively, at room temperature. In general, the high conductivity added to moisture stability and wide thermodynamic electrochemical stability window make NASICONS competitive SE materials for SSBs. NASICONS have high elastic modulus, *e.g.*, 115 GPa for LATP and 125 GPa for LAGP [66], but they have also low fracture toughness, which results in overall unfavorable mechanical properties (as is the case of all oxide-based materials). Moreover, interaction with Li metal limits their direct combination unless protective layers are added [67]. Reduction of Ti/Ge in contact with Li metal leads to the formation of an unstable mixed

(ionic/electronic) conductive interface which has been compared to the SEI layer in liquid electrolytes [68]. It results in a lower voltage limit of 2.17 V (LATP) and 2.7 V (LAGP)[61]. It is important to note that, despite the improved properties, LAGP is nearly 100 times more expensive than LATP owing to the high cost of Ge compared to Ti.

Li-based perovskites respond to the general formula ABO_3 (A= Li, Ca, Sr, La, and B Al, Ti) [63,64]. One of the most promising materials is the $Li_{3x}La_{(2/3)-x}\gamma_{(1/3)-2x}TiO_3$ (LLTO), where $0.04 < x \; 0.17$ and γ is the number of cationic vacancies, obtained by aliovalent substitution of both metal ions in the A site [69]. A high bulk conductivity of 10^{-3} S cm^{-1} was reported, owing to the larger radius and higher valence of La [17]. These are hard materials, reported with an elastic modulus value of 200 GPa [66]. Despite the high ionic conductivity at room temperature, the application of LLTO is also limited due to the reduction of Ti^{4+} to Ti^{3+} in contact with metallic lithium, similar to LATP, LAGP, and LISICON. Hence the lower voltage limit is set at 1.8 V [60]. Moreover, the processability of this material is also challenging as grain boundary resistivity can reduce by two orders of magnitude the total conductivity down to 10^{-5} S cm^{-1} [70]. Hence, proper interfacial engineering is indispensable to permit the integration of LLTO material in battery technology.

The garnet family is characterized by the general formula $A_3B_2(XO_4)_3$, with eight, six, and four coordinated cations [69]. Li-ion conducting garnets were initially reported within the compositions of $Li_5La_3M_2O_{12}$ (M= Nb, Ta) and $Li_6ALa_2M_2O_{12}$ (A= Ca, Sr, Ba and M= Nb, Ta), reaching conductivity values of 10^{-6} S cm^{-1} and 10^{-5} S cm^{-1} at room temperature, respectively [70]. The Li-ion conductivity was then significantly enhanced by maximizing the Li content with the so-called Li-stuffed garnets, responding to the parent formula $Li_7La_3Zr_2O_{12}$ (LLZO) [71], [72]. The conductivity of this material exhibits high dependency on the crystalline structure, showing a difference of two orders of magnitude in ionic conductivity between the cubic and the tetragonal

phases [73], [74]. Controlling Li loss during high-temperature treatments as well as a doping strategy in either the Li, La, or Zr sites has been reported to be fundamental for the stabilization of the cubic garnet phase with high Li-ion conductivity even at room temperature [75]. Among the different dopants tested, Ta [76], Al [77] and Ga [78] are to be highlighted, showing conductivities close to or higher than 1 mS cm^{-1}[79], [80]. Using a dual substitution strategy, the ionic conductivity at room temperature could be enhanced up to 1.8 mS cm^{-1} with the composition $Li_{6.65}Ga_{0.15}La_3Zr_{1.90}Sc_{0.10}O_{12}$ [81]. The average value of elastic modulus for the garnet family has been estimated to be 150 GPa [66]. A wide electrochemical stability window of 0–6 V against metallic lithium, low electronic conductivity, and negligible grain boundary contribution of garnets are very appealing for their use as electrolyte material[20], [82]. However, issues related to a poor wettability with Li metal typically led to high contact resistance at the Li metal-electrolyte interface, requiring certain interfacial modification [83] (see section 1.4) Also, garnets present some limitations in terms of structural stability when exposed to ambient conditions as they are particularly reacting with moisture [84], [85]. The formation of unwanted Li_2CO_3 at the surface leads to detrimental side reactions with Li metal, for which the application of different surface cleaning strategies becomes important [86]. A recent study indicates that, without any surface modification, Li_2CO_3-free LLZO shows intrinsic lithiophilicity [87].

Finally, one of the most studied and even commercially used solid-state materials is lithium phosphorous oxynitride (LiPON) [88]. With a low Li-ion conductivity of ~10^{-6} S cm^{-1} at room temperature, the use of LiPON has been limited to thin film-based batteries, where the reduced electrolyte thickness drastically diminishes the associated ohmic resistance allowing its practical use [45]. An elastic modulus of 77 GPa has been reported for a LiPON thin film in a thickness range of 1–10 μm [89]. LiPON proposes large electrochemical stability (0–5 V against Li/Li^+) [90], although the reason behind the stability

against metallic lithium seems most likely to be associated with the formation of a stable SEI composed of small units of Li_3PO_4, Li_3P, Li_3N and Li_2O [91]. Additionally, LiPON is compatible with a wide range of electrode materials, thus enabling the development of high-voltage micro-batteries. Recently, single-phase LiPON was synthesized via mechano-synthesis [92], which opens the door to new advances for this material in the field of bulk-type solid-state batteries.

1.2.2.2 Sulfides

Glassy sulfides were the first sulfide conductors to be developed and are mainly represented by the binary systems $Li_2S–SiS_2$, $Li_2S–P_2S_5$, and $Li_2S\text{-}GeS_2$, often also combined in ternary systems with other compounds such as Li_3N or LiI [93]–[95]. Heat treatments above the crystallization temperature (T_c) give rise to the so-called glass-ceramic sulfides, with increased conduction properties due to the stabilization of highly conducting crystalline phases precipitated from mother glasses [96]. Typical conductivity values in this family of materials are in the range of 10^{-4} to 10^{-3} S cm^{-1} at room temperature [97], being $Li_7P_3S_{11-x}$ the composition with the highest reported conductivity reaching $5.4\cdot10^{-3}$ S cm^{-1} at 25 °C [98]. Glassy sulfides have low elastic moduli (10–30 GPa) and excellent formability, allowing them to be highly densified by pressing even at room temperature [99], [100]. Notably, a recent report has shown that thermal treatment optimization of $Li_7P_3S_{11-x}$ can lead to further densification that allows for reaching even superior conduction properties ($1.7\cdot10^{-2}$ S cm^{-1} was reported at room temperature by Seino et al. [101]).

Crystalline sulfides, derived from the LISICON γ-Li_3PO_4 parent structure, have emerged in the last decade as a very promising alternative to glassy and glass-ceramic sulfide conductors. Thio-LISICON-like materials exhibit an orthorhombic structure responding to the general formula $Li_{3-x}(P_{1-x}M_x)S_4$ (M-Si, Ge, Sn) [102], [103]. In these compounds, the aliovalent substitution of P^{5+}

by Si^{4+} or Ge^{4+} is resulting in high ionic conductivities, > 10^{-4} S cm^{-1} at room temperature [103]. Some of the most relevant materials within this group are $Li_{4-x}Ge_{1-x}P_xS_4$ or $Li_{4-x}Sn_{1-x}As_xS_4$, with conductivities up to $2.2 \cdot 10^{-3}$ S cm^{-1} [104], [105].

Moreover, a new group of materials derived from the thio-LISICON family has lately attracted enormous attention due to its extraordinary conductive properties. Responding to the general formula $Li_{10}MP_2S_{12}$ (being M= Si, Ge, Sn) and primarily represented by $Li_{10}GeP_2S_{12}$ (LGPS) [106]. The overall conductivity of the parent LGPS compound was reported to be $1.2 \cdot 10^{-2}$ S cm^{-1}at room temperature, although the highest conductivity was found in the related $Li_{9.54}Si_{1.74}P_{1.44}S_{11.7}Cl_{0.3}$ material, which reaches the unprecedented value of $2.5 \cdot 10^{-2}$ S cm^{-1}at 25 °C [107]. LGPS exhibits soft mechanical properties and the reported elastic modulus value is about 20 GPa [108].

Finally, the sulfide-based lithium argyrodite family, with the general formula Li_6PS_5X (X = Cl, Br), is lately gaining increasing attention. They are derived from the mineral argyrodite (Ag_8GeS_6) and have high ionic conductivities close to 10^{-3} Scm^{-1} *e.g.*, the $Li_7P_2S_8I$ structure [109]. The highest conductivity value within this family was recently achieved in the related thioantimonate iodine argyrodite $Li_{6.6}Si_{0.6}Sb_{0.4}S_5I$, reaching $2.4 \cdot 10^{-2}$ S cm^{-1} at room temperature [110].

The main limitation of sulfides (glassy, glass-ceramic, and/or crystalline) relates to their limited chemical (H_2S generation in contact with moisture) [111] and electrochemical stability [112]. Theoretical calculations of Han et al. [113] concluded that the electrochemical stability in a selection of sulfide electrolytes (including LGPS, Li_3PS_4, or $Li_7P_2S_8I$) was very similar, with narrow thermodynamic electrochemical stability windows between 1.6 V (reduction of Ge or P) and 2.3 V (oxidation of S). In the particular case of LGPS, recent reports have experimentally confirmed the narrow kinetic electrochemical stability window [113], [114]. Reduction (at ~1.7 V) and oxidation (at ~2.1 V) of LGPS

leads to the decomposition of the electrolyte into Li_2S, $Li_{15}Ge_4$, and Li_3P at 0 V and S, P_2S_5, and GeS_2 at 2.31 V [115], [116]. In contact with metallic Li, LGPS was also reported to decompose forming an interphase containing Li_3P, Li_2S, and Li–Ge alloy [117]. In this sense, interface engineering and the addition of protective coatings become crucial for the practical application of these materials (see section 1.4).

1.2.2.3 Phosphides

In recent years, a new family of Li superionic conductors has emerged and requires attention as possible electrolyte alternatives for SSBs in the future: lithium phosphides [118]–[120]. Among this family, the most promising materials in terms of conductivity are Li_9AlP_4 and $Li_{14}SiP_6$, with values of $3 \cdot 10^{-3}$ S cm^{-1} and $1 \cdot 10^{-3}$ S cm^{-1}respectively [119], [120]. However, further work is still required to assess the electrochemical stability of these materials, as well as their compatibility with different electrodes

1.2.2.4 Halides

Halide solid electrolytes typically with the crystallographic structure of metal halide superionic conductors of a general formula of Li_3MX_6 (M = trivalent rare earth metal, X = F, Cl, Br, and I) have achieved impressive progress and attracted significant attention for application in SSBs. In 2018, Asano et al. revisited the halide SSEs Li3YCl6 and Li3YBr6, demonstrating high room temperature ionic conductivity (> 1 mS cm^{-1}), high voltage stability, excellent deformability, and desirable dry air stability [121]. This groundbreaking work has sparked global research interest in halide solid electrolytes. [122]–[124] A high RT conductivity of 7.2 mS cm^{-1} has been achieved in the mixed halide, $Li_3Y(Br_3Cl_3)$.[125] The high room-temperature ionic conductivity, wide electrochemical windows, and good compatibility with oxide cathode materials. [126] The main issues hindering halide SSE

development are moisture sensitivity and Li metal instability, high cost, lack of mechanical understanding, and toxic synthesis routes, [127], [128]

Table 1. 1: Summary of the general formula, best reported ionic conductivity, density, elastic modulus, and other specific challenges of the discussed inorganic solid electrolytes.

Material		General formula	Ionic conductivity (RT) [S cm^{-1}]	Density [gcm^{-3}]	Elastic modulus [GPa]	Other specific challenges
Oxide and polyanionic compounds	LISICONS	$Li_{2+2x}Zn_{1-x}GeO_4$	9×10^{-4} $Li_4Al_{1/3}Si_{1/6}Ge_{1/6}P_{1/3}O_4$	-	-	Low ionic conductivity at RT
	NASICON (LATP & LAGP))	$LiM_2(PO_4)_3$ (M=Ge, Ti)	1.09×10^{-3} $Li_{1+X}Al_XTi_{2X}(PO_4)_3$	2.92	115	-
			6.18×10^{-3} $Li_{1+X}Al_XGe_{2-X}(PO_4)_3$	3.56	125	
	Perovskites (LLTO)	ABO_3 (A= Li, Ca, Sr, La, and B Al, Ti)	10^{-3} $Li_{3x}La_{(2/3)-x}\gamma_{(1/3)2x}TiO_3$	-	200	High grain boundary resistance
	Garnets (LLZO)	$A_3B_2(XO_4)_3$	1.8×10^{-3} $Li_{6.65}Ga_{0.15}La_3Zr_{1.90}Sc_{0.10}O_{12}$	5.12	150	Poor Li wettability
	LiPON	$Li_xPO_yN_z$	10^{-6}	2.33	77	Limited to thin film batteries
Sulfides	Glassy sulfides (LPS)	Binary system e.g., Li_2S–P_2S_5	1.7×10^{-2} $Li_7P_3S_{11-x}$	1.87	10–30	Low chemical and electrochemical stability
	Crystalline sulfides (LGPS)	$Li_{3\ x}(P_{1-x}M_x)\ S_4$ (M- Si, Ge, Sn)	2.2×10^{-3} $Li_{4-x}Ge_{1-x}P_xS_4$ or $Li_{4-x}Sn_{1\ x}As_xS_4$	2.0	20	
		$Li_{10}MP_2S_{12}$ (M= Si, Ge, Sn)	1.2×10^{-2} $Li_{10}GeP_2S_{12}$			
	Argyrodite	Li_6PS_5X (X = Cl, Br)	$2.4 \cdot 10^{-2}$ $Li_{6.6}Si_{0.6}Sb_{0.4}S_5I$	1.64	20	
Lithium phosphide		Li_xMP_y	3×10^{-3} Li_9AlP_4	-	-	-
Lithium halides		Li_3MX_6 (M = trivalent rare earth metal, X = F, Cl, Br, and I)	7.2×10^{-3} $Li_3Y(Br_3Cl_3)$	2 - 3	-	Toxic synthesis routes

1.2.3 Selection of material

In summary, voltage limitations at the cathode together with the low capacity of graphite anodes (350 mAh/g) are major barriers to further advances in Li-ion batteries (LiBs). Replacement of the graphite anode with lightweight and high-capacity lithium metal (3860 mAh/g) represents a step change to

achieve the high energy density requirements. Hence lithium metal was considered in this work as the anode.

Considering the energy density demands of transport applications, Ni-rich layered oxide materials with the general formula $LiNi_xMn_yCo_{1-x-y}O_2$ (NMC) are commonly used as positive active materials, because of their high operating voltage, thermal stability, and capacity (Figure 1. 2a). $LiNi_{0.6}Mn_{0.2}Co_{0.2}O_2$ which is one of the well-established compositions in the NMC series, with a specific capacity of 187 mAh/g and an average working voltage of 3.7 V has been chosen as the cathode active material.

Alongside, NASICON-based $Li_{1+x}Al_xTi_{2-x}P_3O_{12}$ (LATP) is an interesting electrolyte by considering primarily its stability at high voltages (>4V) making it in principle compatible with cathodes such as Ni-rich NMC (Figure 1. 2b). Additionally, it's low gravimetric density and high ionic conductivity (Figure 1. 2c) together contributes to high energy density for the battery stack. Finally, the stability under ambient conditions makes it an appealing candidate in terms of easiness in processibility (Figure 1. 2d). Drawbacks are the need of high temperatures for its processability (see Pressing Techniques) and the instability of LATP against lithium, which on the other side is well-studied and interface engineering methods have been reported to overcome it such as; Al_2O_3 surface coating by ALD, polymer or amorphous based interlayers, BN surface deposition by CVD, etc. [129]–[133]

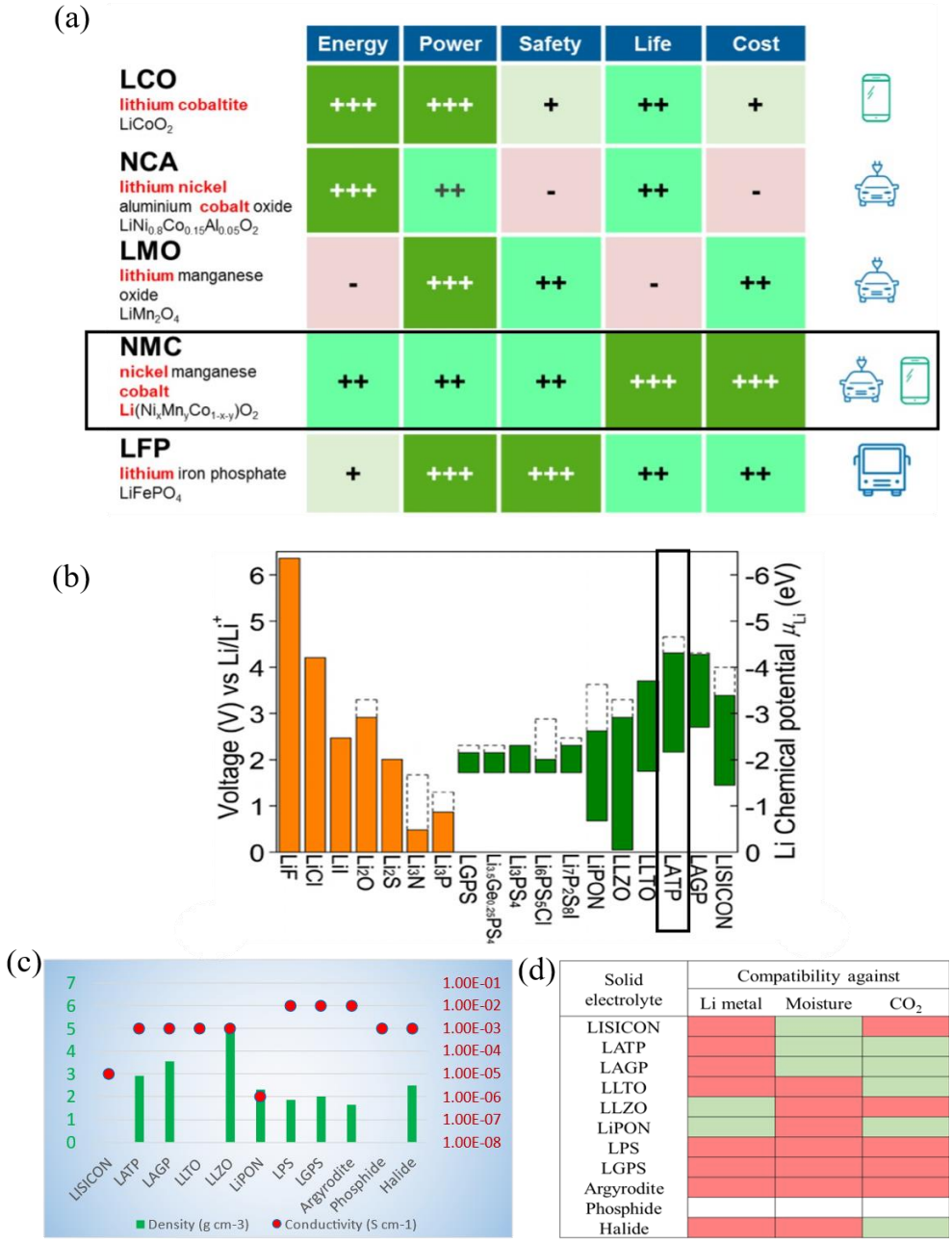

Figure 1. 2: **(a)** Different cathode material solutions available to fit best with the application NMC compound emerge as the best compromise for wide-spread automotive use. [134] **(b)** Electrochemical window (solid color bar) of the solid electrolyte and other materials. The oxidation potential to fully delithiate the material is marked by the dashed line.[61] **(c)** Comparison of ionic conductivity (red dots) and density (green bars) of solid electrolytes. **(d)** solid electrolyte compatibility (green: stable and red: reactive) against Li metal, moisture, and CO_2.

1.3 Processing techniques for solid-state batteries

The development of high-performing materials is also associated with the optimization of scalable processing techniques allowing production at a high speed. Depending on the material and the targeted application, several different processing techniques are available and can be applied to different sets of materials and technological applications (see Table 1. 2). The CAM, SE, and anode components selected (section 1.2.3) for the thesis framework are NMC, LATP, and lithium metal respectively. So, the processing technique should be compatible with oxides and that discards extrusion and cold/low temperature pressing without an ulterior thermal treatment. In this section, generic processing techniques available for SSB technology at laboratory and industrial scales are detailed. These can be combined depending on the selection of materials and components forming the solid-state cell.

Table 1. 2: Comparison of different processing techniques for SSB fabrication.[135]

Process	Candidate materials	Advantages	Disadvantages
Wet coating	Oxides Sulfides Cathodes	• Easily scalable • Simple process • Mature technology	• Use of solvents • Needs drying process • Needs post-process (calendering, sintering, etc.) • Low thickness
Extrusion	• Cathodes • Li anode	• Easily scalable • Simple process • Mature technology • No solvents	• Demanding in terms of material requirements (temperature, melt viscosity)
Printing	• Oxides • Cathodes • Li anodes • Scaffolds	• Versatile process • Multiple technologies • Form-factor-free batteries • Easily scalable • Wide variety of geometries and architectures	• Novel application • Use of solvents • Use of masks • Needs post-process • Scalability • Low throughput
Thin Film Vapor Deposition	• Oxides • Polyanionic compounds • Cathodes • Li metal anode • Interface processing	• High purity with controlled stoichiometry and microstructure • Apt for microbatteries • Conformal coating • Intimate contact between layers	• Cost • Scalability • Deposition time
Cold/low temperature pressing	• Sulfides • Cathodes • Li metal anode	• Easily scalable • Simple process • Wide variety of geometries and architectures	• Limited to mechanically soft materials
High temperature sintering	• Oxides	• High density • Strong mechanical properties • High Li-ion conductivity	• Scalability • Thermal stability issues
Cold sintering	• Oxides • Sulfides • Cathodes, • Anodes	• Low temperature • Fast process • Suitable for hard and soft materials • Simple process • Easily scalable	• Selection of compatible solvent • Solubility of particles limited • Needs post treatment

1.3.1 Wet coating

Wet coating processing techniques are typically used for the production of LIB electrodes at an industrial scale. The material to be deposited is dissolved or dispersed in a liquid solvent, and coated on a substrate. The coated wet film (green sheet) is then dried and calendered (Figure 1. 3a).

Organic solvents are normally used as liquid media to dissolve polymers (either electrolytes or electrode binders), or to disperse ceramic or carbon-based materials. Due to environmental and safety concerns, the importance of aqueous processing is constantly increasing [136]–[139]. Doctor blade also known as knife coating or tape casting, is one of the most common wet coating techniques used for batteries [140], and allows for achieving coating thicknesses lower than 50 μm [141].

Wet coating techniques are interesting for the assembly of solid-state batteries with inorganic electrolytes, and in particular with sulfide-based electrolytes. Sheet-type cells, in which the electrolyte powder is mixed with a polymer binder, can be prepared by wet-coating and by subsequent pressing [142]. Nonetheless, the wet coating is affected by a major drawback, which regards the use of toxic volatile organic solvents. Besides the obvious processing issues (need of adding a drying step, a densification step, solvent recovery, etc.), the use of solvents could lead to several other issues such as the risk of side reactions (*e.g.,* between the residual solvent and the metallic lithium), and inhomogeneities in the membrane (by the concentration gradient of the dissolved material during the drying process).

1.3.2 Solvent-free extrusion

To avoid the use of toxic organic volatile solvents, solvent- free melt processing of SEs is attracting attention as a more economical and environmentally friendly alternative [143], [144]. Furthermore, solvent-free processing is a good option for large and fast-scale cell assembly production.

The extrusion process consists of three steps, namely i) the compounding, *i.e.,* the preparation of viscous formulations by mixing and/or blending materials in a molten state; ii) the film forming process, by passing the melt through a flat film die; and finally, iii) the cooling or quenching, usually performed by rolling the extruded film through a pair of chilled rolls (Figure 1. 3b). During the extrusion, processing temperature, and shear parameters have to be taken into account. The latter, in turn, depends on the degradation mechanism and physical properties of the melted material, *i.e.,* the glass transition temperature, the softening and melting temperatures, and the rheological properties.

With melt extrusion, post-processing steps are not strictly necessary, although it is highly recommendable to accommodate the thickness and increase homogeneity, especially in the case of polymer electrolytes. For inorganic electrolytes, except sulfides which can be extruded directly, a post-annealing step at high temperature is needed [101]. Furthermore, co-extrusion could be used to co-extrude directly the electrolyte onto the electrodes or to extrude multi-layered electrolytes or electrodes [145].

1.3.3 Printing techniques

Printing techniques are gaining interest in battery processing, allowing a wider variety of geometries for standard processing techniques [146]. The fabrication of battery components with complex architectures may be used to increase the surface contact between the battery layers, and thus to decrease the corresponding interface resistances. Furthermore, printing allows the production of batteries with alternative shapes and the direct integration of the battery in the electronic device to be powered, which may be important, for example, for wearable electronics. The most common printing techniques for battery applications are classical 2D-printing techniques, such as screen-printing and stencil-printing, due to their simplicity and scalability [147]. In these techniques, the ink is pressed trough a mesh, a patterned mask, or a stencil

on a substrate while the excess ink is removed from the top of the mask. Other 2D-printing techniques such as flexography could be also appropriate for continuous roll-to-roll processing. It must be noted that the application of printing processing in solid-state electrolyte fabrication is at an early stage, but the field is developing rapidly. For example, screen printing was used to coat $LiTi_2(PO_4)_3$ and $Li_3V_2(PO_4)_3$ electrodes on the two sides of a LATP pellet, resulting in a monolithic all-phosphate cell by processing at a lower temperature [148], compared to other techniques such as spark-plasma sintering. Concerning tape casting, screen printing allows a better attachment of the electrode layers onto the LATP pellet, due to the application of pressure during the process. Furthermore, repeated screen-printing results in more dense electrode layers. Besides 2D printing techniques, the next frontier is additive manufacturing or 3D printing, which allows obtaining more complex geometries, with control of thicknesses down to a micrometric scale, and possibly a wider material choice for 2D techniques. 3D printing techniques which have been applied to the processing of solid- state batteries include stereolithography, in which a photo- polymerizable polymer precursor is locally cured through a light source, material-jetting techniques such as ink-jet printing and aerosol jet- printing, in which the material (ink or aerosol) is ejected through a nozzle, and material extrusion techniques, *i.e.* direct writing and fused deposition modeling, in which an ink or polymer melt is directly deposited on the target. As this field is expanding fast, other 3D-printing techniques may soon join the list. There are few examples in the literature of solid-state electrolytes processed by additive manufacturing. Stereolithography was used to prepare 3D polymer templates with complex geometries, which were then impregnated with LAGP powder [149]. McOwen et al. demonstrated microstructured LLZO electrolytes by direct writing of LLZO inks [150]. In this case, two different inks with different rheological properties were used: a "conformal" ink for the preparation of plane LLZO films, and a "self-

supporting" ink for the drawing of microstructures such as columns, lines, and grids, on top of LLZO films. Altogether, the printing process of solid-state-batteries, and in particular additive manufacturing, is a promising and rapidly expanding field, although still at an early stage. Promising applications for additive manufacturing could be the production of micro-batteries, cables- or fiber-type batteries, for wearable applications (Figure 1. 3c). On the other hand, large-scale battery production, the 2D printing process may have an advantage towards additive manufacturing, thanks to its low throughput.

1.3.4 Thin film vapor deposition

Thin film growth by vapor deposition techniques encompasses all deposition processes that involve the transfer of atoms from a certain source (which may be for example a thick pellet of the corresponding stoichiometry, but also a flow of reactants in the right ratio) to the desired substrate, all occurring through a gas phase. The process always takes place under a controlled vacuum, helping for the effective material transfer towards the substrate and drastically limiting the cross- contamination. The typical high power utilized during the processes usually allows the crystallization of the material in thin film form at temperatures considerably lower than the crystallization temperatures needed for bulky pellets (particularly important in the case of oxide SEs). Vapor deposition techniques are frequently found in SSB technology, either for the deposition of thin film metallic layers, *e.g.* Li thin film anodes [151], or ceramic films for two main applications: the growth of thin film inorganic electrolytes for micro-batteries [45], [152], [153] or the deposition of protective coatings in different instable interfaces (SE, anode, cathode or current collector; more details in section 1.4). [154]. In the former case, the most common examples are the growth of amorphous LiPON [155], or lately other crystalline ceramic materials such as LLZO or LLTO [156], [157]. Additionally, these coatings can be also effectively used as impermeable layers preventing the diffusion of unwanted species through the battery [158].

There are two types of deposition techniques; Physical vapor deposition (PVD) and chemical vapor deposition (CVD) (Figure 1. 3d). PVD techniques refer to deposition processes that are not mediated by a chemical reaction. In SSBs, the most relevant and widely applied are sputtering, [90], [159]–[163] pulsed laser deposition (PLD) [164] and evaporation [151], [165], [166]. As drawbacks, PVD techniques are often criticized for their high costs, greater than other industrialized battery processing techniques. Other important limitations are the low deposition rates, typically in the order of a few nm per minute and limiting the maximum practical thickness achievable to a few μm, and the still relatively high temperatures (usually > 200 ◦C) often needed for the deposition of crystalline ceramic films, which may compromise the integrity of other battery components.

In opposition to PVD techniques, Chemical Vapor Deposition (CVD) requires a chemical reaction between two or more components for the growth of the desired material. At present, Atomic Layer Deposition (ALD) is particularly relevant for SSB technology, especially for the growth of thin film protective layers [167]. In ALD, monolayers of the desired material are sequentially grown on top of a substrate, when exposed to a gas flow of reactants under a controlled atmosphere. Multiple materials for SSBs have been deposited by ALD, including cathodes [168], anodes [169] and ceramic electrolytes [170]–[172]. The main drawbacks are the low deposition rates and cost, which include gas precursors.

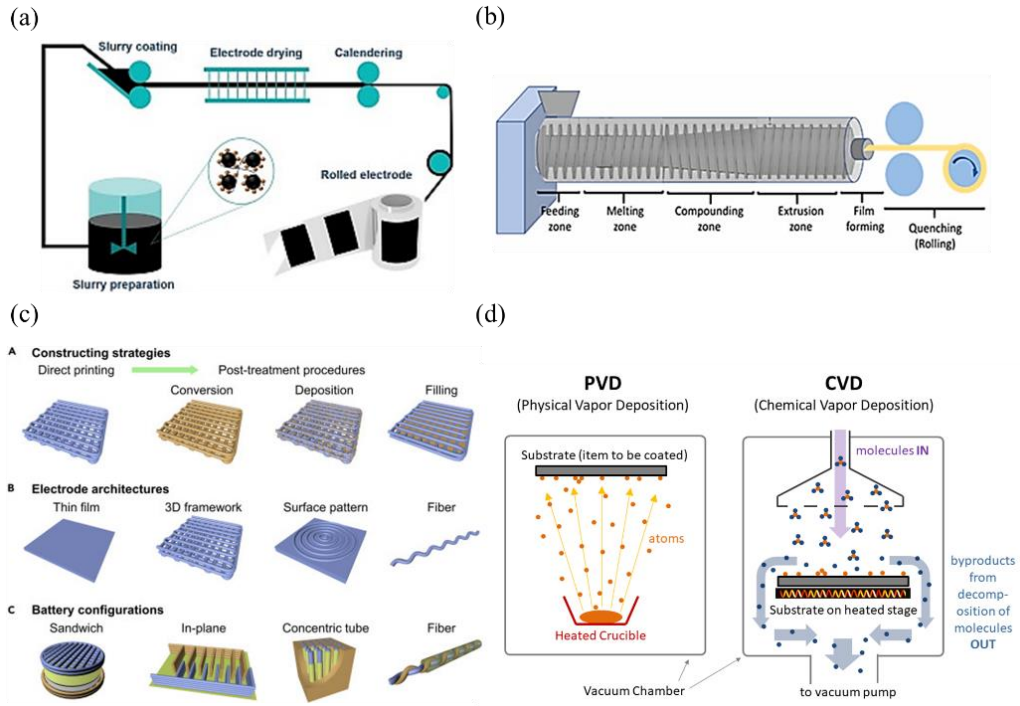

Figure 1. 3: Schematic illustration of **(a)** wet coating processing technique[173] **(b)** melt extruder **(c)** 3D Printing Designs on Battery Structures[174] and **(d)** thin film vapor deposition methods (PVD and CVD)[175]

1.3.5 Pressing Techniques

The assembling of SSBs using pressing techniques considers mainly three aspects: i) the densification of the SE, which should ensure good ionic conductivity, ii) the compactness and chemical stability of the composite cathode (formed by the CAM, an ionic conductive filler and an electronic conductive filler) and iii) the good physical contact between electrode and electrolyte, necessary to reduce the interfacial resistance. Materials are generally placed in form of powder in specific molds and pressed uniaxially, isostatically, or pseudo-isostatically to form green pellets. The control of the pressure and the application time is relevant parameters that will depend on the material properties and required density. The process may or may not be followed by a sintering step at elevated temperatures.

The process of uniaxial pressing leads to the compaction of the powder in the

shape of dies using a rigid punch or piston in a single axial direction. The presses can be mechanic or hydraulic. The method is not expensive and suitable for bulk production, but the uniformity of compaction is a major challenge. This technique is used for the green densification of ceramics before sintering with a pressure of fewer than 200 MPa. Isostatic pressing helps to attain uniform densification since the compaction is achieved by isostatic pressure imposed by the liquid or gaseous medium. The process offers flexibility in shape and dimensions that can be controlled by the pressing medium. However, scalability is a limiting factor because of processing time and tooling costs. Pseudo-isostatic pressing is also utilized to trap the powder within a die so that axial compression produces lateral pressure as well [176]. This process helps to achieve fast and uniform densification [176].

Generally, the total ionic conductivity in a SE is ruled by grain and grain boundary contributions, the latter being greatly influenced by the efficiency of densification (apart from other factors like material property, grain size, misorientation angle, etc.). Depending on the thermo- mechanical properties of the chosen material, the densification process can be temperature-assisted; which involves annealing the pressed green pellets in a controlled atmosphere. This generally implies a limitation for processing certain composite cathodes, or cathode/SE bi- layers, since the temperature can induce chemical reactivity among the elements. Separate densification processes should be followed for electrode and electrolyte, although later cell assembly will generally end-up in a significantly high contact resistance at the interface. There have been several advancements in pressing techniques to face these challenges, mainly aiming to reduce the maximum processing temperature. Depending on the mechanical properties of materials, densification processes can be classified mainly into two: cold pressing, a pressure- driven process; and sintering, which is temperature-driven with or without pressure.

1.3.5.1 Cold/low temperature pressing

Firstly, as reported by Hans et al. in 1966, cold pressing is a pressure-driven densification process at room temperature, initially used for metal densification. [177] Later on, this technique was improved in aspects like the mode of pressing and assistance of temperature and is widely used for a wide variety of materials processing, including commercial manufacturing of batteries. Indeed, calendering, a crucial step in current commercial battery technologies, is a form of (low) temperature-assisted pressing for continuous processing. It consists of smoothing and compressing a material (generally laminates) by passing a single continuous sheet through many pairs of heated rolls, also called calenders. Calendering is a step that commonly follows tape casting [178] as well as extrusion [20], to ensure the compactness of the laminates and assemblies. The main advantage of this processing is the easy low-temperature densification and hence it is recognized for large-scale fabrication. But is limited to either laminates or free-standing membranes, with soft mechanical properties of materials or with the addition of polymeric binders, not in the case of purely inorganic batteries that have hard materials such as ceramic oxides. This process can be used for the densification of cathode laminates, free-standing electrolytes, or even electrode-electrolyte multilayers. Cold pressing at temperatures lower than 100 °C has also been adopted for polymer or composite SE compaction in SSB fabrication [179]. But the ceramic oxide-based inorganic solid-state batteries are still beyond the scope because of their high-temperature requirements for densification.

Additionally, cold pressing is often used for the preparation of sulfide-based soft-SEs, since their mechanical properties allow them to achieve strong compactness at grain boundaries and effective solid-solid interfaces with simple pressure [100]. The process has attracted much interest and R&D progress in the direction of scaling-up for sulfide-based SSBs since it does not need any heat treatment (Figure 1. 4a), which can cause reactivity with cathode materials or

conductive additives. Nevertheless, remaining challenges associated with the ability to reach high enough density, ionic and electronic conductivity requirements at the electrolyte and/or the cathode, along with general mechanical, chemical, and electrochemical compatibility issues at the cathode-electrolyte interface are still to be solved [100], [112]. Again, it should be noted that cold pressing is generally incompatible with the processing of ceramic oxide electrolytes because of their hardness, and hence typically need high-temperature sintering to achieve high density and required conductivity. As an exception, a recent report has shown the implementation of a cold-pressed LISICON-based amorphous oxide as SE in SSB fabrication [180].

1.3.5.2 Temperature assisted sintering

Densification by sintering involves grain growth and atomic diffusion that leads to particle fusion through mass transport, which normally needs a thermodynamic driving force. The conventional sintering process of ceramics is driven by long-duration firing at high temperatures typically above 1000 °C (Figure 1. 4b) which depend on several factors such as the nature of the material, particle size, sintering atmosphere, etc. [181] In battery technology, high-temperature sintering is typically used at the lab scale for the preparation of ceramic oxide electrolytes in all categories mentioned under section 1.3.5.2. However, the needed processing steps at high temperatures generally make this process incompatible with the vast majority of electrode formulations, since the high temperatures needed generally cause chemical reactivity between the components [182]. In this sense, there are several alternative approaches that allow for reducing the densification temperature have been recently explored. Among these, one can mention hot (isostatic) pressing, [183]–[185] flash sintering,[186] microwave sintering[187]–[189], cold sintering [190], [191], and field-assisted or spark plasma sintering[192], [193]. Initial trials for full cell SSB fabrication at the lab scale have already been reported with spark plasma sintering. [194]–[197] However, spark plasma sintering still requires rather high

temperatures (between 650 and 850 ˚C). And, it is still necessary to bring down the temperature and duration of the process even further to enable their application for a vast range of potential materials.

Cold sintering (Figure 1. 4c) ensures a reduction of 100–300 ◦C from the conventional sintering temperature. The technique has achieved major developments towards solid-state battery fabrication for SEs like LAGP ($Li_{1.5}Al_{0.5}Ge_{1.5}P_3O_{12}$) [198], $Li_{1.3}Al_{0.3}Ti_{1.7}(PO_4)_3$ (LATP) [199], LSZG ($Li_{13.9}Sr_{0.1}ZnGe_4O_{16}$) [200], cathode- LFP ($LiFePO_4$) [201] as well as anode- LTO ($Li_4Ti_5O_{12}$) [202]. But the necessity of a solvent makes the technique more challenging when the different components need to be integrated with a full device due to the formation of non-conductive byproducts at the grain boundaries. Especially the water-based additives can cause mixed (lithium + proton) conductivity which is detrimental for battery performance.[203] Some initial trials were made by cold sintering for the full cell assembly, where, the components are densified separately using solvents and the full cell contains either polymer or liquid electrolyte at interfaces.[204], [205] Hence a co-sintered complete oxide-based inorganic SSB remains elusive under cold sintering.

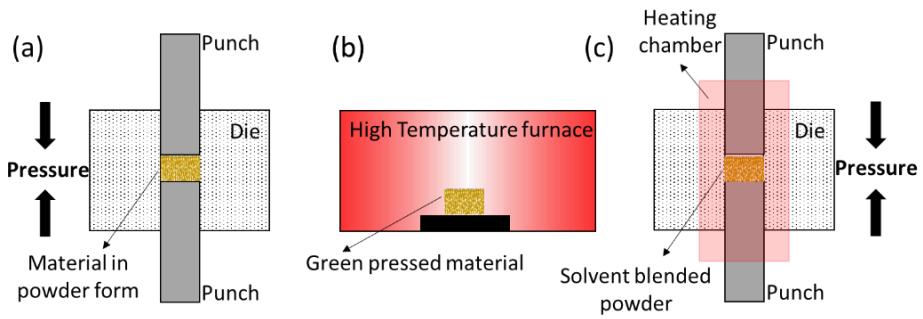

Figure 1. 4: Schematic illustration for material densification by means of (a) Cold pressing (b) High temperature sintering and (c) Cold sintering

1.3.6 Selection of processing technique

Concerning the prospect of large-scale production wet coating is the most

suited technique. The wet coating allows the processing of oxides but solvent compatibility needs to be considered especially when the interface compatibility with CAM will be a concern. Printing techniques are gaining increasing interest, but their application in the field of solid-state batteries is relatively new, and their use will probably be limited to particular applications, such as wearable electronics. Thin film vapor deposition techniques seek attention due to their applicability in a wide range of materials which include cathodes, anodes, and electrolytes. The materials can be processed with high purity and controlled stoichiometry. But low throughput limits its scalability and at the same time makes it suitable for interface processing and micro battery fabrication.

Oxides are generally processed by high-temperature sintering but the method is challenging for SSB fabrication due to thermal-induced interface reactivity between the electrolyte and active material (see section 1.4). The newly emerging cold sintering technique is bridging this gap by reducing the densification temperature of oxides to a limit at which the interface remains unaffected. But the necessity of solvent is challenging since it can induce reactivity among the components in SSB fabrication. In this context, a new approach needs to be investigated that allows processing at a lower temperature without the use of any solvents in such a way it assures good interface contact between components with negligible reactivity.

1.4 Interfacial challenges for full cell development

Contrary to current LIBs, in which the liquid electrolyte is wetting the cathode and anode so that it ensures the transfer of Li-ions, SSBs require well-controlled physical contact between the individual components and materials. The requirements for the interfaces can be summarized as follows: i) intimate contact presenting low resistance to Li transfer, ii) stable interfaces to promote long battery lifetime. In this section, the importance of integrating the interface

layers during the cell processing together with challenges related to materials interfaces will be discussed in detail, suggesting industrially-viable solutions (Figure 1. 4).

In SSB, several solid-solid interfaces can be found between the different components and materials. The cathode is a composite composed of a CAM, a solid ionic conductor which can be the same SE material as the one used as the separator and electrically conductive additives (typically carbonaceous materials), and the ensemble is designated as the composite solid cathode. Hence, several interfaces coexist such as between the CAM and the SE, between the conductive additive and the CAM (and/or the SE); and finally, the interface between the current collector and the cathode is also of importance. At the anode, the major interface is between the Li metal and the SE; at the SE, interfaces emerge if the SE is a composite material. It is of paramount importance to redesign and adapt the production chain of batteries to the solid-state technology, taking into account the coexistence of the different interfaces and their corresponding physical properties. Possible processing techniques for each component are presented in Figure 1. 4.

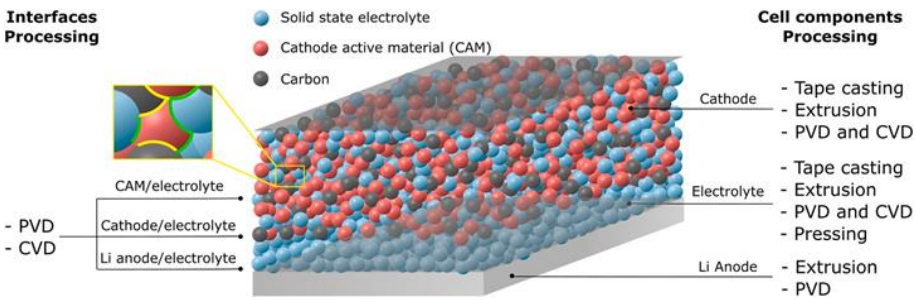

Figure 1. 4: Schematic of the battery components present in a solid-state battery containing a Li metal negative electrode (grey bottom), the SE (blue balls), the CAM (composed of CAM -red balls-, conductive carbon additive black balls, and SE). The grey upper plane represents the current collector. The processes that could be applied for each component are listed in the column on the right- hand side whereas the processes for the interfaces are listed in the left-hand side column. The inset shows the different interfaces present in the cathode (green and yellow lines represent the CAM-SE and CAM-conductive additive interfaces, respectively).[135]

1.4.1 Interfaces at composite solid cathodes

Cell integration leads to many interfaces at the cell component level (electrode/electrolyte) as well as at the composite electrode level (CAM/ electrolyte, current collector/electrolyte material), and interfacial problems account for much of the difficulties encountered in the course of realizing an SSB. Poor contact is a major source of charge accumulation and mass transfer resistance between electrode materials, SE, and the current collector. In some cases, performance can be enhanced by maximizing the contact area between CAM, ion-conductive phase, and electron-conductive phase.

However, volume changes of the electroactive cathode particles during electrochemical cycling (mechanical challenges) and the thermal and electrochemical stability of electrode and electrolyte materials (chemical challenges) are also major causes of cell impedance growth and cell failure. These are described below in more detail together with technical approaches to overcome them

1.4.1.1 Chemical and electrochemical challenges

Interfacial side reactions resulting in the diffusion of elements and possibly the formation of an interphase between a SE and a CAM are generally thermally-induced processes. The temperatures required in certain processing techniques (which in turn will depend on the selected electrolyte, *vide supra*) will thus have a strong impact on the chemical stability between the two materials. As previously mentioned, some processing techniques require high temperatures to densify the materials together and to decrease the interfacial resistance, particularly for oxide-based electrolytes (high-temperature sintering, section 1.3.5.2. Thermal degradation of positive electrode materials in contact with SEs often leads to new phases, most often unwanted products, which cause high interfacial resistance leading to severe degradation of the electrochemical performances [196], [206]. Such chemical reactivity between the SE and the CAM has also been observed after operation at room temperature [207] since

oxidation of the anion by reduction of the transition metal is often favorable for many cathode/conductor couples [208]–[210]. On the other hand, the reactivity between impurities adsorbed at the cathode surface and the SE is also to be taken into account, *e.g.*, carbonates and other species are detrimental, as reported for sulfide solid-state cells [211]. A better understanding of the kinetic and thermodynamic reactivity pathways between the CAM at different states of charge, surface species, and the electrolyte is thus key for determining the electrochemical performance of such systems. Therefore, to overcome the above-mentioned challenges, the approaches listed below should be taken into consideration to obtain an SSB with adequate cell performance.

Stable electrolyte-active materials combinations: When designing a solid-state cell, appropriate combinations of materials and adequate processing techniques must be identified to ensure the chemical and electrochemical stability of the material, and decomposition interfacial products must be equally considered in the design of composite cathodes. It is essential that the decomposition products exhibit poor electronic transport, otherwise continuous decomposition will occur.

Figure 5a summarizes DFT-computed chemical mixing reaction energies between fully lithiated CAM and electrolytes. Sulfide and thiophosphate are less stable when combined with oxide cathodes than with $LiFePO_4$, as predicted from chemical mixing calculations [207] and in explicit interface calculations [212]. On the other hand, oxides and phosphate SEs exhibit improved chemical stability with oxide cathodes compared to sulfide SEs. They are also predicted to be compatible with LFP, though [207]. These calculations represent a powerful tool to identify appropriate matching of materials, however, further research is needed to understand the impact of the presence of third species such as conducting additives, or the reaction atmosphere. Additionally, a much higher reactivity is expected for (partially) delithiated CAMs and the results might be chemistry-dependent within the same family of materials.

Multi-layer configurations: in which the catholyte and the SE are different, represent a related strategy that has been successfully demonstrated. Several examples can be found in literature, where combinations of different inorganic SEs are complementarily used. As an example of a fully inorganic cell, LATP has been used as a catholyte when using an NMC cathode and a β-Li_3PS_4 separator, allowing to employ of LATP in a bulk-type SSB without a sintering step of the full cell, which would result in undesired decomposition interfacial products at the cathode [213].

Artificial coating layers: The use of protective layers between the cathode material and the SE is a demonstrated method to extend the experimentally-measured electrochemical stability window at the cathode/SE interface and avoid electrolyte decomposition when subjected to high voltage. The coating material must be an ionic conductor and electronic insulator, following the same operating principle of the SEI in liquid cells. Moreover, the potential drop will be sufficient only if the electronic conductivity of the coating is lower than that of the SE.

The material choices for cathode/inorganic SE interfaces are larger, also because the requirements for ionic conductivity are less stringent than the bulk electrolyte as coatings must be thin uniform layers [208]. Therefore, oxides like $LiNbO_3$ or LTO [207], [214], [215] or phosphates like Li_3PO_4 [148] can successfully stabilize cathode/inorganic SE interfaces leading to improved cycling stability. These materials exhibit thermodynamic stability limits close to 4 V, which might be further extended by slow oxidation kinetics [61]. However, careful assessment concerning specific cathode/SE combinations is still needed. As discussed, previously, a recent computational screening study of chemical reactivity between pairs recommends phosphate coatings for sulfide SEs and oxide coatings for oxide SEs as general guidelines (see Figure 1. 5a) [207].

The coating techniques for cathode active material particles and electrode sheets have been recently reviewed by Du et al. [216] The most common coating techniques include magnetron sputtering (MS), spark plasma sintering, pulsed laser deposition (PLD), sol-gel synthesis, chemical vapor deposition (CVD), atomic layer deposition (ALD) and wet coating techniques such as spray coating, spin coating, and solvent casting. More recently, sol-gel synthesis has been used to prepare various types of core-shell active material particles, [217]–[219].

In situ formation of cathodic-SEI (CEI): As illustrated in Figure 1. 5b, the formation of a cathodic SEI (CEI) could help enhance the SSB performances and maintain long cycle life. A possible candidate as cathodic-SEI (CEI) former is the salt lithium bis(oxalato)borate (LiBOB). PEO electrolytes containing the salt cocktail LiTFSI-LiBOB-$LiNO_3$ showed electrochemical stability up to 4.6 V (by floating test) and good cyclability in NMC111/Li cells [220]. Another candidate as CEI former is AlF_3. This Lewis acid was recently proposed as an additive, with the double function of the current collector passivating agent and CEI former [221]. Its use as an additive in poly-DOL (poly-dioxolane) electrolyte allowed cycling with NMC622 as cathode material with a cut-off voltage of 4.2 V. Additionally, the formation of the CEI should be tuned to enhance the SSB performances and maintain long cycle life. As previously noted, Li et al. demonstrated that it is possible to obtain good cyclability through the combined use of cathode material coating and electrolyte additives [222]. In this specific case, LiBOB and $LiPF_6$ were used as salt additives (together with LiTFSI as the main salt), the first one as CEI former and the second as passivating agent for the current collector.

Interfaces with current collector: Current collectors are a fundamental part of the battery since they ensure the transport of electrons to and from an external circuit and, often, they are used as mechanical support for the casting of the composite cathode on top of them. A low resistive interface is important to limit

localized high current densities and consequently a higher internal resistance and decreased round-trip efficiency. Often overlooked in the literature, these interfaces might present chemical and electrochemical instability issues that need to be addressed [167]. In general, aluminum current collectors are the preferred choice for the cathode side, widely used with lithium transition metal oxides up to 5 V *vs.* Li/Li^+ [223]. The electrochemical stability of the current collector also needs to be considered. Koerver et al. investigated the effect of upper voltage limit in SSBs with NMC-LPS composite cathodes [224]. Alternative materials have also been explored aiming for better contact with the CAM and/or gaining flexibility in the cells. For example, carbon nanotubes (CNT) sheets as current collectors in sulfide-based SSBs [225], PEO polymer and Cu-coated carbon fibers [226], Ag micro-flakes as a conductive layer on a stretchable carbon–polymer composite [227] and Ni–Al–Cr current collectors for oxide-based SSBs, when high-temperature sintering steps are required [228], [229].

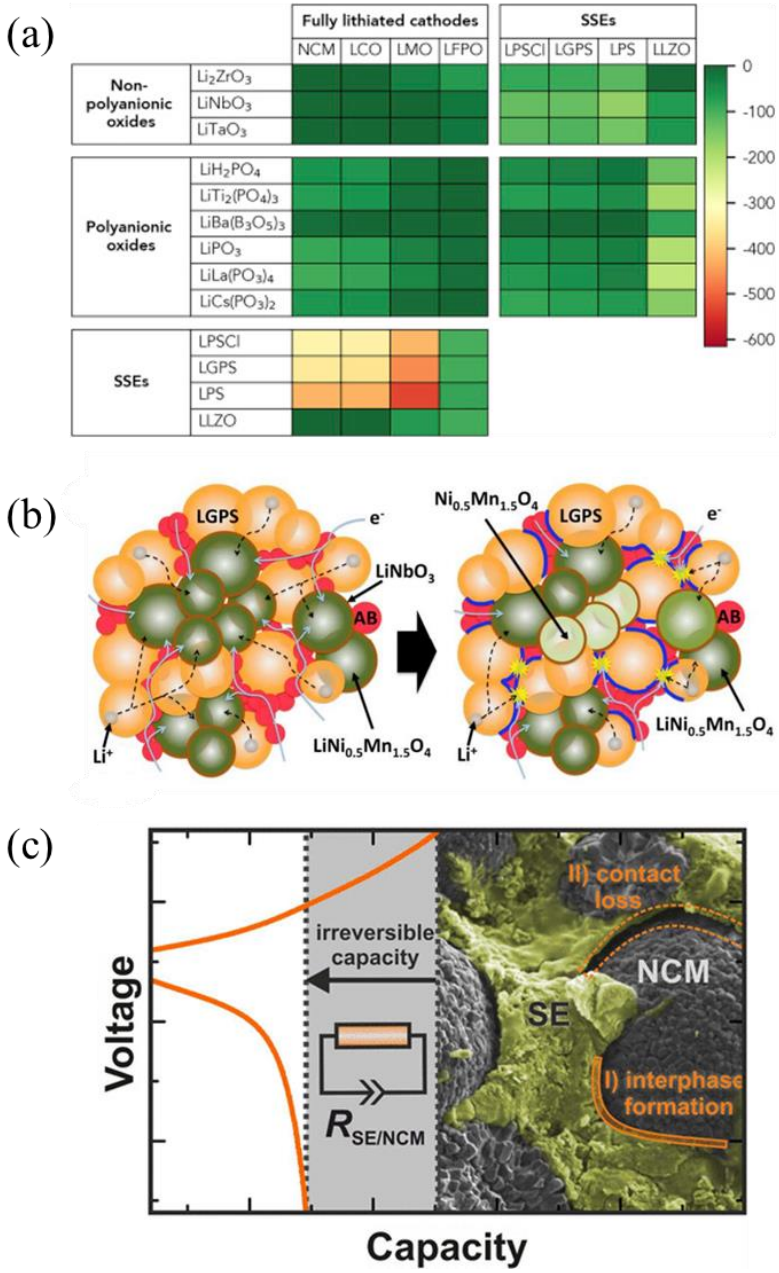

Figure 1. 5: **a)** DFT-computed chemical mixing reaction energies of fully lithiated cathode/SE, fully lithiated cathode/coating, and coating/SE interfaces in meV/atom [207]. **b)** Schematics of the interfacial reactions in a composite solid cathode under charge/discharge operation. The cathode contains LNMO as CAM (green particles) coated with $LiNbO_3$, LGPS SE (orange particles), and acetylene black (AB) as electron conducting additive (pink particles). Reversible Li intercalation occurs between the LNMO cathode and the LGPS electrolyte. The $LiNbO_3$ coating layer acts as a buffer to facilitate Li diffusion at high voltages. In contrast, oxidative decomposition of LGPS occurs at the LGPS/AB interface during the charging process, which causes irreversible

capacity loss. The decomposition layer could isolate the delithiated LNMO phase from ion and/or electron percolative pathways resulting in capacity fading upon cycling [230]. **c)** Capacity fading caused by the contraction of the CAM upon delithiation resulting in contact loss between the SE (β- Li_3PS_4) and CAM particles (NCM, referred to as NMC in this review) observed by ex-situ SEM [231]

All electrode materials experience mechanical stress during electrochemical cycling. This stress is caused by the volumetric and structural changes during reversible Li-ion insertion and extraction. The anisotropic cell parameter variation of typical Li-ion cathode materials ranges between 2% (*e.g.*, between $LiCoO_2$ and $Li_{0.5}CoO_2$ in the *c* direction) to >5% (between $LiFePO_4$ and $FePO_4$ in a direction) leading to cracks and loss of contact at the interfaces between CAM, electronic conducting material and SE in the cathode (see Figure 1. 5c). Such mechanical fatigue is a barrier for electronic and ionic transport and has been associated to capacity fading and battery failure [232]–[234].

The mechanical properties of the interface between CAM and SE differ strongly depending on the choice of electrolyte. Rigid ceramics like oxides (*i.e.*, with a high Youngs modulus, over 100 GPa, see section 1.2.2.1) will accumulate important local stresses that could lead to fracture of the ceramic cathode, whereas ductile ceramics, like sulfides (~20 GPa [235]), thiophosphates or polymers (<1 GPa) will support mechanically the volume expansion more effectively. The physical contact between the solid electrolyte and the CAM will be affected (Figure 1. 5c). This enables keeping good interfacial contact during lithiation/delithiation. Several solutions have been proposed to mitigate the impact of the mechanical degradation of the interfaces between the electrolyte and the CAM:

Use of conductive additives: To avoid any electronic contact loss compulsory for electron collection and power density, conductive additives are key to maintaining electronic conductivity within the electrode despite the volume changes, although this solution does not solve ionic transport losses. In particular, high aspect ratio conducting additives, *e.g.*, carbon fibers, allows for

mitigating the loss of electronic conduction between CAM particles and current collector with the progress of cell cycling [236].

AM morphology: Particle size and morphology play a critical role not only in the packing density of the material but as well on the contact surface between the materials composing a solid electrode. In this sense, decreasing the size of the CAM particles increase the surface area of exchange of the CAM with the SE and conductive additive [237]. With smaller particle size, the mechanical stress and effective volume expansion per particle are less important.

External conditions: Mechanical integrity of the electrode and the complete cell can also be achieved by maintaining external forces such as pressure on the cell. This has been particularly proven for sulfide electrolyte-containing cells [238], [239]. Thanks to the soft properties of these materials, the constant pressure facilitates the SE reorganization and provides constant intimate contact with the CAM and conductive additive.

1.4.2 Li metal/electrolyte interface

In solid-state batteries, Li metal is the mostly used anode material, independently of the solid electrolyte. However, severe issues need to be overcome to achieve good cyclability and enhance cycle life and high power: i) accommodate the volume change produced during the plating/stripping process, while maintaining the interfacial contact between anode and electrolyte; ii) hinder the formation of lithium dendrites, which could lead to short-circuiting; iii) protect the electrolyte from degradation due to contact with lithium metal [240].

Mechanical stability and lithium dendrites formation

During battery cycling, lithium metal is constantly electrodeposited and stripped on/from the anode surface leading to a constant evolution and thickness change that alters both the mechanical and electrochemical properties of the interface. The accommodation of this extra layer is therefore extremely

dependent on the mechanical properties of the electrolyte, and on the ability to accommodate additional stress. Furthermore, inhomogeneous lithium plating/stripping leads to low coulombic efficiency, continuous electrolyte degradation, and to the risk of short circuits. Additionally, the local accumulation of lithium metal deposits results in inhomogeneous pressure distribution, thus contributing to a further decrease in the mechanical stability of the cell. The dendrite formation mechanism has been correlated to the mechanical properties of the SE (*i.e.*, shear modulus, density, and presence of pores), physicochemical properties of the SE (*e.g.*, electronic conductivity), or interfacial issues (composition and instability) [241]–[244]. There are different strategies to enhance the electrodeposition process and prevent dendrite formation, including the use of external pressure [245], SE or Li surface treatments [165], [246], [247], use of 3D lithium metal anodes [248], an increase of Li metal wettability and stabilization of the interface through interlayers [160], [216], [249]–[251]

Chemical and electrochemical stability

The extremely reactive nature of Li metal favors electrolyte decomposition on its surface. The electrochemical stability of the electrolyte-anode assembly depends on the nature of the SE and, more particularly, on the specific composition of the surface. If the electrolyte is degraded, or if a stable interlayer is not formed, the application of an artificial interlayer may be necessary.

Oxide-based SE is usually stable with Li metal thanks to the low reduction potential of this category of materials. Chemical and electrochemical reactions occur for materials containing certain elements that oxidize and reduce the operation potential of the battery. [157], [252], [253] [253] The chemical inhomogeneities at the surface of garnet SEs could lead to instabilities against Li metal, in particular at the grain boundaries [254]. For example, Ge reduction in LAGP electrolytes with Li metal negatively affects the SE properties [255].

In this case, the addition of protective interlayers is necessary, *e.g.* metallic Ge [256], conductive polymer coatings [257], [258], glass ceramics [259] or composite films [67]. LiPON electrolytes, widely used for micro-batteries, have been re- ported to be thermodynamically unstable against Li metal [61], [91], [260]. Therefore, LiPON electrolyte does not require any protecting interlayer and can be even used as a protective coating for other types of SE.

Sulfide materials show strong reducing properties when in contact with Li metal. The solid electrolyte interface (SEI) layer formed at the interface can be tailored by tuning the sulfide material composition. For instance, the presence of Ge in $Li_{10}GeP_2S_{12}$ leads to a thinner SEI layer upon cycling of symmetric cells [261], compared to samples prepared with Si, such as $Li_{10}SiP_2S_{12}$ [262]. Other strategies used to stabilize the sulfide electrolyte with Li metal include the use of a Li metal alloy as a protective layer on top of Li metal [263], [264] or a polymer electrolyte inter- layer can be used [265].

1.4.3 Summary of interfacial challenges

In summary, a cathode electrode composed of at least three materials (cathode active material, catholyte, and conductive additive) leads undoubtedly to many challenges at the interfaces. These are electrochemical, chemical, and mechanical challenges. Chemical and electrochemical issues are correlated to the challenges of processing and cycling cathode components. Research efforts should be concentrated on finding the best combination of materials to avoid premature degradation, and trying innovative configurations. It is not to forget that the cathode-electrolyte interface is still overlooked, mainly due to technical challenges in its study. Understanding such interface layers would shed some light on developing new composite solid cathodes.

The nature of the active material and its restless volume expansion and contraction throughout cycling is naturally affecting the physical contact between the three materials. To overcome this mechanical challenge, it is

recommended to focus on adapting active material particles so they have a limited volume expansion at the outer particle level or adapt the solid electrolyte so it can follow the volume changes with deformable properties.

On the other hand, despite assured higher density, the use of Li as the anode is accompanied by certain challenges. The most important is dendrites growth, which has hindered insofar the development of Li-metal rechargeable batteries. In the last years, much progress has been reported through the application of several strategies, such as the application of pressure, nano- structuration, application of interlayers, etc. This last approach, in particular, is a promising, versatile, and easily scalable tool to improve cyclability, and is effective with inorganic electrolytes. The application of interlayers is also necessary to address the chemical and electrochemical instability of some SSEs, such as sulfides and NASICON-type SSEs. Most probably, the use of Li metal anodes with SEs will rely on the application of this kind of solution.

In the context of the thesis, the cathode is comprised of a composite of selected CAM (NMC) and SE (LATP) along with the carbon conductive additive. So, the interfacial challenges; both (electro)chemical and mechanical, at the cathode will have multi-sources from each component. And they need to be investigated initially upon processing and later during the cycling. On the anode side, the chemical and mechanical compatibility of SE (LATP) against lithium metal would have to be addressed by using one of the adequate interfacial engineering techniques that have already been reported, but is out of the scope of this work.

1.5 Conclusions and thesis framework

The success of SSBs as advanced electrochemical energy storage systems must involve necessarily a further development of the technology in terms of advanced materials, processing techniques (for cell components manufacturing and protective coatings), and, most importantly, full cell integration. In this

sense, a deep understanding of interfaces and interphase formation upon battery fabrication is critical for the achievement of high-performing and long-lasting cells.

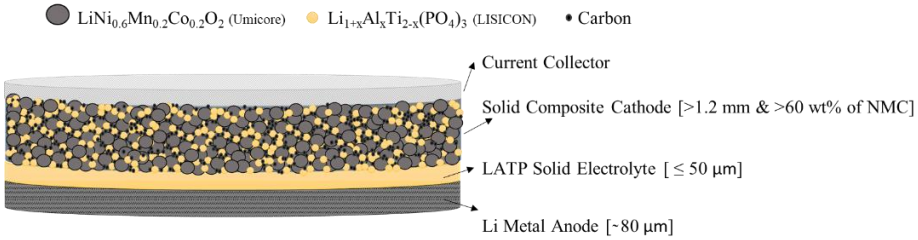

Figure 1. 6: An SSB model that conveys the energy density of >300 Wh/kg (>700 Wh/l), composed of a thick composite cathode, thin solid electrolyte separator thin lithium metal anode, and aluminum current collector. The composite cathode consists of NMC active material, LATP ionic conductive filler, and carbon electronic conductive filler in the weight ratio of 65:30:05 respectively.

The system chosen for this thesis (Figure 1. 6) is composed of a thick composite solid cathode based on NMC (CAM), LATP (SE), and carbon conductive additive; a thin SE layer of LATP which plays the role of electrolyte as well as separator and a lithium metal anode. A theoretical calculation was performed using MATLAB (Figure 1. 7) for optimizing the cell parameters (NMC weight percentage in the composite, active loading, and electrolyte thickness) to ensure energy densities >300 Wh/kg and >700 Wh/l. Figure 1. 7a indicates the dependence of NMC wt% on energy density, which is more or less linear. From previous internal works, a ratio of 30 wt.% of LATP was chosen to assure ionic conductivity and mechanical strength. And carbon has fixed to 5wt% which is equivalent to the conventional lithium-ion batteries. So, the composite ratio will be- NMC: LATP: carbon = 65:30:05. NMC and LATP have densities of nearly 2.9 and 4.8 g cm^{-3}. In that sense, the chosen composite wt.% offers almost equal volume content of these two elements which is a key factor in terms of conductivity. Figure 1. 7b shows the correlation between active loading (effectively the cathode thickness) and energy density. There is a saturation of energy density above 5 mAh cm^{-2}. Anode loading has been set to 15 mAh cm^{-2}. With these specifications, SE thickness should be below 50 µm

to effectively reach the desired energy density in the range of>300 Wh/kg and >700 Wh/l (Figure 1. 7c).

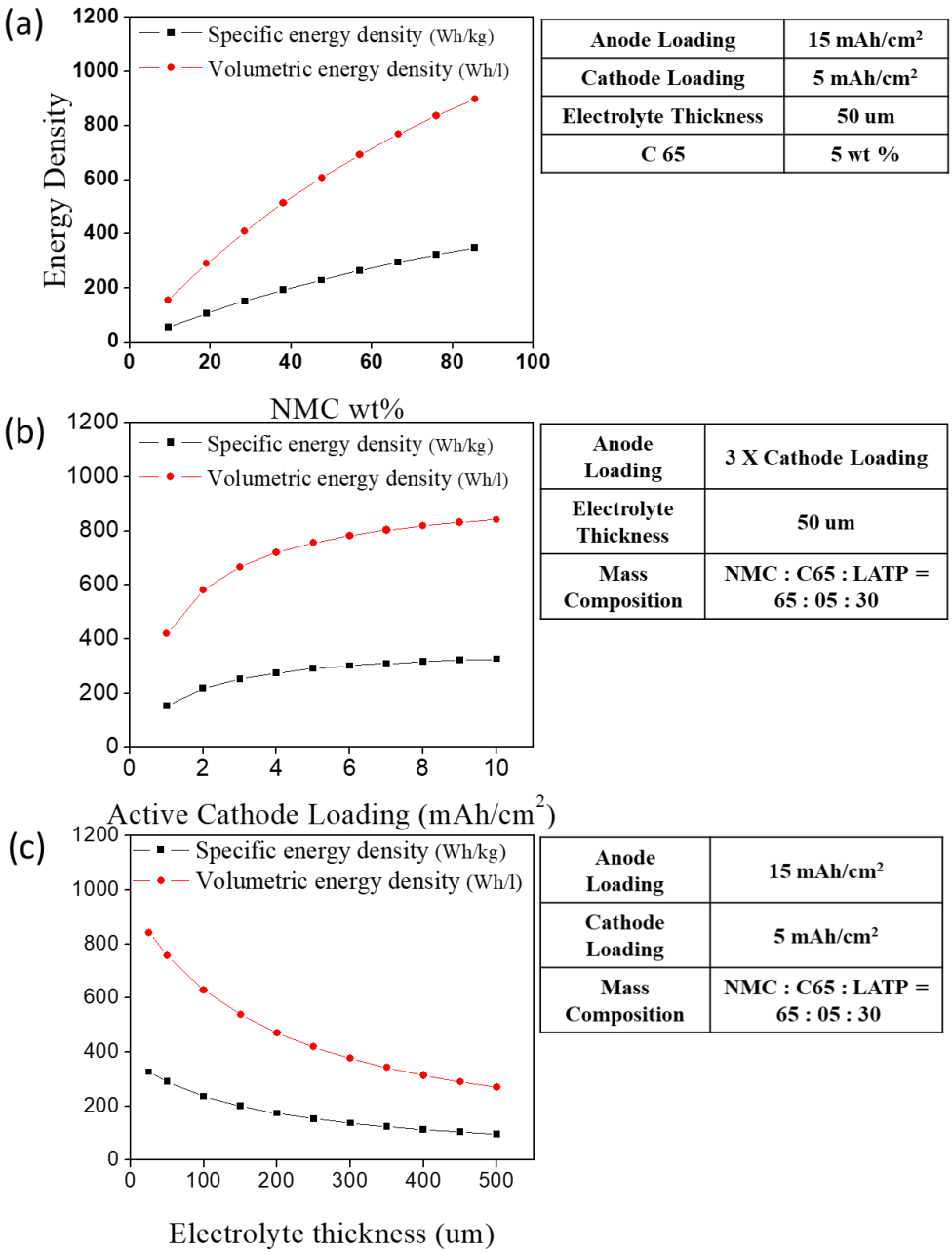

Anode Loading	**15 mAh/cm²**
Cathode Loading	**5 mAh/cm²**
Electrolyte Thickness	**50 um**
C 65	**5 wt %**

Anode Loading	**3 X Cathode Loading**
Electrolyte Thickness	**50 um**
Mass Composition	**NMC : C65 : LATP = 65 : 05 : 30**

Anode Loading	**15 mAh/cm²**
Cathode Loading	**5 mAh/cm²**
Mass Composition	**NMC : C65 : LATP = 65 : 05 : 30**

Figure 1. 7: Theoretical calculation of energy densities as a function of (a) NMC wt% for fixed loading of 5 mAh cm^{-2} and electrolyte thickness of 50 µm (b) active cathode

loading for fixed NMC wt% of 65 and electrolyte thickness 50 µm (c) electrolyte thickness for fixed NMC wt% of 65 loading of 5 mAh cm^{-2}.

But the realization of this model has multi-challenges since a co-processing technique is required for SSB assembly to assure good interface contact with negligible resistance. Hence the focus of the thesis will be on the (electro) chemical compatibility of selected components under processing conditions. A temperature of more than 1000˚C is necessary for the processing of ceramic oxide electrolyte (LATP), and it limits the co-processing of the battery stack since the composite cathode components will be reactive at this temperature range. There are previous studies about the thermal compatibility of NMC-LATP composite system, however, the necessity of carbon in the system was overlooked. [182], [266] Even if the intrinsic electronic conductivity is high,[267] NMC622 requires the use of an additive, generally carbon[268] to construct a conductive percolation in the cathode (extrinsic conductivity). An SSB composed of NMC-LATP composite cathode (without carbon) and LLZO electrolyte was previously reported, in which the electrochemistry was achieved at 100˚C with very low current densities.[269] So, our system: NMC+LATP+carbon represents a key step towards the realization of SSB and systematic and step-by-step evaluation was carried out in the thesis.

We first focused on the thermal compatibility of composite components to define threshold conditions such as heating atmosphere and temperature under which the composite remains stable. The reaction mechanism of the composite after the threshold values has been investigated to propose strategies for co-sintering of the proposed all-inorganic solid-state battery model. The strategies to enhance composite thermal stability were investigated in detail such as the impact of conductive additives and the role of a stabilizing agent. On the other hand, a novel low-temperature sintering technique has been optimized for reducing the sintering temperature of LATP down to the temperature threshold of the composite cathode.

CHAPTER 2: HIGH-TEMPERATURE THERMAL REACTIVITY AND INTERFACE EVOLUTION OF NMC-LATP-CARBON COMPOSITE CATHODE

2.1 Introduction

Cathode formulation is a key challenge in the transition from conventional liquid cells to SSB. In liquid cells, the electrolyte penetrates inside the porous cathode enabling the mobility of ions in and out of the electrodes. In a solid-state battery, this role is played by the catholyte, a solid ionic conductor which can be the same solid electrolyte material as the one used as the separator, but not necessarily. In both liquid and solid batteries, electrically conductive additives are also imperatively required (typically carbonaceous materials), and the ensemble of active material, catholyte, and carbon are designated as the composite cathode.

While considering the low extrinsic electronic conductivity of NMC compared to conventional layered oxides, it is necessary to have the electronic conductive filler in the composite. And, the selection of electrically conductive additives should be based on high electrical conductivity, but also on low density, cost, processability, thermal stability and diffusivity, and chemical stability against active material and catholyte. Different carbon types such as graphite and carbon black are typically used. The low density, purity, and high electrical conductivity of Ketjenblack (KB) make it a good choice among them.

Oxide-based ceramics such as LATP require temperature-assisted densification techniques, with temperature ranges typically around 1000 °C and above.[270] However, at such temperatures, the cathode components are not stable and can react to form resistive by-products as well as to the structural degradation of active material,[271]–[275] which leads to severe decay of the electrochemical performance. Ideally, the composite properties should remain unchanged, although chemical and structural modifications at the interfaces could be accepted provided Li ion mobility is not obstructed.[272], [276]

The aim of the current chapter is two-fold: to evaluate the impact of having a carbon additive as well as the impact of the heating atmosphere on the thermal compatibility of NMC-LATP-carbon composite. The reactivity between composite cathode components in the NMC622+LATP+KB system has thus been thoroughly evaluated. The composite ratio was chosen to be NMC: LATP: KB=65:30:05, as the weight ratio of carbon in the composite was maintained as same as in conventional cathodes (5%). NMC and LATP have a density of 4.8 g/cc and 2.7 g/cc respectively. So, their ratios were chosen in such a way they have more or less equal volume distribution. In that way, the composite has sufficient ionic and electronic conductive pathways, maximum active material utility, and compactness while implemented in SSB. A methodology has been designed to evaluate the impact of co-sintering conditions that includes fast assessment of the electrochemical properties of the annealed composite material in liquid cells, in-situ and ex-situ high-temperature X-ray diffraction (XRD), transmission electron microscopy (TEM) and X-ray photoelectron spectroscopy (XPS). Noteworthy our system includes electrically conductive additives, as cannot be eluded in cathode compositions. This is an essential aspect that has been often overlooked in previous works. [271], [272], [275] The threshold conditions at which the selected materials remain compatible have been determined given the unified effects of structural, chemical, and electrochemical stability of the components after heat treatments at different atmospheres and temperatures. From the combination of our observations, a degradation mechanism is proposed.

2.2 Results

2.2.1 Bulk crystallinity: X-ray diffraction (XRD)

2.2.1.1 In-situ high-temperature XRD

The structural evolution of the composite mixture NMC+LATP+KB (C-Mixed) at different temperatures and under air and nitrogen atmospheres was

followed by in-situ XRD (Figure 2. 1 a and b). Up to 500 °C only the expected peak shift towards lower angles due to the thermal expansion of the materials is observed for both atmospheres, which indicates that no major structural or chemical changes occur in the bulk of the materials. However, from 600 °C onwards, several prominent changes are detected. Under air atmosphere several NMC reflections become asymmetric (see for example (104) peak at $2d_{K\alpha_{Co}}$ = 52° (marked with an arrow)), and above 700 °C new reflections appear that can be indexed with a MO rocksalt phase ($Fm\bar{3}m$; $a = b = c$ = 4.0907(4) Å). These become intense as temperature increases, accompanied by complete degradation of layered NMC at 800 °C. Reflections corresponding to LATP also experience an apparent decrease in intensity from 700 °C, although new peaks corresponding to Li_3PO_4 (see for example reflection at $2d$ = 26°) emerge from 600 °C. From a qualitative phase identification analysis of the pattern at 800 °C under air it can be concluded that the main contributing by-products are MO [M=Ni (main)/Co/Mn], Li_3PO_4, spinel M_3O_4 and/or $Li_xM_2O_4$ [M= Co, Ni, Mn], anatase TiO_2 and [Li]metal-phosphates.

As expected, the thermal response and degradation by-products are different under nitrogen. Degradation also starts at 600 °C, with the formation of MO secondary phases. However, at 800 °C, there is no significant evidence for the presence of (Li)metal phosphates, while Li_3PO_4 and rutile TiO_2 can be identified.

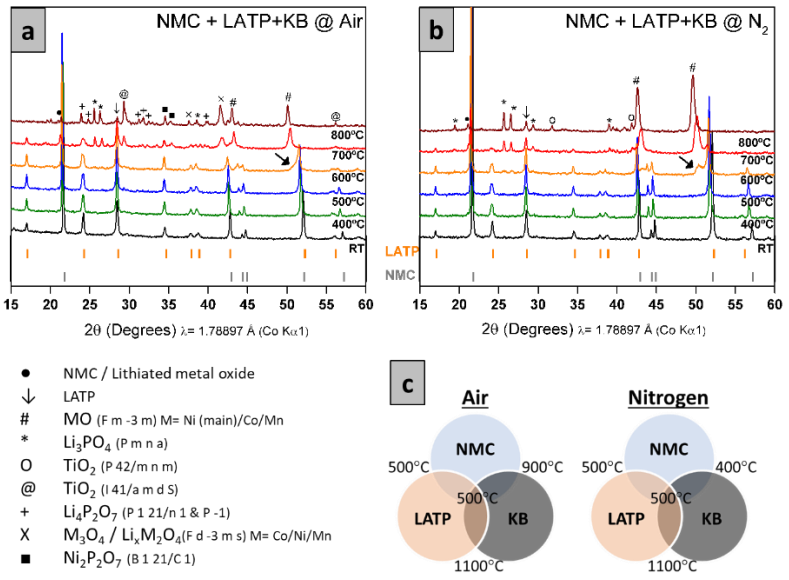

Figure 2. 1: In-situ thermal XRD data of NMC+LATP+KB (65:30:05) composite mixture for the selected temperatures ranging from 400 to 800 °C for an interval of 100 °C under **a)** open air and **b)** nitrogen atmospheres along with the list of identified secondary phases at 800 °C and standard peak positions for NMC and LATP. The arrows on 600 °C data at $2\theta_{K\alpha Co}$ = 52° in both cases locate the onset of NMC phase change **c)** Schematic illustration of the thermal stability limits of the different material combinations under air and nitrogen atmospheres.

To further understand the reactivity between the different components of the cathode composite, the binary combinations were also studied under both atmospheres (Figure 2. 2). Apart from the reversible unit cell thermal expansion, LATP maintains its crystal structure in the mixture of LATP+KB at least up to 800 °C, under both air and nitrogen atmospheres (Figure 2. 2 e and f). For the NMC+LATP mixture under air and nitrogen atmospheres, the temperature threshold and reaction by-products are similar to that of NMC+LATP+KB under air, except for slight differences in intensity ratios. This indicates that NMC-LATP reactivity is independent of the atmosphere and the presence of KB does not have a direct impact on the composite reactivity under air atmosphere.

Other than carbon oxidation (that was evident as the composite turned from black to grey after heat treatment but not observable from XRD), the NMC+KB

mixture does not show any apparent decomposition products under the air. However, NMC+KB reactivity is vigorous under nitrogen, starting from 400 °C onwards, and results in the complete decomposition of NMC, which evolves into metal oxides and is even partially reduced to the metallic elements at 800 °C. Interestingly, under nitrogen, the temperature threshold for NMC+LATP+KB as well as for NMC+LATP is 500 °C (see below), which is 100 °C higher than the NMC+KB threshold temperature. This indicates that despite KB promoting NMC degradation, LATP can partially hinder it. However, since the NMC+LATP+KB mixture remains structurally stable up to 500 °C under both atmospheres, the involvement of KB in the mixture reactivity under air has no supporting evidence from XRD data and reactivity seems to be localized between NMC and LATP.

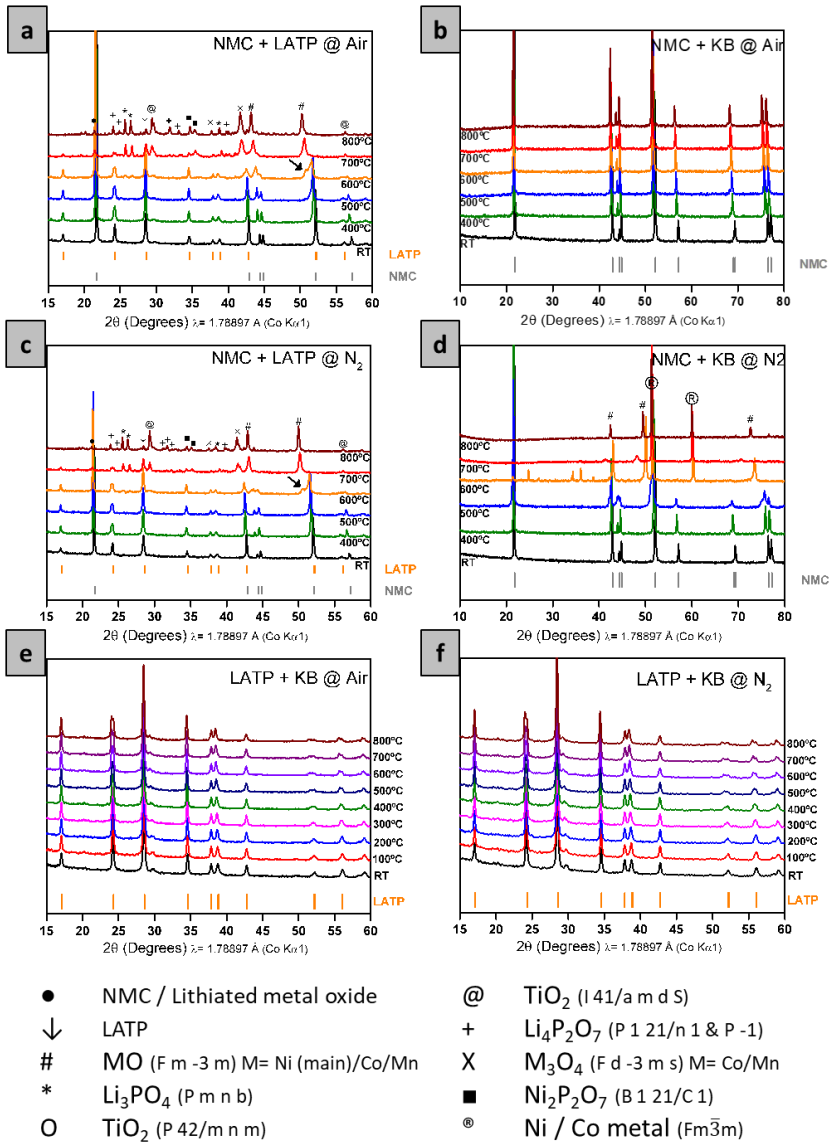

Figure 2. 2: In-situ thermal XRD data of composite combinations under different atmospheres for temperatures in the transition range [from 400ºC to 800ºC for an interval of 100ºC] along with the list of identified secondary phases at 800ºC and standard peak positions for NMC and LATP. NMC+LATP under **a)** air and **c)** nitrogen. NMC+KB under **b)** air and **d)** nitrogen. LATP+KB under **e)** air and **f)** nitrogen

In conclusion from the in-situ XRD analyses, the different combinations between LATP, NMC, and KB exhibit a complex reactivity scheme that is dependent on the atmosphere. The different stability threshold temperatures for

each possible combination are summarized in Figure 2. 1 c and in no case exceed 500°C for the full composite mixture.

2.2.1.2 Ex-situ XRD

Further analysis was conducted by ex-situ XRD of composites heated at temperatures close to the threshold limit; 400, 500, and 600 °C (C400-air, C500-air, and C600-air respectively). A longer time/step was used in the data acquisition to obtain a better signal-to-noise ratio and to shed more light on the degradation reaction of NMC material. In Figure 2. 3a, a close view of the most relevant NMC peaks is shown. C400-air sample resembles pristine NMC (except for a slight shoulder at (101) peak that comes from an overlap with LATP (018) peak at $2d = 36.52°$). An asymmetrical broadening of the peaks is observed for both C500-air and C600-air; the asymmetry being less pronounced at lower temperatures as highlighted for (104) peak. This indicates that transition metal redistribution and further secondary phase transition to spinel first and later to rocksalt-MO is possibly occurring from 500 °C onwards. Le Bail fitting of C600-air confirms the presence of NMC ($R\bar{3}m$), LATP ($R\bar{3}c$) and reaction byproducts- rocksalt-MO ($Fm\bar{3}m$) and Li_3PO_4 (Pmna), in agreement with what was observed from in-situ XRD at higher temperatures (Figure 2. 3b). A quantitative phase analysis by Rietveld refinement was unfortunately precluded by the variety of compositions of secondary phases. However, the average NMC lattice parameters obtained from this refinement indicate a slight volume increase from the pristine to C600-air samples (Table 2. 1), which is more prominent for the *c* direction. The O−O Coulombic repulsions between adjacent MO_2 layers that result from Li depletion could be at its origin. Indeed, Li and oxygen losses from the NMC layered structure, as previously reported,[277], [278] could explain the onset of NMC degradation.

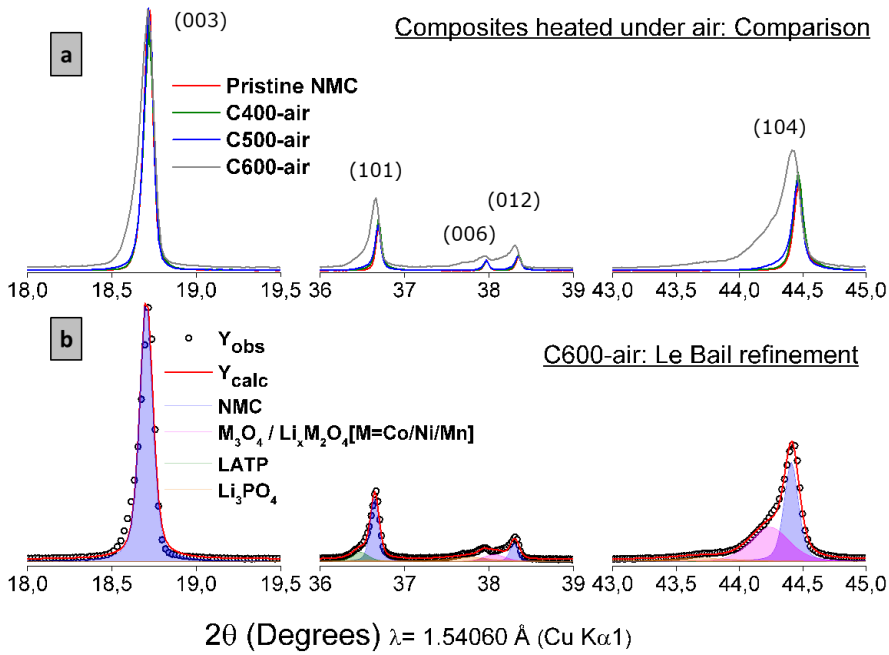

Figure 2. 3: a) Comparison of selected NMC diffraction peaks from ex-situ XRD measurements of pristine NMC and composites heated at 400, 500, and 600 °C under air (C400-air, C500-air, and C600-air). **b)** Selected peaks of C600-air X-ray diffraction pattern in which the colored area below the peaks indicates the contribution of the different phases (NMC ($R\bar{3}m$), LATP ($R\bar{3}c$), and identified secondary phases MO ($Fm\bar{3}m$) and Li3PO4 (Pcmn)) as obtained from Le bail refinement using FullProf.

Table 2. 1: The comparison of NMC and LATP unit cell parameters for pristine and heat-treated composites (500 and 600 °C under air atmosphere)

Lattice parameters	$LiNi_{0.6}Mn_{0.2}Co_{0.2}O_2$			$LiTi_2(PO_4)_3$		
	Pristine	C500-air	C600-air	Pristine	C500-air	C600-air
a=b (Å)	2.8679(4)	2.8692(4)	2.8721(4)	8.4804(4)	8.4858(4)	8.4852(4)
c (Å)	14.2044(4)	14.2081(4)	14.2198(4)	20.8823(4)	20.9232(4)	20.8917(4)

2.2.2 Electrochemistry: Galvanostatic cycling with potential limitation (GCPL)

Electrochemistry tests in conventional half-cell configuration using liquid electrolytes were used as a rapid assessment technique to measure the impact of

heat treatments on composite powders under air and nitrogen atmospheres above and below the threshold values determined by XRD (C400-air, C500-air, C600-air, C400-N2, C500-N2, and C600-N2). The results of the heat-treated samples were compared to those of the as-mixed (C-mixed) sample. It should be noted that we do not expect the same performance in solid-state cells as in the latter the only ionic conductivity channel will be the catholyte and the conductivity at solid-solid interfaces is more demanding. However, as shown below, liquid half-cell data is an effective proxy indicator for chemical and electrochemical modifications both at bulk and surface levels of electrode components, and it is expected that the formation of insulating secondary phases after the heat-treatment results in a similar capacity decrease.

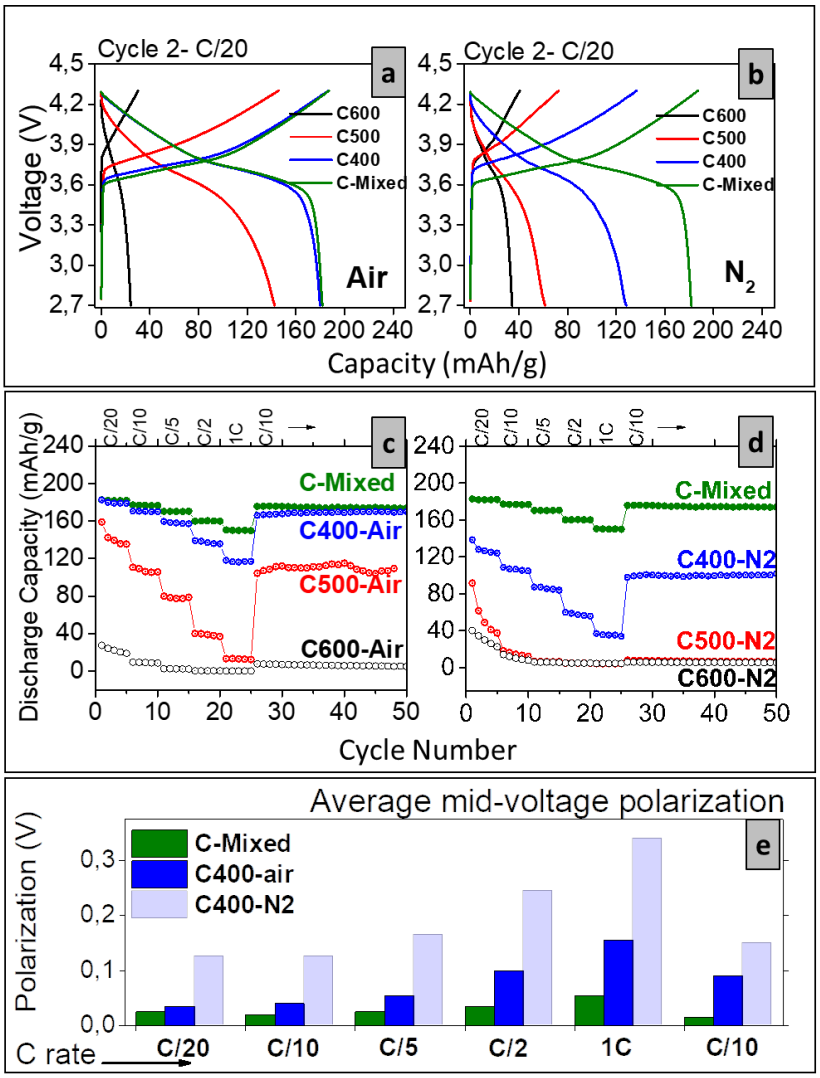

Figure 2. 4: Second charge-discharge cycle at C/20 for composite C-mixed, heat-treated samples at 400, 500, and 600 °C under **a)** air and **b)** nitrogen atmospheres. Corresponding C-rate capability tests with the C-rates: C/20, C/10, C/5, C/2, 1C [5 cycles each], and C/10 [long cycling] for **c)** air and **d)** nitrogen atmospheres. **e)** Comparison of average mid-voltage polarization of every second cycle for the tested C-rates for C-Mixed, C400-air, and C400-N2.

The second charge-discharge cycles at the C/20 rate of the studied samples are compared in Figure 2. 4 a and b, for air and nitrogen atmospheres, respectively, together with C-rate capability tests (Figure 2. 4 c and d). The results obtained indicate that, even if we have not observed relevant bulk structural changes in the XRD analysis, significant changes in the electrochemical properties of the

materials are already detected from 500 °C under air and even before under nitrogen. The C-mixed shows a discharge capacity of 182, 177, and 150 mAh/g at C/20, C/10, and 1C, respectively, and with capacity retention above 95% up to 100 cycles, which is comparable to the capacity delivered by electrodes prepared with NMC and KB only (Figure 2. 5). The second cycle capacity of the C400-air sample resembles that of the C-mixed, reaching 180 mAh/g; however, lower capacity retention is obtained at higher C-rates in the rate capability test, due to an increased internal cell resistance (see Figure 2. 4e for average mid-voltage polarization). For the C500-air sample, the electrochemical performances are more severely affected by the heat treatment. The discharge capacity reduces to 143 mAh/g, with higher polarization but 100% reversibility. Capacity fading is prominent in the first 5 cycles but then stabilizes, although when the current density is increased in the C-rate capability test, the capacity loss is significantly higher than for the C400-air sample and drops close to zero at 1C. The C600-air sample presents even poorer electrochemical performances, as the charge-discharge curve shows a high internal resistance and the second cycle capacity is far below the C-mixed reference, reaching only 28 mAh/g. This latter result is in agreement with the XRD analyses, which revealed that high-temperature treatment induces a decomposition of NMC to electrochemically inactive and insulating spinel and rocksalt MO compounds and the formation of Li_3PO_4, which is non-conductive[279] at 600 °C. However, at a lower temperature, the samples have already started to degrade, either at the surface level or in a negligible amount, as were not detected by XRD.

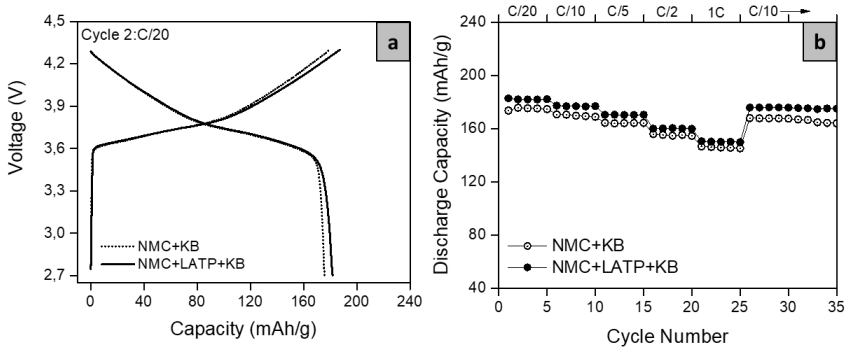

Figure 2. 5: a) Second charge-discharge curve [at C/20] and **b)** C-rate capability test with the C-rates: C/20, C/10, C/5, C/2, 1C [5 cycles each] and C/10 [long cycling] for NMC+KB and NMC+LATAP+KB.

Contrary to an air atmosphere, the galvanostatic behavior of the C400-N2 composite does not resemble that of C-mixed. The discharge capacity has already dropped to 128 mAh/g with 6% irreversibility. The galvanostatic curve exhibits an over-potential of above 100 mV (which is much higher compared to the C-mixed sample profile that shows an over-potential below 30 mV at low C-rates, Figure 2. 4e), but the capacity is retained over cycling. When increasing the temperature to 500 and 600 °C, the electrochemical performance further degrades. The first 10 cycles (corresponding to C/20 and C/10) show some residual capacity, but the fading is fast and a capacity close to zero is obtained for the rest of the cycles.

These results further demonstrate that the chosen atmosphere for the heat treatment plays a major role in the thermal response of composites. The same experiments were conducted in argon and oxygen atmospheres to rule out the possibility that another atmosphere will show better performances, but the results indicate that the capacity fading is fast and the over-potential is high in both cases (electrochemistry results, Figure 2. 6). Air treatment is thus giving the best properties despite the threshold temperature is still low (<500 °C) compared to conventional ceramic processing techniques (>1000 °C).

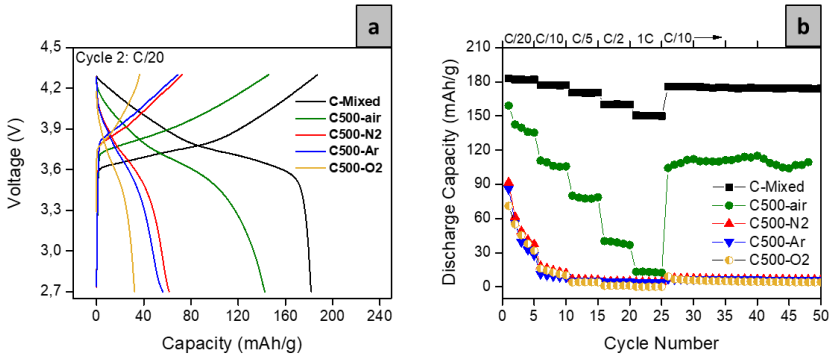

Figure 2. 6: a) Second charge-discharge curve [at C/20] and **b)** C-rate capability test with the C-rates: C/20, C/10, C/5, C/2, 1C [5 cycles each] and C/10 [long cycling] for composite heated at 500ºC under different atmospheres.

2.2.3 Particle morphology: Electron microscopies

2.2.3.1 Surface morphology by Scanning electron microscopy (SEM)

SEM images of NMC particles in pristine, C-Mixed, C400-air, C500-air, and C600-air samples are shown in Figure 2. 7. The smooth surface of NMC particles are lost in the C-mixed sample (Figure 2. 7 a and b), indicating a homogeneous distribution of the carbon additive. No major evolution of the surface of the particles is observed for the C400-air sample (Figure 2. 7c), whereas C500-air and C600-air samples show surface degradation (Figure 2. 7 d and e). In particular, NMC particles in C600-air exhibit an increase of porosity located at the surface of the particles, as confirmed by the cross-section of the NMC particles (Figure 2. 7f). Surface porosity may come from oxygen release from the NMC crystalline structure and/or secondary phase formation and eventual disconnection from the particle, in agreement with the formation of metal oxides and metal phosphates that was observed by XRD. The NMC-LATP composite mixture without KB was taken to the heat treatment at 500 °C under air atmosphere and the SEM morphology reveals the surface degradation is not visible in the particles (Figure 2. 8). This implies the particle surface degradation or porosity appears (in NMC, for example) after heat treatment above 500 °C is initiated by KB.

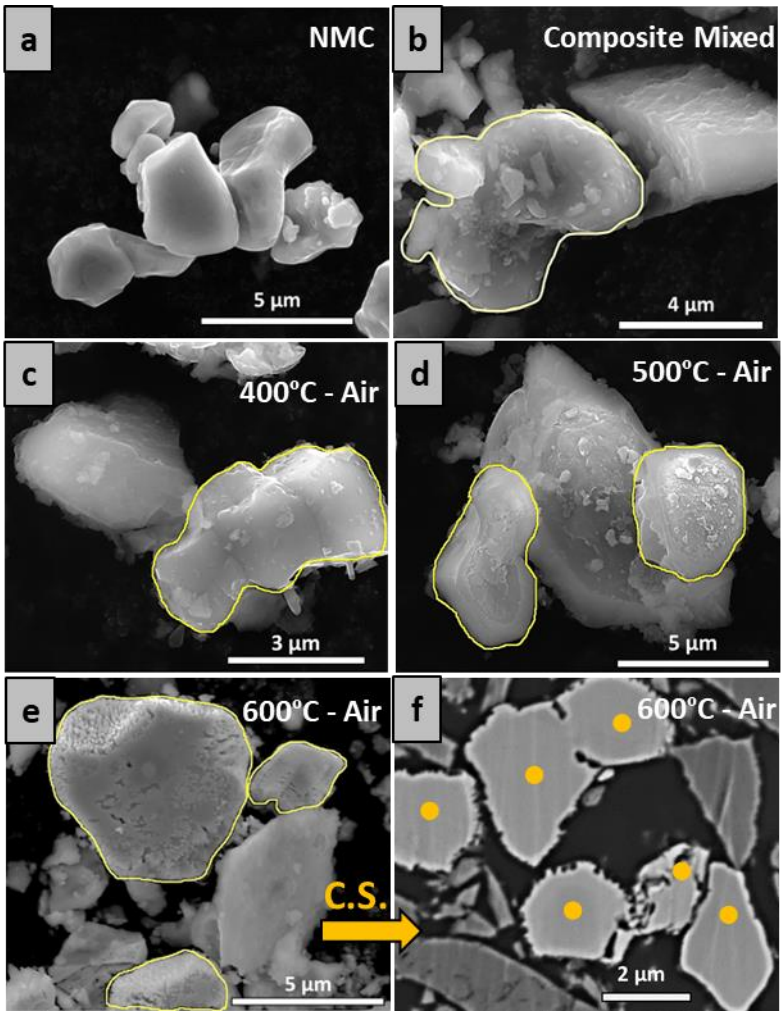

Figure 2. 7: Surface morphology comparison of NMC in heat-treated (air) composites to that of pristine, where the NMC particles in composites are highlighted with yellow outlines or spots. Surface morphology from SEM (ETD detector) image for **a)** pristine NMC, **b)** As mixed composite: C-mixed, **c)** C400-air composite, **d)** C500-air composite, **e)** C600-air composite**, f)** Ion milled grain cross-section (C.S.) of C600-air composite after embedding in epoxy.

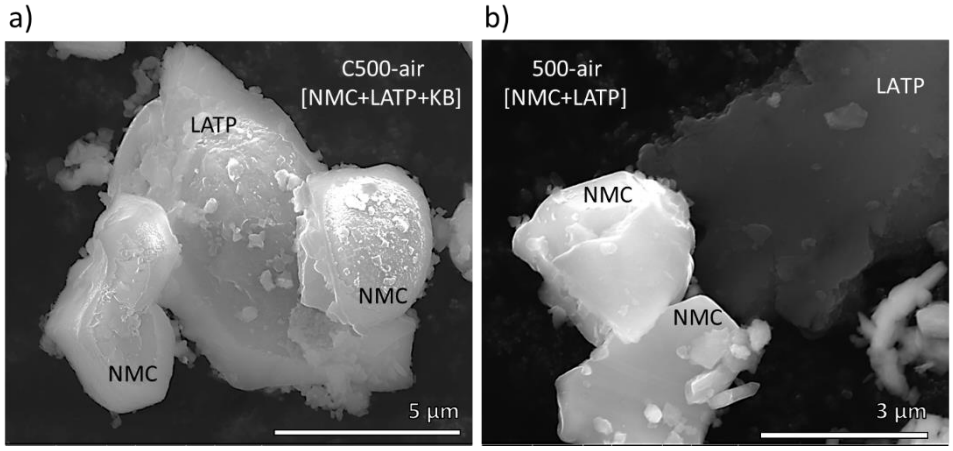

Figure 2. 8: SEM surface morphology of a) C500-air, where NMC+LATP+KB was heated at 500 ºC under air atmosphere and b) NMC+LATP was heated at 500 ºC under air atmosphere, without KB.

An insight into the local chemistry is followed by low-magnification EDX-TEM (see Figure 2. 9 and Figure 2. 10) indicating that the average bulk ratio of transition elements remains unchanged independently of the thermal treatment. However, a significant drop of Mn content from 300 nm to the edge of the particle can be observed for C500-air and C600-air as compared to that observed for the pristine NMC as shown in Figure 2. 9. This suggests that Mn is leaching out of the NMC structure even at 500 ºC. The increased surface porosity of NMC (C600-air) can be correlated to surface degradation that seems to be diminished for NMC (C500-air).

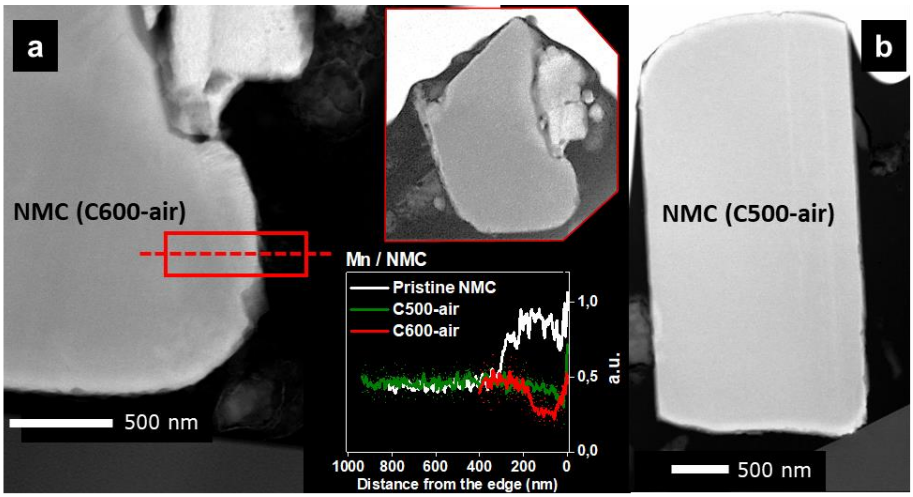

Figure 2. 9: TEM images of an NMC particle of the **a)** C600-air and **b)** C500-air samples that were acquired using a lamella of thickness less than 100 nm prepared by a focussed ion beam (FIB). the TEM-EDX profile of the Mn content (in-situ) acquired along the line indicated in red is compared with analogous ones acquired from pristine NMC and from C500-air samples, respectively core to edge for the selected regions.

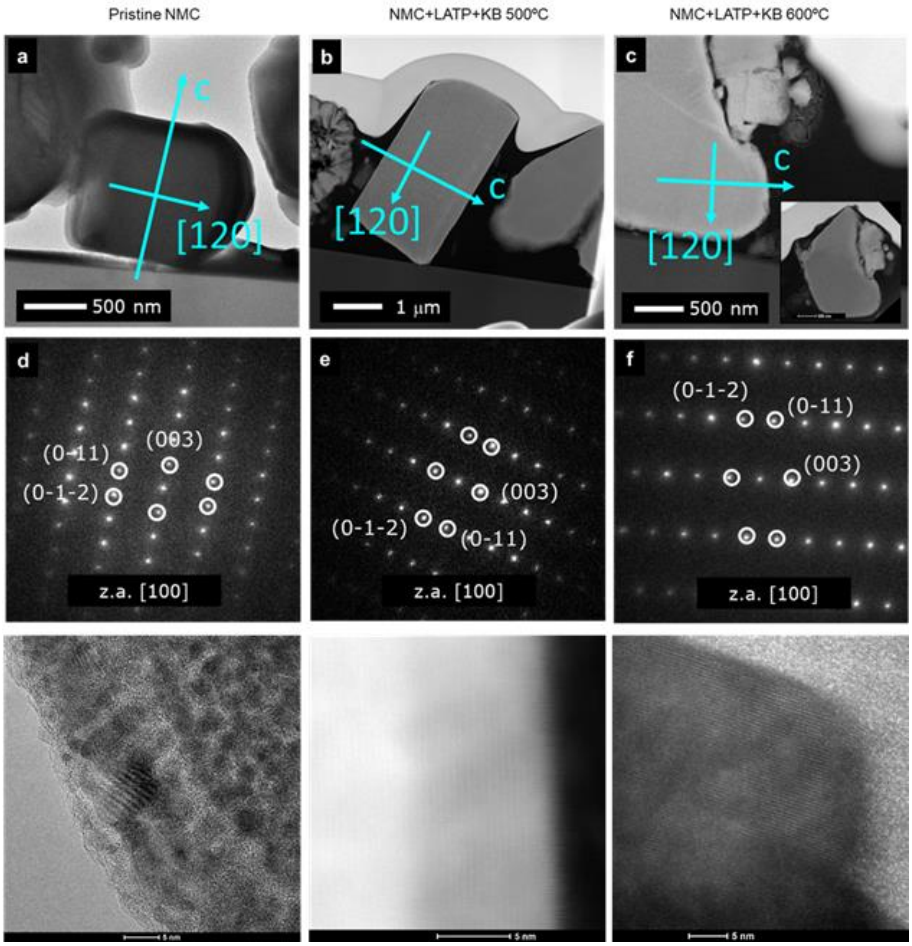

Figure 2. 10: (**a,b,c**) micrographics of pristine and as mixed particles and their respective SAEDs (**d,e,f**). High-resolution images showing the crystallinity of the samples at the edges of the particles (**g,h, i**).

2.2.4 Surface chemistry: X-ray photoelectron spectroscopy

To gain further insight into the average surface chemical changes revealed by electrochemical data and electron microscopy, XPS measurements were conducted in the C-mixed, C400-air, C500-air, and C600-air composites are compared to pristine NMC and LATP (Figure 2. 12). No chemical differences are observed in the non-heat-treated materials (see in (Figure 2. 11 I)). Apart from the slight tail that appears at the higher BE region due to mild surface oxidation in the case of C 1s and P 2p, there is no significant difference between C400-air and pristine materials (Figure 2. 11 II). This is in correlation with electrochemistry, where C400-air was comparable to the reference, C-mixed.

However, dramatic changes are observed in C500-air and, more particularly, in C600-air samples revealing important chemical modifications during the heat-treatment at these temperatures.

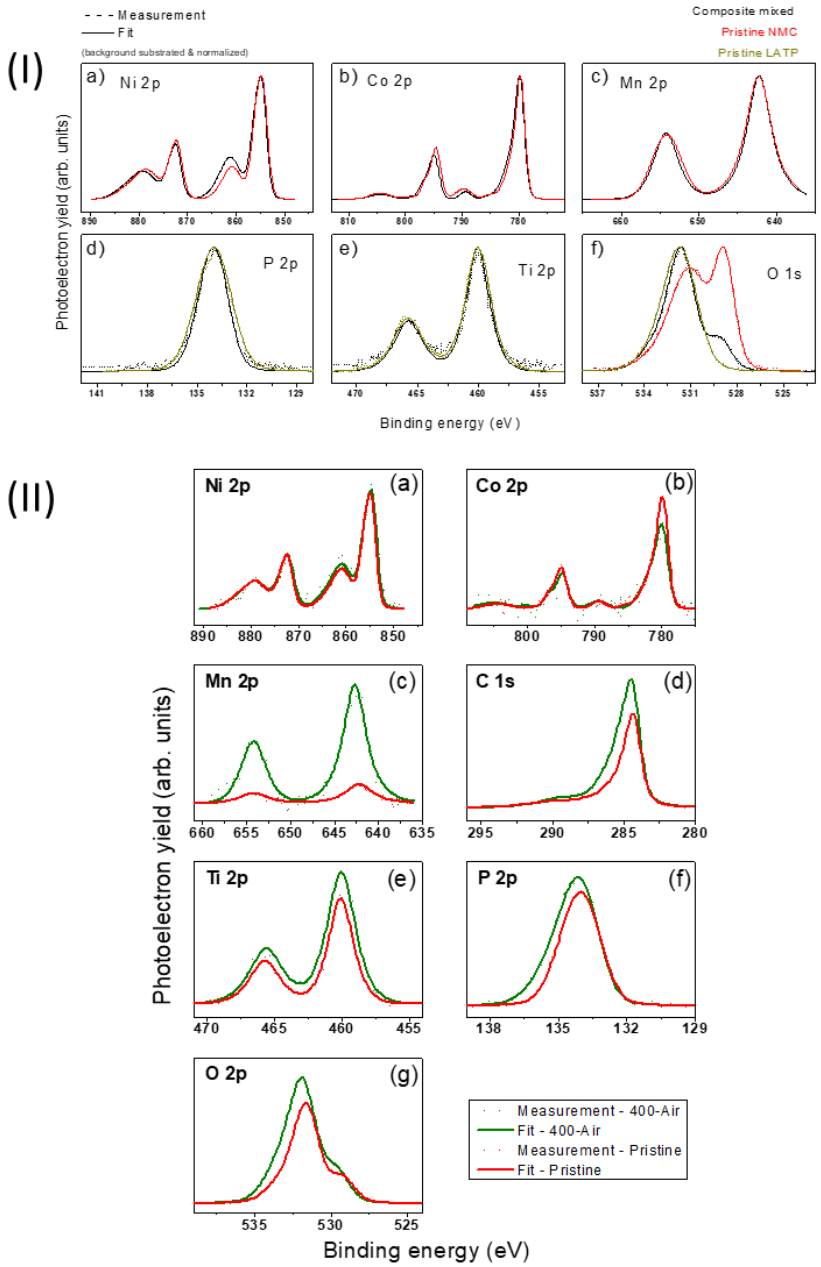

Figure 2. 11: Surface chemical composition using X-ray photoelectron spectroscopy. Comparison of signals for – **(I)** NMC elements Ni 2p **(a)**, Co 2p **(b)**, Mn 2p **(c)** major

LATP elements- P 2p **(d)**, Ti 2p **(e)** as well as O 1s **(f)** in composite mixed and pristine materials. **(II)** NMC elements: Ni 2p **(a)**, Co 2p **(b)**, Mn 2p **(c)**, Carbon: C 1s **(d)**, major LATP elements: Ti 2p **(e)**, P 2p **(f)** as well as oxygen: O 1s **(g)**

On the one hand, the ratio between Ni: Co: Mn obtained from the 2p (Figure 2. 12) and 3p (Appendix 2. 1) high-resolution regions differ significantly upon heating: Mn content strongly increases at the surface of the probed area, whereas Co and Ni diminish. For C500-air and C600-air, the Mn proportion (with respect to the total transition metals amount) increases by a factor of 2.50 and 2.76, respectively. Since XPS measurement samples a wide area that encompasses several hundreds of NMC particles, as well as KB, LATP, and all the other related decomposition products, these results further support the migration of Mn outside NMC particles. Indeed, the deconvolution of the Mn peaks reveals the emergence of a new Mn environment at C500-air and C600-air, in addition to the Mn 4+ signal corresponding to the NMC structure. The comparable width of the new peaks with the initial ones for Mn in NMC suggests that this extra phase should have an oxidation state close to 4+[280]. This could correspond to MnO_2 or Li_2MnO_3 starting to be formed on the surface in small amounts undetectable by XRD, while its shift to higher binding energy (BE) would be caused by differential charging effects].[281] However, their positions could also be attributed to the formation of an Mn-rich spinel [282] ($LiNi_{0.5}Mn_{1.5}O_4$ or slightly richer in Mn) in the surface of NMC particles as a consequence of lithium and oxygen loss in NMC.

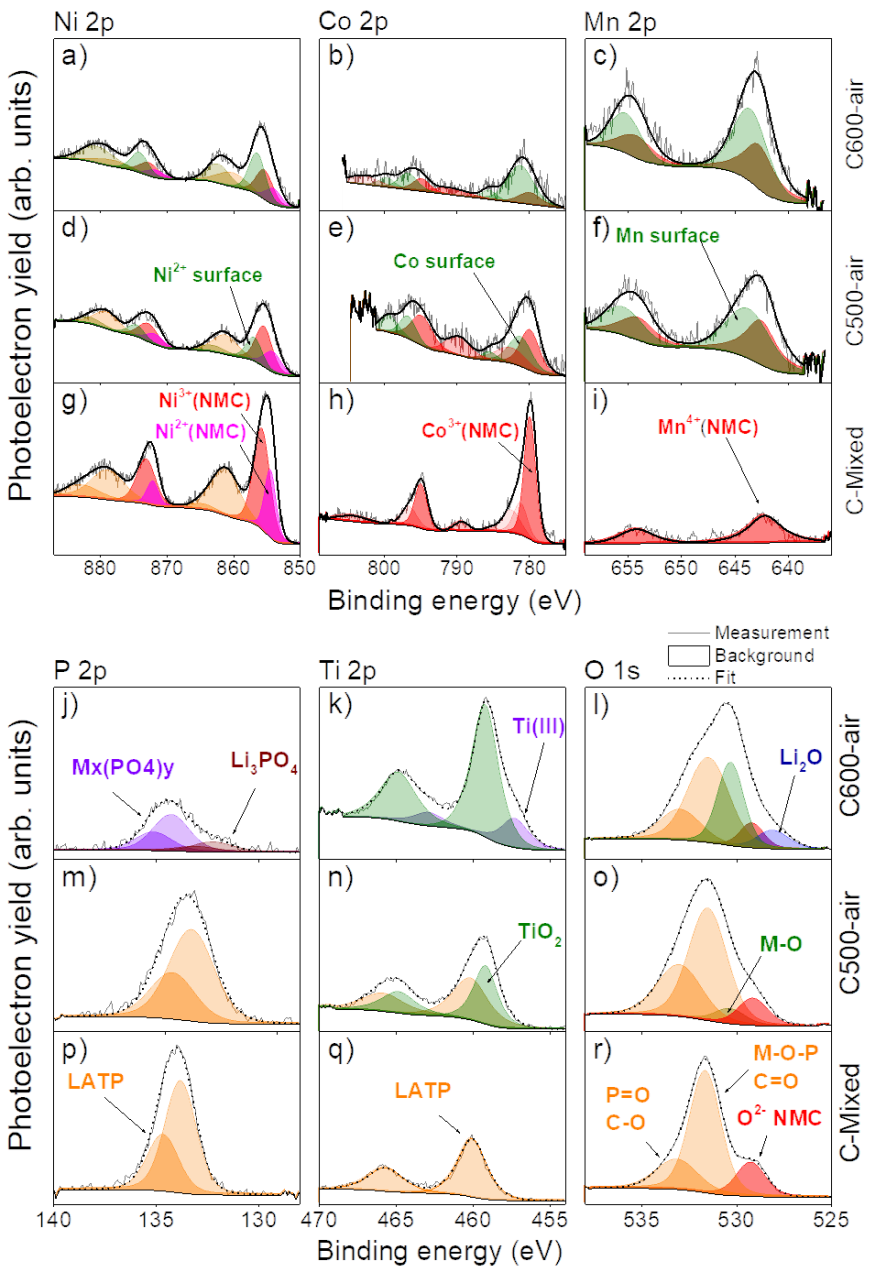

Figure 2. 12: Surface chemical composition using X-ray photoelectron spectroscopy. Comparison of signals for NMC elements- Ni 2p (**a, d, g**), Co 2p (**b, e, h**), Mn 2p (**c, f, i**) major LATP elements- P 2p (**j, m, p**), Ti 2p (**k, n, q**) as well as O 1s (**I, o, r**) in C600-air, C500-air, and C-Mixed respectively.

Similarly, extra doublets for Ni 2p ($2p_{3/2}$ component at 856.6 eV and $2p_{1/2}$ at 874.3 eV) as well as for Co 2p (peaks at 781 eV and 786.6 eV) are appearing and increase in intensity from C500-air to C600-air. These, not present for C-mixed, could be ascribed to the formation of a Ni (II) phosphate,[283] NiO and/or $LiNi_xMn_{2-x}O_4$, and to the formation of CoO 31 and/or delithiated Co in the layered structure.[285], [286] (refer to Appendices-Chapter 2 for further details). These observations are in agreement with the phases identified for the XRD of the composite heated at elevated temperatures, where the spinel to rock-salt transformation can be followed by the shift of the reflection around 50º towards lower angles. However, XRD is not surface-sensitive and therefore the temperatures at which each phase appears are higher.

On the other hand, LATP is also affected by heating. Peak fitting of C500-air reveals the surface coexistence of LATP with TiO_2 [36] and possibly different metal-phosphates (with different Li proportion) as suggested by the wider peak of P 2p, [287], [288]; whereas for C600-air, LATP contribution disappears from the surface, fully transforming into other M-phosphates (P doublet with $2p_{3/2}$ signal at 134.2 eV [287], [288]), Li_3PO_4 (P $2p_{3/2}$ shifted to lower BE), increased amount of TiO_2 and likely Ti_2O_3 or $Ti(PO_4)$ observed from an extra Ti(III) doublet at 457.22 eV ($2p_{3/2}$).[289], [290] These results indicate the involvement of LATP in the thermal reactivity of the composite mixture, starting at least from 500 °C, and the new environments observed fully agree with XRD data.

The formation of new metal oxide phases at 500 ºC and more especially at 600 ºC is further proven by the appearance of a second metal-oxide peak in O1s spectra, at 1 eV higher BE than the original lattice O signal in NMC (529.2 eV). Oxygen oxidation to form O_2^{-1} upon surface delithiation would also contribute to this higher BE component.[291] Theoretical calculations demonstrate that the transition from a layered to a cation-disordered rock-salt structure also produces a shift to higher BE together with a broadening of the M-O spectral distribution.[292] An extra metal oxide peak appears at lower BE in C600-air

(close to 528 eV), being explained by the formation of Li_2O after NMC surface delithiation.

Above 500 °C, the carbon signal fades upon heating (see C 1s in Appendix 2. 1) and graphitic carbon bonds (284.4 eV) almost disappear, promoting the formation of C-C and C-O bonds in heated composites (increased signal around 285 and 286 eV respectively) that get reduced from 500 to 600 °C, while a signal that can be ascribed to carbides starts appearing at 600 °C. These transformations can significantly affect the electrical conductivity of the composite after heat treatments and effectively prove that the role of KB is non-negligible in the composite thermal stability (despite previously it was shown to be idle in bulk reactivity through XRD).

2.3 Discussion

Layered NMC is stable at high temperatures [293] and the only change observed in the bulk structure is the temperature-dependent unit cell volume expansion (in-situ XRD results- Figure 2. 13). From the combined results of bulk and surface techniques our results undoubtedly unveil that the composite mixture of NMC+LATP+KB undergoes severe degradation reactions above 400 °C. The threshold temperature is much lower than that predicted in a recent study of NMC-LATP thermo-mechanical compatibility (<550 °C) as the impact of electrically conductive additive was not considered.[275] Under air, the transformations involve a cation redistribution in the NMC cathode material, leading to Mn-depletion at the surface. This cation migration is further accompanied by the loss of lithium and oxygen from the lattice as temperature increases and finally results in a phase transition from layered to spinel-type compounds and/or rocksalt oxides (depending on the temperature) as determined from XPS, EDX, and XRD. The roughness and porosity observed by microscopy emphasize this surface reconstruction on NMC.

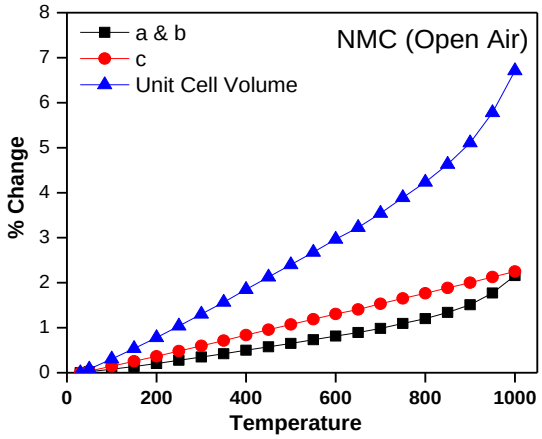

Figure 2. 13: percentage change in NMC unit cell parameters with respect to temperature. Unit cell values are obtained from Le-Bail refinement of in-situ XRD data

Our results indicate that this degradation at such low temperature is interplayed by LATP acting as a lithium sink, similar to what has been reported for NASICON, which results in multiple resistive secondary phases such as Li(M)PO_4[271], [272], [275], [294]. A severe loss of Li destabilizes the NMC structure[278] and acts as a driving force for transition metal redistribution. When taking up lithium, LATP decomposes and forms new compounds such as Li_3PO_4, TiO_2, and other phosphates and oxides that eventually act as barriers to Li-ion diffusion resulting in increased impedance and poor electrochemistry.

In our system, KB does not remain inactive but gets oxidized to CO_2 or CO at these high temperatures. The thermal response of the composite under air and inert atmospheres are compared using TGA in Figure 2. 14. Under air, there is a weight loss catered slightly below 600 ˚C (Figure 2. 14 a). This loss corresponds to carbon oxidation, as confirmed using QMS (Figure 2. 14 b), and by the fact that this weight loss is not visible under the nitrogen atmosphere. This implies both the air atmosphere and the oxides (NMC and LATP) can be a potential oxygen source in the system. The composite heated under the oxygen atmosphere (C500-O_2) was giving poor performance (electrochemistry results, Figure 2. 15). However, after adding additional KB to C500-O_2, the

performance became better than C500-air, although still worse than C400-air (Figure 2. 4). Excess oxygen in the heating atmosphere might reduce O^{2-} consumption from NMC or LATP but it favors the oxidation rate of KB which results in bad electrical conductivity and then poor electrochemistry. Indeed, the thermogravimetry analysis performed with KB reveals that the rate of KB oxidation is faster under the oxygen atmosphere compared to air (Figure 2. 16). So, under air, in the presence of external agents that consume lithium and oxygen such as LATP and carbon, the NMC structure is destabilized and the migration and redistribution of transition metals at the surface are promoted. These surface-oriented reconstructions affect the electrochemistry of the composite even though the NMC bulk structure was preserved at 500 °C.

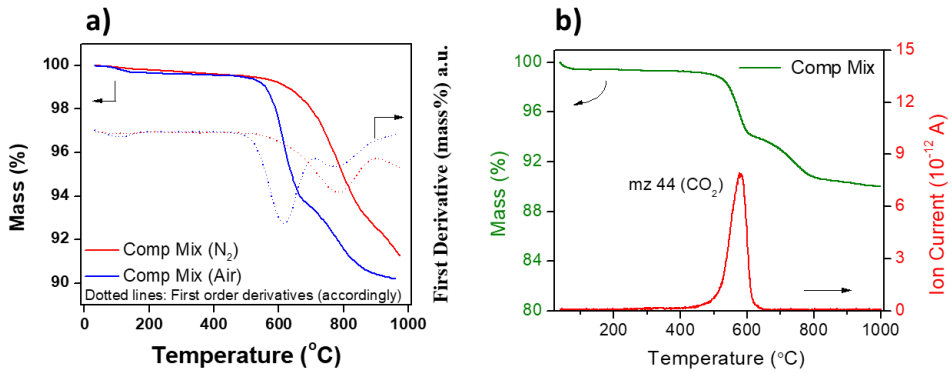

Figure 2. 14: a) TGA analysis of Comp Mix at a temperature range from RT to 1000 ˚C and a heating rate of 5 ˚C /min performed under air (blue) and nitrogen (red) atmospheres along with the derivative curves. **b)** Quantitative mass spectrometry (QMS) of the Comp Mix performed under air atmosphere.

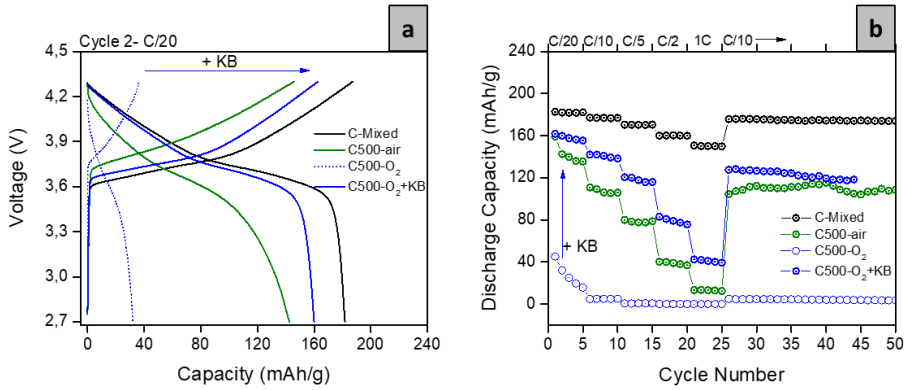

Figure 2. 15: a) Second charge-discharge curve [at C/20] and **b)** C-rate capability test with the C-rates: C/20, C/10, C/5, C/2, 1C [5 cycles each] and C/10 [long cycling] for composite heated at 500ºC under oxygen (blue hollow circles) and added additional KB after heating the composite at 500ºC to compensate the loss by oxidation (blue solid circles).

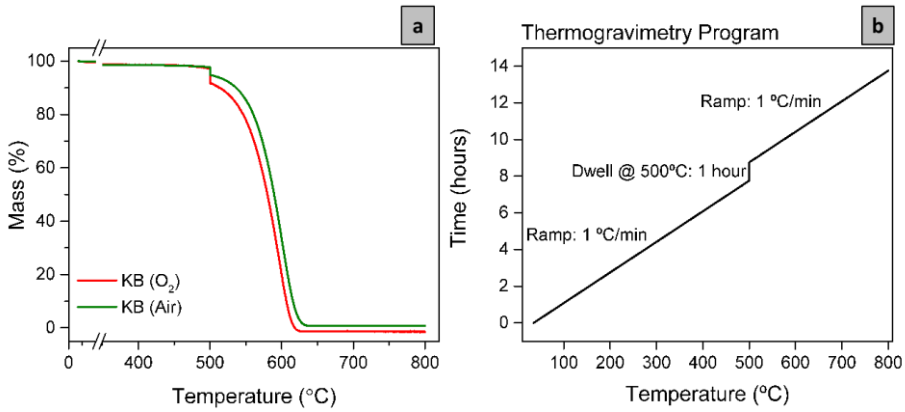

Figure 2. 16: a) Thermogravimetry (TG) comparison of KB performed under air and oxygen atmospheres. **b)** Graphical illustration of measuring parameters.

In summary, during the composite [NMC+LATP+KB] heat treatment process under air, the following reaction mechanism takes place above the temperature threshold (as summarized in Figure 2. 17): 1) LATP consumes Li from NMC that later leads to the formation of non-conductive metal phosphates and oxides like Li_3PO_4 and TiO_2. 2) Li-ion vacancy and temperature cause a transition metal cation redistribution in NMC and promotes layered to electrochemically inactive rocksalt phase transition (through the formation of an intermediate spinel-phase) leading to O^{2-} release; 3) This is further stimulated by the O^{2-} consumption in presence of a reducing agent (KB) at high temperature and 4)

Interdependence of all these processes amplifies the degradation and causes destruction of NMC into metal oxides and metal phosphates at 700 °C under air. While similar degradation processes have been reported for NMC in the case of high voltage cycling, [277], [295], [296] long-term cycling, [297]–[299] temperature-assisted cycling or long-term storage, [300] we propose that the heat treatment of the composite under air causes similar impacts in NMC at temperatures as low as 500 °C.

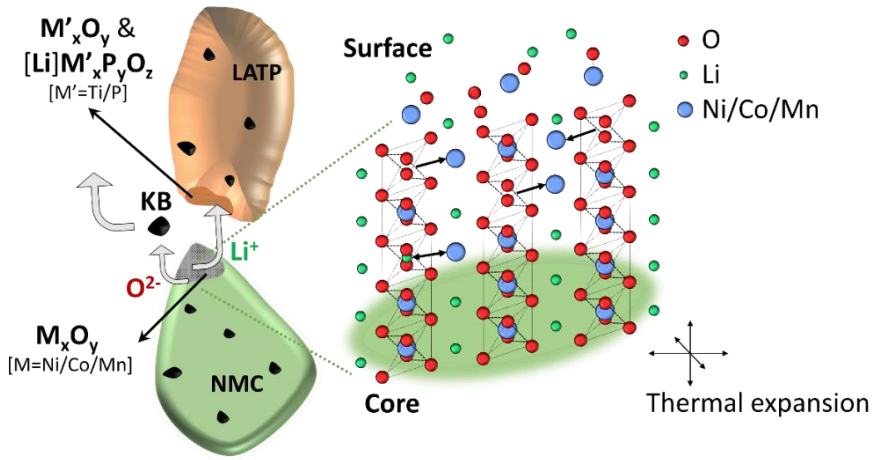

Figure 2. 17: NMC-LATP-KB composite reaction mechanism under air atmosphere. A schematic illustration of thermal induced reactivity between NMC (green), LATP (brown), and KB (black) at the contact surfaces. A zoom on the NMC contact surface portrays the core-shell comparison of crystal structure.

Under the nitrogen atmosphere, the KB oxidation rate will be negligible due to the absence of oxygen but will lead to faster utilization of oxygen from NMC and LATP that enhances the reduction of NMC to MO and an important degradation of LATP under a reducing environment. The electrochemistry results are strongly affected by that degradation as observed in this work. Since inert atmospheres do not bring any benefit to the processing of composite cathodes for ceramic solid-state batteries as shown in this work, the practicality and cost-effectiveness of co-sintering processes under air will be preferred for the manufacturing process. Our findings show that careful evaluation of material compatibility and reactivity under different processing conditions is

imperative for the fabrication of an all-inorganic oxide-based solid-state lithium battery. It should be noted that NMC composition can also play a role in the thermal compatibility of the composite and therefore should also be considered a relevant parameter for the evaluation of threshold temperatures. Indeed, it has been shown that Al_2O_3 coatings can become dopants (i.e. diffuse into the bulk) with increasing Ni content in the NMC, and therefore a different reactivity can also be expected in our system for different NMC compositions.[301], [302] The limiting threshold temperature of <500 °C found for this particular system calls for smart strategies to mitigate the reactivity between components, such as through doping, gradient-structures, surface modifications with protective coatings [278] or the addition of sacrificial sintering aids. Apart from temperature and heating atmosphere, other parameters such as heating time and pressure also become relevant when the system needs to be considered in the fabrication of an all-inorganic oxide-based solid-state lithium battery. In that sense, the evaluation of composite response to low-temperature densification processes like cold sintering and spark plasma sintering represent interesting alternatives, for which scalability, and mechanical and chemical compatibility should also be evaluated.

2.4 Conclusion

The thermal reactivity of composite cathode mixtures $LiNi_{0.6}Co_{0.2}Mn_{0.2}O_2$ (NMC), $Li_{1+x}Al_xTi_{2-x}P_3O_{12}$ (LATP) and Ketjenblack (KB) under different atmospheres has been thoroughly studied through the combination of bulk and surface techniques. Our findings show that the composite remains stable up to 400 °C under air. The thermal response of the composites was found to be highly dependent on the chosen atmosphere. Inert atmospheres such as nitrogen and argon enhance composite reactivity, which is initiated by KB, while the oxygen atmosphere leads to faster oxidation of KB.

The reaction mechanism of the composite cathode above the threshold limit was investigated so that mitigation strategies can be henceforward proposed. The decomposition reactivity involves Li^{+} and O^{2-} loss from NMC triggered by the presence of LATP and KB, and transition metal cation redistribution in the NMC subsurface ultimately resulting in metal oxides and phosphates when combined with LATP. These insulating secondary phases restrict the electrochemistry of the composite after heating at 500 °C under air. Our results show that the presence of conductive additives (imperatively required in NMC-based cathodes) leads to lower threshold heat-treatment temperatures and accentuates the relevance of evaluating the full system in determining the composite thermal stability.

CHAPTER 3: THERMAL STABILITY ENHANCEMENT OF NMC-LATP-KB COMPOSITE: INFLUENCE OF LIF ADDITIVE

3.1 Introduction

In the previous chapter, the reactivity between composite cathode components has been thoroughly evaluated following an *ad hoc* methodology designed to simulate cathode densification under temperature. It has been found that above 400ºC, Li^+ consumption from NMC by LATP leads to NMC crystal decomposition which gets intensified by O^{2-} consumption by carbon. In this chapter, we explore the impact of additives in this decomposition reaction with the aim to raise the threshold temperature. Two approaches are possible: 1) Introduce a sacrificial material that decomposes around the threshold limit able to provide Li^+ (and/or O^{2-}) to the mixture (with the expectation that it leaves NMC unaffected and that the decomposition products do not hinder the electrochemistry); 2) Addition of a light-weight, electrochemically inactive, and thermally stable material to the mixture such that it can partially mask the particle surfaces and hence prevent them from temperature-induced surface reactivity due to interfacial contacts. Based on these requirements, different materials such as lithium fluoride (LiF-848˚C), lithium oxalate ($Li_2C_2O_4$-183˚C), lithium hydroxide (LiOH-462˚C), lithium nitrate ($LiNO_3$-255˚C), lithium carbonate (Li_2CO_3-723˚C) and lithium peroxide (Li_2O_2-340˚C) were considered (melting or decomposition temperature in brackets). A quick screening using X-ray diffraction and liquid cell electrochemistry after mixing an additional 5 wt % of the element in the composite followed by a heat treatment at threshold limits was used as a methodology to evaluate the impact of having such additives (see Appendices Chapter 3 for more information). Our results show that the composite mixed with LiF showed a slight suppression in thermal reactivity at the threshold limits and the optimum amount of additive was determined.

3.2 Results

3.2.1 Thermal stability: Thermogravimetry (TGA) and Differential Scanning Calorimetry (DSC) analyses

The thermal response of the composite mixture with the higher LiF content (Comp+LiF10 Mix, with 10 wt% of LiF) and without LiF (Comp Mix) were analyzed using TGA-DSC (Figure 3. 1). The program with 1-hour dwelling at 400 ˚C has been used to compare the composite response at this range with and without LiF, which is the threshold limit for composite thermal stability. The TGA curves don't show much variation. The rate of KB oxidation with onset at 400 ˚C and followed by heating is unaffected by the presence of LiF. From the DSC experiments, the nature of the heat flow curve is similar for composites with and without LiF. That implies that the presence of LiF doesn't make any bulk chemical changes in the composite thermal reaction that can be evaluated through DSC. But there is a reduction in the rate at which the heat flow of the composite when LiF is present. This indicates that the rate at which the composite components react with each other has reduced in presence of LiF.

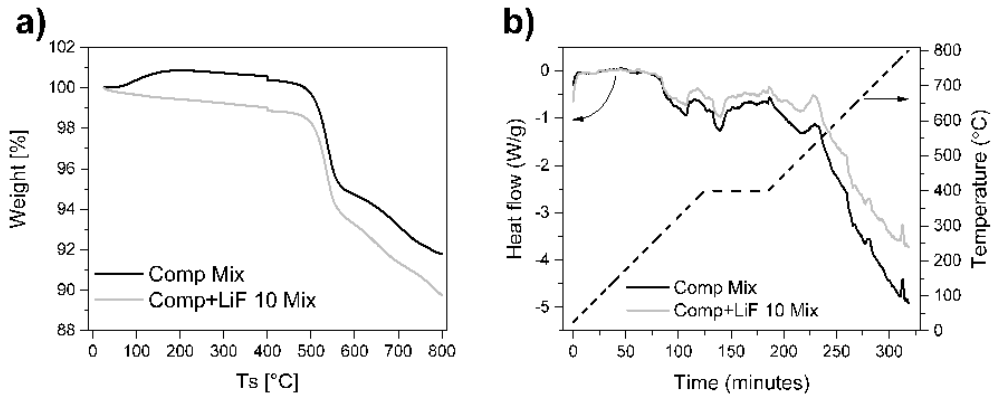

Figure 3. 1: TGA-DSC analysis of composite mixture with and without LiF evaluated by the program that has a 1-hour dwelling at 400 ˚C **(a)** Thermogravimetry curves and **(b)** heat flow vs time curves for comp mix with 10% LiF compared to the composite without LiF.

3.2.2 Bulk crystallinity: X-ray diffraction

The main X-ray diffraction peaks of NMC in three different samples are compared in (Figure 3. 2) to evaluate the impact of LiF in NMC bulk

crystallinity after the heat treatment. These correspond to Comp Mix, Comp 400-SA (corresponding to the composite heated at 400˚C under synthetic air), and Comp+LiF 10 400-SA (the composite with 10 wt.% LiF heated at 400˚C under synthetic air). Comp 400-SA exhibits a change in the intensity of reflection 006 and slight peak broadening in certain reflections (indicated by arrows in Figure 3. 2) compared to Comp Mix. In the previous chapter, it was concluded that this phenomenon is the result of temperature-induced surface changes (transition metal migration) in NMC caused by interaction with LATP and KB. Therefore, at 400 ˚C and in absence of LiF, the components start to react but the reaction byproducts are not yet visible in bulk. On the other hand, these changes are overall suppressed in Comp+LiF 10 400-SA. This indicates that LiF probably hinders the mutual reactivity of composite elements. However, since the diffraction peaks from LiF are retained in the composite after heat treatment, LiF is not directly involved in the thermal reactivity, at least in the bulk scale.

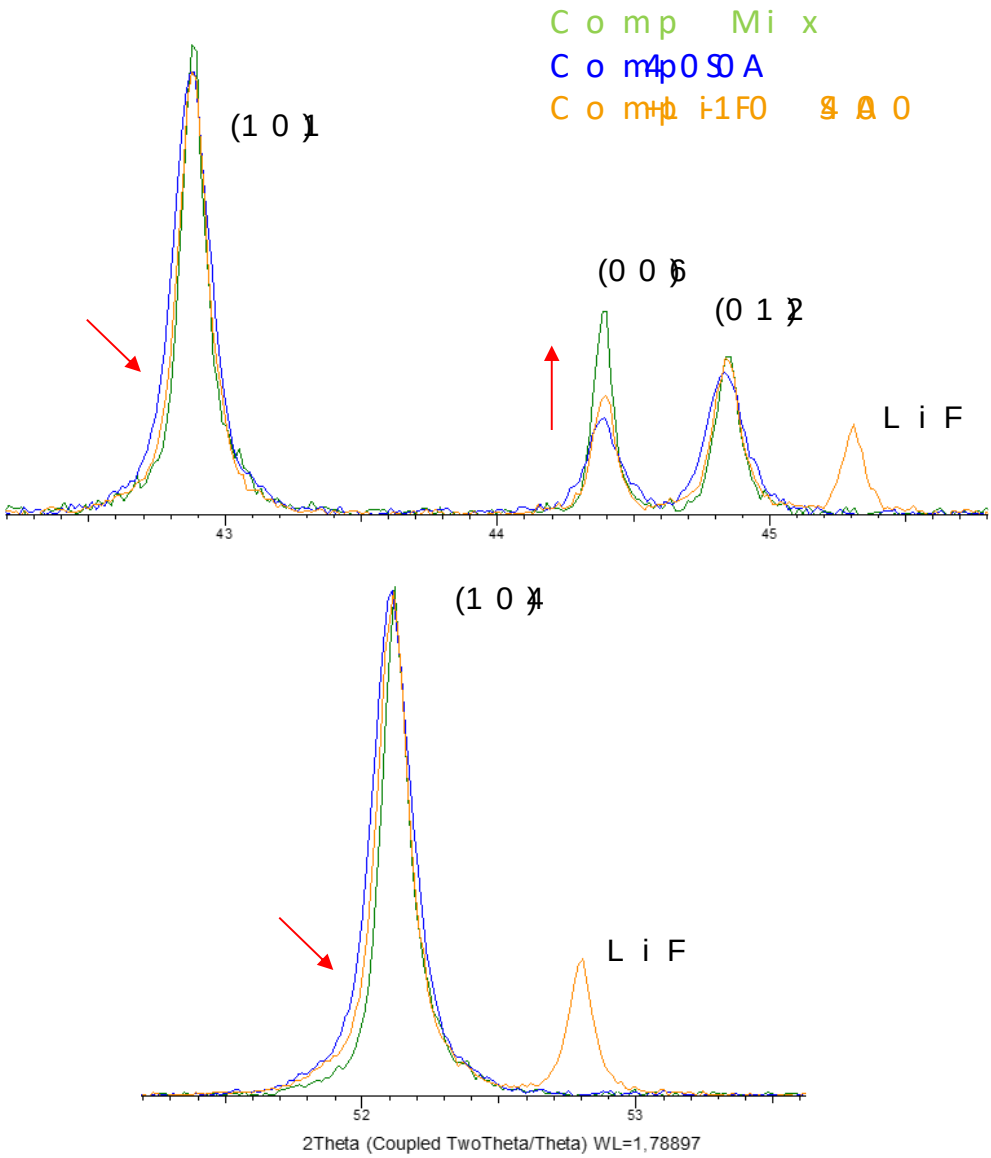

Figure 3. 2: X-ray diffraction of Comp Mix, Comp 400-SA, and comp+ LiF 10 400-SA where the evolution of main peaks of NMC has been examined. Additional peaks arising from the added LiF are indicated. Arrows indicate the direction in which the changes are observed for the peaks.

3.2.3 Electrochemistry: Galvanostatic cycling with potential limitation (GCPL)

The impact of LiF has been initially studied in the as-mixed composite. Different weight ratios of LiF were considered for the comparison, such as 2, 5, and 10 wt.%. Figure 3. 3 a and b show the electrochemical performance of

composite mixtures with different weight ratios of LiF compared with Comp Mix. The second charge-discharge cycle conveys similar discharge capacities for all the composites irrespective of LiF content present in it. Also, the capacity value is comparable to the composite mixture without LiF. The rate capability results reveal that the electrochemical performance of composite mixtures is better with LiF, which probably indicates LiF has a positive influence on the mixed composite electrochemistry itself. There could be different possible causes such as the solubility of LiF in the electrolyte, Li^+ supply from LiF, etc.

A comparison of the electrochemical performance of 400 ˚C heat-treated composites with different weight ratios of LiF is summarized in Figure 3. 3 c and d, and the performance is compared to the Comp 400-SA. The composite with LiF has a slightly higher second cycle capacity compared to the composite without LiF after heat treatment. But differences become more relevant in the rate capability tests where the composite without LiF has a retention of only 20% at 1C that becomes 45% with 2 and 5 wt% of LiF, and finally close to 60% with 10 wt% of LiF. Therefore, the higher the content of LiF, the better the electrochemistry of the composite after heat treatment, which suggests that LiF has a significant role in the thermal stability of the composite.

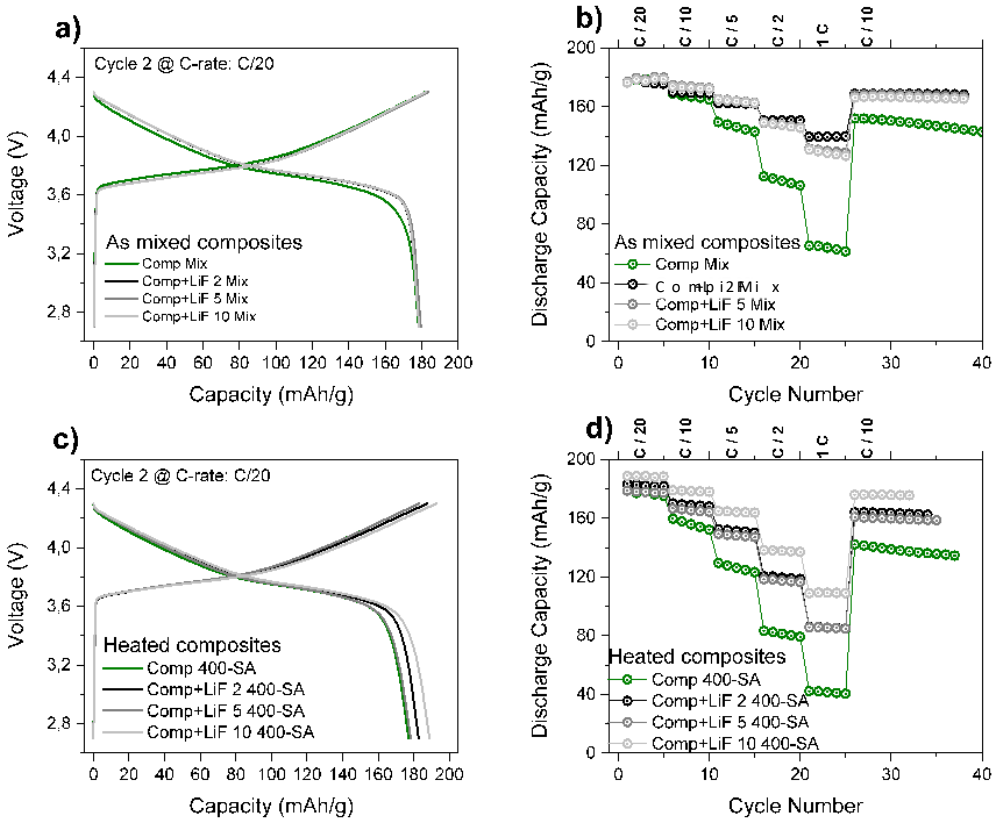

Figure 3. 3: Comparison of electrochemistry of the composites with different weight ratios (2, 5, and 10%) of LiF before and after heat treatment; with respect to composites without LiF before and after heat treatment. **a)** and **c)** second charge-discharge curves at a C rate of C/20. **b)** and **d)** rate capability tests.

The electrochemical properties of composites with 10 wt% of LiF are compared before and after heat treatment at 400 ˚C to closely look at the influence of temperature in the mixture (Figure 3. 4). The second charge-discharge curve at C/20 shows a slight enhancement in discharge capacity for the heated mixture that is independent of polarization. It probably indicates the involvement of LiF in the reactivity that in turn enhances the composite electrochemistry after heat treatment. A recent study reports the protective thin film of LiF coated to grains of LNMO cathode material by atomic layer deposition (ALD) could enhance the electrochemical performance by providing additional Li^+ to the system as well as by preventing the cation mixing.[303] Here, even though the initial capacity values were higher, the rate capability is comparatively lower at higher

C rates. This may indicate the temperature-induced composite reactivity is still present in the mixture but less intense compared to the composite without LiF.

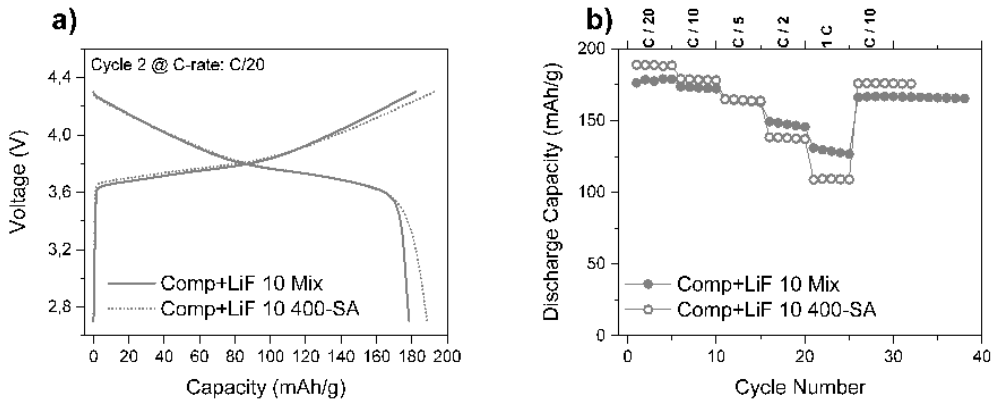

Figure 3. 4: Electrochemistry of coin cells made by composites with 10 wt% of LiF compared before and after heat treatment at 400 ˚C. **a)** second charge-discharge curves at a C rate of C/20. **b)** rate capability tests

3.2.4 Surface chemistry: X-ray photoelectron spectroscopy (XPS)

To gain further insight into the average surface chemical changes XPS was conducted in Comp Mix, Comp 400-SA, Comp+LiF 10 Mix and Comp+LiF 10 400-SA (Figure 3. 5). The main difference was observed for the C 1s peaks (Figure 3. 5 a and b). In Comp 400-SA a slight tail appears at the higher BE region (increased intensity around 286 eV in C 1s core level compared to Comp Mix) due to C-O bonds formation under mild carbon surface oxidation during the heat treatment. But this is not observed for Comp+LiF 10 400-SA, which suggests that the presence of LiF is somehow supressing the oxidation of carbon. Considering the transition metals from NMC, some conclusions can be made by looking to the changes of Co 2p, Mn 2p and Ni 2p core levels between mix and heated composites (Figure 3. 5). Compared to Comp Mix, Comp 400-SA shows a clear transition metal disproportionation at surface level, where the surface becomes Mn rich (increased intensity in Figure 3. 5e). But there is no significant difference in Ni 2p and Co 2p peaks, not only in the intensity but also in the shape, meaning that no big chemical changes occur. This disproportion has retained even with the presence of LiF (evidenced

by the increased intensity of Mn 2p peak of Comp+LiF 10 400-SA in Figure 3. 5f in contrast to, for example, Co 2p in Figure 3. 5d). However, it is difficult to know whether the disproportionation is higher or smaller than in the previous case or derive conclusive information about transition metals chemistry in the case of composites with LiF because Ni 2p photoelectron peak overlaps with other Auger peaks (F KLL when the Al anode is employed and Ti LMM if we use the Mg one) and differential charging issues. Further characterizations are required to understand the role of LiF in composite stability enhancement mechanism.

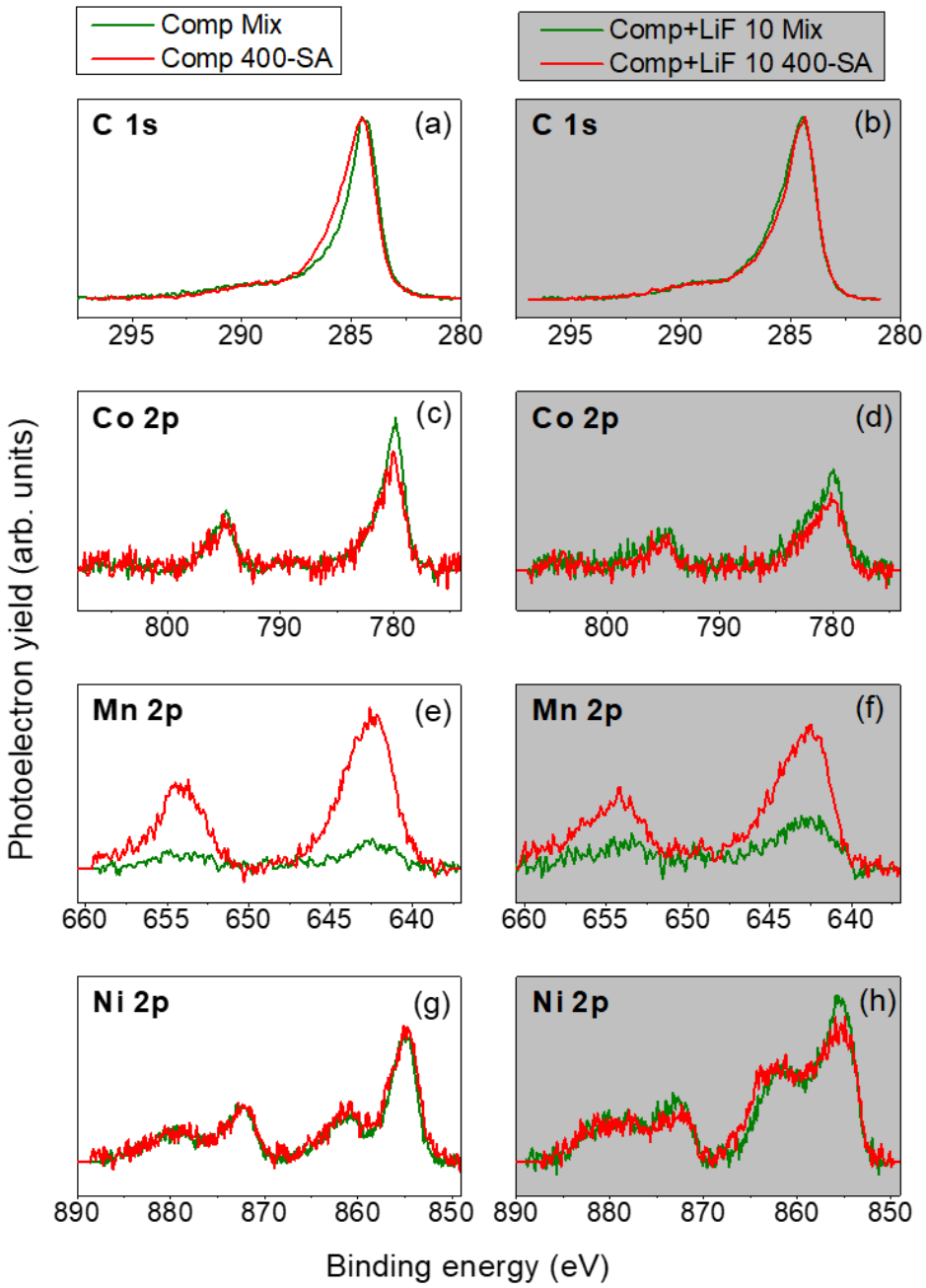

Figure 3. 5: Surface chemical composition by means of X-ray photoelectron spectroscopy. Al radiation employed ($E_{K\alpha}$ = 1486.6 eV). Comparison of signals for photoelectron peaks of C 1s, Co 2p, Mn 2p and Ni 2p respectively compared between Comp Mix and Comp 400-SA (a, c, e, g) and Comp+LiF 10 Mix and Comp+LiF 10 (b, d, f, h)

3.3 Conclusions and perspectives

The presence of LiF helps to enhance the NMC-LATP-KB composite thermal stability. The higher the content of LiF, the better the electrochemical performance of both mixed and heated composites. From the results and discussions, there are three possibilities in which LiF acts in the composite thermal response:

1. LiF involves in reactivity such that it provides Li^+ to the system and Li^+ is not consumed from NMC
2. LiF remains idle and it acts as a partial barrier between the composite elements that prevent them from mutual reactivity by reducing the contact area
3. LiF partially reacts and supplies Li^+ to the system by controlling Li^+ loss from NMC at the same time acts as a barrier between components that effectively reduces the mutual reactivity.

XPS-based surface characterizations confirm a reduced carbon oxidation from the composite in the presence of LiF during heat treatment. Unfortunately, limited information was extracted from transition metal peaks and further detailed characterizations are required to understand the composite thermal reaction in presence of LiF. If the assumptions are confirmed from advanced characterizations, a thin surface coating of LiF on the NMC grains without affecting its ionic and electronic conductivities could be an effective solution to enhance the thermal stability of the composite. A schematic representation of the composites: without LiF, LiF as an additive, and LiF as the coating has presented in Figure 3. 6.

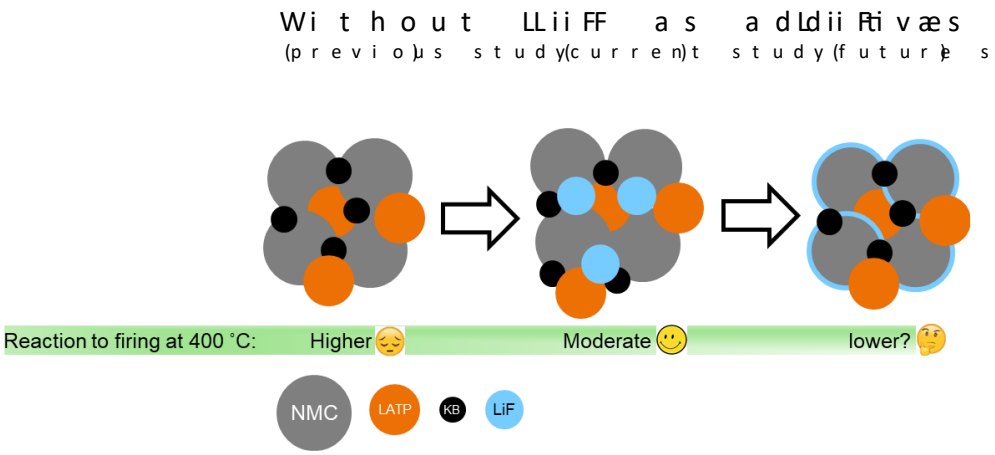

Figure 3. 6: Pictorial representation of the composites: without LiF, LiF as an additive, and LiF as the coating is illustrated, where the thermal stability of the composite has enhanced in the presence of LiF. Hence the future of the study could be the surface coating of NMC by LiF to enhance its impact.

CHAPTER 4: CHOOSING CARBON CONDUCTIVE ADDITIVES FOR NMC-LATP COMPOSITE CATHODES: IMPACT ON THERMAL STABILITY

4.1 Introduction

The thermo-mechanical compatibility of densified NMC-LATP composite cathodes was previously reported by Beaupain et al., where a processing temperature threshold of 550 °C was identified to prevent cathode degradation.[304] However, we have found in chapter 2 that the presence of carbon Ketjenblack in NMC-LATP composite has a huge impact on its thermal compatibility, and brings down the temperature threshold to 400 °C under air.[305] Therefore, the role of carbon in the thermal compatibility of the composite cathode components should not be overlooked. However, while the use of a conducting additive cannot be avoided in this system, the different nature of the available carbonaceous materials can be exploited to maximize thermal compatibility. There are indeed different types of carbonaceous materials available (one can cite for example carbon black, activated carbon, or carbon nanotubes) which are ubiquitously established in traditional lithium-ion batteries to enhance the electronic conductivity within the electrodes.[306]

In the present chapter, we take a step further and evaluate the impact of the carbon nature on the thermal stability of the NMC-LATP-carbon composite. We have selected four grades of carbon that differ in morphology, surface area, and porosity, to identify the impact of each feature on the reactivity. These include: i) Ketjenblack (KB) ii) carbon 65 (C65) iii) Acetylene black (AB) and iv) multiwalled carbon nanotubes (mwCNT). To establish correlations between the carbon type and their impact on the reactivity between cathode components, the physicochemical, structural, thermal, and morphological properties of pristine carbons are first evaluated by bulk and surface characterization techniques. Next, the impact of carbon on the electrochemical properties of the

NMC-LATP-carbon composite is investigated before and after the heat treatment of the materials mixture.

4.2 Results

4.2.1 Physico-chemical and thermal characterizations of pristine carbons

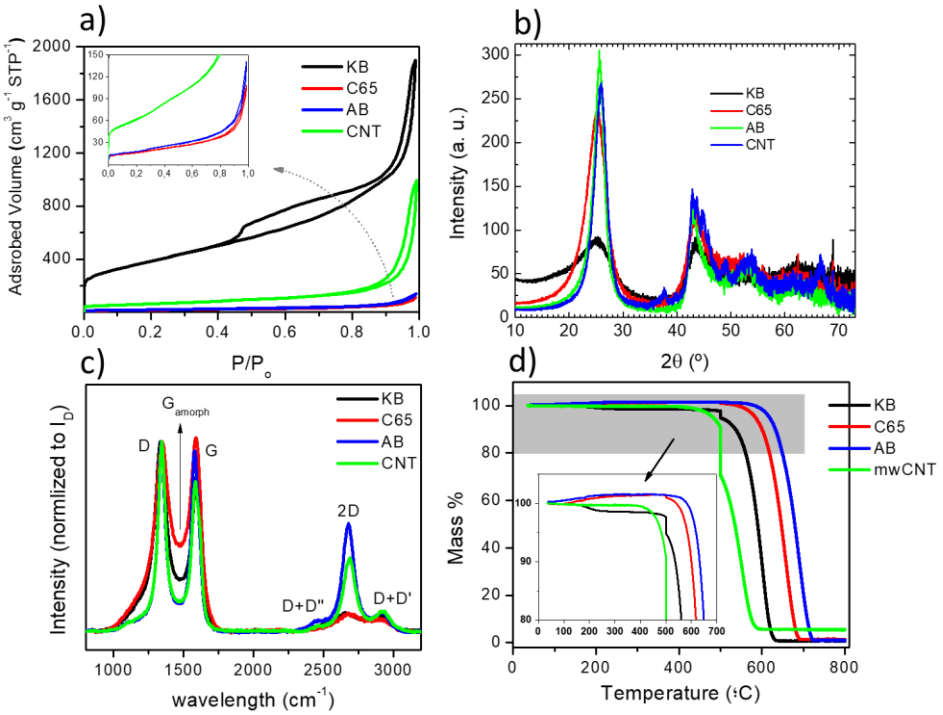

Figure 4. 1: Physical, structural, and thermal characterizations of pristine carbons; KB, C65, AB, and mwCNT. **a)** Nitrogen adsorption-desorption isotherms at –196 °C **b)** X-ray diffraction pattern **c)** Raman spectrum and **d)** Thermogravimetric curves.

4.2.1.1 Surface area and porosity: N_2 physical adsorption

N_2 physical adsorption analyses were initially performed to investigate the surface area and porosity of the different carbon additives, (Figure 4. 1a). It is worth mentioning that this technique only evaluates the presence of micro- (≤ 2nm) and mesopores (≥2nm and ≤ 50 nm) but not the macroporosity (≥ 50nm). C65 and AB yielded a very low specific surface area (57-65 m^2 g^{-1}) and did not adsorb nitrogen significantly in the whole relative pressure range, indicating a non-porous nature. mwCNTs exhibit a larger specific surface area of 219 m^2 g^{-1} and noticeable capillary adsorption at high relative pressures, indicating the

existence of both micropores and large mesopores (inter-tube spaces) in its structure. Finally, KB exhibits a much larger surface area (1383 m^2 g^{-1}) as compared with the other carbons. The large hysteresis loop and the slopy increase of the nitrogen adsorption from low to medium relative pressures indicates the presence of narrow mesopores while, similar to mwCNTs, the significative increase of adsorbed gas at high pressure reveals the presence of large mesopores. From the pore size distribution (Figure 4. 2a), it is verified that all the carbons yield micropores of 0.9 nm wide, where the contribution of these pores for KB and mwCNT is much more significant. Unlike other carbons, KB also exhibits a great contribution of narrow micropores around 0.48 nm and mesopores larger than 2 nm. mwCNT yields a moderate distribution of mesopores over 6nm. The surface area from BET is summarized in Table 4. 1.

4.2.1.2 Bulk crystallinity: X-ray diffraction (XRD)

The sharp diffraction peaks at 2θ= 26.45°and 42.31° (Figure 4. 1b) correspond to (002) and (110) hkl reflections respectively and reveal the layered nature of these carbons. 2H-graphite refection (101) is not observed, confirming the non-graphitic nature of these carbons, i.e., their layered structure is fully turbostratic. In Figure 4. 1b, the (002) diffraction peaks of AB and mwCNT are narrower and shifted towards larger angles, compared to C65 and KB, denoting a smaller interlayer distance and larger crystallite size L_C in the stacking direction (see Table 4. 1). According to the width of the diffraction peaks, AB and mwCNT is the most crystalline, followed by C65, and KB is the least crystalline. This is confirmed by the inverse trend in the interlayer distance (largest for KB, smallest for AB and mwCNT), as the more crystalline an sp2 carbon is the closer its interlayer distance is to ideal graphite (3.36 Å). Moreover, an additional intensity at a low angle overlaying the main interlayer reflection (002) can be observed for KB, see Figure 4. 1b. Such a raising background at low angles can be ascribed to a SAXS signal owing to the presence of a large amount of fine structure microporosity.[307]–[309] This

intense SAXS signal points out to its superior microporosity, in agreement with pore size distribution (Figure 4. 2a) and the larger surface area detected by gas adsorption for KB compared to the other tested carbons.

4.2.1.3 Chemical structure: Raman spectroscopy

The Raman spectra (Figure 4. 1c) yield the characteristic peaks found in sp^2 carbon materials[310]–[312]: (1) The G–band at 1585 cm^{-1}, related to the stretching vibration of sp^2–based C=C bonds in a high ordered defect-free environment, whose sharpness is related to the uniformity of the bonds; (2) the D–band at 1340 cm^{-1}, representing the breathing vibration of sp^2–hybridized aromatic carbon rings located next to an edge or defect in the lattice, which is associated with the presence of disorder and (3) the second-order Raman spectra (i.e., the 2300–3300 cm-^{1} region), where different low–intensity bands appear. The most relevant one is the 2D peak, located at about 2695 cm^{-1}, which is the overtone of the D band but contrary to the D band, it does not need to be activated by the presence of defects. As the G band, the 2D band is sensitive to structural disorder and tends to increase as the structural order of the carbon increases.

Table 4. 1: Summary of pristine carbon physicochemical properties: BET surface area, crystallinity, thermal stability, purity, and morphology.

	KB	C65	AB	mwCNT
Surface area (m^2/g) [BET]	1383	57	65	219
Average interlayer distance c/2 (Å) [XRD]	4.05 +/- 0.09	3.64 +/- 0.02	3.551 +/- 0.006	3.48 +/- 0.007
L_C (nm) [XRD]	0.8 +/- 0.2	1.85 +/- 0.08	3.2 +/- 0.1	3.09 +/- 0.08
Onset oxidation temperature in °C [TGA]	430	510	540	400
Inorganic impurity after 800°C firing [TGA]	0.76%	1.51%	1.04%	5.61%
Surface adsorbed species [XPS]	absent	absent	absent	absent
Agglomeration [SEM]	lowest	low	high	highest

Table 4. 1 gathers a summary of the physicochemical properties of the selected carbon materials. Overall, KB exhibits a high surface area (1383 m^2 g^{-1}) with high microporosity and low crystallinity (highest c/2 and lowest L_c), while AB is the most crystalline carbon material (second lowest c/2 and higher L_c) with the lowest porosity (57 m^2 g^{-1}), suggesting a correlation between surface area and crystallinity. C65 has an equivalent surface area to AB but slightly lower crystallinity (i.e., higher c/2 and lower L_c). According to XRD and N_2 adsorption, mwCNT has high crystallinity similar to AB but a moderate surface area (219 m^2 g^{-1}) due to a different type of porosity in this material, which arises from the inner space of the tubes and their nanometric width, with no structural prejudice of the carbon lattice structure. The observations from Raman spectroscopy (i.e. sharper D/G bands, the larger intensity of the 2D band, presence of more asymmetric line shape in the second order spectra (2D band) for AB and mwCNT) indicate a higher degree of crystallinity compared to that of C65 and KB, which is in agreement with XRD.

4.2.1.4 Thermal stability: Thermogravimetric analysis (TGA)

The thermal stability of pristine carbons was studied by thermogravimetric analysis under air atmosphere (TGA) (Figure 4. 1d). As expected, all carbons exhibit a weight loss starting between 400˚C and 550˚C indicating decomposition into CO_2. However, the onset of carbon oxidation temperature significantly varies, and follows the order mwCNT < KB < C65 < AB. Except for mwCNTs, this trend correlates well with the surface area (and in turn crystallinity) as a higher surface led to the enhanced contact area between carbon and oxygen, and therefore higher reactivity.[313], [314] Interestingly, the diffraction patterns and Raman spectra of mwCNTs and AB are very similar, yet the thermal stability of the former is significantly lower because their 1D structure facilitates the accessibility of reactive agents (i.e., air/oxygen in this case), resulting in the lowest thermal stability. A close inspection of the dwelling time at 500 °C for 1 h reveals a slight degradation of KB and mwCNTs from

the early stages of the treatment. In contrast, both AB and C65, with lower surface area, seem to undergo a slight mass increase, probably caused by the oxidation or oxygen physisorption at mild temperatures; but with no degradation into CO_2 and CO until 600°C, which represents a significant difference of more than 100°C compared to mwCNT and KB. The purity of KB, C65, and AB is acceptable considering that the remaining mass at 800 °C corresponding to inorganic impurities is in the range of 0.76 wt. %- 1.51 wt.%. This is however not the case of mwCNT as a residue of 5.61 wt.% is obtained (Figure 4. 2b). The presence of inorganic impurities of commercial mwCNT is commonly acknowledged due to their preparation process where metal nanoparticles (such as silicon, iron or aluminum) are used as catalyzers to prepare the nanotubes by Chemical Vapor Deposition (CVD)[315].

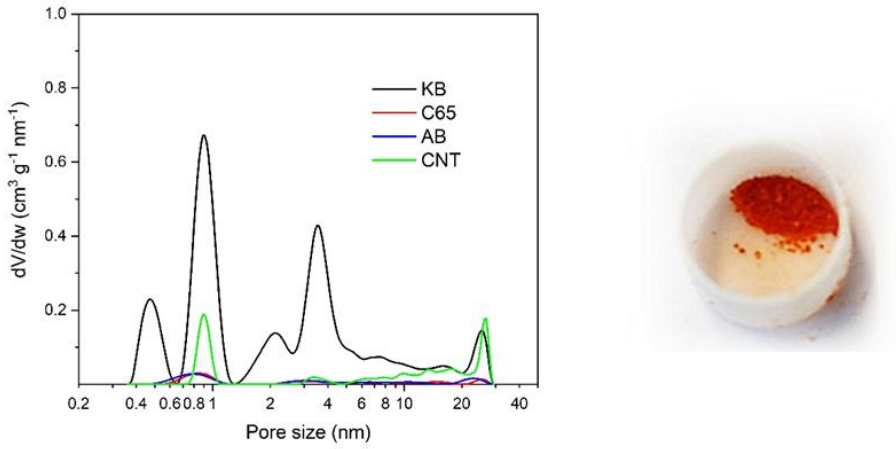

Figure 4. 2: a) The pore size distribution obtained from nitrogen adsorption-desorption isotherms at –196 °C by 2D-NLDFT-Heterogeneous surface model for Carbon. **b)** the residue left by mwCNT after TGA measurement.

4.2.1.5 Surface purity: X-ray photoelectron spectroscopy

X-ray photoelectron spectroscopy (XPS) analysis indicates the absence of surface-adsorbed species and organic impurities in all carbons (refer to Figure 4. 3).

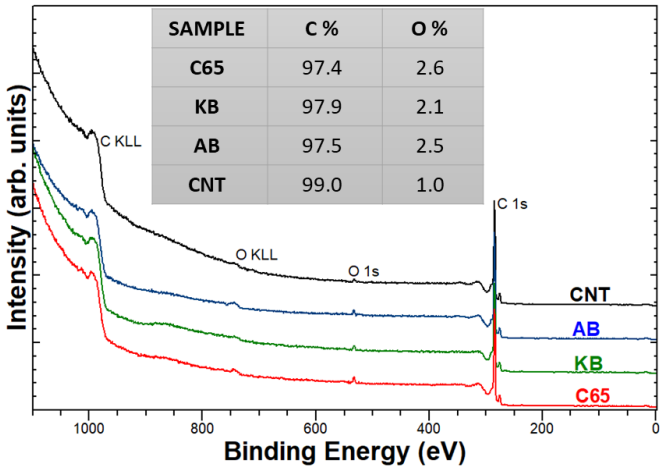

Figure 4. 3: Survey spectra of the 4 carbons under XPS study. The resulting O and C percentages got from the O 1s and C 1s high-resolution regions are given in Table (inset) and do not indicate significant adsorbed species.

4.2.2 Pristine carbon and composite surface morphology: Scanning electron microscopy (SEM)

The morphology of the pristine carbon materials is shown in the Scanning electron microscopy (SEM) images of Figure 4. 4 a-d**.** Figure 4. 4a reveals a very small particle size and very little agglomeration for KB. C65 and AB have similar morphology, but AB suffers from slightly higher particle agglomeration compared to C65. In contrast, mwCNTs present large particle agglomerates of about 0.5 µm. The agglomeration of pristine carbons is also reflected in the carbon distribution in the composites (Figure 4. 4 e-h). For example, KB results in the highest volume distribution cathode giving a highly homogeneous composite (Figure 4. 4e). On the other hand, mwCNTs, with the higher degree of agglomeration, show poor homogeneity in the composite cathode (Figure 4. 4h). Hence the order of agglomeration and its resulting inhomogeneity in the composite is mwCNT > AB > C65 > KB.

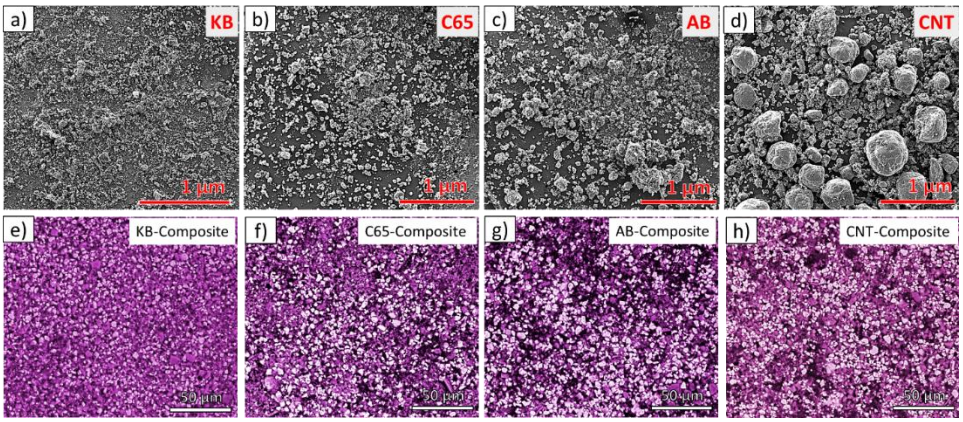

Figure 4. 4: SEM morphology comparison of pristine carbons: **a)** KB **b)** C65 **c)** AB **d)** mwCNT and mixed composite cathode laminates: **e)** KB-composite **f)** C65-composite **g)** AB-composite **h)** mwCNT-composite, where the color codes white, violet and black represents NMC, LATP, and carbon respectively (the image has been artificially colored to enhance the contrast between the different components).

4.2.3 Electrochemistry: Galvanostatic cycling with potential limitation (GCPL)

The electrochemical behavior of the composite cathodes before (hereafter as-mixed composite cathodes) and after thermal treatment at 500˚C has been compared to understand the role of carbon in the cathode thermal stability upon densification. The choice of such conditions was based on a former study in which mutual reactivity was observed at the surface from 500 °C and in the bulk at 600 °C, and this severely affected the electrochemical performance of the composite.[305]

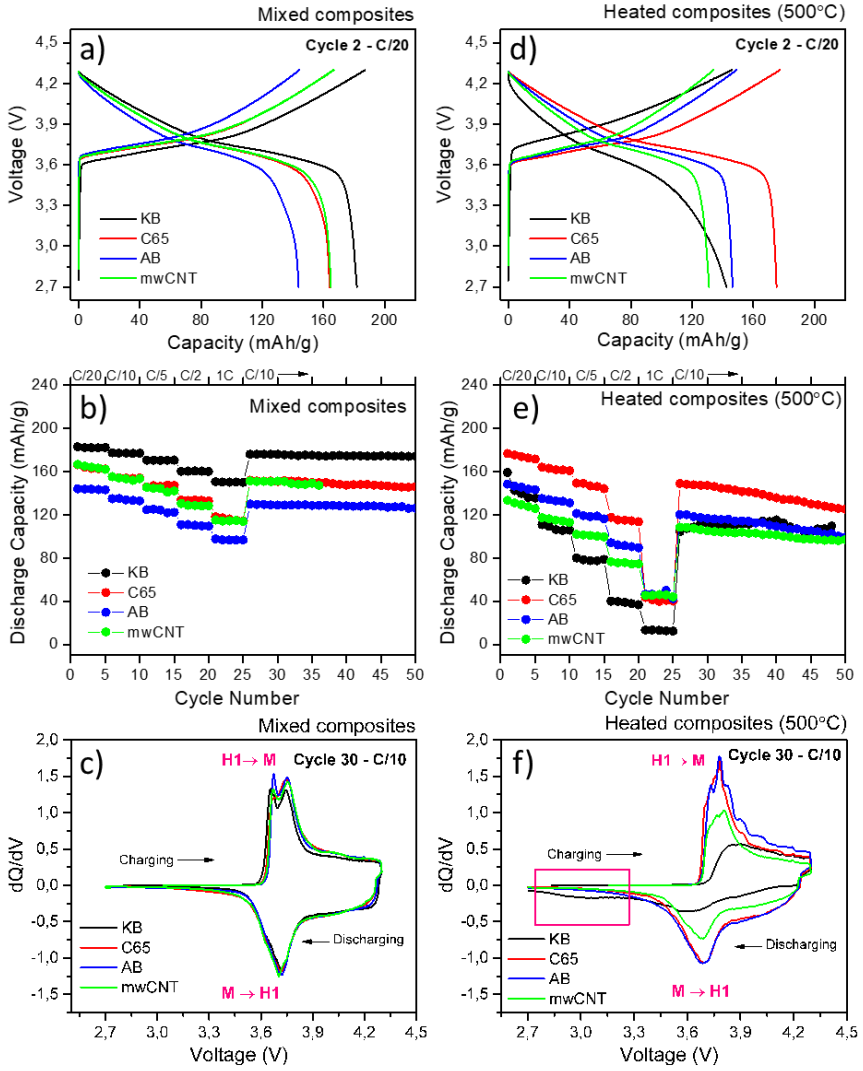

Figure 4. 5: NMC-LATP-carbon composite cathode electrochemistry tests in conventional half-cell configuration using the liquid electrolyte. Comparison of mixed composites (**a, b, c**) and 500°C-air heat-treated composites (**d, e, f**) with different grades of carbon as a conductive additive (KB, C65, AB, and mwCNT). a) and d): Second charge-discharge cycle at a C rate of C/20. **b)** & **e)**: C-rate capability tests with the C-rates; C/20, C/10, C/5, C/2, 1C [5 cycles each] and C/10 [long cycling]. **c)** & **f)**: Differential capacity (dQ/dV) vs voltage curves.

First, the ability of these different types of carbon to provide a percolative conductive network in composite electrodes with a ratio NMC: LATP: carbon=65:30:5 was evaluated in a half-cell configuration. Figure 4. 5a compares the second charge-discharge curves of as-mixed composite cathodes,

with different grades of carbon, in Li-half-cells cycled between 4.3 and 2.7 V vs Li^+/Li. These results show that the choice of the type of carbon has a very significant impact on the obtained capacity. The KB-composite gives the most promising results with a discharge capacity of 182 mAh/g at C/20 with negligible irreversibility and maintains 82% of this capacity at 1C (to that of C/20), which is the highest among all the carbon grades. The C65- and mwCNT-composites give a capacity of 164 mAh/g at C/20 and maintain 70% at 1C. The AB composite has a capacity of 144 mAh/g at C20 and only keeps 67 % at 1C, which is the lowest obtained in this study. It is worth mentioning that both the initial charge-discharge capacity and the rate capability exhibit the same trend, i.e., KB > C65 ~mwCNT > AB (Figure 4. 5b). The differential capacity (dQ/dV) vs voltage curves (Figure 4. 5c) confirm that in all cases the expected redox processes occur in NMC (hexagonal H1 ↔ monoclinic M around 3.7V) [316]–[321].

The electrochemical performance of heat-treated composites reveals that the heat treatment significantly alters the composite electrochemical performance with all grades of carbons. Figure 4. 5d shows the second charge-discharge curve of the heated composites at C/20, where it can be observed that 500-KB composite has a significant drop in capacity (more than 20 %) along with an enhanced polarization and a more slopy discharge curve compared to the corresponding mixed composite. This material is also the most affected in rate capability, and the capacity fading is prominent for initial cycles, though later stabilizes upon cycling. 500-mwCNT composite also exhibits lower capacity, however, the polarization has not significantly increased, and the shape of the voltage-capacity curve is overall maintained. In line with this, the reduction in rate capability is less salient compared to other carbon grades. However, capacity fading is noticeable upon cycling, and the obtained capacity values are below those of the mixed composite. For the 500-AB composite, there is no difference in the capacity values at low C-rates and the polarization

has slightly reduced, although the capacity reduces drastically with increasing C rates and upon cycling. Interestingly, the 500-C65 composite delivers improved performance at C/20. The initial capacity after heat treatment has increased to 180 mAh/g which is more than a 10 % increment compared to the mixed composite. It also exhibits better performance at C/10 and C/5 compared to the as-mixed composite, but the capacity value diminishes at higher C rates (C/2, 1C) as well as with the number of cycles (Figure 4. 5e). Overall, the rate capability and cyclability performance follow the order C65>AB>mwCNT>KB. Interestingly C65 is found to exhibit favorable thermal stability compared to other carbon grades, although the poor rate capability at high C rates is still a concern. A summary of the electrochemical discharge capacity and mid voltage polarization at lower (C/20) and higher (1C) C rates for mixed and heated composites made of the different carbon grades is given in Table 4. 1.

Table 4. 2: Summary of electrochemical parameters of mixed and heated composites made of different carbon grades; Discharge capacity and mid voltage polarization at lower (C/20) and higher (1C) C rates.

Cathode Composition		Discharge capacities (mAh/g)		mid voltage polarization (mV)	
		Cycle 2 (C/20)	Cycle 23 (1C)	Cycle 2 (C/20)	Cycle 23 (1C)
Mixed	KB	182	150 (82%)	44	117
	C65	164	116 (70%)	58	278
	AB	144	97 (67%)	86	219
	mwCNT	165	114 (69%)	63	279
500°C	KB	142	13 (9%)	292	1148
	C65	175	40 (23%)	21	705
	AB	146	46 (32%)	35	635
	mwCNT	131	46 (35%)	46	854

The differential capacity (dQ/dV) vs voltage plots of the 30th charge-discharge curve for heated composites is compared in Figure 4. 5f, where significant changes can be observed. First, the oxidation peak doublet during charging, which is a specificity of Ni-rich NMCs (>50% Ni),[320] has become less defined and has even disappeared for 500-KB composite. This is pointing to a probable loss of Ni in the NMC structure after the heat treatment that gets enhanced upon cycling. Another observation is the shift in the second oxidation peak to higher voltages (3.78 V for 500-C65 and 500-AB composites, 3.80 V for 500-mwCNT, and 3.87 V for 500-KB composite respectively). A significant broadening for the reduction peak at 3.7 V and a shift towards lower voltage values can also be observed (this is visible for the KB composite). This indicates an increment in polarization that is more pronounced for KB composite as it is already visible in the initial charge-discharge curve in Figure 4. 5d. Besides, in this sample there is a reduction peak appearing around 3 V, in agreement with the more slopy voltage-composition curve in this voltage range. It probably indicates the lithiation of an electrochemically active secondary phase formed after the heat treatment. A close look at the evolution of this peak with the number of cycles (Figure 4. 6) indicates that the peak appears from the second cycle onwards, intensifies with increasing cycle number and later fades with further cycling. It has been previously reported in Li-rich oxides that the slow growth of a peak between 3 and 3.5 V during the reduction process indicates Mn^{4+} reduction. [322], [323] The formation of an Mn^{4+} rich phase (for example, MnO_2) could thus be occurring during the heat treatment and be responsible for the new reduction peak. [322], [323] To understand the source of these changes, the composite was taken to heat-treatment in binary systems (see Appendices-Chapter 4 for more details). A similar trend is observed in the system in which NMC+ KB was heated first and LATP was added later, more intensely in the initial cycle (Appendix 4. 1c) as well as with further cycling (Appendix 4. 2). This indicates the secondary phase that undergoes lithiation during discharge

(reduction peak at 3V) is the byproduct of NMC-KB reactivity during the heat treatment of the NMC-LATP-carbon composite.

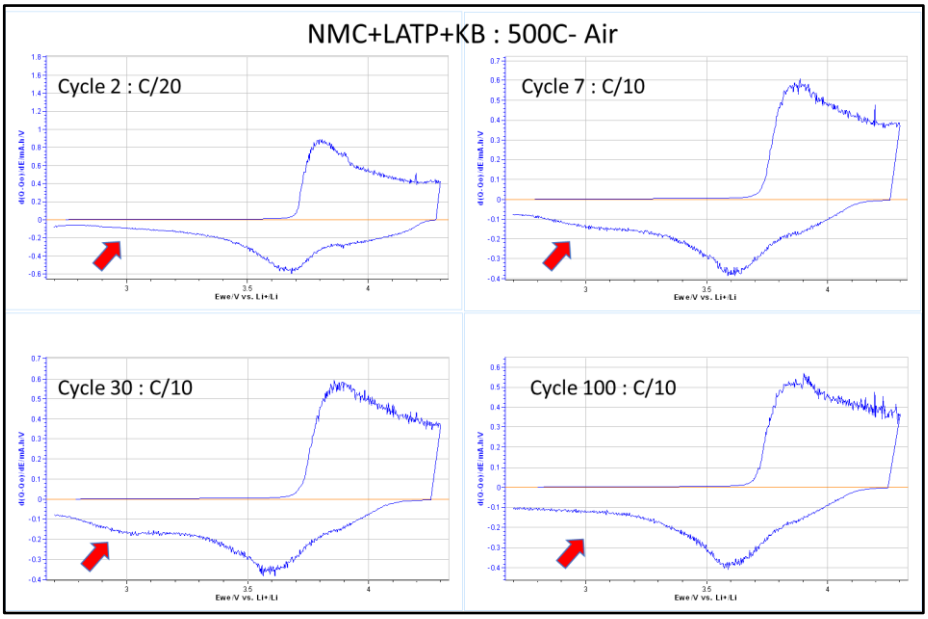

Figure 4. 6: Comparison of the differential capacity (dQ/dV) vs voltage plots of cycle 2 (C/20), cycle 7, 30, and 100 (C/10) of heat-treated KB composite. The evolution of the reduction peak around 3V can be observed, which arises after the second cycle, and intensifies with the number of cycles before fading with further cycling.

The impact of the amount of carbon in the composite: was also evaluated in the 500-C65 composite by increasing the weight percentage of C65 from 5 to 10. However, this resulted in worse electrochemical performance for both mixed and heated composites (Figure 4. 7). This highlights the high sensitivity of the amount of carbon in the composite towards their reactivity under temperature.

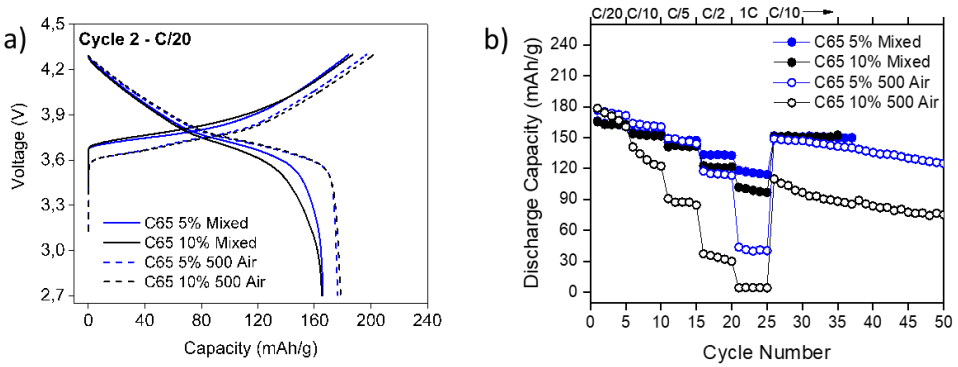

Figure 4. 7: Comparison of electrochemistry for mixed and heated NMC-LATP-C65 composites with 2 different weight percentages of C65 (5 & 10%) in the composite where the NMC-LATP ratio was maintained. **a)** Second charge-discharge cycle at a C rate of C/20. **b)** C-rate capability tests with the C-rates; C/20, C/10, C/5, C/2, 1C [5 cycles each] and C/10 [long cycling].

4.2.4 Structural analyses: X-ray techniques

4.2.4.1 X-ray diffraction (XRD)

To investigate the origin of the significant differences observed for the different types of carbon, X-ray diffraction (XRD) was performed on composites based on KB and C65. The XRD peaks of NMC were compared between 500-KB, 500-C65, and pristine NMC (Figure 4. 8). An asymmetrical broadening is observed in certain peaks for 500-KB (see for example, 101 and 104) which indicates a transition metal redistribution that further results in the phase transition of NMC to spinel first and later to rocksalt-MO.[305] In 500-C65 the NMC is preserved despite an increment in intensity ratio between 003 and 104 peaks. The origin of such change remains unclear, as all simulated scenarios involving changes in TM or O occupancies or stacking faults were unsuccessful in reproducing this result.

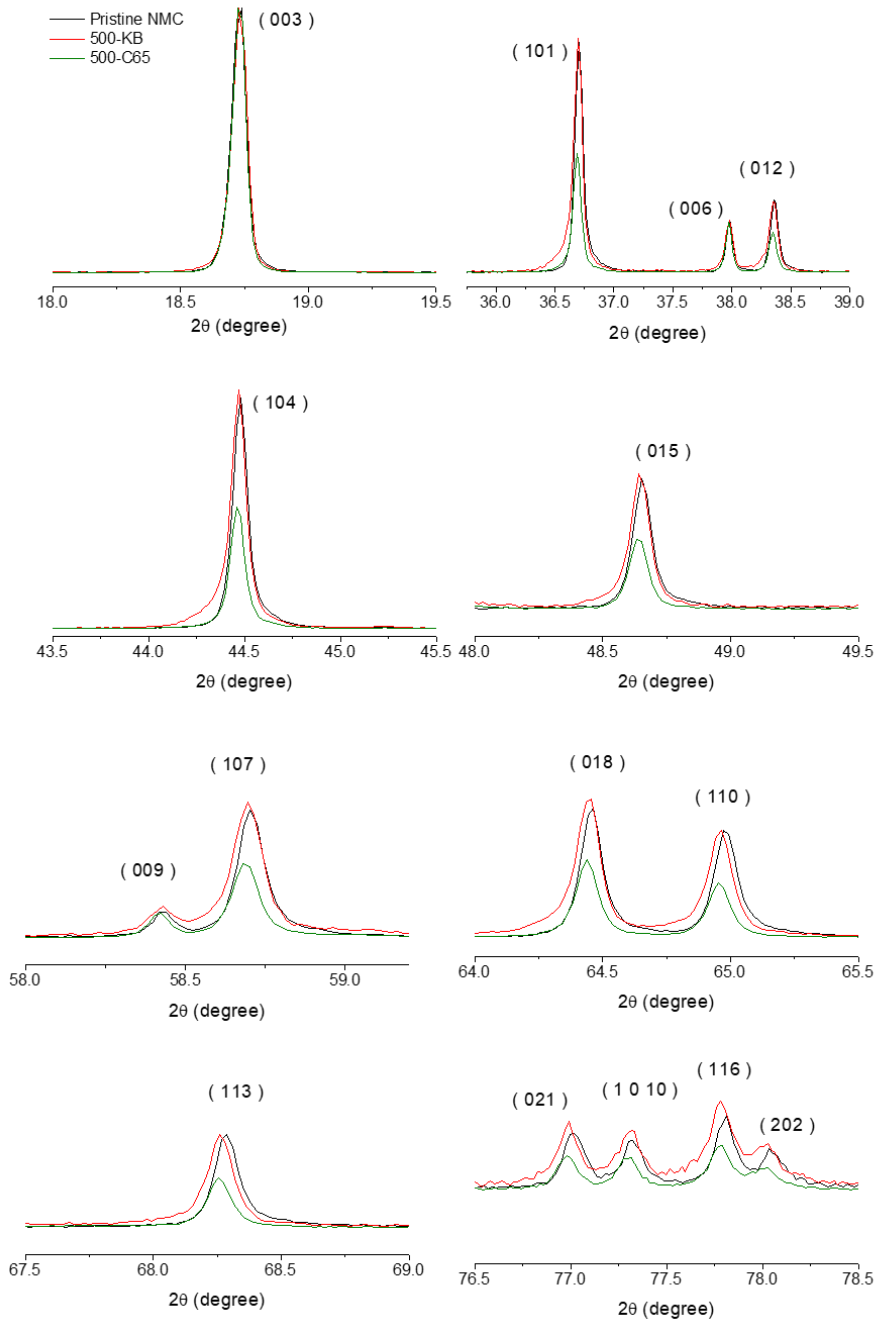

Figure 4. 8: X-ray diffractogram of selected peaks arising from NMC compared between pristine NMC (black), 500-KB (red), and 500-C65 (green)

4.2.4.2 X-ray absorption spectroscopy (XAS)

XAS was performed in both TEY (Total electron-yield) and TFY (Total fluorescence-yield) modes on pristine materials (NMC, KB, and C65) and heated composites 500-KB and 500-C65 to evaluate the oxidation state of both transition metal elements and the carbon atoms and their evolution after heat treatment. The spectra shown in Figure 4. 9 correspond to the TEY mode, which, because of the reduced path of electrons in matter, contains information on the near-surface of the sample (typically <10 nm). As depicted in Figure 4. 9a, the Ni L edge shifts to lower energies in the heated composites compared to the pristine NMC, especially in the case of 500-KB composite. This is characteristic of the chemical reduction of Ni at the surface of the particles. From the ratio between the two main peaks in the L_3 edge, we estimate the following trend in the Ni oxidation state (see Appendices-Chapter 4 for more details): +2.7 for pristine NMC, +2.3 for 500-C65 composite and +2.2 for 500-KB composite. In the case of Co (Figure 4. 9b) and Mn (Figure 4. 9c), the spectra of pristine NMC and 500-C65 composite are quite similar, and a shifted spectrum is obtained for the heated composite with KB. Based on the shift of the spectrum centroids (see Appendices-Chapter 4 for more details) we estimate the following trend for the Co oxidation state: +3.0 for pristine NMC, +3.0 for 500-C65 composite, and +2.9 for 500-KB composite. The same inspection in Mn gives us: +4.0 in NMC, +4.0 in 500-C65 composite, and +3.8 in 500-KB composite (Table 4. 3 shows the summary). Hence, Ni is preferentially reduced on the surface of the particles, followed by Co and Mn. In all cases, the reduction is stronger when KB is used in the composite.

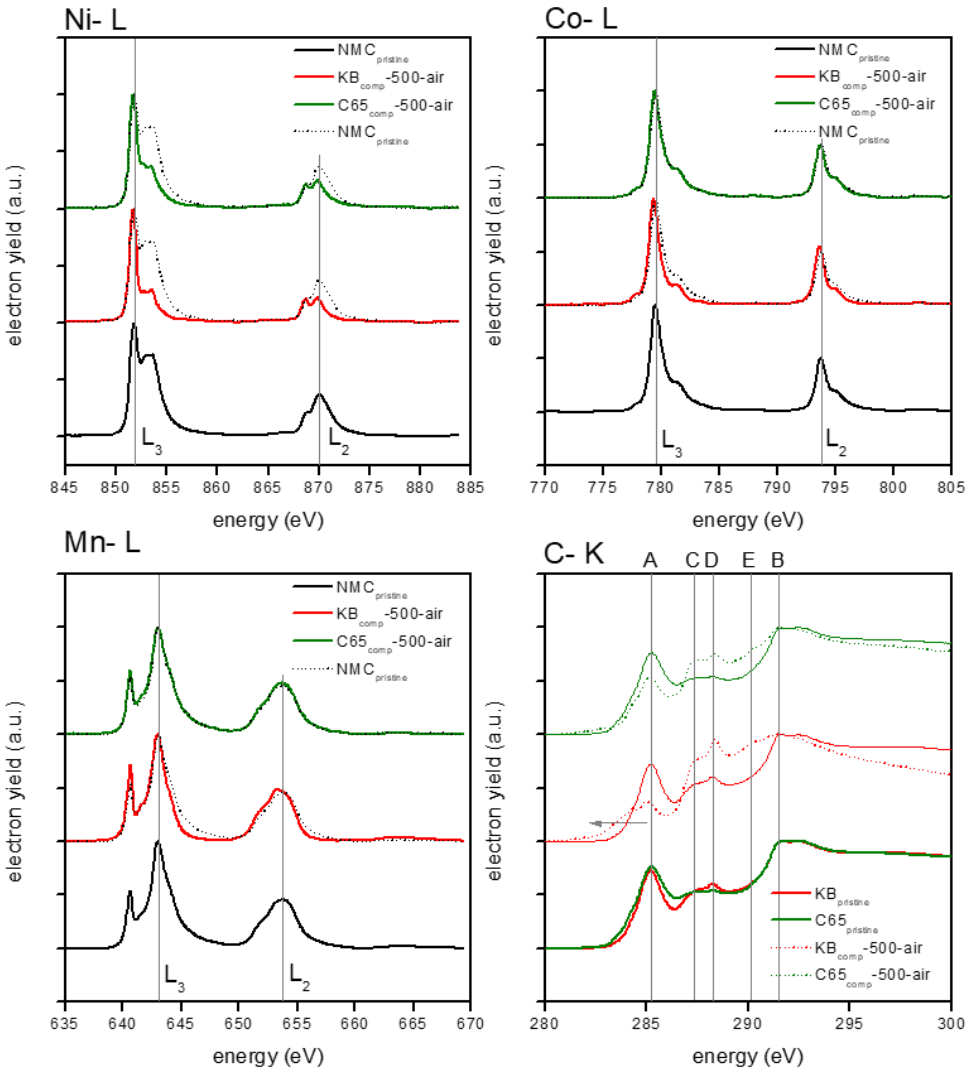

Figure 4. 9: Element-specific soft X-ray absorption edges of active material transition metals (L edges) of **a)** Ni, **b)** Co, **c)** Mn, and **d)** C (K edge) measured in total electron yield (TEY) mode.

Table 4. 3: Summary of oxidation states of transition metals (Ni, Co, and Mn) in the pristine NMC, 500-KB composite, and 500-C65 composite.

Oxidation states	Pristine NMC	500-C65 composite	500-KBS composite
Ni	+2.7	+2.3	+2.2
Co	+3.0	+3.0	+2.9
Mn	+4.0	+4.0	+3.8

The corresponding spectra measured in TFY (Figure 4. 10), with a probe depth of 100-200 nm, show that the reduction of Ni in heated composites is still apparent in the under-surface region, though there is no or little change for Co. Given the reduction order of transition metals in the surface we may expect a similar unaffected change for Mn in the bulk. Still, we could not measure a reliable Mn nor C spectrum by TFY because of saturation effects. [324]

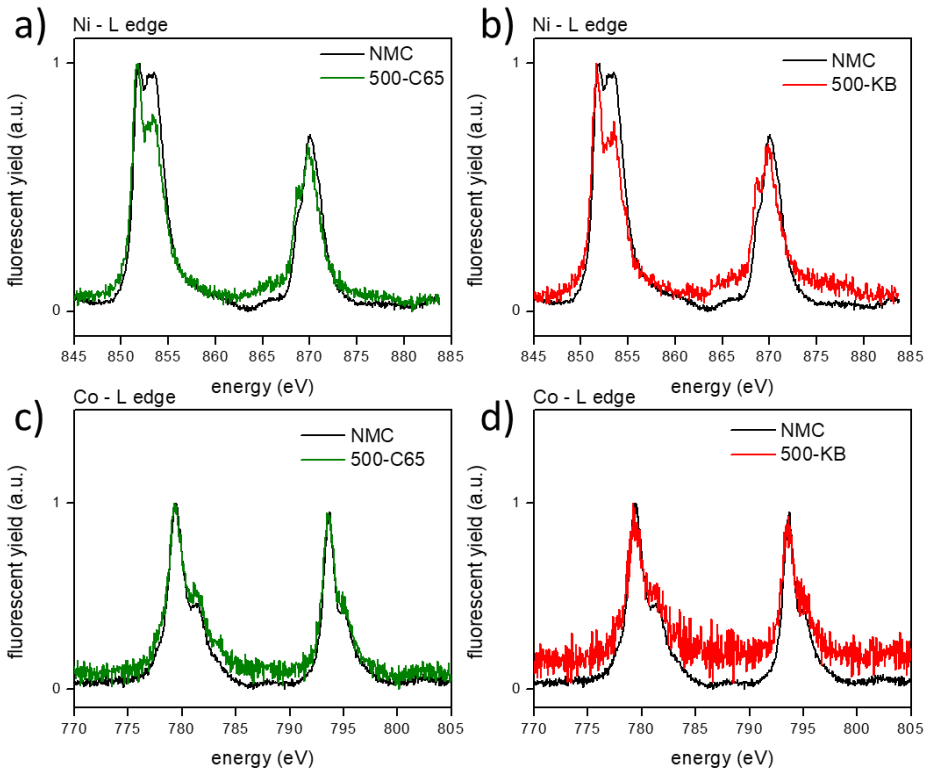

Figure 4. 10: Element-specific soft X-ray absorption spectra measured in TFY of active material transition metals ($L_{3,2}$ edges). **a)** Ni L edge in 500-C65 composite **b)** Ni L edge in 500-KB composite **c)** Co L edge in 500-C65 composite and **d)** Co L edge in the 500-KB composite

Figure 4. 9d represents the C K edge of pristine C65 and KB, together with 500-C65 and 500-KB composites. Observations from the 500-KB composite indicate a high degree of structural (and electronic) rearrangement of the aromatic ring that is accommodating oxygen and the presence of edge/defect states indicating the prominent oxidation of KB and defect formation in its

structure. As well as the formation of these new oxygen functionalities upon carbon oxidation. (See Appendices-Chapter 4 for further details)

The TEY XAS comparison of pristine materials with 500-KB and 500-C65 composites is thus showing that the heating process is causing a superficial degradation of the NMC that involves the reduction of the transition metals, especially Ni, accompanied by carbon oxidation and that these effects are more pronounced for the composite with KB than for the C65 one. Part of the Ni has been consumed to form an electrochemically inactive Ni^{2+} phase upon heating, likely NiO, as pointed out in our previous study.[305] It is worth mentioning that while only Ni is somewhat reduced in the 500-C65 composite, the three metals (Ni, Co, and Mn) experience some reduction if KB is employed, pointing to a higher destabilization of NMC and the possible formation of new phases. Although not shown here, surface changes are not silent for LATP, as the degradation of NMC is accompanied by a Li loss that leads to LATP decomposition as well. The bigger impact of KB compared to C65 on the active material degradation together with its higher oxidation (leading to a decreased electrical conductivity) correlates well with the electrochemical results.

4.3 Discussion

The higher electrochemical discharge capacity and better rate capability of the as-mixed KB-composite can be ascribed to the high surface area of KB that gives enhanced volume distribution and abundant conducting pathways for electrical conductivity. On the other hand, the lower surface area carbons, C65 and AB lead to comparatively poor electrochemical performance in corresponding mixed composites. In the mwCNT-composite, the higher surface area and the aspect ratio of the carbon favor the electrochemistry but the high content of agglomeration and the presence of a metal oxide impurity limits further enhancement in the electrochemical performance beyond that of C65. Hence, the carbon with a higher surface area, lower content of agglomeration,

and high purity offers the best electrochemistry of NMC-LATP-carbon composite cathode without heat treatments.

In the heated composites, the properties of carbon additives (surface area, crystallinity, agglomeration, and on-set oxidation temperature) are highly interdependent and they combinedly impact the NMC-LATP-carbon composite thermal stability. KB, with the highest surface area and low crystallinity, is found to be easily oxidized from TGA. As a result, the 500-KB composite is the most affected in its electrochemical performance. To assure electrical conductivity, the carbon mustn't oxidize completely from the system during the heat treatment. The reduced electrical conductivity of KB as a consequence of its oxidation leads to electrochemical polarization. Also, XAS analysis of 500-KB shows the reduced nickel and cobalt at the surface, possibly in the form of insulating surface rock-salt phases of transition metal oxides that also contribute to cell polarization. The lowest oxidation temperature (on-set from TGA) of mwCNT due to its special morphology and the high surface area doesn’t favor either the electrochemistry after heat treatment. On the other hand, AB with the lowest surface area and high crystallinity shows the highest thermal stability towards oxidation, with no considerable difference in electrochemical performance between AB-composites before and after heat treatment, except for a very slight degradation in the rate capability and capacity retention. Finally, even though C65 has a slightly lower on-set oxidation temperature than AB, its lower agglomeration favors the 500-C65 electrochemistry and becomes the best among all the heated composites and therefore should be preferentially chosen as a carbon additive in composite oxide-based cathodes thermally processed.

4.4 Conclusions

The choice of the conducting carbon material used in composite cathodes has a very significant impact on the electrochemical properties of the cell. From all the carbons studied (AB, C65, KB, and mwCNTs), the KB-composite exhibits

the best performance owing to the high surface area and negligible agglomeration of KB, offering high volume distribution for the electrically conductive pathways in the electrode. However, because of the same reasons, KB plays a negative role in the heated composite (500-KB composite), as the high surface area of KB leads to its faster oxidation, resulting in significant degradation of NMC as well as KB in the 500-KB composite. On the other hand, C65 with the lowest surface area, lower crystallinity, and high oxidation temperature shows promising electrochemistry for 500-C65 composite. According to XAS and XRD investigations, a reduced degradation of the composite components was observed, which confirms that C65 is the best candidate for NMC-LATP-carbon composite processed at temperatures around 500˚C.

CHAPTER 5: HIGH-PRESSURE LOW-TEMPERATURE (HPLT) TECHNIQUE: OPTIMIZATION OF LATP SOLID ELECTROLYTE DENSIFICATION & COMPOSITE CATHODE RESPONSE

5.1 Introduction

Among the reported oxide-based solid lithium-ion conductors, NASICON type $Li_{1+x}Al_xTi_{2-x}(PO4)_3$ (LATP) is in the spotlight owing to its stability under ambient conditions, low density, high ionic conductivity, and stability at high voltages when paired with cathodes such as Ni-rich NMC. [325]–[330] For the practical application of LATP as a solid electrolyte, processing techniques resulting in a dense microstructure allowing high Li^+ mobility are required. These typically involve grain growth through particle fusion through mass transport, leading to a relative density above 95%. [181] The highest reported room temperature ionic conductivity of LATP is $1.09x10^{-3}$ S cm^{-1} , which was achieved under very particular conditions (mechanically milling -40 hours- to obtain a glassy phase followed by high-temperature sintering at 900˚C for 6h).[331] However, conventional high-temperature sintering of LATP is typically done at temperatures >1000˚C, below melting temperature, for several hours.[332] The exposure at high temperatures during densification unavoidably leads to several undesired effects which include 1) Li^+ loss from the crystal structure resulting in a lower number of charge carriers and therefore lower conductivity; 2) temperature-induced non-uniform unit cell expansion (along c-axis) that leads to grain cracking during densification; 3) evolution of unfavorable secondary phases (e.g., $AlPO_4$) that overall will inhibit ionic transport; and 4) undesired porosity, which may disrupt the Li^+ mobility and provide a path for Li dendrite growth during cycling, producing a short circuit and cell failure.[333]–[335] Apart from that the high cost (high electricity is consumed and the processing time can be delayed up to days), low production rates, and high complexity are general demerits of high-temperature sintering. [336]

There are several advancements in sintering techniques to reduce the temperature, as already mentioned in chapter 1. However, it is still necessary to bring down the temperature and duration of the process even further without the addition of any solvents to reach key performance indicators for scalability. Previous compatibility studies indicate that the threshold temperature to avoid chemical reactivity between cell components should be below 500 ˚C for LATP-NMC-C systems. [305] Despite of one order lesser conductivity (1.26×10^{-5} Scm^{-1}) the cold sintering technique allows to reduce the densification temperature of LATP further (down to 200˚C) but involves the presence of water as a transient liquid phase, which can lead to undesired mixed (lithium and proton) conductivity.[199][203] Thus decreasing the sintering temperature without employing solvent is thus necessary for the deployment of competitive low-energy processing of solid electrolytes and to ensure thermal compatibility when co-sintering composite cathodes with active materials. [182], [266], [337]

Herein we explore an alternative technique for the preparation of dense LATP solid electrolyte that involves the simultaneous application of high quasi-isostatic pressure (above 1 GPa) and mild temperatures (100-300 ºC) allowing for densification within only a few minutes (Figure 5. 1, refer experimental section for more details). The application of the high-pressure low-temperature (HPLT) treatment has not been explored so far for ceramic solid electrolytes and provides a new approach to solid electrolyte processing. The use of significantly lower temperatures and times could help increase manufacturing yields and decrease energy consumption, and therefore would be more environmentally friendly. The aim of this work is thus to explore the application of HPLT to densify LATP powders with different microstructures (micro- and nanometric-sized particles). First, we focus on the impact of temperature, pressure, and time on the densification of LATP micrometric particles. Next, we evaluate the impact of post-heat (PH) treatments on the conductivity of a

selection of the HPLT-densified micrometric-LATP pellets, and finally, the obtained results are used to evaluate the effect of HPLT+PH parameters for the densification of nano-LATP.

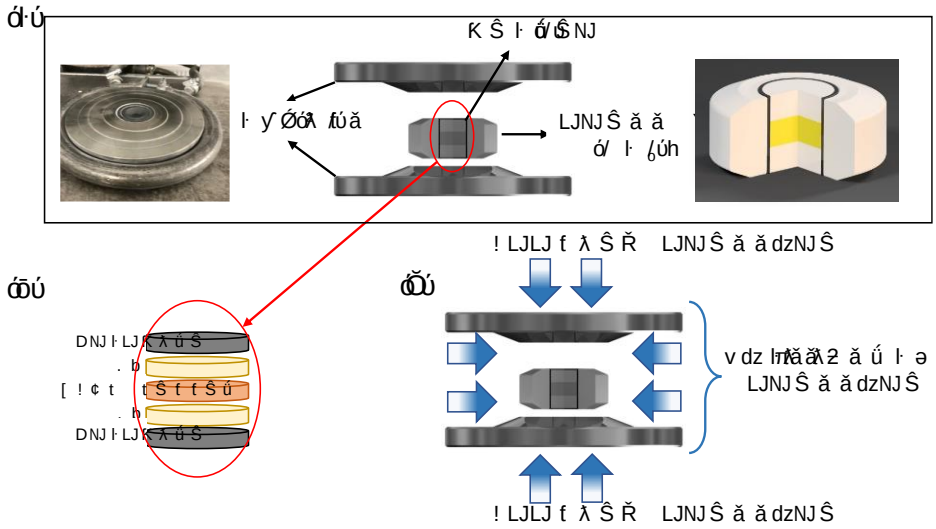

Figure 5. 1: The schematic representation of **a)** components for the high pressure and low temperature (HPLT) technique **b)** Zoomed view of the sample assembly in between BN and followed by the graphite. **c)** Mode of pressure distribution inside the pressing medium where the applied pressure in uniaxial and the effective pressure is quasi-isostatic.

5.2 Micro-LATP under HPLT and PH

5.2.1 Impact of HPLT parameters on the densification of LATP

The HPLT processing comprises three variables: temperature, pressure, and time. The impact of all three parameters on the microstructure and ionic transport properties of micro-LATP has been systematically evaluated to select the best conditions. A set of samples was densified by conventional sintering at high temperatures for comparison.

5.2.1.1 Physical density and appearance

The physical density of conventionally sintered LATP (Conv-LATP) is found to be 2.47 g cm^{-1} (See Figure 5. 3 for the density comparison of different samples). First, a set of samples were HPLT-processed at a pressure of 5.5 GPa

for 2 min, with the processing temperature ranging from 100 to 400°C. The density of the HPLT samples rose with applied temperature from 2.36 g cm^{-1} (sample HPLT-5.5-100-2) up to 2.77 g cm^{-1} (sample HPLT-5.5-400-2) (Figure 5. 3 a). Interestingly, the HPLT approach allows achieving higher density than conventional sintering even at T ≥ 200˚C. However, >300 ˚C, the color of the pellet slightly changed towards grey and became black at 400˚C due to carbon contamination (Figure 5. 2 a). Therefore, 200˚C was the temperature selected to evaluate the impact of time and pressure.

The associated chemical and structural changes due to the change in coloration are explained using Raman spectroscopy in the following section. The LATP pellet, densified at 400 °C using HPLT was further fired at 600°C in a muffle furnace under an air atmosphere for 2 minutes to confirm the carbon diffusion. As expected, the black coloration has been reduced (Figure 5. 2 b) with the heat treatment indicating the oxidation of carbon contamination occurred while HPLT processing. The appearance of a few pores is also spotted on the pellet's surface. The mosaic-like pattern that remains on the pellet even after the post-treatment could indicate the formation of secondary phases (As discussed in later XRD results).

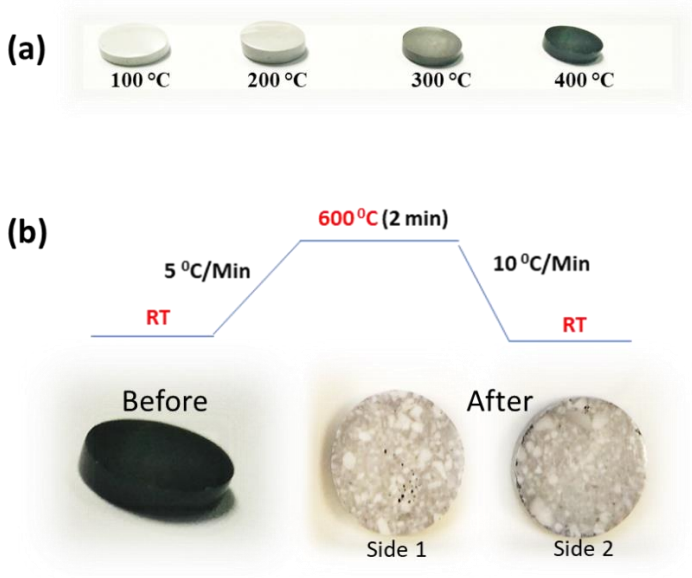

Figure 5. 2: (a) images of LATP pellets sintered using HPLT at different temperatures (100-400 °C), **(b)** the color variation due to carbon diffusion after heat treatment at 600 °C.

Reducing the pressure from 5.5 to 3 GPa while maintaining the processing time at 2 min did not result in a significant difference in density (Figure 5. 3 b). However, the density slightly decreased with 1 GPa (2.49 g cm-1), being almost equivalent to Conv-LATP. Further reduction in pressure caused a significant change in density, as expected from the major contribution of pressure to densification using this technique. On the other hand, no changes

were observed when increasing the time to 20 minutes, evidencing the low impact of this variable on the densification process (Figure 5. 3 c).

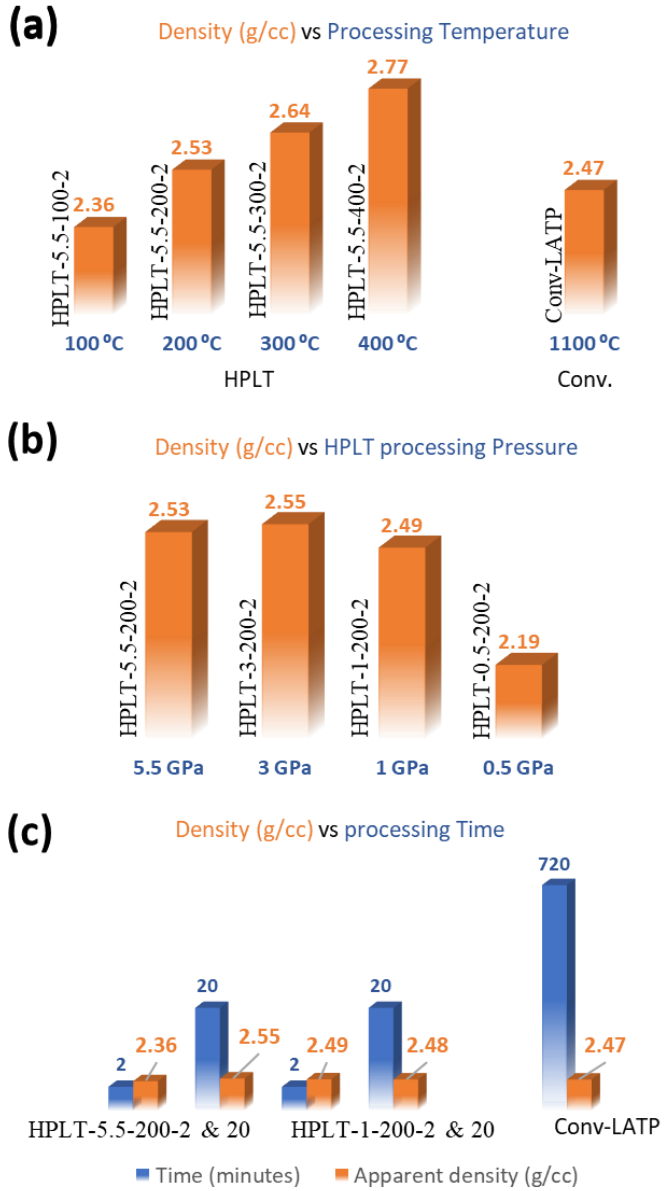

Figure 5. 3: Physical density comparison of LATP pellets densified by HPLT processing and conventional sintering. (a) LATP density vs processing HPLT time for pellets processed at 5.5 GPa and 2 during minutes compared to processing temperature by conventional sintering. (b) Change in LATP density under varying HPLT processing pressure while maintaining the temperature at 200 ˚C and for 2 min. (c) Impact of HPLT processing time in LATP density at 200 ˚C and under high (5.5GPa) and low (1GPa) processing pressures compared to conventional sintering conditions.

5.2.1.2 X-ray tomography of HPLT pellet

The X-Ray tomography analysis (Figure 5. 4, Video 5. 1, Video 5. 2, and Video 5. 3) of HPLT-5.5-200-2 reveals that density decreases from the outer volume to the core. It possibly indicates a slight density gradient caused by the fast processing. However, it is worth mentioning that the high average density of the pellet indicates that the differences are not major.

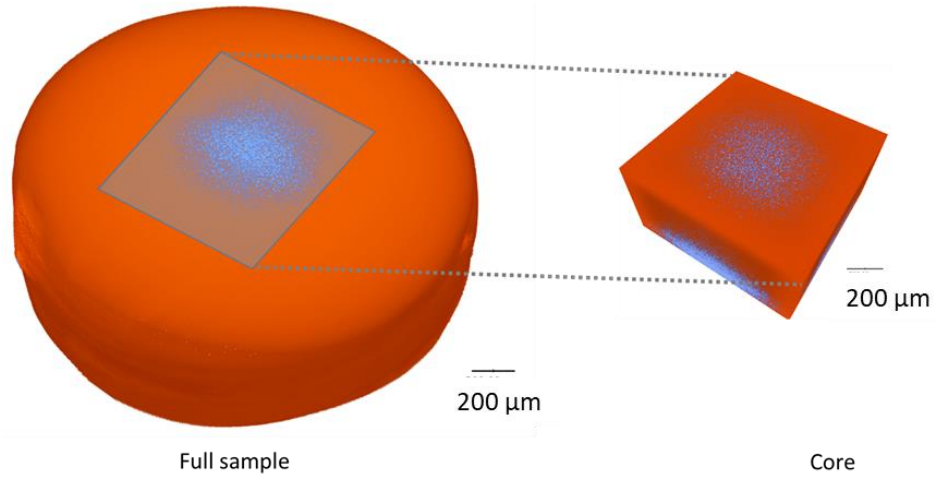

Figure 5. 4: The X-Ray tomography analysis of HPLT-5.5-200-2 LATP pellet. Full sample vs core view. Color indication from blue to red implies low x-ray absorption to high x-ray absorption region.

Video 5. 1: Animation full sample view. Suggesting relatively lower material density at the core compared to the exterior

Video 5. 2: Color gradient established at mid-cut off. (blue: lower 51.5% of total voxel distribution assigned as low density) (red: higher 48.4% of total voxel distribution assigned as high density)

Video 5. 3: Color gradient established at low-cut off (blue: 0.2% assigned as low density) (red: 99.8% assigned as high density)

5.2.1.3 Chemical structure: Raman spectroscopy

Figure 5. 5 depicts the Raman spectra of pristine LATP powder, HPLT-5.5-200-2, and HPLT-5.5-400-2. The pristine sample exhibits the standard peaks from LATP arising from asymmetrical (1098 and 1007 cm^{-1}) and symmetrical (446 cm^{-1}) vibration of $(PO_4)^{3-}$, translational vibration of Ti^{4+} (280 cm^{-1}) and modes of other $(PO_4)^{3-}$ motions (355, 314, 240 and 187 cm^{-1}).[338]

HPLT-5.5-200-2 is comparable to that of the pristine material except for slight intensity variations of the peaks. Conversely, HPLT-5.5-400-2 displays distinct and intense peaks at 1603 and 1343 cm^{-1}, attributed to G and D bands of carbon, [339], [340] confirming that the coloration of pellets at higher temperatures is due to carbon contamination. In addition, HPLT-5.5-400-2 shows a significant shift of the peak positions and widths, likely due to the presence of secondary phases. Moreover, the widening of peaks (for example, at 1007 cm^{-1}) indicates Ti^{4+} reduction.[131]

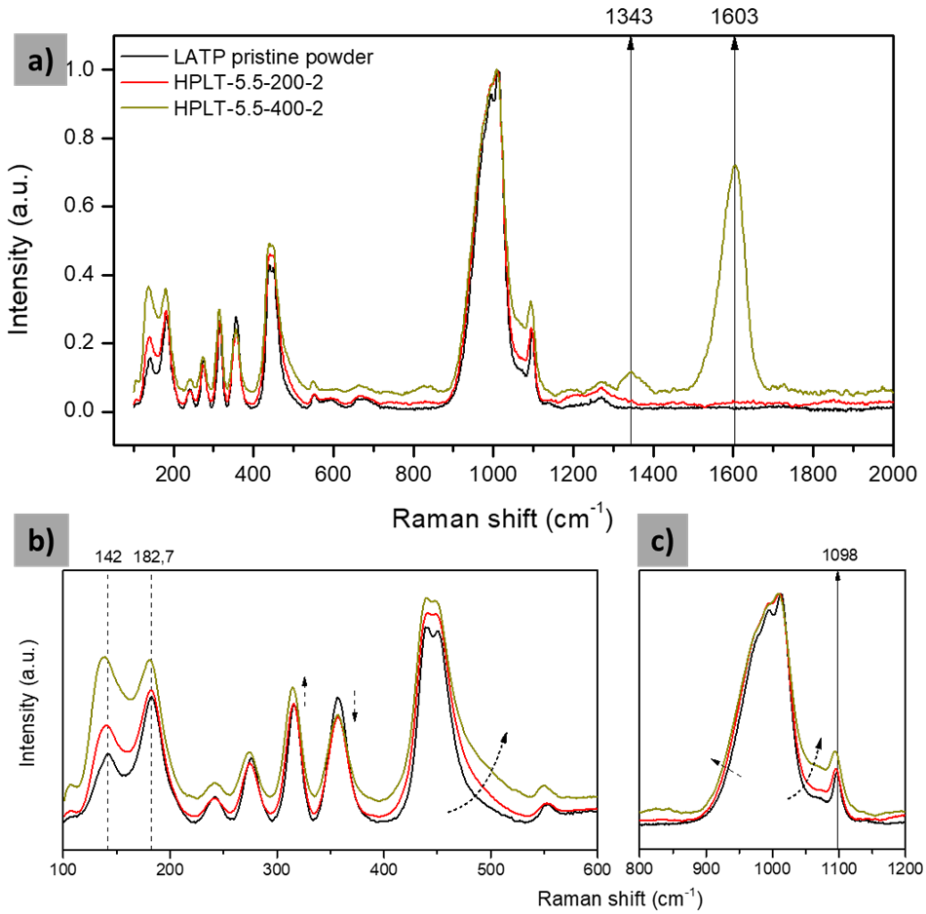

Figure 5. 5: **(a-c)** Raman spectra of pristine LATP powder, HPLT-5.5-200-2, and HPLT-5.5-400-2.

5.2.1.4 Bulk crystallinity: X-ray diffraction (XRD)

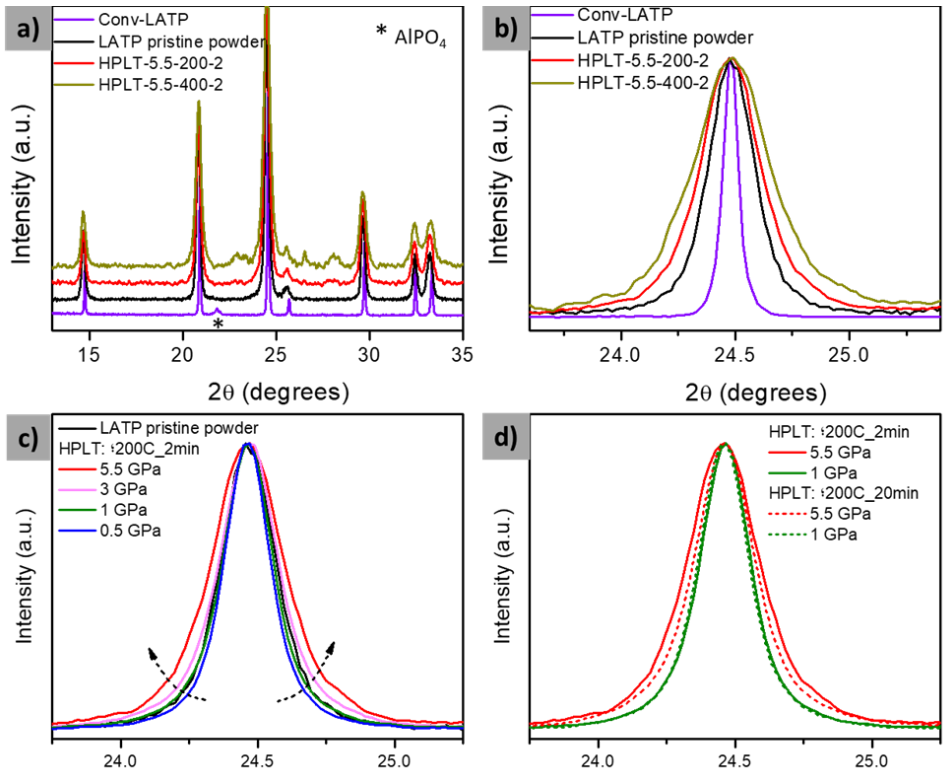

Figure 5. 6: XRD pattern comparison of HPLT densified pellets (a) HPLT-5.5-200-2 and HPLT-5.5-400-2 along with the pristine LATP powder and Conv-LATP. Zoomed view of (113) peak around 2θ=24.5˚; (b) HPLT-5.5-200-2, HPLT-5.5-400-2, pristine LATP powder, and Conv-LATP (c) HPLT-5.5-200-2, HPLT-3-200-2, HPLT-1-200-2, HPLT-0.5-200-2, and pristine LATP powder (d) HPLT-5.5-200-2, HPLT-5.5-200-20, HPLT-1-200-2, and HPLT-1-200-20

Figure 5. 6 shows the XRD patterns of pristine LATP powder, Conv-LATP, and HPLT-treated pellets with different processing parameters. Le Bail refinements using the FullProf program were used to evaluate the unit cell parameters and microstructural parameters including the crystallite size and strain of the pristine and HPLT-treated samples, and the results are tabulated in Table 5. 1.

Table 5. 1: Unit cell dimensions, crystallite size, and strain of the evaluated samples obtained from Le Bail refinements

LATP comparison / Properties	Derived from XRD refinement (Le Bail)			
	a=b (Å)	c (Å)	Crystallite size (nm)	Strain (10^{-4})
LATP Powder	8.5013	20.7719	46	36
Conv- LATP	8.5009	20.8191	284	12
HPLT-5.5-100-2	8.4956	20.8751	51	45
HPLT-5.5-200-2	8.5062	20.7905	24	39
HPLT-5.5-300-2	8.4946	20.8589	37	53
HPLT-5.5-400-2	8.4835	20.9407	14	47
HPLT-3-200-2	8.5031	20.7982	32	30
HPLT-1-200-2	8.5020	20.7987	41	25
HPLT-0.5-200-2	8.5030	20.8022	47	24
HPLT-5.5-200-20	8.5011	20.7899	30	32
HPLT-1-200-20	8.4995	20.7984	42	24

All samples can be indexed with R$\bar{3}$cH space group, with unit cell parameters of a=b= 8.5013(4) Å and c=20.7719(4) Å, for LATP pristine powder. However, the sample Conv-LATP exhibits an extra peak that can be attributed to $AlPO_4$ (Figure 5. 6 a -indexed with a star) likely segregating at the grains interface, thus hindering lithium diffusion across grain boundaries and decreasing the overall ionic conductivity of LATP.[341], [342] This sample exhibits also other differences when compared to pristine LATP powder (Figure 5. 6 a & b) as diffraction peaks have significantly sharpened, which indicates there has been a substantial growth of the crystallites as expected from the high temperature used, which promotes grain growth and fusion of the grains (from 46 to 284 nm, according to Le Bail refinement). Also, the c-cell parameter is slightly larger, reaching 20.8191(4) Å.

For all the HPLT samples, irrespective of the processing conditions, the XRD peak intensity distribution does not exhibit major changes, which indicates that the pellets are not significantly textured by the processing. On the other hand, samples HPLT-5.5-200-2 and HPLT-5.5-400-2 exhibit a peak broadening corresponds to reduction in crystallite size and an increase in strains (Figure 5. 6 b). This indicates that the high pressure induces grain cracking (as confirmed later by SEM, see below) and/or disorder in densified pellets. There isn't a clear trend in the crystallite parameters of samples densified at 5.5 GPa under different temperatures. This probably indicates that the cracking also depends on the amount of material, initial pellet density …etc., which may vary from sample to sample. It can be however concluded that, in general, particles crack at high pressure and irrespective of the temperature. Additionally, sample HPLT-5.5-400-2, shows the presence of a secondary phase and the emergence of an amorphous background in the 2θ range of 20-30°, in agreement with the coloration due to carbon mentioned before. The cell c parameter also significantly increases with temperature, reaching 20.9407 Å at 400˚C. This would be in agreement with a slight reduction of Ti^{4+} (in agreement with Raman results) and the loss of lithium ions. [343] This sample also exhibits peaks corresponding to oxides and phosphates of Ti, and Al, which is indicative of the secondary phase formation.

By fixing the processing temperature and time at 200 °C and 2 min, respectively, the impact of processing pressure has been compared in Figure 5. 6 c and Table 5. 1. The XRD peak broadening progressively increases with the increment in pressure from 1 to 5.5 GPa (samples HPLT-1-200-2 and HPLT-5.5-200-2). At the highest pressure of 5.5 GPa, the crystallite size has decreased to 24 nm, which is half of that of the pristine powder. Also, there is a consequent increase in the crystal strain while increasing the pressure, although there is no significant difference in unit cell parameters. LATP has higher elastic modulus but low fracture toughness which probably makes the material brittle under high

pressure.[344] In contrast, a low pressure of 0.5 GPa (sample HPLT-0.5-200-2) allows for retaining the crystallite size close to that of the pristine material. These results indicate that cracking can be avoided at 1 GPa and below.

Time is the last parameter herein evaluated under both high (5.5 GPa) and low (1 GPa) pressure at 200 °C. At high pressure, increasing the processing time from 2 to 20 min (samples HPLT-5.5-200-2 and HPLT-5.5-200-20) causes a slight increment in the crystallite size and a reduction in strain (Figure 5. 6 d). These results indicate that the grains that broke due to pressure are probably fusing after an increased processing time of 20 minutes. On the contrary, at low pressure, there is no difference in any crystalline parameters (unit cell, crystallite size, and strain) for 2 and 20 min (samples HPLT-1-200-2 and HPLT-1-200-20).

5.2.1.5 Surface morphology: Scanning electron microscopy (SEM)

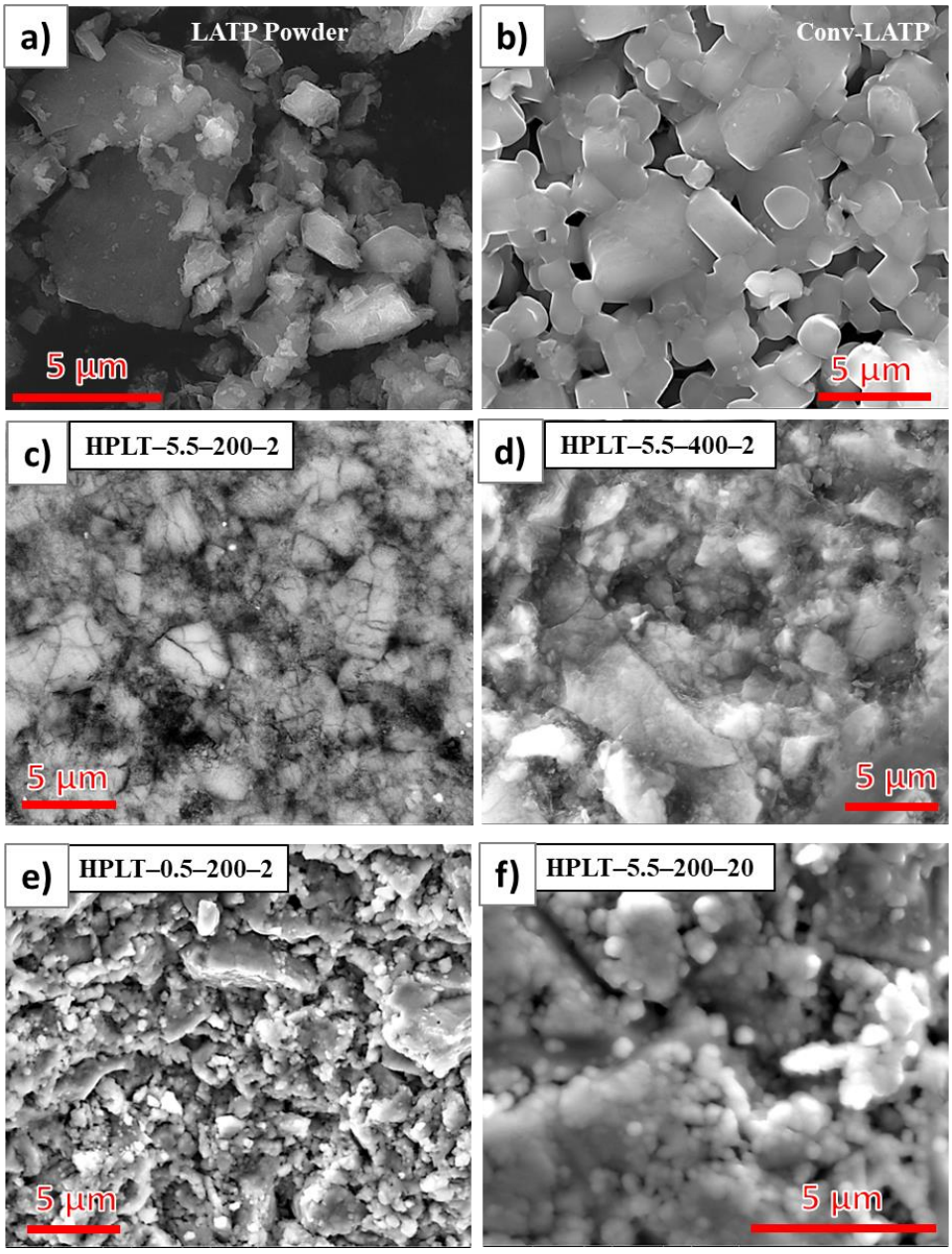

Figure 5. 7: SEM images of (a) pristine LATP powder, (b) conv-LATP, HPLT densified pellet at 5.5 GPa and for 2 min (c) at 200 and (d) 400 °C, HPLT densified pellets at 200 °C (e) under low (0.5GPa) pressure and short processing time (2 min) and (f) high (5.5GPa) pressure with long processing time (20 minutes).

Surface morphology of conv-LATP and HPLT densified LATP was analyzed by SEM and was compared to the pristine LATP powder (Figure 5. 7).

The latter, as shown in Figure 5. 7 exhibit a wide range of particle size distribution that varies between nano and micro. For Conv-LATP Figure 5. 7 b sintered at 1100 °C, there is evident grain growth, being all particles above ~1 µm. Figure 5. 7 c-f shows the surface morphology of HPLT-densified LATP pellets under different processing conditions. Irrespective of all the processing parameters, the pellets are tightly packed and without voids. Figure 5. 7 c and d compare samples HPLT-5.5-200-2 and HPLT-5.5-400-2. There is a clear indication of grain cracking for 200 °C caused by high processing pressure, which is in agreement with XRD peak broadening. The ion-milled cross-section of the same pellet reveals that grains closer to the core region are less or not cracked (Figure 5. 8**)**. Cracking of grains at 400 °C is less pronounced or probably masked by the secondary phases identified from XRD. Considering Figure 5. 7 c and e, corresponding to samples HPLT-5.5-200-2 and HPLT-0.5-200-2, the grain cracking is nearly negligible or not present at low pressure. Instead, the particles are loosely packed in agreement with the lower density (Figure 5. 3). The comparison of samples HPLT-5.5-200-2 and HPLT-5.5-200-20, shows evidence for the fusion of cracked grains for the latter (Figure 5. 7 f).

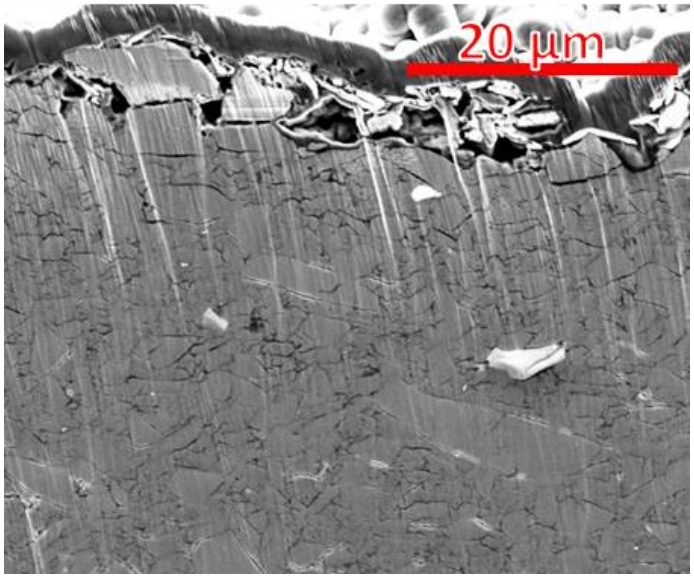

Figure 5. 8: A cross-sectional view of HPLT-5.5-200-2 LATP pellet

All these results indicate that processing at 200 °C should be selected as the threshold temperature to avoid carbon diffusion. On the other hand, the high pressure contributes to cracking and strains that can ultimately lead to large grain boundary resistance, as shown below. Hence, lower processing pressures preserve better the positive features of the system. However, it is important to recall that the density of the HPLT-treated pellet at a pressure of 0.5 GPa was significantly lower than at higher pressure (Figure 5. 3). Therefore, 1 GPa can be considered the optimum pressure for HPLT processing of LATP. Finally, there was a negligible impact on the processing time at low pressure, and therefore 200 °C with 1 GPa for 2 minutes is selected as the best set of HPLT parameters for micro-LATP.

5.2.1.6 Lithium-ion conductivity: Electrochemical impedance spectroscopy (EIS)

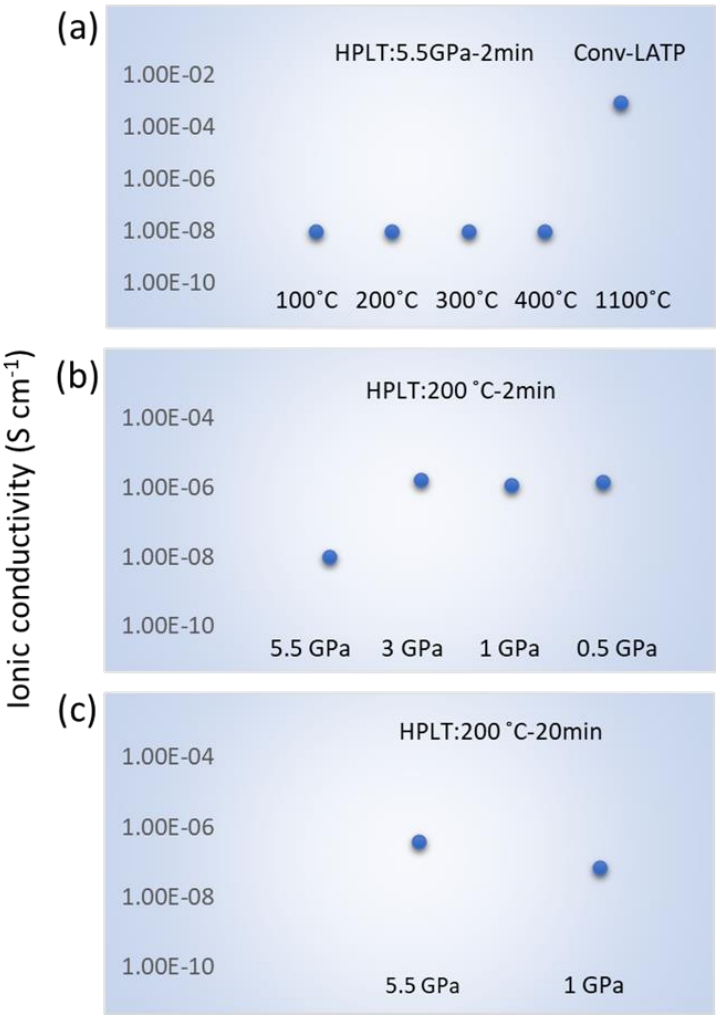

Figure 5. 9: Ionic conductivity comparison of HPLT-densified LATP pellets to conv-LATP. **(a)** Influence of HPLT processing temperature with a constant pressure of 5.5GPa and time 2 min. **(b)** variation of ionic conductivity with respect to HPLT processing pressure with a constant temperature of 200˚C and time 2 min **(c)** Impact of HPLT processing pressure with a constant temperature of 200˚C and time 20 min

Electrochemical impedance spectroscopy (EIS) was used to determine the ionic conductivity of the sintered pellets (Figure 5. 9). The Nyquist plots of Conv-LATP and HPLT-treated LATP under different processing conditions are shown in Figure 5. 10. The total (bulk + grain-boundary) ionic conductivity of

the Conv-LATP emanated from the high-frequency semicircles intercept with the real axis was found to be 9.0×10^{-4} S cm^{-1} at 25 ^{o}C. The impedance data were fitted with an equivalent circuit consisting of resistance (R) and constant phase element (CPE), indicating the total (bulk + grain-boundary) and electrode response, respectively, (RCPE) (CPE) shown as an inset of Table 5. 2**.**

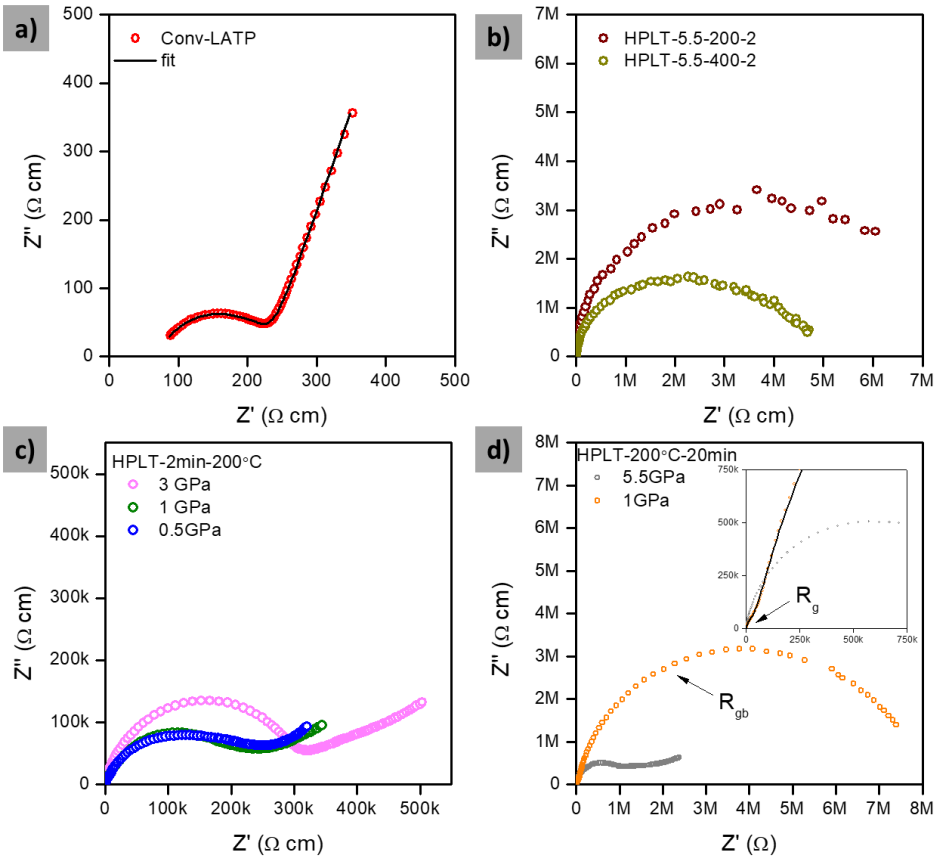

Figure 5. 10: Nyquist plot of **(a)** Conv-LATP, HPLT densified pellets at **(b)** at varied temperatures of 200 and 400 °C and a constant processing pressure and timing of 5.5 GPa, and 2 minutes, **(c)** varied pressure of 3GPa, 1GPa and 0.5GPa at a constant processing temperature and timing of 200 °C and 2 minutes, **(d)** at varied pressure of 5.5GPa, and 1GPa at a constant processing temperature and timing of 200 °C and 20 minutes.

Table 5. 2: Equivalent circuit and the circuit elements for the Nyquist plot of Conv-LATP consisting of resistance (R) and constant phase element (CPE)

	Model	Element	Value	Error %
Conv: 1100°C-12h	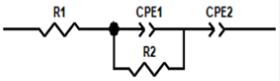	R1 (Ω)	70.94	0.3257
		CPE1-T ($\Omega^{-1}s$)	4.5238×10^{-8}	2.9228
		CPE1-P ($\Omega^{-1}s$)	0.79789	0.2616
		R2(Ω)	159.5	0.3054
		CPE2-T($\Omega^{-1}s$)	1.6228×10^{-6}	1.2406
		CPE2-P($\Omega^{-1}s$)	0.79391	0.1627

As shown in Figure 5. 9 a irrespective of temperature, both samples HPLT-5.5-200-2 and HPLT-5.5-400-2 exhibit a very low conductivity (~10^{-8} S cm^{-1}), which is out of the measurement accuracy of the equipment. The total Li^+ conductivity increased a magnitude of 2 orders (from 10^{-8} to 10^{-6} Scm^{-1}) for HPLT-3-200-2 (Figure 5. 9 b). Further decreasing of the pressure (sample HPLT-0.5-200-2) doesn't impact the conductivity and it remains in the same order (10^{-6} Scm^{-1}). The impact of processing time was compared in the case of high (5.5 GPa) and low (1 GPa) pressures by fixing the temperature at 200 °C (Figure 5. 9 c). HPLT-5.5-200-20 resulted with slightly better conductivity (10^{-7} Scm^{-1}) than HPLT-5.5-200-2 (10^{-8} Scm^{-1}). This is in agreement with the grain fusion observed for HPLT-5.5-200-20 by SEM and a slight increase in crystallite size observed by XRD, expected to favor ionic transport. In contrast, the sample HPLT-1-200-20 displays very low ionic conductivity (10^{-8} Scm^{-1}), which is lower than the sample HPLT-1-200-2 (10^{-6} Scm^{-1}). The Nyquist plot (Figure 5. 10 d) indicates that the high impedance of sample HPLT-1-200-20 has a major from the grain boundaries.

As observed from SEM, despite the lower density of Conv-LATP, the well-connected and low relative volume of grain boundaries are the key factors for the high ionic conductivity. In the case of HPLT pellets, the conductivity is mainly determined by the applied pressure, as high pressure (5.5 GPa) leads to grain cracking and a moderate pressure is more favorable. The difference

between the evaluated conditions leads to a 2-order enhancement, although in all cases the obtained values were at least two orders of magnitude lower than Conv-LATP. And on the other hand, despite exhibiting similar conductivity compared to moderate pressures, the low pressure (0.5GPa) results in very low densification, which can promote dendrite growth in contact with lithium metal and should therefore be avoided.

5.2.2 Impact of PH on the conductivity of HPLT densified pellets

To use LATP as a solid electrolyte in lithium batteries; the ultimate aim of the processing technique is to achieve the required lithium ionic conductivity (in the order of 10^{-4} to 10^{-3} Scm^{-1}). For further conductivity enhancement, HPLT-densified pellets were post-heated (PH) and the influence of heating temperature (between 600ºC and 800ºC) and duration (between 1 minute and 1h) was considered. Two extreme pellets were selected for this: HPLT-1-200-2 (10^{-6} Scm^{-1}) and HPLT-1-200-20 (10^{-8} Scm^{-1}).

5.2.2.1 Bulk crystallinity: X-ray diffraction (XRD)

XRD results indicate that the bulk crystallinity and composition of HPLT-densified LATP pellets remained similar after the PH treatments (Figure 5. 11). The parameters derived from Le Bail refinements (Table 5. 3) such as unit cell dimensions, crystallite size, and strain show negligible variation among HPLT and PH samples. The intensity distribution also does not exhibit major changes, which indicates that the pellets are not significantly textured.

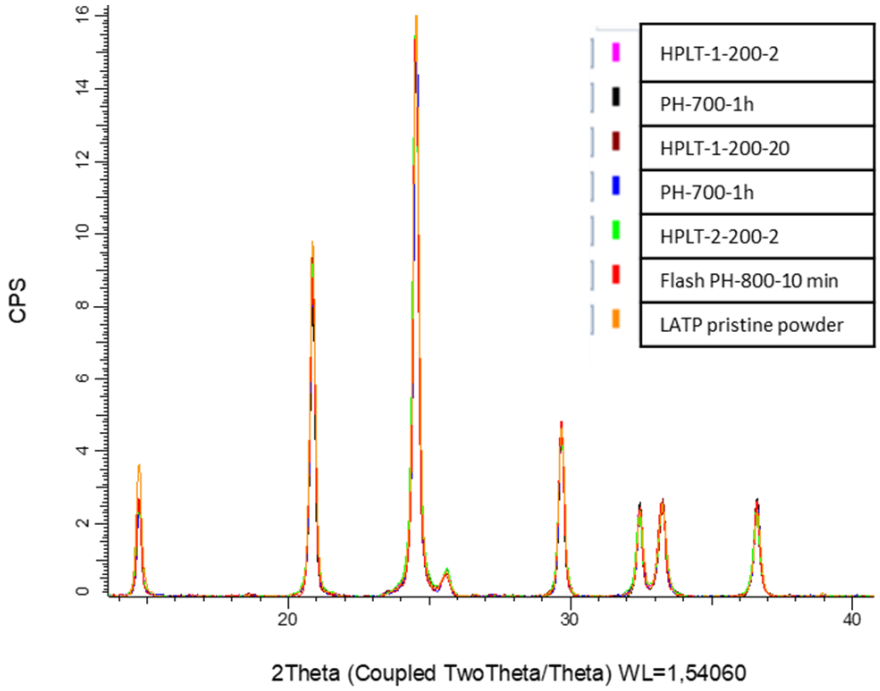

Figure 5. 11: X-ray diffractogram of HPLT densified pellets before and after PH under different PH conditions and those are compared to pristine LATP powder.

Table 5. 3: Compound, calculated crystalline parameters such as unit cell dimensions, crystallite size, and strain of the HPLT densified samples before and after PH. Values are obtained from Le Bail refinements of X-ray diffractogram.

LATP Properties comparison	Derived from XRD refinement (Le Bail)			
	a=b (Å) (deviation)	c (Å) (deviation)	Crystallite size (nm)	Strain
HPLT-1-200-2	8.5020(4)	20.7987(4)	40.908	25.4365
PH-700-1h	8.5040(4)	20.7860(4)	44.709	25.5711
HPLT-1-200-20	8.4995(4)	20.7984(4)	41.649	23.8314
PH-700-1h	8.5054(4)	20.7925(4)	44.522	25.7498
HPLT-2-200-2	8.5027(4)	20.7981(4)	36.433	26.2989
Flash PH-800-10 min	8.5088(4)	20.7945(4)	45.904	28.1275

5.2.2.2 Cross-sectional morphology: Scanning electron microscopy (SEM)

Figure 5. 12 a and b show the SEM image of the ion milled cross-section of the HPLT-1-200-2 pellet before and after the treatment (sample PH-800-1h). Overall, both images are similar, however, some differences can be observed with the smaller particles and/or at the particle boundaries. There are individual particles condensed by the high pressure in Figure 5. 12 a. And in Figure 5. 12 b neck formation starts and the particles get some first connection. This is even more visible in the higher magnification image (Figure 5. 12 b). This indicates the start of sintering and explains the higher ion conductivity. In Figure 5. 7 b of Conv-LATP which is full sintered structure, this interconnectivity is better visible. However, backscattered electron SEM images show that there is a compositional change in the particle boundaries of sample PH-800-1h (Figure 5. 12 c). Figure 5. 12 d shows an enlarged view of different particles in which: 1- has a different composition but similar morphology, 2- has similar morphology and composition to that of pristine LATP, and 3- has a different morphology and different composition. In addition to the crystalline LATP an amorphous phase with a different chemical composition plays a role in the sintering behavior. Crystallization of this amorphous phase after PH is expected to be the reason for neck formation between grains, for example the yellow area at the grain boundaries.

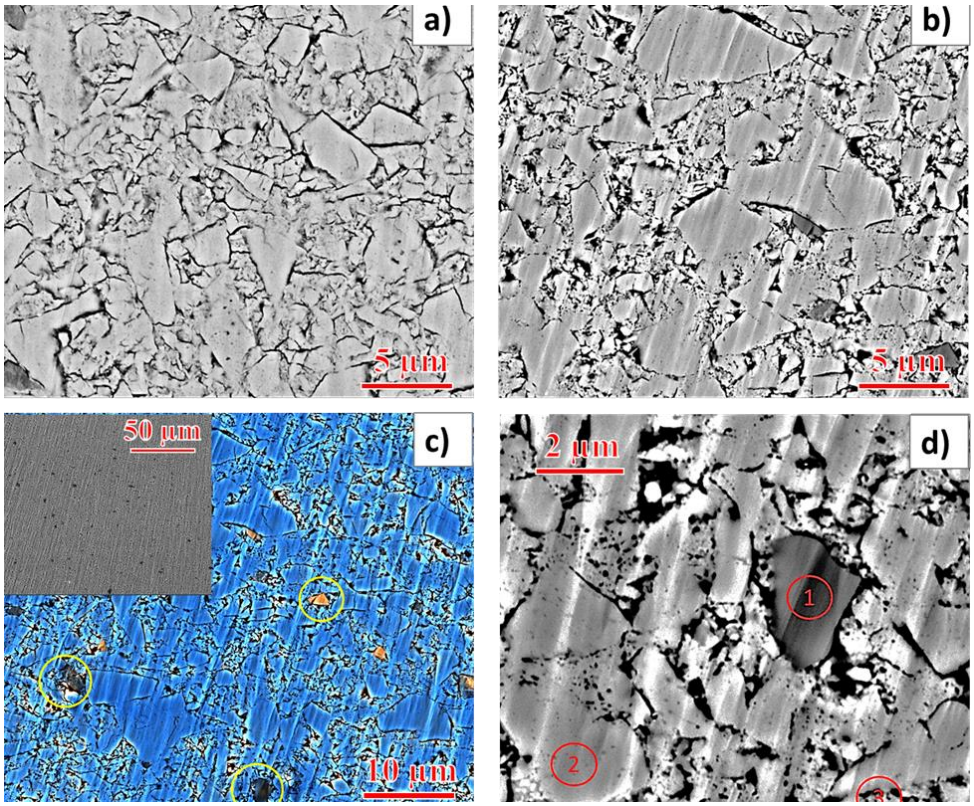

Figure 5. 12: SEM cross-sectional morphology by secondary electron imaging using ETD detector of (a) HPLT-1-200-2 (b) PH-800-1h. (c) backscattered electron SEM image of sample PH-800-1h (blue color indicates LATP composition, orange and black indicate compositions different from LATP) where compositional changes are highlighted with yellow circles (d) enlarged view showing the different particles

5.2.2.3 Lithium-ion conductivity: Electrochemical impedance spectroscopy (EIS)

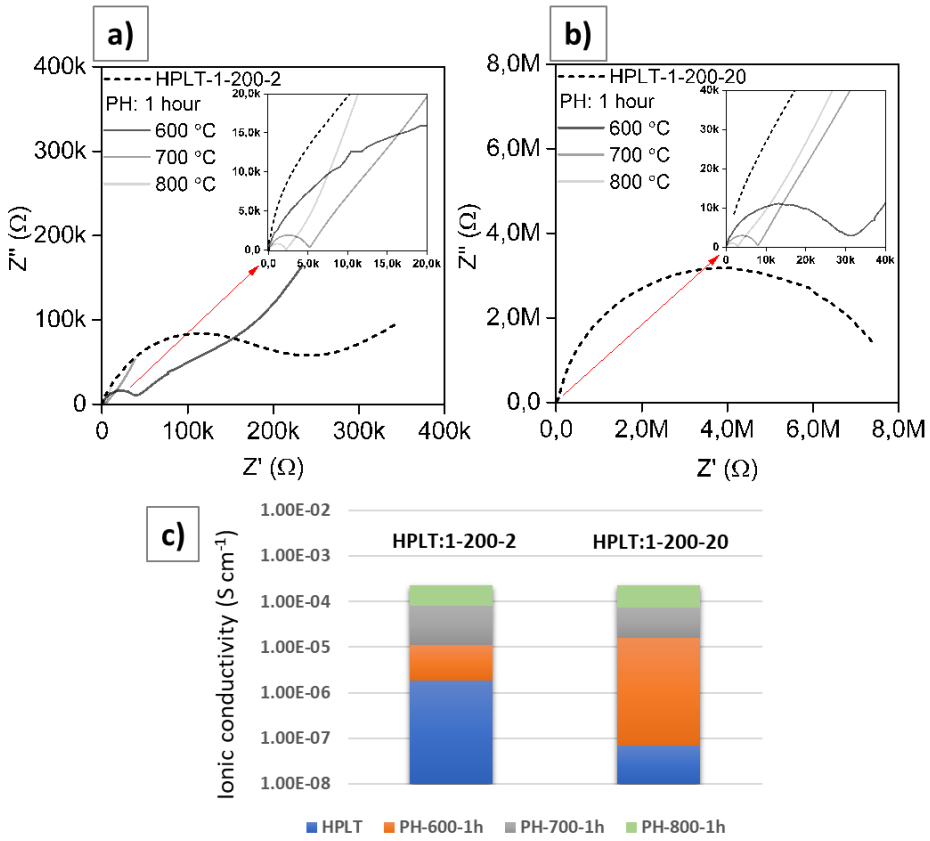

Figure 5. 13: Nyquist plots compare the impedance of HPLT densified LATP pellets after PH with different temperatures and at a fixed duration of 1 hour of **(a)** pellet: HPLT-1-200-2 **(b)** pellet: HPLT-1-200-20 **(c)** Evolution of lithium-ion conductivity with increase in PH temperature.

The Nyquist plots of PH samples are displayed in Figure 5. 13 a and b respectively. The impact of the PH treatment on the conductivity is remarkable as an increment up to 10^{-4} Scm^{-1} is obtained for samples treated between 600°C and 800°C. Impressively, this temperature is 300°C lower than the conventional sintering temperature and also a significant gain in processing time is achieved (1 hour and 2 minutes versus 12 hours, which were optimized for Conv-LATP). Remarkably, the increment in conductivity with PH is independent of the initial pellet conductivity after HPLT, as both samples HPLT-1-200-2 and HPLT-1-

200-20 attained a conductivity of 10^{-5} Scm^{-1} under PH-600-1h (Figure 5. 13 c). To evaluate the impact of time during the PH step, the temperature was fixed to 800°C and the sample (HPLT-3-200-2) was flash exposed for 2 or 10 min. The Nyquist plot in Figure 5. 14 conveys that the PH duration has also a significant contribution to the conductivity enhancement, as a short exposure of 2 and 10 minutes at 800°C lead to a conductivity of 1.9 and 5.1 x 10^{-5} Scm^{-1}, respectively, which is still one order less than the conductivity achieved after 1 hour at 800°C (~1.5 x 10^{-4} Scm^{-1}).

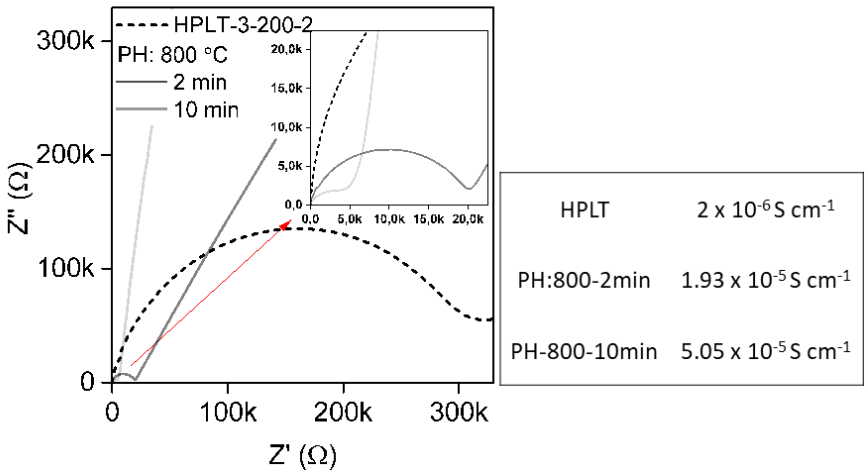

Figure 5. 14: Impedance evolution of pellet: HPLT-3-200-2 with the increase in PH duration of flash exposure at a fixed PH temperature of 800°C. And lithium ionic conductivity values of HPLT densified LATP pellets before and after PH, derived from Nyquist plots.

5.2.3 Discussion

Conventional high-temperature sintering of LATP results in grain growth and a low relative volume of grain boundaries, which are generally considered favorable conditions for the ionic transport of ceramic materials. Phase purity and compositional homogeneity are also relevant parameters, and some secondary phases are known to be detrimental (e.g., $AlPO_4$, which is frequent in high temperature sintered LATP and results from Li-loss)[341] although others can be favorable for LATP ionic conductivity. For example, Si doping[345] or

sintering additives such as lithium borates, carbonates, and phosphates have been reported to lead to high conductivities.[346]–[350]The semi-crystalline interphase between well-crystallized LATP and an amorphous glass phase obtained by spark plasma sintering has also allowed reaching a high ionic conductivity of 1.3×10^{-3} S cm^{-1} without any doping, which is higher than that derived by the conventional method.[351] Similarly, the formation of LATP nano-crystalline precipitates at the grain boundaries obtained by cold sintering has been proposed to form lithium conduction channels that lead to better conductivity.[352]

Interestingly, the improvement of conductivity achieved in our study after the PH treatments cannot be attributed to the grain growth and removal of grain boundaries as occurs with high-temperature conventional sintering. Indeed, the comparison of Figure 5. 12 a and b clearly show that, at the selected temperature, no significant grain growth has occurred and XRD confirms that the bulk properties were preserved after PH. The main difference before and after the PH treatment is the compositional change of smaller particles and/or at the particle boundaries, which results in enhanced conductivity. In fact, HPLT treatment might lead to a lower grain boundary conductivity in these regions, which would be in agreement with the lower ionic conductivity observed for HPLT-1-200-20 (sample processed for longer duration) compared to HPLT-1-200-2. However, the similar conductivity enhancement for HPLT-1-200-2 and HPLT-1-200-20 under PH-600-1h implies that the PH treatment allows recovering from resistive grain boundaries irrespective of their initial condition. In any case, the current results highlight the efficiency of the combination of HPLT and PH treatment at lower temperatures and shorter duration in contrast to conventional long-time sintering at higher temperatures. And it should be noted that conductivities as high as 10^{-4} Scm^{-1} can be achieved in this material without the suppression of grain boundaries.

5.3 Nano-LATP under HPLT and PH

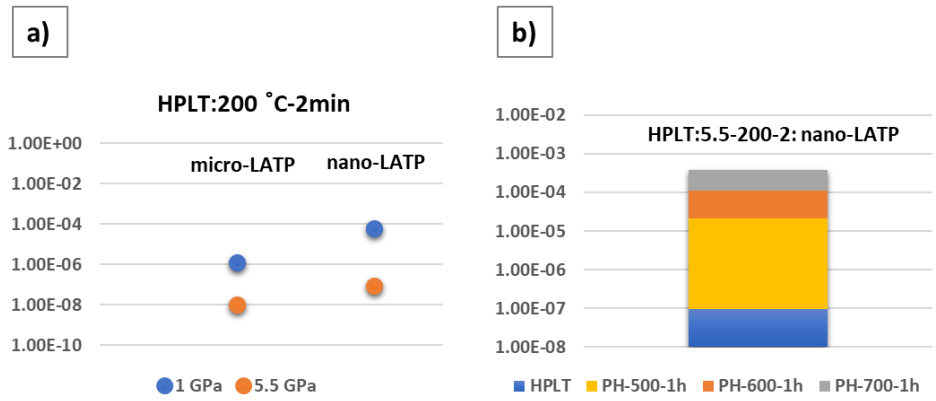

Figure 5. 15: (a) Comparison of lithium-ion conductivity values of micro and nano LATP under processing conditions; HPLT-1-200-2 and HPLT-5.5-200-2. **(b)** Evolution of lithium-ion conductivity of HPLT-5.5-200-2: nano-LATP with the increase in PH temperature

Finally, in this section, we compare the impact of initial LATP microstructure on the lithium ionic conductivity values obtained by HPLT. As discussed previously, the best optimized HPLT densification conditions for micro-LATP (average particle size of 1 µm) are 200°C, 1 GPa, and 2 minutes, which allow reaching a conductivity of 10^{-6} Scm^{-1} prior to PH treatment. Under the same conditions, nano-LATP (average particle size of 500 nm) exhibits a much higher conductivity (6.15 x 10^{-5} Scm^{-1}) than micro-LATP (Figure 5. 15 a and Figure 5. 16 a). A total ionic conductivity of 1.26 × 10^{-5} S cm^{-1} (room temperature) was previously achieved by cold sintering at 200 ˚C and using a uniaxial pressure of 510 MPa by using water as an additive.[199] HPLT allows achieving a higher conductivity with a very fast processing (2 minutes) and more importantly, without the use of any solvents that might result in mixed conductivity and/or compositional changes those are detrimental for the conductivity.

A slight coloration was observed for sample nano-HPLT-1-200-2 possibly arising from carbon contamination, however, the results obtained by chronoamperometric analysis (Figure 5. 16 b and c) indicate that the

contribution of electronic conductivity in the sample is only 1.05 x 10^{-8} Scm^{-1}, which represents only 0.02 % of the total conductivity. It is worth mentioning that the coloration was not present at high pressure (sample nano-HPLT-5.5-200-2). However, the conductivity obtained for this sample was lower although still higher than that of micro-LATP treated under the same conditions (10^{-7} Scm^{-1} vs 10^{-8} Scm^{-1}).

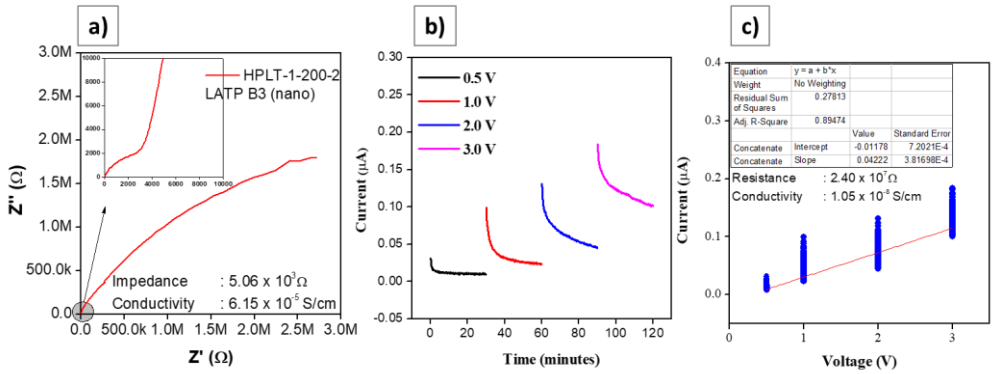

Figure 5. 16: **(a)** Nyquist plot of HPLT:1-200-2: nano-LATP pellet from which the ionic conductivity has been deduced to be 6.15 x 10^{-5} Scm^{-1}. Chronoamperometry analysis of **(b)** current vs time plots at different voltages **(c)** current vs voltage plot and corresponding concatenate linear fit (ohmic plot) where the electronic conductivity has been calculated from the slop and tabulated the details inset.

Pellet nano-HPLT-5.5-200-2 was also subjected to PH treatments starting from 500°C. An enhancement of two orders of magnitude was obtained after 1h at 500°C (2 x 10^{-5} Scm^{-1}). Further improvement was obtained at 600°C (8.8 x 10^{-5} Scm^{-1}) and at 700°C, reaching 2 x 10^{-4} Scm^{-1} (Figure 5. 15 b). Therefore, nano-LATP has allowed to reach comparable ionic conductivity to that of the conventional sintering temperature albeit at 400°C lower and with a much shorter duration.

In conclusion, this is the first study reported so far employing HPLT processing for ceramic solid electrolytes. The potentiality of the technique is here confirmed through the study of the conditions required to achieve high ionic conductivity in LATP pellets prepared using micro- and -nano LATP commercial powders. This work calls for further exploration of the technique,

to further increase the ionic conductivity, understand better the chemical nature of grain boundaries after HPLT and PH treatments, and evaluate the applicability of this technique to other oxide-based lithium conductors. Indeed, this technique is compatible with a wide range of solid electrolyte materials since it obviates the use of solvent and related side reactions.

5.4 Composite cathode under HPLT

The ultimate aim of optimizing the HPLT technique is to assemble the SSB that is composed of a solid composite electrode and the electrolyte (Figure 1. 6). In the previous chapters the composite cathode thermal compatibility was studied where the temperature threshold, and reaction mechanism and threshold enhancement methodologies were discussed. The current chapter optimizes the HPLT technique for the densification of LATP. But, while considering this composite cathode (NMC+LATP+carbon) for the HPLT processing there is an additional parameter apart from temperature, which is the applied pressure. Hence, the composite mixture was densified under the HPLT conditions selected for the electrolyte, 200 ˚C, 1 GPa, and 2 min to form a dense pellet (Figure 5. 17), and further characterized.

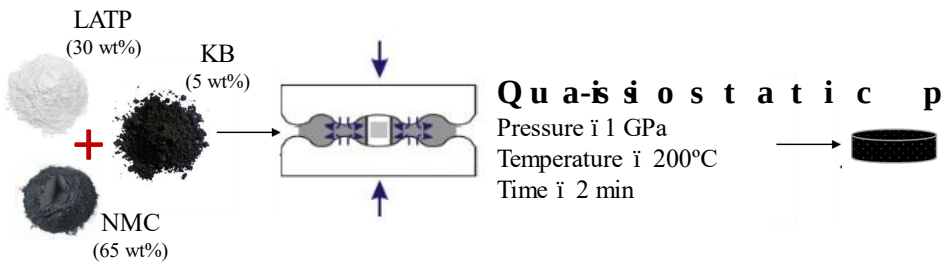

Figure 5. 17: Schematic illustration of composite cathode densification by HPLT process to form the dense pellet. The considered composite ratio and the HPLT densification parameters are specified.

The X-ray diffractogram of the composite cathode after HPLT is compared to the pristine NMC and LATP in Figure 5. 18. As already mentioned in the previous section, there is no significant difference for LATP peaks under the selected HPLT conditions. But the NMC peaks show significant broadening.

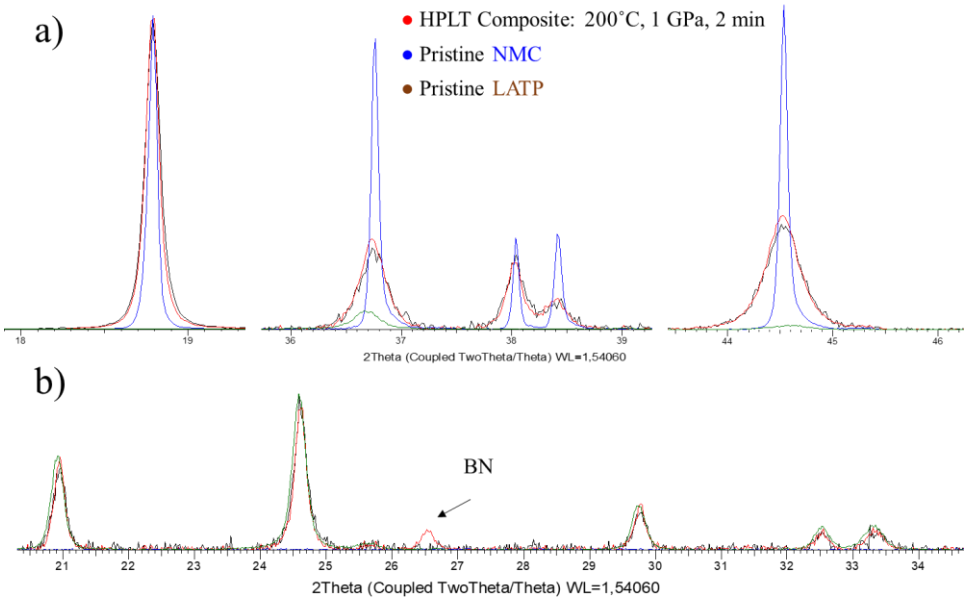

Figure 5. 18: XRD spectra of HPLT densified composite cathode (red) compared to that of pristine NMC (blue) and LATP (brown).

The SEM surface morphology comparison of the composite cathode densified under HPLT is illustrated in Figure 5. 19. There is a clear indication of grain cracking in the case of NMC particles (Figure 5. 19b) which is an impact of the applied pressure during the processing. This is in agreement with the observations from XRD since the cracked grains lead to smaller-sized particles and that results in higher FWHM or broader peaks.

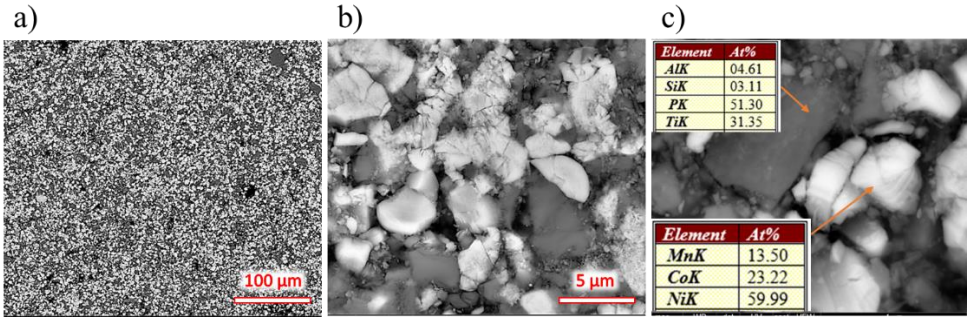

Figure 5. 19: SEM Surface morphology of HPLT densified composite cathode a) wide view that confirms the composite homogeneity in the pellet b) zoomed view of the composite elements and c) elemental ratio by EDX that distinguishes NMC (white) and LATP (grey) from the images.

Figure 5. 20 indicates the electrochemistry (GCPL) of the HPLT densified composite cathode, where the pellet was crushed into powder and laminated (using composite pellet directly as cathode results in very high active loading and improper electrochemical comparison). And as expected, the initial charge-discharge curve itself shows significant capacity decay for the HPLT-processed composite compared to the mixed one. The capacity degradation becomes prominent with the number of cycles and at higher C rates.

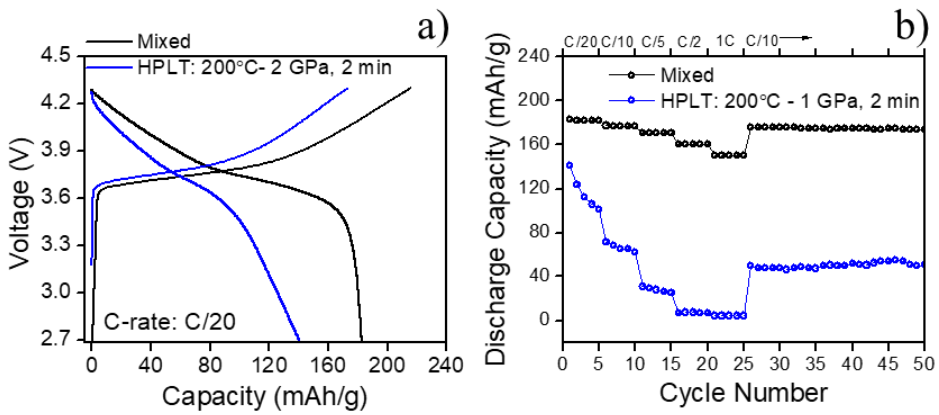

Figure 5. 20: Electrochemistry of coin cells made with mixed composite and the HPLT processed composite pellet that crushed into powder and made the cathode laminate out of it. **(a)** second charge-discharge curves at a C rate of C/20. **(b)** rate capability tests.

These observations collectively point to a higher mechanical sensitivity of NMC towards HPLT processing compared to LATP. There are previous studies on the mechanical properties of NMC where they have observed electrode fracture during the electrochemical performance. [353], [354] These preliminary results indicate that the HPLT processing conditions for composite cathodes should be optimized further and that different conditions (or densification approaches) might be needed to densify electrolytes and composite cathodes.

5.5 Conclusions

The High-Pressure Low-Temperature (HPLT) processing technique is here explored as a densification technique for ceramic lithium conducting materials to be used in solid-state batteries. Several parameters were explored (temperature, time, pressure) to identify the best HPLT conditions for micro-LATP. Independently of the selected conditions, the measured physical densities under HPLT were higher than that of conventionally sintered LATP. Our results indicate that 200˚C, 1 GPa, and 2 minutes lead to the best conductivity, 10^{-6} Scm^{-1}. Temperatures >300 ˚C resulted in the formation of secondary phases, and pressures > 3GPa resulted in particle cracking, both detrimental for ion conductivity. Further improvement of the ionic conductivity was achieved through short post-heat treatments, reaching the impressive value of ~2 x 10^{-4} Scm^{-1} after treatment at 800˚C for 1 hour, irrespective of conductivity after HPLT. No or negligible changes were found in the bulk properties of LATP after PH, and we hypothesize that the ionic conductivity enhancement under PH is related to changes in the grain boundaries composition and microstructure. Finally, even higher conductivities were obtained for nanometric-LATP, reaching 6.15 x 10^{-5} Scm^{-1} after HPLT processing at 200˚C, 1 GPa, and 2 minutes. This is the highest conductivity reported so far for LATP under such mild conditions without the necessity of any solvents, and it can be further improved after a post-treatment for 1h at 700ºC reaching 2 x 10^{-4} Scm^{-1}. These results show for the first time the potential of the HPLT approach as a cost-effective densification technique for ceramic ion conductors which deserves to be further explored. This production process can be automated since the reduced pressure and temperature does not require the use of advanced hydraulic presses. The lower pressure is also important when obtaining larger ceramics due to the dependence of the maximum applied pressure on the surface on which it is exerted. Considering the above facts, it

can be emphasized that the presented technology has a high commercial potential.

Finally, the NMC-LATP-carbon solid composite cathode was considered for the initial trials under HPLT densification. Compact and dense pellets were achieved with the processing parameters; 200˚C, 1 GPa, and 2 minutes. Although more mechanical understanding is required since the NMC particles were found to be fractured due to applied pressure.

GENERAL CONCLUSIONS

The success of SSBs as advanced electrochemical energy storage systems must involve necessarily a further development of the technology in terms of advanced materials, processing techniques, and, most importantly, full cell integration. A detailed bibliographic study was conducted in chapter 1 (previously published as a review article). In this chapter, the theoretical performance of an SSB model based on NMC+LATP+carbon composite cathode, LATP solid electrolyte, and lithium metal anode was calculated and it was shown that an energy density of >300 Wh/kg and >700 Wh/l can be achieved provided the electrolyte thickness is < 50 micron.

One of the main technical challenges that oxide-based solid-state batteries face today is the densification of their components. The most common approach to reach dense composite cathodes with good interfacial contact requires high-temperature co-sintering of the different components (electroactive material, catholyte, and conducting additive- NMC, LATP, and carbon respectively in this case) along with the electrolyte at high temperatures. This often results in the inter-diffusion of elements among the different components that deteriorate the overall cathode performance. The thesis was planned to address these challenges and a step-by-step investigation was performed.

In the second chapter, we evaluated the impact of temperature and heating atmosphere in the NMC, LATP, and KB systems. A rationale of the chemical reactions between components was proposed from the combination of bulk and surface techniques, and overall involves a cation redistribution in the NMC cathode material that is accompanied by the loss of lithium and oxygen from the lattice enhanced by LATP and KB, which act as lithium and oxygen sinks. The final result is the formation of several degradation products, starting at the surface, that leads to a rapid capacity decay above 400 ˚C. Both the reaction mechanism and threshold temperature depend on the heating atmosphere, being

air atmosphere is more favorable compared to oxygen or any other inert gases, which is encouraging in the aspects of easiness in processibility.

Even though the threshold limit of the NMC-LATP-KB composite cathode was found to be 400 ˚C, the electrochemical performance of heated composites at higher C rates was slightly worse compared to the non-heated composite. To address this issue, LiF was considered as an additive in chapter 3. It was observed that the addition of LiF enhances both the as mixed and the heated composite cathode electrochemical performance, and reduces the carbon oxidation kinetics. Later, the investigations were filed as a patent.

As a continuation, the impact of different carbon grades in the thermal response of LATP-NMC-Carbon composite electrodes was evaluated and shown to significantly influence the chemical compatibility between components (chapter 4). Through a combination of bulk and surface characterization techniques including gas adsorption, X-ray diffraction, X-ray absorption spectroscopy, X-ray photoelectron spectroscopy, Raman spectroscopy, and thermogravimetric analysis, it is shown that carbons with a low surface area are more adequate as result in higher oxidation temperatures and hence are less reactive. Replacing KB with C65, which has low surface area, low crystallinity, and high oxidation temperature shows promising electrochemistry in the heated composite and could elevate the temperature threshold up to 500 ˚C, which is an increment of 100 ˚C compared to the composite that contains KB.

On the other hand, the necessity of densification under high-temperature challenges the processability of oxide-based SSBs towards upscaling and their implementation into practical devices. In chapter 5, we investigate a High-Pressure Low-Temperature (HPLT) processing technique for the densification of LATP solid electrolyte, providing an understanding of several key parameters such as temperature, pressure, and time. Our results show that nanometric LATP can be densified using the HPLT technique at 200˚C within 2 minutes delivering

an ionic conductivity of 6.15 x 10^{-5} Scm^{-1}, which is the highest reported value at this temperature without the addition of solvents. On the other hand, by combining HPLT with a short post-heat treatment at 700 or 800 ˚C for 1 hour highly dense pellets with an ionic conductivity of 10^{-4} Scm^{-1} can be obtained. This represents a reduction of the densification temperature of more than 400˚C compared to conventional high-temperature sintering and shows that HPLT represents a processing technique for ceramic electrolytes that allows for overcoming current densification constraints derived from the use of very high temperatures.

Initial trials made in chapter 5 of HPLT processing of the composite cathode indicate that the mechanical sensitivity of NMC towards pressure leads to grain fracture which affects the composite electrochemistry. This indicates, the necessity of deeper understandings in composites' mechanical compatibility.

Hence the future aspects of the study can be directed to the mechanical compatibility of composite cathodes under pressure-assisted processing. Once optimized, the realization of a composite cathode-electrolyte bilayer can be considered by means of HPLT processing. The thermo-mechanical properties of individual materials as well as the interfacial compatibility of electrode and electrolyte components should then be evaluated to optimize the cell performance. In general, the methodologies used in this study can be extended to other potential candidates in the family of ceramic oxides and high potential cathodes. However, along with energy density requirements, the material selection should also be based on characteristics such as particle size, morphology, purity and mechanical properties since they play a major role in thermo-mechanical compatibility of composite mixture.

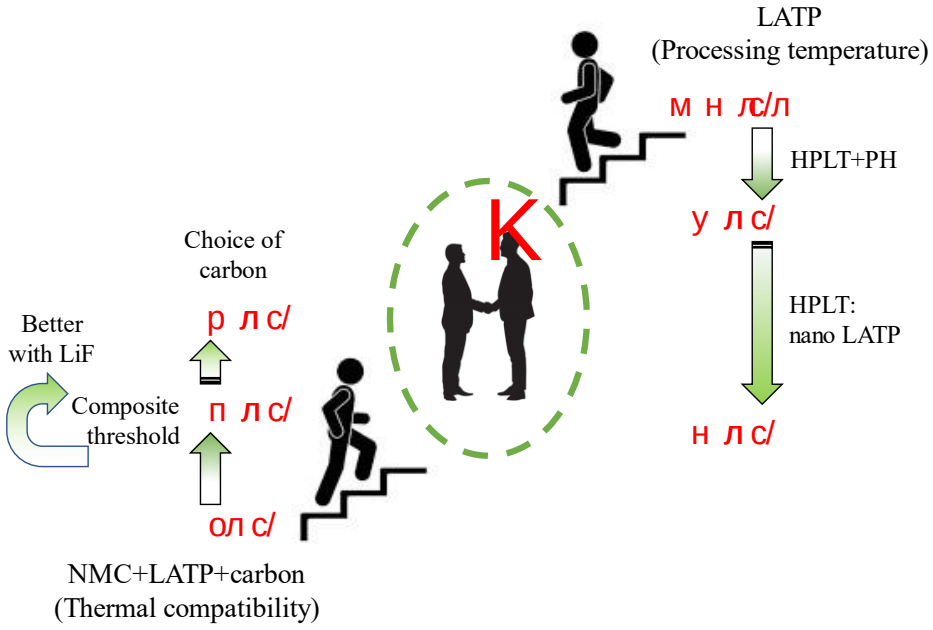

Conclusion Figure: The schematic illustration of the conclusions and progress with respect to the aim of the thesis.

EXPERIMENTS

Materials

Cathode active material- $LiNi_{0.6}Mn_{0.2}Co_{0.2}O_2$ (NMC) was supplied by Umicore, Corporate R&D (CRD, Belgium).

Electrolyte material LATP was provided by SCHOTT AG, Mainz. Two grades of materials were considered for the studies: LATP-micro which has an average particle size of 1 µm (though out the study) and LATP-nano which has an average particle size of 500 nm (only in chapter 5). Both are phase-pure materials with a theoretical density of 2.94 g/cc.

Lithium fluoride, 99.98% (metal basis) (LiF) was purchased from Alfa Aesar

Ketjenblack (KB) was purchased from Akzo Nobel Polymer Chemicals, Netherlands. Acetylene black (AB) purchased from Alfa Aesar (39724 Carbon black, acetylene, 50% compressed, 99.9+%). TIMCAL SUPER C65 Carbon Black Conductive Additive made by IMERYS. Multiwall carbon nanotubes (mwCNT) from Arkema (GraphistrengthTM C100).

Composite mixing

Chapters 2 and 4: Composite of NMC+LATP+carbon was mixed using agate mortar and pestle in the weight ratio 65:30:05 respectively. Carbons were vacuum dried before introducing into the glovebox. A total quantity of 2g was fixed for each batch of mixing to ensure homogeneity. The elements were added in the order NMC, carbon followed by LATP and was mixed for 1 hour. A mixture was made inside the glovebox (O_2 <1 ppm and H_2O <1 ppm).

Chapter 3: In the case of composites with LiF additive (Comp+LiF Mix), mixtures were made inside the glovebox (O_2 <1 ppm and H_2O <1 ppm). An additional wt% of LiF was added to the composite where the wt% of 2, 5, and 10 (Comp+LiF 2 Mix, Comp+LiF 5 Mix, and Comp+LiF 10 Mix respectively)

were considered for comparison. The elements were added in the order; NMC, LiF, KB, and finally LATP.

Composite heat treatments

Composite mixtures of NMC+LATP+KB = 65:30:05 (C-Mixed) were annealed at different temperatures for electrochemical evaluation. Batches of 500 mg were taken in alumina crucibles followed by tap densification for heat treatments, which were done in a high-temperature furnace attached to the glove box.

Chapter 2: Heat treatments were carried out at three different temperatures 400, 500, and 600 °C) under different atmospheres (synthetic air (H_2O < 2 ppm; CO_2 < 0.2 ppm)., nitrogen, argon, and oxygen), with a heating rate of 1 °C/min and 1-hour dwell at the specified temperatures before cooled back to room temperature with a rate of 10 °C /min. The resulting samples are labeled C400-air, C500-air, C600-air, C400-N2, C500-N2, and C600-N2 respectively for air and nitrogen.

Chapter 4: Heat treatments were carried out with a heating rate of 1 °C /min and 1-hour dwell at 500 °C before being cooled back to room temperature at a rate of 10 °C /min. The mixed composites before heat treatment are labeled as; KB-composite, C65-composite, AB-composite, and mwCNT-composite. And the composites after heat treatment are labeled; 500-KB, 500-C65, 500-AB, and 500-mwCNT, corresponding to the carbon present in the composite and the temperature chosen for heat treatment.

Chapter 3: Composites were taken to the heat treatments in GAF (Muffle) furnace, which was pre-calibrated under similar heating conditions. Synthetic air [Nippon Gases, O_2 = 80%, N_2 =21% (+/-1 vol%) H_2O <2ppm, CO_2 <0.02 ppm] was used as a medium for heat treatment and the flow rate was fixed to 2 ln/min. Samples were heated with a heating rate of 1 ˚C/min followed by a dwelling of 1 hour at a temperature of 400 ˚C and cooled back to room

temperature. Comp Mix after heat treatment was labeled as Comp 400-SA. Depending on the weight ratio of LiF present in the samples (2, 5, and 10%), Comp+LiF composites after heat treatments were labeled as Comp+LiF 2 400-SA, Comp+LiF 5 400-SA and Comp+LiF 10 400-SA respectively. All the samples were heated in a 30 ml alumina (Al_2O_3) crucible with an open lid. The transfer time of samples between the glovebox and furnace was controlled to avoid exposure to ambient conditions. Also, after the heat treatments, samples were transferred to the glovebox at a temperature range of 120-150 ˚C to avoid moisture absorption.

Densification of LATP by conventional sintering

Chapter 5: LATP (micro) powders were also densified using the conventional high-temperature sintering (LATP-Conv) technique for comparison. The powder was green densified using uniaxial pressure of 0.3 MPa and later fired in a muffle furnace at 1100 °C for 12 h under an open-air atmosphere. The firing was done in an alumina crucible, and the pellet was covered with the same powder (LATP) to avoid the volatilization of lithium from the pellet during high-temperature exposure. Heating was done in steps applying different rates; 150 °C/h from room temperature to 900 °C, a dwelling of 1 hour at 900 °C, 50 °C/h from 900 °C to 1100 °C, a dwelling of 12 hours at 1100 °C and finally cooling back to room temperature at 300 °C/h. The sintered pellets were polished to smoothen the surface with a series of SiC sandpapers (400, 600, 1200, and 2500 grits) for further characterization.

Densification of LATP by HPLT sintering

Chapter 5: The schematic representation of the HPLT technique is shown in Figure 5. 1**.** The LATP powder (~400 mg) is first greenly densified applying uniaxial pressure of 0.3 MPa with a diameter of 10mm. Later, for HPLT processing, the pellet is placed in the center of the toroid (container made of $CaCO_3$) in the graphite tube coated on the inside with hexagonal boron nitride

(h-BN), which prevents contact of the graphite with the sample. The graphite tube acts here as a resistance heater. Toroid is positioned between two anvils and plays the role of a pressure transfer unit. The force excreted by the anvils creates a quasi-isostatic pressure. The LATP pellet was sandwiched between BN and followed by graphite, where graphite ensures heat conductivity and BN blocks LATP green body from direct contact with graphite. A pressure in the range of 0.5 – 5.5 GPa was used in this study by controlling the applied force. The processing temperatures considered for optimization were 100, 200, 300, and 400 °C. The processing time was between 2 and 20 minutes. A 240-grit SiC polishing disk was used to clean the pellet surface to remove surface impurities from the processing. Later pellets were polished with different grit sheets to make the pellet surface flat and smooth. Sample nomenclature was used in the format: HPLT-(pressure)-(temperature)-(time). For example, in the case of LATP pellet densified by HPLT at 5.5 GPa, 200°C for 2 min, the nomenclature is: HPLT-5.5-200-2

Post-heat treatment (PH)

Chapter 5: The selected pellets after HPLT processing were post-treated at moderate temperatures (from 500 - 800 ˚C, PH treatments) in a muffle furnace – under an open-air atmosphere. The pellets were placed in an alumina slab for firing. A heating rate of 150 °C/h, a dwelling duration of 1 hour, and a cooling rate of 300 °C/h were used. Two different approaches were explored: 1) exposing the pellet during the heating, dwelling, and cooling steps of the PH treatment. This PH program was performed on the same set of pellets by exposing them initially at 600˚C (PH-600-1h) later 700 ˚C (PH-700-1h) and finally at 800 ˚C (PH-800-1h). 2) Flash exposed, for which the same heating program was used in the furnace, but the pellet was placed only when the dwelling stage was reached. In this case, we used a temperature of 800 ˚C with a flash exposure duration of 2 (PH-800-2min) and 10 minutes (PH-800-10min).

Density calculation

Chapter 5: The apparent density of sintered pellets was obtained from the weights and the dimensions (diameter and thickness using a screw gauge). The thickness was averaged from several measurements at different locations to consider possible inhomogeneity of the pellet shape.

X-ray diffraction (XRD)

In-situ XRD

An HTK 1200N temperature chamber (Anton-Paar) coupled to a BRUKER D8 Advance X-Ray Diffractometer equipped with LYNXEYE detector using Co radiation (λ: Kα1 = 1.78886 Å, Kα2 = 1.79277 Å) were used. The samples were weighed and mixed using an agate mortar and pestle inside an argon-filled glovebox. Then samples were heated in an alumina holder from room temperature to 1100 °C with a heating rate of 2 °C /min, and a diffraction pattern was obtained after each 50 °C. Measurements were obtained with a step size of 0.019° and a total time of 185 seconds/step in the 2θ range 10°- 80°.

Chapter 2: Four different combinations of components were evaluated by in-situ thermal X-ray diffraction: NMC+LATP (50:50), NMC+KB (80:20), LATP+KB (80:20) and NMC+LATP+KB (65:30:05). The ratios were chosen so that there is sufficient contact between the elements and to ensure a significant intensity of diffraction peaks for each component. To have an idea of the impact of heating the atmosphere, measurements were repeated under open air and nitrogen atmospheres. For the latter, the gas pressure was maintained constant up to 1 bar above atmospheric pressure.

Ex-situ XRD

Measurements were carried out with a BRUKER D8 Discover X-Ray Diffractometer equipped with LYNXEYE XE detector using monochromatic Cu tube-source radiation (λ: Kα1=1.54060 Å). Samples were measured in a 2θ range of 10°- 100° with a step size of 0.020° and a total time of 2 hours.

Chapter 2: Measurements were carried out for selected samples such as pristine NMC, C400-air, C500-air, and C600-air. Le Bail refinements were performed on C600-air data using the software package FullProf Suite (Windows version, September 2019).[355] The microstructure was refined using an isotropic size and strain broadening model and the instrumental contribution was subtracted by including an IRF to the refinement.

Chapter 4: Measurements were carried out for pristine carbons, pristine NMC, 500-KB composite, and 500-C65 composite. In the case of pristine carbons, XRD data has been corrected for the Lorentz-Polarization factor (see Appendices-Chapter 4 for more information). L_C has been calculated from the Scherrer formula assuming (002) peak broadening is only due to a reduced crystallite size. The average interlayer distance c/2 has been calculated as the average of the two contributions used to fit the (002) peak, weighted by their intensity. Both L_C and c/2 are indicators of crystallinity, as the more crystalline an sp2 carbon is the closer its c/2 will be to that of ideal graphite (c/2 = 3.36 Å).

Chapter 5: Samples were measured in a 2θ range of 10°- 80° with a step size of 0.020° and a total time of 192 seconds/step. For a visual representation, the peaks are background subtracted and normalized to a high intense (113) peak at 2θ= 24.6°. Le Bail refinements were performed using the software package FullProf Suite (Windows version, September 2019) [355] The microstructure was refined using an isotropic size and strain broadening model and the instrumental contribution was subtracted by including an IRF to the refinement.

Chapter 3: Ex-situ XRD measurements were carried out for Composites mixed as well as heated with and without LiF, with a BRUKER D8 Endeavor X-Ray Diffractometer equipped with LYNXEYE XE-T detector using Co radiation (λ: Kα1 = 1.78897 Å, Kα2 = 1.79285 Å). Samples were measured in a 2θ range of 10°- 130° with a step size of 0.016° and a total time of 19.20 seconds/step. Silicon holders were used to avoiding the amorphous background from normal

holders due to the limited quantity of samples. A comparison of peaks was obtained after background subtraction and Kα2 stripping. The peaks considered for comparison were (101), (012), (006), and (104) from NMC around which the crystal structure transitions were observed from previous studies. Intensities were normalized to 104 peaks of NMC at 2θ=52°.

Raman spectroscopy

Raman spectra were recorded with a Renishaw spectrometer (Nanonics Multiview 2000) operating with an excitation wave-length of 532 nm, focused with a 50-long working distance objective. The spectra were obtained by performing 10 acquisitions with 10 s of exposure time of the laser beam to the sample. A silicon wafer was used for calibration.

Thermogravimetry (TGA), Differential scanning calorimetry (DSC), and Quadrupole mass spectroscopy (QMS)

Chapters 2 and 4: Thermogravimetric analysis (TGA) was conducted on a NETZSCH TG 209 F1 Libra® equipment in synthetic air (and/or oxygen) atmosphere (2 atm). The heating program used for TGA consists of the same heating rate (1°C/min) dwelling temperature (500°C) and duration (1 h) as that of composite heat treatment. Further elevated the temperature up to 800°C to estimate the temperature at which carbon gets oxidized completely and to evaluate the residues if any. Later cooled down to room temperature at a rate of 10°C/min.

Chapter 2: TGA was performed on Comp Mix under a nitrogen atmosphere in the temperature range of 20-1000°C (heating rate: 5°C/min) under N_2 gas flow (50 cm3 /min). A simultaneous thermogravimetric analyzer [STA 449 F3 system connected to QMS 403 Aëolos (Netzsch)] was used to determine the thermal stability of Comp Mix under an air atmosphere. Experiments were performed on around 20 mg of the powder samples placed in alumina crucibles,

in the temperature range of 20-1000°C (heating rate: 5°C/min) under air flow (50 cm3 /min).

Chapter 3: TGA/DSC measurements on the composites were performed with Mettler Toledo TGA/DSC 1 STAR^e System equipped with Gas Controller GC100. Compressed dry air was used as a medium with a flow rate of 50 ml/min. The program is composed of a heating rate of 3 ˚C/min, in the temperature range of 25 ˚C – 800 ˚C and a dwelling duration of 1 hour at 400 ˚C. Comp Mix and Comp+LiF Mix were measured for comparison. A sample quantity of 20 mg was used in each measurement.

Electron microscopies

Scanning electron microscopy (SEM)

SEM was performed in a Quanta 200 FEG-FEI microscope operated at 20 kV.

Chapter 2: The SEM measurements were initially carried out on the powder materials. Afterward, to compare the morphology of the surface with the core, the particles were sectioned transversally using the ion milling technique performed in the IM4000plus from the Hitachi company.

Chapter 4: The SEM measurements were initially carried out on pristine carbon materials and cathode disks made of mixed composites without heat treatments.

Chapter 5: The SEM measurements were initially carried out on the pristine LATP. Later the surface morphology of pellets densified by conventional sintering and HPLT processing were compared. Afterward, to compare the morphology of the surface with the core, the particles were sectioned transversally using the ion milling technique performed in the IM4000plus from the Hitachi company. Analysis of elemental composition was done on selected samples by using an X-ray Dispersive Energy (EDX) spectrometer.

Tunneling electron microscopy (TEM)

Chapter 2: TEM was performed using an FEI Tecnai F20 electron microscope operated at 200 keV and equipped with a High Angle Annular Dark Field (HAADF) detector. For the TEM technique, the samples were prepared by the FIB technique by using the FEI Helios dual-beam FIB/SEM. For the preparation, the powder materials have been dispersed onto a substrate, fixed with a Pt-mask, and then milled from two sides with Ga-ions producing a lamella with a thickness lower than 100 nm, which is enough to let the electrons from the TEM to cross the sample. Local EDX and EDX profiles were performed on the samples to observe the distribution of elements in the particles. Additionally, electron diffraction was done for orienting the crystals along some specific crystal directions (I.e., crystal main axis) and also for studying the crystallinity of materials.

X-ray photoelectron spectroscopy (XPS)

Chapters 2 and 3: A Phoibos 150 XPS spectrometer (SPECS Surface Nano Analysis) installed in a UHV chamber with a base pressure of $1 \cdot 10^{-10}$ mbar was used for the measurements. Spectra were collected in Fixed Analyzer Transmission mode with a 2 mm lateral view on the sample and a non-monochromatic twin anode X-ray source (Mg Kα with hν = 1253.6 eV and Al Kα with hν = 1486.6 eV). The binding energy scale was calibrated by setting the aliphatic C-C bond at 284.8 eV, except in heated composites where that signal was not so identified, for which an iterative calibration using different peaks was done until reaching self-consistency. The inelastically scattered photoelectrons' background was simulated by a Shirley function and Voigt profiles (30% Gaussian, 70% Lorentzian) were employed as line shapes. The relative quantification of atomic surface species was done after applying tabulated Scofield cross-sections for each element and core level to the corresponding integrated intensity. Geometrical corrections for the 45º source-analyzer configuration were considered, as well as the energy-dependent analyzer transmission function and differences in effective attenuation length

(EAL) of the collected photoelectrons with different kinetic under the assumption of a homogenous distribution of elements. It is important to remind that XPS has a probing depth lower than 10 nm.

Chapter 4: X-ray Photoelectron Spectra of pristine carbons were recorded using a Phoibos 150 XPS spectrometer (SPECS Surface Nano Analysis) installed in a UHV chamber with a base pressure of $5 \cdot 10^{-10}$ mbar using a non-monochromatic Mg source (Mg K$\check{U}$ with h ɜ= 1253.6 eV). The spectra were collected in Fixed Analyzer Transmission mode with a 2 mm lateral view on the sample. Pass energies of 90 eV and 30 eV were used respectively for acquiring the survey spectra and the high-resolution regions (C 1s and O 1s). Quantification of atomic surface species (Figure 4. 3) was done by applying tabulated Scofield cross sections for each element and core level to the corresponding integrated intensity[356] after correcting the energy-dependent analyzer transmission function and differences in effective attenuation length of the collected photoelectrons with different kinetic energies.[357], [358] The background of inelastically scattered photoelectrons was removed before integration and it was simulated using a Shirley function.

X-ray absorption spectroscopy (XAS)

Chapter 4: X-ray Absorption Spectroscopy (XAS) measurements were carried out at the C K-edge and Mn, Co, and Ni L edges with the BL29- BOREAS beamline at the ALBA synchrotron light source (Barcelona, Spain).[359] The spectra were measured in total electron yield (TEY, registering the sample drain current after the photo-absorption) and total fluorescence yield (TFY, taking the signal provided by a calibrated photodiode) modes simultaneously under ultrahigh vacuum conditions (1.5 × 10−10 Torr). To avoid artifacts coming from changes in the beam intensity, the signal was normalized to the incident photon flux. For the sake of comparison, all spectra were normalized to the maximum intensity.

X-ray tomography

Synchrotron Radiation X-Ray Tomographic Microscopy (SRXTM) of the pellets was conducted at the high-flux 2.4 Tesla multipole wiggler beamline (BL1.2W) of the Synchrotron Light Research Institute (Thailand). For the sample preparation, pellet laminates were cut into longitudinal strips measuring 0.5 to 1 mm in width and meticulously aligned to stand vertically on 90° Al pin stubs. For this step, the field-of-view was adjusted such that a vertical clearance of at least 5 mm from the metallic pin stubs was achieved, to minimize fringe effects from any stray radiation. The pellets were scanned using a filtered white beam at the mean X-ray energy of 6 keV. The X-ray projections were acquired at a pixel size of 0.72 µm with the detection system comprising a YAG-Ce scintillator, 10X objective lens-coupled microscope, and the PCO edge 5.5. For each sample, a total of 2001 projections were collected in a 180° angular range, corresponding to a step size of 0.100°. Sinogram processing and filtered back projection algorithms were iteratively applied using the Octopus Reconstruction software package[360] and the Drishti project software[361] to finally achieve the optimal noise speckling – smoothening – compiling – thresholding segmentation of computed tomography (CT) slices for 3D visual exploration.

Electrode Preparation

Chapters 2 and 4: Slurries of the heated and pristine composite powders, mixed with PVDF binder in a ratio of 90: 10 by using NMP as the solvent, were tape-casted on Al foil. Tape-casts were dried in a vacuum oven at 80 °C. All the processes were carried out inside the Argon-filled glovebox. Dried sheets were punched into disks and pressed with an isostatic pressure of 5 T. Disks were dried under vacuum at 120 °C.

Chapter 3: Slurries were made in quantities of 400 mg each excluding the NMP solvent, where the composite to PVDF ratio was fixed to 90:10. Quantity of NMP was varying with respect to composites due to the difference in volume

by oxidation of carbon after heat treatment; 1.6 ml for Comp Mix and 1.4 ml for Comp 400-SA. PVDF was dissolved in NMP solvent using a magnetic stirrer for 2 hours. Stirring was continued overnight after adding the composite that was made previously. Slurries were tape cast on aluminum foils with a wet thickness of 300 µm using a doctor's blade. Laminates were dried overnight at 80 ˚C under a dynamic vacuum. Dried laminates were punched into disks and diameters were chosen in such a way the areal capacity (mAh/cm^2) remains comparable. Disks were densified with a uniaxial pressure of 3 T and dried at 120 ˚C overnight before cell assembly. All the processes were carried out in a dry room (due point~37 ˚C).

Electrochemistry: Galvanostatic cycling with potential limitation (GCPL)

Chapters 2 and 4: 2032-coin cells were assembled with composite cathode disks, lithium metal anode, and $LiPF_6$ 1M in EC-DEC (1:1) as electrolytes. Active mass loading was in the range of 2 – 3 mg/cm^2 in all cases. Coin cells were galvanostatically charged-discharged between 2.7 – 4.3 V along with C-rate tests using a BioLogic VMP3 Potentiostat. The cycling protocol consisted of 5 cycles at C-rates C/20, C/10, C/5, C/2, and 1C followed by 50 cycles at C/10. Capacity values are normalized with respect to the wight of active material (NMC) and results were verified with reproducibility.

Chapter 3: 2032-coin cells were assembled with composite cathode disks, lithium metal anode, and $LiPF_6$ 1M in EC-DMC (3:7) as electrolytes. Coin cells were galvanostatically charged-discharged immediately after the cell assembly (without aging) between 2.7 – 4.3 V along with rate capability tests using a TOYO battery cycler. The cycling protocol consisted of 5 cycles each at C-rates C/20, C/10, C/5, C/2, and 1C followed by 100 cycles at C/10. Capacity values are normalized with respect to the wight of active material (NMC) and results were verified with reproducibility. Glass fiber was used as the separator. Along with rate capability, the second charge-discharge cycle at a C-rate of C/20 was

considered in all the analyses since the first cycle is usually considered to have contributions from SEI formation which is characteristic of liquid electrolyte interaction at the electrode interfaces.

Electrochemical impedance spectroscopy (EIS)

Chapter 5: EIS was performed on LATP electrolytes with sputtered gold (Au) as blocking electrodes, and the cell was assembled in Swagelok units. The measurements were carried out using a Solartron 1260 FRA module, with AC frequencies ranging between 32 MHz to 1 Hz with 50 mV excitation amplitude. Experiments were carried out at room temperature (RT).

Chronoamperometry (CA) analysis

Chapter 5: The pellet was taken for chronoamperometry analysis, where the electrode current was measured as a function of time for different square wave potentials. The hike in current in the beginning for each voltage value is arising from the ionic transport where it gets saturated since the pellet is sandwiched between blocking electrodes. Later the constant or saturated current is arising from electronic transport alone. The resistance corresponding to saturated current for each voltage was calculated from the ohmic plot (current vs voltage) and the electronic conductivity accordingly.

PUBLICATIONS AND CONTRIBUTIONS TO CONFERENCES

Publications and patents

1. Nicola Boaretto, Iñigo Garbayo, **Sona Valiyaveettil-SobhanRaj**, Amaia Quintela, Chunmei Li, Montse Casas-Cabanas, and Frederic Aguesse. "Lithium solid-state batteries: State-of-the-art and challenges for materials, interfaces and processing." Journal of Power Sources 502 (2021): 229919. https://doi.org/10.1016/j.jpowsour.2021.229919
   Content of **chapter 1** of the thesis

2. **Sona Valiyaveettil-SobhanRaj**, Rosalia Cid, Travis Thompson, Francisco Bonilla, Gabriel A. López, Frederic Aguesse and Montse Casas-Cabanas. "High temperature thermal reactivity and interface evolution of NMC-LATP-carbon composite cathode." ACS Applied Materials and Interfaces. (2023) https://doi.org/10.1021/acsami.2c20097
   Content of **chapter 2** of the thesis

3. Florencia Marchini, Travis Thompson, **Sona Valiyaveettil-SobhanRaj**, Montserrat Casas-Cabanas and Frederic Aguesse. "Composite cathode material comprising ceramic oxide electrolyte, lithium electrode material and enhancing agent". European Patent-Ref No. P6111109EP (accepted)
   Content of **chapter 3** of the thesis

   Sona Valiyaveettil-SobhanRaj, Marina Enterría, Rosalía Cid, Damien Saurel, Gene Medard Nolis, Florencia Marchini, Travis Thompson, Frederic Aguesse and Montse Casas-Cabanas. "Choosing carbon conductive additives for NMC-LATP composite cathodes: impact on thermal stability". Journal of The Electrochemical Society (under revision)
   Content of **chapter 4** of the thesis

4. **Sona Valiyaveettil-SobhanRaj**, Paweł Głuchowski, Pedro López-Aranguren, Frederic Aguesse, Ramakumar Sampathkumar, Travis Thompson, Catleya Rojviriya, William Manalastas Jr, Madhavi Srinivasan and Montse Casas-Cabanas. "High-Pressure Low-Temperature densification of NASICON-based LATP electrolytes for solid-state lithium batteries" (manuscript about to be submitted)
   Content of **chapter 5** of the thesis

Contributions to Conferences

1. Umicore PhD Students and Postdoc Networking Event. Umicore, Olen, Belgium. 20-21, June, 2019. **Oral presentation**

2. 4th International forum on Progress and Trends in Battery and Capacitor Technologies- Power our Future 2019. Vitoria-Gasteiz, Spain. 02-05 of July, 2019. **Poster presentation**

3. lV School on solid stare Nuclear Magnetic Resonance and Applications. Cerámica y Vidrio del CSIC, Madrid, Spain. 28-30 of October, 2019. **Assistance.**

4. 4th Young Researcher Day, CIC energiGUNE, Vitoria-Gasteiz, Spain. 22, 29 of September and 13 of October, 2020. **Oral presentation** and **Best presentation award**

5. 239th ECS Meeting with the 18th International Meeting on Chemical Sensors. Chicago, Illinois (online event). May 30 – June 03, 2021. **Oral presentation**

6. XVII Simposio de Investigadores Jóvenes RSEQ. University of Alcalá de Henares, Alcalá de Henares, Madrid Spain. 23 -26 of November, 2021. **Oral presentation**

7. 5th Young Researcher Day, CIC energiGUNE, Vitoria-Gasteiz, Spain. 01 and 16 of December, 2021. **Oral presentation**

8. Umicore Science and Technology days, 2022. Antwerp, Belgium and Cheonan, South Korea. 02 - 04 of November, 2022. **Poster presentation**

APPENDICES

Chapter 2

X-ray photoelectron spectroscopy (XPS)

The analysis of the core-level signals of the elements involved can give us extra information about the processes taking place at the surface/interface of the particles and the new species formed. Figure 2. 12 of the main text shows the relevant core levels of the NMC and LATP elements: Ni 2p, Co 2p, Mn 2p, Ti 2p, P 2p, and O 1s. In Appendix 2. 1 C 1s and a lower binding energy (BE) region ranging from Al 2p to Ti 3p where all the metals have partially overlapped signals are also provided. Having a look at Ti 2p and P 2p regions, it can be seen how the initial LATP surface signal in the as-mixed sample (Ti doublet with 5.66 eV of spin-orbit splitting and $2p_{3/2}$ peak at 460 eV, P doublet with $2p_{3/2}$ signal at 133.7 eV) slightly decreases in C500-air, transforming partly in TiO_2 (extra Ti(IV) doublet at 1 eV lower BE[290] and probably other M-phosphates that partially overlap with LATP in P2p[287], [288] (as suggested by the wider peaks), making its separation difficult. Heating to 600 makes LATP disappear from the surface, transforming into other M-phosphates (P doublet with $2p_{3/2}$ signal at 134.2 eV[287], [288]), Li_3PO_4 (P $2p_{3/2}$ shifted to lower BE), increased amount of TiO_2 and an extra Ti doublet at even lower BE ($2p_{3/2}$ at 457.22 eV) ascribed to Ti(III)[289], [290] forming likely Ti_2O_3 or $Ti(PO_4)$.

Ni 2p signal, originally fitted with 2+ and 3+ contribution in NMC[362]–[364] (with a 2.7+ average oxidation state) contains extra intensity at higher BE after thermal treatment. In heated composites, it can be fitted with a fraction of the original NMC 2+/3+ peaks and an extra doublet with $2p_{3/2}$ component at 856.6 eV. Notice how the intensity of the new doublet increases from C500-air to C600-air. The comparable height of satellites with $2p_{1/2}$ peak suggests that this new contribution corresponds to Ni (II).[363], [364] It may be ascribed to Ni (II) phosphate[283] and/or NiO that appears shifted due to differential charging effects.

The shape of Co 2p also differs importantly in heated vs as-mixed composites. Initially, it corresponds to Co 3+ in layered NMC[365], with pronounced main peaks at 779.8 eV ($2p_{3/2}$) and 794.8 eV ($2p_{1/2}$) and satellites at 789.4 eV and 804.4 eV. After heating, an extra phase appears which causes an important increase of intensity at 781 eV ($2p_{3/2}$), 786.6 eV ($2p_{1/2}$), and small satellite at 785.4 eV. These features can be ascribed to the formation of CoO[284] and/or even delithiated Co in the layered structure.[285], [286]

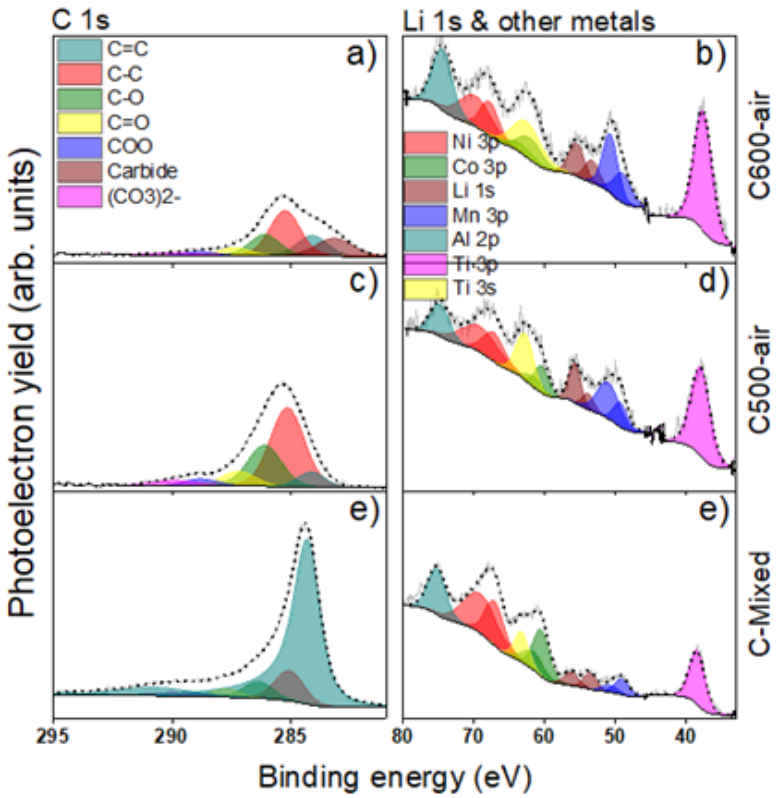

Appendix 2. 1: Surface chemical composition using X-ray photoelectron spectroscopy. Comparison of signals for – C 1s (**a, c, e**), Co 2p (**b, e, h**), in C600-air, C500-air, and C-Mixed respectively.

Chapter 3

Selection criteria for additive

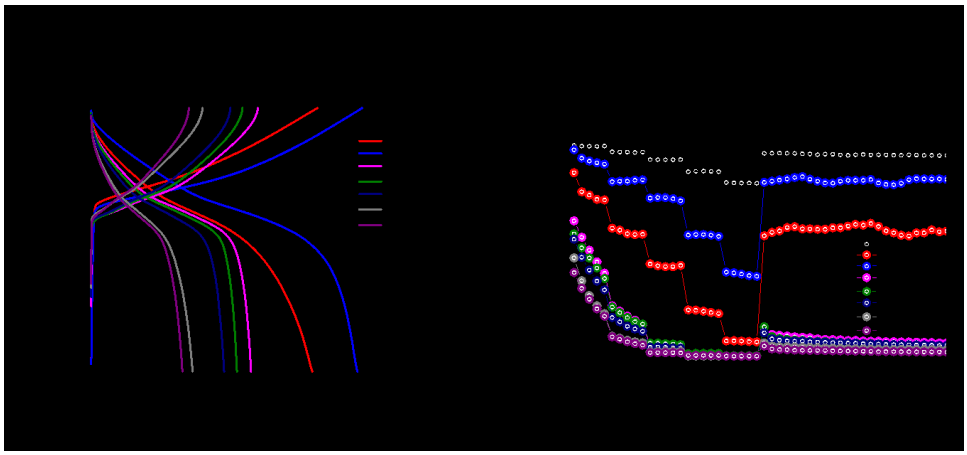

Appendix 3. 1: **a)** Second charge-discharge cycle at C/20 for composite C-mixed, heat-treated samples at 500°C under air with different additives b) Corresponding C-rate capability tests with the C-rates: C/20, C/10, C/5, C/2, 1C [5 cycles each] and C/10 [long cycling]

Appendix Table 3. 1: Comparison of melting or decomposition temperature of additives and their response to C500-air composite electrochemistry

	LiF	$Li_2C_2O_4$	LiOH	$LiNO_3$	Li_2CO_3	Li_2O_2
Melting/decomposition temp (ºC)	848/_	_ /183	462/_	255/_	723/_	_ /340
Response in electrochemistry (500ºC Air)						

Appendix Table 3. 2: Summary of observations from the XRD diffractogram of C500-air composites with different additives followed by XRD patterns of each composite.

500 °C (air)	LiF	$Li_2C_2O_4$	LiOH	$LiNO_3$	Li_2CO_3	Li_2O_2
Secondary phase	No	Yes (Li_2CO_3)	Yes (Li_2CO_3)	No	No	Yes (Li_2CO_3)
Peak broadening (003)	Yes	Yes	Yes	Yes	No	Yes
Peak asymmetry (104)	No	No	No	No	No	No
Peak intensity reduction (104)	No	No	Yes	No	Yes	No

NMC + LATP + KB [65:30:5] + 5% LiF

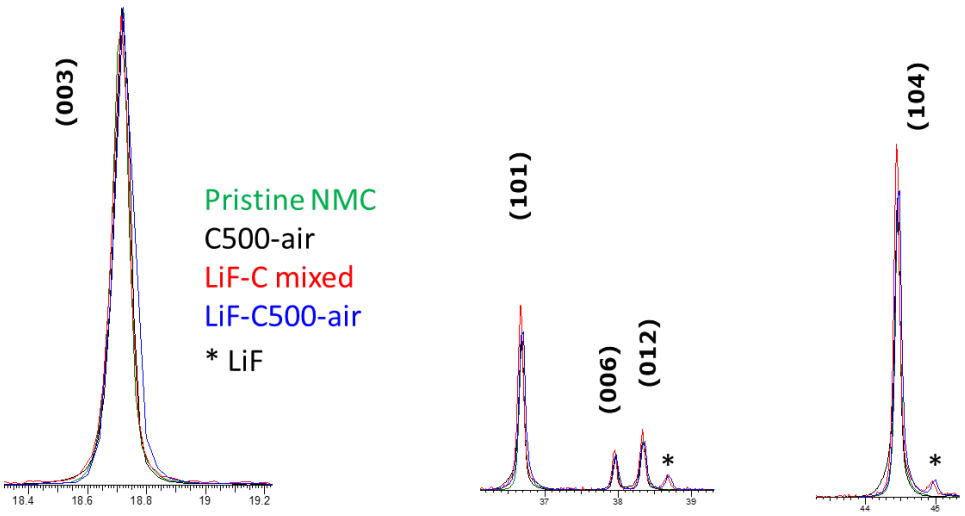

NMC + LATP + KB [65:30:5] + 5% $Li_2C_2O_4$

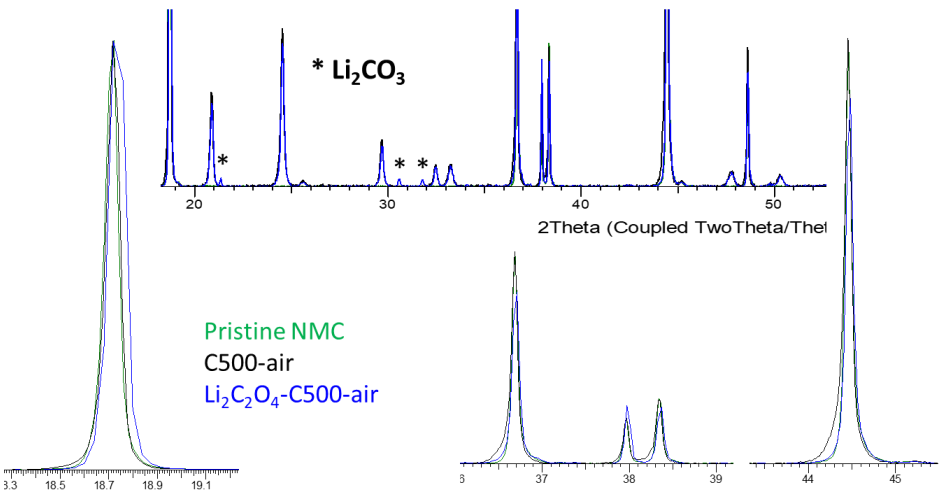

- NMC-peak asymmetry of C500-air has disappeared in $Li_2C_2O_4$-C500-air (exception with 003 peak). But shows slight difference in peak intensities
- Shows Li_2CO_3 secondary phase for $Li_2C_2O_4$-C500-air and mixed

NMC + LATP + KB [65:30:5] + 5% LiOH

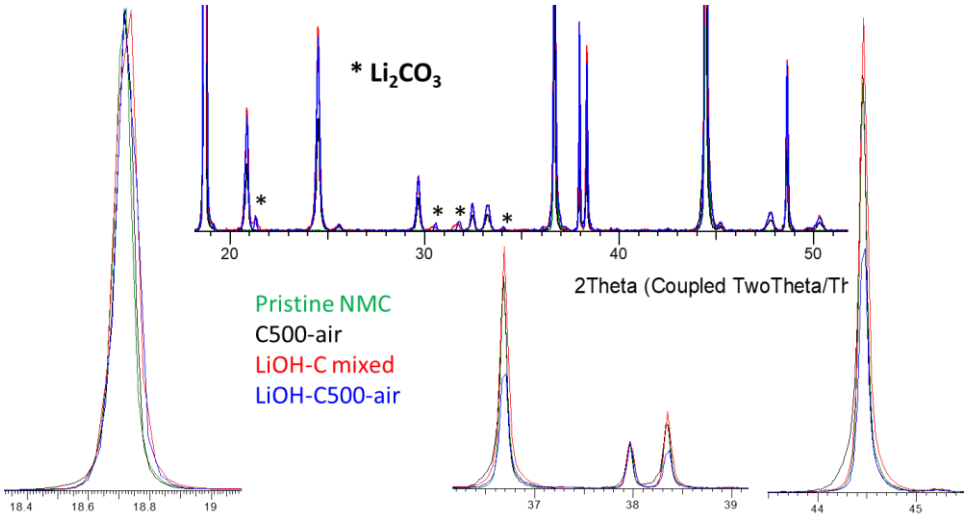

- NMC-peak asymmetry of C500-air has disappeared in LiOH-C500-air (exception with 003 peak). But shows difference in peak intensities
- Shows Li_2CO_3 secondary phase for LiOH-C500-air and mixed

NMC + LATP + KB [65:30:5] + 5% $LiNO_3$

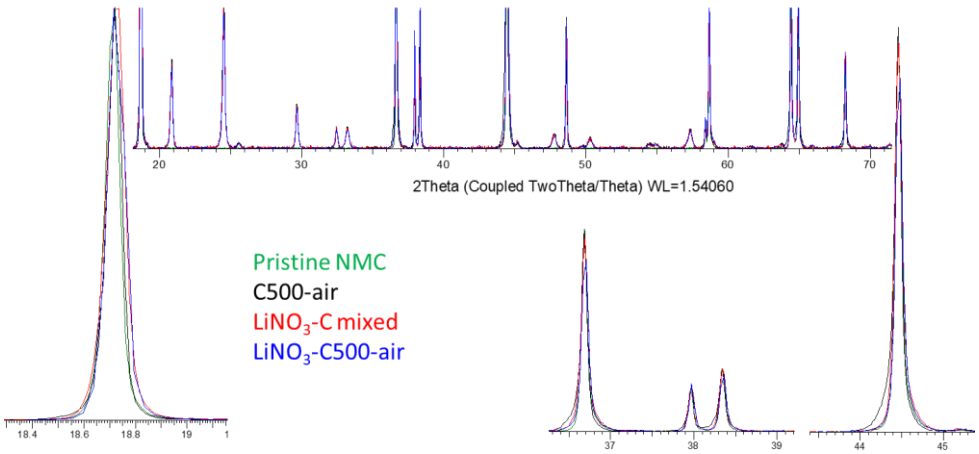

- NMC-peak asymmetry of C500-air has disappeared in $LiNO_3$-C500-air (exception with 003 peak). But shows slight difference in peak intensities
- No evidence for secondary phases

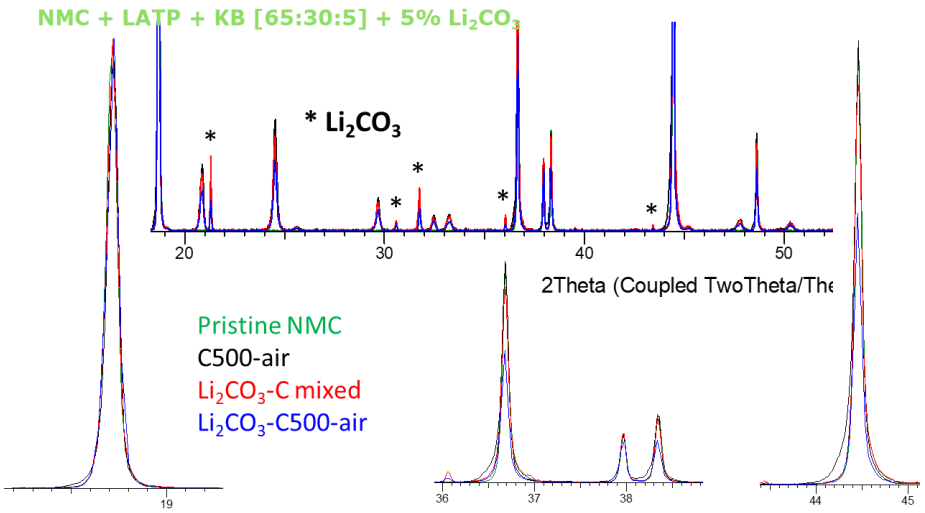

- NMC-peak asymmetry of C500-air has disappeared in Li_2CO_3-C500-air. But shows difference in peak intensities
- No evidence for secondary phases

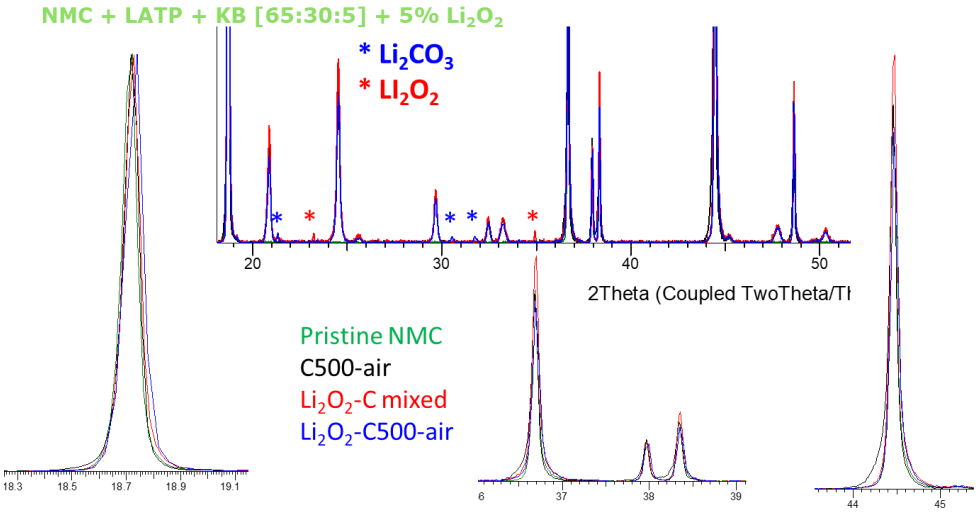

- NMC-peak asymmetry of C500-air has disappeared in Li_2O_2-C500-air (exception with 003 peak)
- Li_2O_2-C500-air doesn't have Li_2O_2 peaks instead shows Li_2CO_3 secondary phase

Chapter 4

XRD Data correction

The X-ray powder diffraction patterns shown in Figure 4. 1b have been corrected for Lorentz-Polarization factor (LPF):

$$LPF = \frac{1 + \cos^2(2\theta)}{\sin(2\theta) \cdot \sin\theta}$$

Where $1 + \cos^2(2\theta)$ is the polarization factor, $\sin(2\theta)$ is the change in irradiated volume, and $\sin\theta$ the powder ring distribution factor, the two later constituting the Lorentz factor for powder sample in Bragg-Brentano geometry.[366][367] The correction of the experimental intensity by this factor is of prime importance for non-graphitic carbons since it affects the apparent peak position at a low angle, that is of the (002) peak, and hence the proper estimate of the interlayer distance.[307]

Electrochemistry of binary systems

To distinguish the contribution of LATP and KB in the thermal reactivity with NMC at 500°C under air atmosphere, composites were taken in different binary combinations for heat treatments. NMC+LATP were heated and then KB was added (NMC+LATP _500-air+KB) such that it reflects the mode of reactivity only between NMC and LATP during the heat treatment; NMC+KB were heated and then LATP was added (NMC+KB_500-air+LATP) so that the nature of NMC-KB thermal reactivity can be highlighted. The electrochemical performance of each system was compared with the composite as mixed and heated at 500C (500-KB) [Appendix 4. 1].

For NMC+LATP _500-air+KB the discharge capacity has reduced to 160 mAh/g at C/20 and 18 mAh/g at 1C. Charge discharge polarization is higher than in the mixed composite and it indicates increased cell resistance possibly arising from low-conducting reaction byproducts formed from NMC-LATP thermal reactivity. [272], [276], [305] Capacity fading is drastic with the number of cycles as well as with higher C rates and gives the least capacity retention among all the combinations.

NMC+KB_500-air+LATP discharge capacity has also reduced to 159 mAh/g at C/20 and 18 mAh/g at 1C. The charge-discharge polarization is higher

than NMC+LATP _500-air+KB but the capacity loss is evident only with higher C rates and retains with the number of cycles. Polarization is still high compared to as mixed composite and shows an extra discharge plateau around 3 V that is maintained throughout cycling, it possibly indicates partial phase change of NMC due to thermal reactivity with KB (layered + spinal mixture) which is still electrochemically active. [368], [369]

In 500-KB, the discharge capacity of 142 mAh/g at C/20 and 12 mAh/g at 1C together with the highest polarization reflects a simultaneous contribution of every component in thermal reactivity. Capacity reduction is prominent with higher C rates but not with the number of cycles and retention is moderate compared to previous combinations. This might indicate that there is mutual masking among the elements that moderates the reactivity.

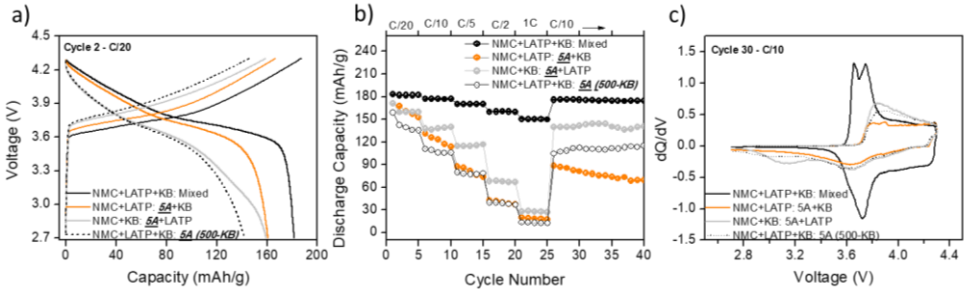

Appendix 4. 1: NMC-LATP-carbon composite cathode electrochemistry tests in conventional half-cell configuration using the liquid electrolyte. Comparison of the impact of heat treatment in the binary combination of components. 5A represents the heat treatment at 500˚C under an air atmosphere. a) Second charge-discharge cycle at a C rate of C/20. b) C-rate capability tests with the C-rates; C/20, C/10, C/5, C/2, 1C [5 cycles each] and C/10 [long cycling]. c) Differential capacity (dQ/dV) vs voltage curves.

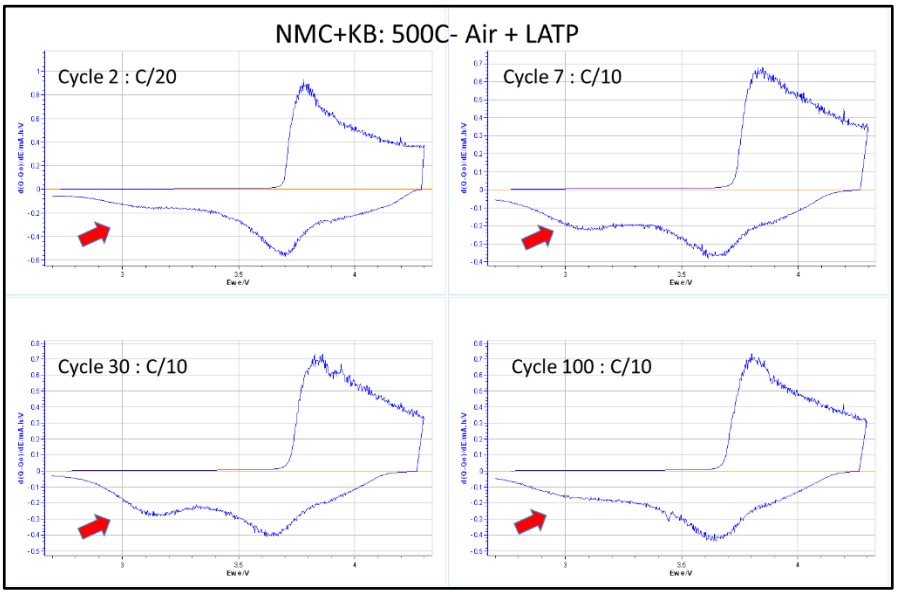

Appendix 4. 2: Comparison of the differential capacity (dQ/dV) vs voltage plots of cycle 2 (C/20), cycle 7, 30, and 100 (C/10) of NMC+KB_500-air+LATP composite. Indicating the evolution of reduction peak around 3V, where it arises after the second cycle, intensifies with the number of cycles later fades with further cycling.

Calculation of average oxidation states of TM in NMC:

To calculate the average oxidation states of the NMC metals in the probed area by TEY XAS, different approaches have been used for each transition metal based on the literature. Ni L_3 region is composed of two main peaks A and B whose ratio changes very noticeably with the Ni oxidation state (see Appendix 4. 3a**).** While B/A height intensity ratio is around 1 for Ni3+ [370], [371], a close inspection of the Ni2+ spectrum [372], [373] shows that this ratio goes down to around 0.1. We make a linear interpolation between these two extremes to get a calibration rule for our set of samples (see Appendix 4. 3b). Based on the correct oxidation state obtained for Ni in the pristine NMC using this calibration law (2.7+, as theoretically expected) we are confident on the suitability of our approach.

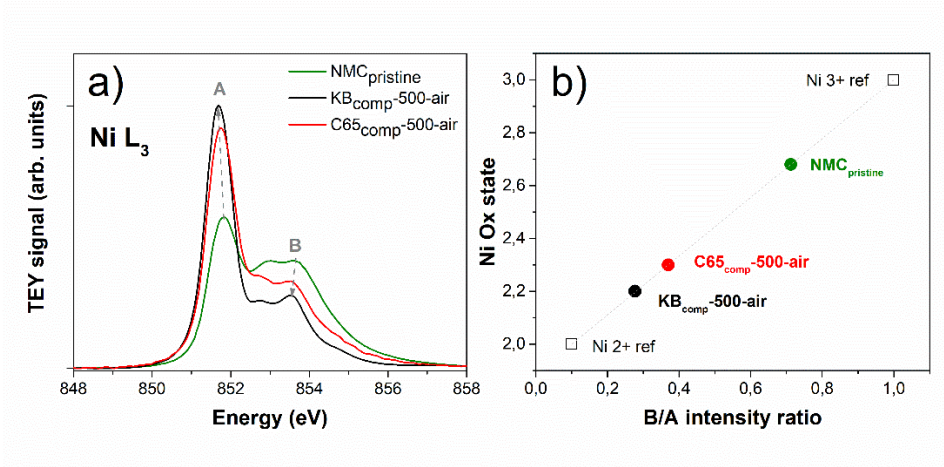

Appendix 4. 3: a) Ni L3 edge of pristine NMC and heated composites with KB and C65. The normalization of the spectra is different than the one shown in Fig 4. a **b)** Ni oxidation state got from the calibration law arising from B/A peaks height ratio.

For Mn and Co we obtained the oxidation state based on the energy shift of the L_3 edge centroid. In both cases, the L_3 XAS signal after background removal (Figure 4. 9) was integrated and then normalized to the overall integral after this edge, so that the L_3 centroid position was calculated as the energy for which this normalized integral is equal to 0.5 (see Appendix 4. 4). A shift of 2 eV per oxidation state is reported for Mn compounds in literature[374] and references therein]. A thorough inspection of Co L_3 XAS reference spectra given in the literature[375] shows that around 2 eV shift also occurs between Co+3 and Co+2 L_3 centroid. We have checked that a 2 eV shift in the L_3 centroid per oxidation state change is an appropriate rule using Mn and Co references. For calculating the final oxidation state of Mn and Co in heated composites, we consider that Mn and Co in our pristine NMC have respectively +4 and +3 oxidation states, as confirmed by XPS[305] and also in agreement with XAS references found in the literature.[376]–[378]

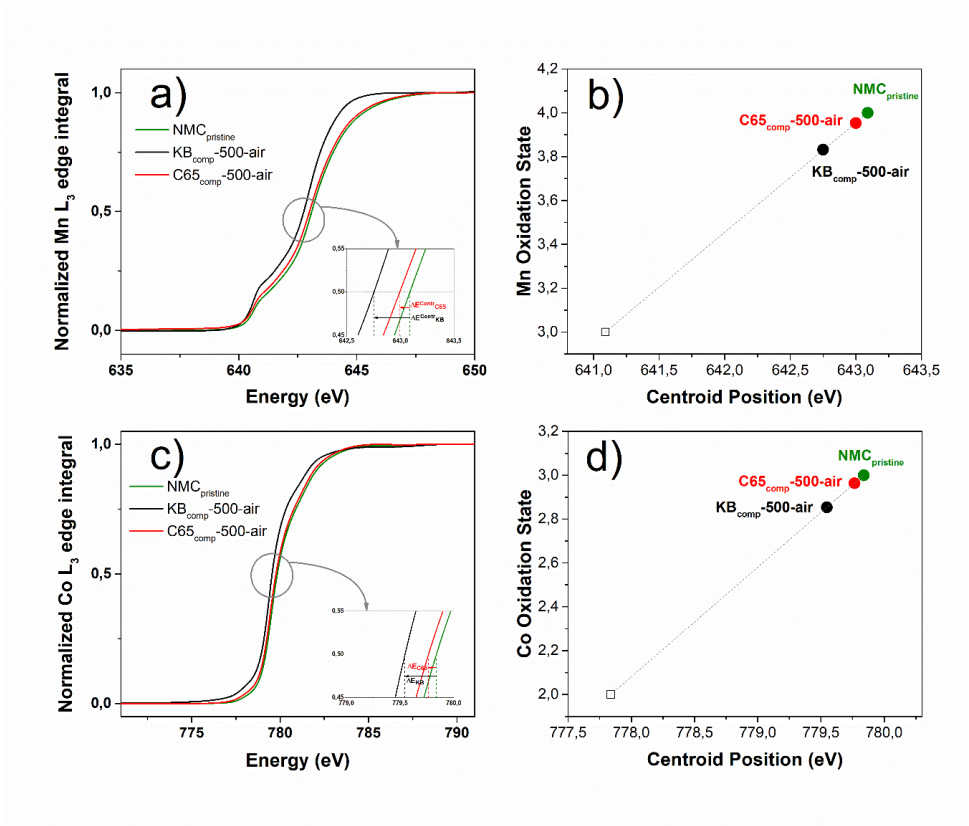

Appendix 4. 4: a) Mn and **c)** Co normalized L_3 edge integral ($I_n(E)$) of pristine NMC and heated composites with KB and C65. The shift in the L_3 centroid is highlighted in the zoomed region (E_c for which $I_n(E_c)$=0.5 shifts among samples). Based on a centroid shift of 2eV/oxidation state, the calculation of the average Mn and Co oxidation states is plotted in **b)** and **d)** respectively.

C-K edge comparison of pristine C65, KB and composites 500-KB and 500-C65 (Figure 4. 9d in the main text):

Two main features are distinguished for the pristine carbons: peak *A* at 285.2 eV and threshold *B* at 291.6 eV. Peak *A* results from transitions from the C 1s core level to π* orbitals, indicating the presence of C=C sp^2 bonding, while *B* represents the threshold of transitions from C 1s to σ* orbitals, revealing the presence of C-C bonds. A decreased *A* to *B* peak height ratio reveals the reduced content in the planar C=C bonds for the heated composites, which is especially important in the case of 500-KB composite. Together with this, a shift of peak *A* to lower energy and its broadening is also evident in the 500-KB composite. Similarly, a shift of this feature to 284.87 eV is observed in the oxygen-

containing lattice of graphene oxide.[379] The shift and broadening observed for the 500-KB composite is thus probably a consequence of the high degree of structural (and electronic) rearrangement of the aromatic ring that is accommodating oxygen and the presence of edge/defect states [380], [381], indicating the prominent oxidation of KB and defect formation in its structure. Moreover, the increase of features C (~287.3 eV) and D (~288.4 eV) as well as the appearance of a new feature E (~290.2 eV) relates to the formation of these new oxygen functionalities upon carbon oxidation. Though the precise assignment of features in the range 286-289 eV between C π* and σ* transitions is controversial, they are typically attributed to C bound to O and H. According to other works, we may ascribe peak C to the formation of C-H, C-OH, or C-O-C (ether-like) functionalities and peak D to C=O, -COOH, or C-O-C epoxide bonds.[379], [380], [382]–[384] On the other hand, peak D can be assigned to the formation of carbonates, being representative of the C=O 1s to π* electronic transitions in the planar $(CO_3)^{2-}$ groups.[385]

REFERENCES

[1] Mike. Sanders, 'The Rechargeable Battery Market and Main Trends 2016–2025', 2017, pp. 1–98.

[2] M. Armand, J. T.- nature, and undefined 2008, 'Building better batteries', *nature.com*, Accessed: Mar. 10, 2022. [Online]. Available: https://www.nature.com/articles/451652a

[3] B. Scrosati, 'Recent advances in lithium ion battery materials', *Electrochim Acta*, vol. 45, no. 15–16, pp. 2461–2466, May 2000, doi: 10.1016/S0013-4686(00)00333-9.

[4] Ying Shirley Meng, 'Lithium metal anode – advanced characterization, slides from the web seminar by Dr. Y. Shirley Meng'.

[5] X. Feng, M. Ouyang, X. Liu, L. Lu, Y. Xia, and X. He, 'Thermal runaway mechanism of lithium ion battery for electric vehicles: A review', *Energy Storage Mater*, vol. 10, pp. 246–267, Jan. 2018, doi: 10.1016/j.ensm.2017.05.013.

[6] Q. Wang, P. Ping, X. Zhao, G. Chu, J. Sun, and C. Chen, 'Thermal runaway caused fire and explosion of lithium ion battery', *J Power Sources*, vol. 208, pp. 210–224, Jun. 2012, doi: 10.1016/j.jpowsour.2012.02.038.

[7] A. Iturrondobeitia *et al.*, 'Post-Mortem Analysis of Calendar-Aged 16 Ah NMC/Graphite Pouch Cells for EV Application', *The Journal of Physical Chemistry C*, vol. 121, no. 40, pp. 21865–21876, Oct. 2017, doi: 10.1021/acs.jpcc.7b05416.

[8] A. Perea, M. Dontigny, and K. Zaghib, 'Safety of solid-state Li metal battery: Solid polymer versus liquid electrolyte', *J Power Sources*, vol. 359, pp. 182–185, Aug. 2017, doi: 10.1016/j.jpowsour.2017.05.061.

[9] W. Zhang, J. Nie, F. Li, Z. L. Wang, and C. Sun, 'A durable and safe solid-state lithium battery with a hybrid electrolyte membrane', *Nano Energy*, vol. 45, pp. 413–419, Mar. 2018, doi: 10.1016/j.nanoen.2018.01.028.

[10] J. Janek and W. G. Zeier, 'A solid future for battery development', *Nat Energy*, vol. 1, no. 9, p. 16141, Sep. 2016, doi: 10.1038/nenergy.2016.141.

[11] A. Gutiérrez-Pardo *et al.*, 'Will the competitive future of solid state Li metal batteries rely on a ceramic or a composite electrolyte?', *Sustain Energy Fuels*, vol. 2, no. 10, pp. 2325–2334, 2018, doi: 10.1039/C8SE00273H.

[12] 'https://esmito.com/blog/lithium-ion-batteries.html'.

[13] J. B. Goodenough and P. Singh, 'Review—Solid Electrolytes in Rechargeable Electrochemical Cells', *J Electrochem Soc*, vol. 162, no. 14, pp. A2387–A2392, 2015, doi: 10.1149/2.0021514jes.

[14] A. Manthiram, X. Yu, and S. Wang, 'Lithium battery chemistries enabled by solid-state electrolytes', *Nat Rev Mater*, vol. 2, no. 4, p. 16103, Apr. 2017, doi: 10.1038/natrevmats.2016.103.

[15] F. Zheng, M. Kotobuki, S. Song, M. O. Lai, and L. Lu, 'Review on solid electrolytes for all-solid-state lithium-ion batteries', *J Power Sources*, vol. 389, pp. 198–213, Jun. 2018, doi: 10.1016/j.jpowsour.2018.04.022.

[16] X. Zhang, J.-C. Daigle, and K. Zaghib, 'Comprehensive Review of Polymer Architecture for All-Solid-State Lithium Rechargeable Batteries', *Materials*, vol. 13, no. 11, p. 2488, May 2020, doi: 10.3390/ma13112488.

[17] I. Gracia, M. Armand, and D. Shanmukaraj, 'Li Metal Polymer Batteries', in *Solid Electrolytes for Advanced Applications*, Cham: Springer International Publishing, 2019, pp. 347–373. doi: 10.1007/978-3-030-31581-8_15.

[18] P. Knauth, 'Inorganic solid Li ion conductors: An overview', *Solid State Ion*, vol. 180, no. 14–16, pp. 911–916, Jun. 2009, doi: http://dx.doi.org/10.1016/j.ssi.2009.03.022.

[19] Q. Liu *et al.*, 'Challenges and perspectives of garnet solid electrolytes for all solid-state lithium batteries', *J Power Sources*, vol. 389, pp. 120–134, Jun. 2018, doi: 10.1016/j.jpowsour.2018.04.019.

[20] V. Thangadurai, D. Pinzaru, S. Narayanan, and A. K. Baral, 'Fast Solid-State Li Ion Conducting Garnet-Type Structure Metal Oxides for Energy Storage', *J Phys Chem Lett*, vol. 6, no. 2, pp. 292–299, Jan. 2015, doi: 10.1021/jz501828v.

[21] J. Schnell *et al.*, 'All-solid-state lithium-ion and lithium metal batteries – paving the way to large-scale production', *J Power Sources*, vol. 382, pp. 160–175, Apr. 2018, doi: 10.1016/j.jpowsour.2018.02.062.

[22] J. Wu, Z. Rao, Z. Cheng, L. Yuan, Z. Li, and Y. Huang, 'Ultrathin, Flexible Polymer Electrolyte for Cost-Effective Fabrication of All-Solid-State Lithium Metal Batteries', *Adv Energy Mater*, vol. 9, no. 46, p. 1902767, Dec. 2019, doi: 10.1002/aenm.201902767.

[23] K. Murata, S. Izuchi, and Y. Yoshihisa, 'An overview of the research and development of solid polymer electrolyte batteries', *Electrochim Acta*, vol. 45, no. 8–9, pp. 1501–1508, Jan. 2000, doi: 10.1016/S0013-4686(99)00365-5.

[24] R. C. Xu, X. H. Xia, S. Z. Zhang, D. Xie, X. L. Wang, and J. P. Tu, 'Interfacial challenges and progress for inorganic all-solid-state lithium batteries', *Electrochim Acta*, vol. 284, pp. 177–187, Sep. 2018, doi: 10.1016/j.electacta.2018.07.191.

[25] Z. Gao *et al.*, 'Promises, Challenges, and Recent Progress of Inorganic Solid-State Electrolytes for All-Solid-State Lithium Batteries', *Advanced Materials*, vol. 30, no. 17, p. 1705702, Apr. 2018, doi: 10.1002/adma.201705702.

[26] Y. Wang *et al.*, 'Design principles for solid-state lithium superionic conductors', *Nat Mater*, vol. 14, no. 10, pp. 1026–1031, Oct. 2015, doi: 10.1038/nmat4369.

[27] S. Xia, X. Wu, Z. Zhang, Y. Cui, and W. Liu, 'Practical Challenges and Future Perspectives of All-Solid-State Lithium-Metal Batteries', *Chem*, vol. 5, no. 4, pp. 753–785, Apr. 2019, doi: 10.1016/j.chempr.2018.11.013.

[28] W. D. Richards, L. J. Miara, Y. Wang, J. C. Kim, and G. Ceder, 'Interface Stability in Solid-State Batteries', *Chemistry of Materials*, vol. 28, no. 1, pp. 266–273, Jan. 2016, doi: 10.1021/acs.chemmater.5b04082.

[29] J. W. Fergus, 'Recent developments in cathode materials for lithium ion batteries', *J Power Sources*, vol. 195, no. 4, pp. 939–954, Feb. 2010, doi: 10.1016/j.jpowsour.2009.08.089.

[30] L. Wang, B. Chen, J. Ma, G. Cui, and L. Chen, 'Reviving lithium cobalt oxide-based lithium secondary batteries-toward a higher energy density', *Chem Soc Rev*, vol. 47, no. 17, pp. 6505–6602, 2018, doi: 10.1039/C8CS00322J.

[31] S.-T. Myung *et al.*, 'Nickel-Rich Layered Cathode Materials for Automotive Lithium-Ion Batteries: Achievements and Perspectives', *ACS Energy Lett*, vol. 2, no. 1, pp. 196–223, Jan. 2017, doi: 10.1021/acsenergylett.6b00594.

[32] A. Ueda and T. Ohzuku, 'Solid-State Redox Reactions of $LiNi_{1/2}Co_{1/2}O_2$ ($R\bar{3}m$) for 4 Volt Secondary Lithium Cells', *J Electrochem Soc*, vol. 141, no. 8, pp. 2010–2014, Aug. 1994, doi: 10.1149/1.2055051.

[33] C. Delmas, I. Saadoune, and A. Rougier, 'The cycling properties of the LixNi1−yCoyO2 electrode', *J Power Sources*, vol. 44, no. 1–3, pp. 595–602, Apr. 1993, doi: 10.1016/0378-7753(93)80208-7.

[34] T. Ohzuku, A. Ueda, and M. Kouguchi, 'Synthesis and Characterization of $LiAl_{1/4}Ni_{3/4}O_2$ ($R\bar{3}m$) for Lithium-Ion (Shuttlecock) Batteries', *J Electrochem Soc*, vol. 142, no. 12, pp. 4033–4039, Dec. 1995, doi: 10.1149/1.2048458.

[35] M. Guilmard, 'Effects of aluminum on the structural and electrochemical properties of LiNiO2', *J Power Sources*, vol. 115, no. 2, pp. 305–314, Apr. 2003, doi: 10.1016/S0378-7753(03)00012-0.

[36] O. Srur-Lavi *et al.*, 'Studies of the Electrochemical Behavior of $LiNi_{0.80}Co_{0.15}Al_{0.05}O_2$ Electrodes Coated with $LiAlO_2$', *J Electrochem Soc*, vol. 164, no. 13, pp. A3266–A3275, 2017, doi: 10.1149/2.1631713jes.

[37] H.-J. Noh, S. Youn, C. S. Yoon, and Y.-K. Sun, 'Comparison of the structural and electrochemical properties of layered Li[NixCoyMnz]O2 (x = 1/3, 0.5, 0.6, 0.7, 0.8 and 0.85) cathode material for lithium-ion batteries', *J Power Sources*, vol. 233, pp. 121–130, Jul. 2013, doi: 10.1016/j.jpowsour.2013.01.063.

[38] S.-M. Bak *et al.*, 'Structural Changes and Thermal Stability of Charged $LiNi_xMn_yCo_zO_2$ Cathode Materials Studied by Combined *In Situ* Time-Resolved XRD and Mass Spectroscopy', *ACS Appl Mater Interfaces*, vol. 6, no. 24, pp. 22594–22601, Dec. 2014, doi: 10.1021/am506712c.

[39] Y.-K. Sun *et al.*, 'Nanostructured high-energy cathode materials for advanced lithium batteries', *Nat Mater*, vol. 11, no. 11, pp. 942–947, Nov. 2012, doi: 10.1038/nmat3435.

[40] D.-W. Jun, C. S. Yoon, U.-H. Kim, and Y.-K. Sun, 'High-Energy Density Core–Shell Structured Li[Ni $_{0.95}$ Co $_{0.025}$ Mn $_{0.025}$]O $_{2}$ Cathode for Lithium-Ion Batteries', *Chemistry of Materials*, vol. 29, no. 12, pp. 5048–5052, Jun. 2017, doi: 10.1021/acs.chemmater.7b01425.

[41] 'BMW iX3 to introduce Gen5 BMW eDrive technology; NMC-811 batteries - green Car Congress." '.

[42] P. LIMA, 'BMW iX3 gets a NCM 811 battery from CATL', Jul. 2020.

[43] A. K. Padhi, K. S. Nanjundaswamy, and J. B. Goodenough, 'Phospho-olivines as Positive-Electrode Materials for Rechargeable Lithium Batteries', *J Electrochem Soc*, vol. 144, no. 4, pp. 1188–1194, Apr. 1997, doi: 10.1149/1.1837571.

[44] D. H. Jang, Y. J. Shin, and S. M. Oh, 'Dissolution of Spinel Oxides and Capacity Losses in 4 V Li / Li x Mn2 O 4 Cells', *J Electrochem Soc*, vol. 143, no. 7, pp. 2204–2211, Jul. 1996, doi: 10.1149/1.1836981.

[45] N. J. Dudney, 'Solid-state thin-film rechargeable batteries', in *Materials Science and Engineering B: Solid-State Materials for Advanced Technology*, Feb. 2005, vol. 116, no. 3 SPEC.ISS., pp. 245–249. doi: 10.1016/j.mseb.2004.05.045.

[46] N. J. Dudney *et al.*, 'Nanocrystalline Li x Mn2 − y O 4 Cathodes for Solid-State Thin-Film Rechargeable Lithium Batteries', *J Electrochem Soc*, vol. 146, no. 7, pp. 2455–2464, Jul. 1999, doi: 10.1149/1.1391955.

[47] Y. Kobayashi, 'All-solid-state lithium secondary battery with ceramic/polymer composite electrolyte', *Solid State Ion*, vol. 152–153, pp. 137–142, Dec. 2002, doi: 10.1016/S0167-2738(02)00366-1.

[48] A. A. Delluva, J. Dudoff, G. Teeter, and A. Holewinski, 'Cathode Interface Compatibility of Amorphous LiMn $_{2}$ O $_{4}$ (LMO) and Li $_{7}$ La $_{3}$ Zr $_{2}$ O $_{12}$ (LLZO) Characterized with Thin-Film Solid-State Electrochemical Cells', *ACS Appl Mater Interfaces*, vol. 12, no. 22, pp. 24992–24999, Jun. 2020, doi: 10.1021/acsami.0c03519.

[49] A. Mauger and C. Julien, 'Nanoscience Supporting the Research on the Negative Electrodes of Li-Ion Batteries', *Nanomaterials*, vol. 5, no. 4, pp. 2279–2301, Dec. 2015, doi: 10.3390/nano5042279.

[50] A. Kato Yamahira, 'United States Patent', US5053297, 1991

[51] M. Winter, B. Jürgen O., Michael E. Spahr, and N. Peter, 'Insertion electrode materials for rechargeable lithium batteries', *Advanced materials*, vol. 10, no. 10, pp. 725-763., 1998.

[52] S. Chae, S. Choi, N. Kim, J. Sung, and J. Cho, 'Integration of Graphite and Silicon Anodes for the Commercialization of High-Energy Lithium-Ion Batteries', *Angewandte Chemie International Edition*, vol. 59, no. 1, pp. 110–135, Jan. 2020, doi: 10.1002/anie.201902085.

[53] T. Ohzuku, A. Ueda, and N. Yamamoto, 'Zero-Strain Insertion Material of Li [Li1 / 3Ti5 / 3] O 4 for Rechargeable Lithium Cells', *J Electrochem Soc*, vol. 142, no. 5, pp. 1431–1435, May 1995, doi: 10.1149/1.2048592.

[54] C. Han *et al.*, 'A review of gassing behavior in Li $_4$ Ti $_5$ O $_{12}$ -based lithium ion batteries', *J Mater Chem A Mater*, vol. 5, no. 14, pp. 6368–6381, 2017, doi: 10.1039/C7TA00303J.

[55] K.-C. Moeller, *Overview of battery systems*, vol. 3–10. Berlin, Heidelberg: Lithium-Ion Batteries: Basics and Applications, Sringer, 2018.

[56] C. Fang, X. Wang, and Y. S. Meng, 'Key Issues Hindering a Practical Lithium-Metal Anode', *Trends Chem*, vol. 1, no. 2, pp. 152–158, May 2019, doi: 10.1016/j.trechm.2019.02.015.

[57] H. Y.-P. Hong, 'Crystal structure and ionic conductivity of Li14Zn(GeO4)4 and other new Li+ superionic conductors', *Mater Res Bull*, vol. 13, no. 2, pp. 117–124, Feb. 1978, doi: 10.1016/0025-5408(78)90075-2.

[58] Y. Deng *et al.*, 'Structural and Mechanistic Insights into Fast Lithium-Ion Conduction in Li $_4$ SiO $_4$ –Li $_3$ PO $_4$ Solid Electrolytes', *J Am Chem Soc*, vol. 137, no. 28, pp. 9136–9145, Jul. 2015, doi: 10.1021/jacs.5b04444.

[59] Y. Deng *et al.*, 'Enhancing the Lithium Ion Conductivity in Lithium Superionic Conductor (LISICON) Solid Electrolytes through a Mixed Polyanion Effect', *ACS Appl Mater Interfaces*, vol. 9, no. 8, pp. 7050–7058, Mar. 2017, doi: 10.1021/acsami.6b14402.

[60] P. G. Bruce and A. R. West, 'Ion trapping and its effect on the conductivity of LISICON and other solid electrolytes', *J Solid State Chem*, vol. 53, no. 3, pp. 430–434, Jul. 1984, doi: 10.1016/0022-4596(84)90122-1.

[61] Y. Zhu, X. He, and Y. Mo, 'Origin of Outstanding Stability in the Lithium Solid Electrolyte Materials: Insights from Thermodynamic Analyses Based on First-Principles Calculations', *ACS Appl Mater Interfaces*, vol. 7, no. 42, pp. 23685–23693, Oct. 2015, doi: 10.1021/acsami.5b07517.

[62] V. Thangadurai and W. Weppner, 'Recent progress in solid oxide and lithium ion conducting electrolytes research', *Ionics (Kiel)*, vol. 12, no. 1, pp. 81–92, May 2006, doi: 10.1007/s11581-006-0013-7.

[63] T. Takahashi and H. Iwahara, 'Ionic conduction in perovskite-type oxide solid solution and its application to the solid electrolyte fuel cell', *Energy Conversion*, vol. 11, no. 3, pp. 105–111, Sep. 1971, doi: 10.1016/0013-7480(71)90121-5.

[64] X. XU, Z. WEN, X. YANG, J. ZHANG, and Z. GU, 'High lithium ion conductivity glass-ceramics in Li2O–Al2O3–TiO2–P2O5 from nanoscaled

glassy powders by mechanical milling', *Solid State Ion*, vol. 177, no. 26–32, pp. 2611–2615, Oct. 2006, doi: 10.1016/j.ssi.2006.04.010.

[65] B. Kumar, D. Thomas, and J. Kumar, 'Space-Charge-Mediated Superionic Transport in Lithium Ion Conducting Glass–Ceramics', *J Electrochem Soc*, vol. 156, no. 7, p. A506, 2009, doi: 10.1149/1.3122903.

[66] J. Wolfenstine, J. L. Allen, J. Sakamoto, D. J. Siegel, and H. Choe, 'Mechanical behavior of Li-ion-conducting crystalline oxide-based solid electrolytes: a brief review', *Ionics (Kiel)*, vol. 24, no. 5, pp. 1271–1276, May 2018, doi: 10.1007/s11581-017-2314-4.

[67] S. Xiong *et al.*, 'Design of a Multifunctional Interlayer for NASCION-Based Solid-State Li Metal Batteries', *Adv Funct Mater*, vol. 30, no. 22, p. 2001444, May 2020, doi: 10.1002/adfm.202001444.

[68] P. Hartmann *et al.*, 'Degradation of NASICON-Type Materials in Contact with Lithium Metal: Formation of Mixed Conducting Interphases (MCI) on Solid Electrolytes', *The Journal of Physical Chemistry C*, vol. 117, no. 41, pp. 21064–21074, Oct. 2013, doi: 10.1021/jp4051275.

[69] V. Thangadurai, S. Narayanan, and D. Pinzaru, 'Garnet-type solid-state fast Li ion conductors for Li batteries: critical review', *Chem Soc Rev*, vol. 43, no. 13, p. 4714, 2014, doi: 10.1039/c4cs00020j.

[70] V. Thangadurai, H. Kaack, and W. J. F. Weppner, 'Novel Fast Lithium Ion Conduction in Garnet-Type $Li_5La_3M_2O_{12}$ (M = Nb, Ta)', *Journal of the American Ceramic Society*, vol. 86, no. 3, pp. 437–440, Mar. 2003, doi: 10.1111/j.1151-2916.2003.tb03318.x.

[71] R. Murugan, V. Thangadurai, and W. Weppner, 'Fast Lithium Ion Conduction in Garnet-Type Li7La3Zr2O12', *Angewandte Chemie International Edition*, vol. 46, no. 41, pp. 7778–7781, Oct. 2007, doi: 10.1002/anie.200701144.

[72] L. Xu *et al.*, 'Garnet Solid Electrolyte for Advanced All-Solid-State Li Batteries', *Adv Energy Mater*, vol. 11, no. 2, p. 2000648, Jan. 2021, doi: 10.1002/aenm.202000648.

[73] S. Adams and R. P. Rao, 'Ion transport and phase transition in $Li_{7-x}La_3(Zr_{2-x}M_x)O_{12}$ (M = Ta^{5+}, Nb^{5+}, x = 0, 0.25)', *J. Mater. Chem.*, vol. 22, no. 4, pp. 1426–1434, 2012, doi: 10.1039/C1JM14588F.

[74] C. A. Geiger *et al.*, 'Crystal Chemistry and Stability of "$Li_7La_3Zr_2O_{12}$" Garnet: A Fast Lithium-Ion Conductor', *Inorg Chem*, vol. 50, no. 3, pp. 1089–1097, Feb. 2011, doi: 10.1021/ic101914e.

[75] A. Paolella *et al.*, 'Discovering the Influence of Lithium Loss on Garnet $Li_7La_3Zr_2O_{12}$ Electrolyte Phase Stability', *ACS Appl Energy Mater*, vol. 3, no. 4, pp. 3415–3424, Apr. 2020, doi: 10.1021/acsaem.9b02401.

[76] J. L. Allen, J. Wolfenstine, E. Rangasamy, and J. Sakamoto, 'Effect of substitution (Ta, Al, Ga) on the conductivity of Li7La3Zr2O12', *J Power*

Sources, vol. 206, pp. 315–319, May 2012, doi: 10.1016/j.jpowsour.2012.01.131.

[77] X. X. Pan, J. X. Wang, X. H. Chang, Y. D. Li, and W. B. Guan, 'A novel solid-liquid route for synthesizing cubic garnet Al-substituted Li7La3Zr2O12', *Solid State Ion*, vol. 317, pp. 1–6, Apr. 2018, doi: 10.1016/j.ssi.2017.12.034.

[78] C. Bernuy-Lopez, W. Manalastas, J. M. Lopez del Amo, A. Aguadero, F. Aguesse, and J. A. Kilner, 'Atmosphere Controlled Processing of Ga-Substituted Garnets for High Li-Ion Conductivity Ceramics', *Chemistry of Materials*, vol. 26, no. 12, pp. 3610–3617, Jun. 2014, doi: 10.1021/cm5008069.

[79] J.-F. Wu, W. K. Pang, V. K. Peterson, L. Wei, and X. Guo, 'Garnet-Type Fast Li-Ion Conductors with High Ionic Conductivities for All-Solid-State Batteries', *ACS Appl Mater Interfaces*, vol. 9, no. 14, pp. 12461–12468, Apr. 2017, doi: 10.1021/acsami.7b00614.

[80] J.-F. Wu *et al.*, 'Gallium-Doped $Li_7La_3Zr_2O_{12}$ Garnet-Type Electrolytes with High Lithium-Ion Conductivity', *ACS Appl Mater Interfaces*, vol. 9, no. 2, pp. 1542–1552, Jan. 2017, doi: 10.1021/acsami.6b13902.

[81] L. Buannic *et al.*, 'Dual Substitution Strategy to Enhance Li^+ Ionic Conductivity in $Li_7La_3Zr_2O_{12}$ Solid Electrolyte', *Chemistry of Materials*, vol. 29, no. 4, pp. 1769–1778, Feb. 2017, doi: 10.1021/acs.chemmater.6b05369.

[82] E. J. Cussen, 'Structure and ionic conductivity in lithium garnets', *J Mater Chem*, vol. 20, no. 25, p. 5167, 2010, doi: 10.1039/b925553b.

[83] L. Cheng *et al.*, 'Effect of Surface Microstructure on Electrochemical Performance of Garnet Solid Electrolytes', *ACS Appl Mater Interfaces*, vol. 7, no. 3, pp. 2073–2081, Jan. 2015, doi: 10.1021/am508111r.

[84] G. Larraz, A. Orera, and M. L. Sanjuán, 'Cubic phases of garnet-type Li7La3Zr2O12: the role of hydration', *J Mater Chem A Mater*, vol. 1, no. 37, p. 11419, 2013, doi: 10.1039/c3ta11996c.

[85] W. Xia *et al.*, 'Reaction mechanisms of lithium garnet pellets in ambient air: The effect of humidity and CO_2', *Journal of the American Ceramic Society*, vol. 100, no. 7, pp. 2832–2839, Jul. 2017, doi: 10.1111/jace.14865.

[86] D. Wang, C. Zhu, Y. Fu, X. Sun, and Y. Yang, 'Interfaces in Garnet-Based All-Solid-State Lithium Batteries', *Adv Energy Mater*, vol. 10, no. 39, p. 2001318, Oct. 2020, doi: 10.1002/aenm.202001318.

[87] J.-F. Wu *et al.*, 'In Situ Formed Shields Enabling Li_2CO_3-Free Solid Electrolytes: A New Route to Uncover the Intrinsic Lithiophilicity of Garnet Electrolytes for Dendrite-Free Li-Metal Batteries', *ACS Appl Mater Interfaces*, vol. 11, no. 1, pp. 898–905, Jan. 2019, doi: 10.1021/acsami.8b18356.

[88] J. B. Bates *et al.*, 'Fabrication and characterization of amorphous lithium electrolyte thin films and rechargeable thin-film batteries', *J Power Sources*, vol. 43, no. 1–3, pp. 103–110, Mar. 1993, doi: 10.1016/0378-7753(93)80106-Y.

[89] E. G. Herbert, W. E. Tenhaeff, N. J. Dudney, and G. M. Pharr, 'Mechanical characterization of LiPON films using nanoindentation', *Thin Solid Films*, vol. 520, no. 1, pp. 413–418, Oct. 2011, doi: 10.1016/j.tsf.2011.07.068.

[90] X. Yu, J. B. Bates, G. E. Jellison, and F. X. Hart, 'A stable thin-film lithium electrolyte: Lithium phosphorus oxynitride', *J Electrochem Soc*, vol. 144, no. 2, pp. 524–532, 1997, doi: 10.1149/1.1837443.

[91] A. Schwöbel, R. Hausbrand, and W. Jaegermann, 'Interface reactions between LiPON and lithium studied by in-situ X-ray photoemission', *Solid State Ion*, vol. 273, pp. 51–54, May 2015, doi: 10.1016/j.ssi.2014.10.017.

[92] P. López-Aranguren *et al.*, 'Crystalline LiPON as a Bulk-Type Solid Electrolyte', *ACS Energy Lett*, vol. 6, no. 2, pp. 445–450, Feb. 2021, doi: 10.1021/acsenergylett.0c02336.

[93] R. Mercier, J.-P. Malugani, B. Fahys, and G. Robert, 'Superionic conduction in Li 2 S - P 2 S 5 - LiI - glasses', *Solid State Ion*, vol. 5, pp. 663–666, Oct. 1981, doi: 10.1016/0167-2738(81)90341-6.

[94] M. KBALA, M. MAKYTA, A. LEVASSEUR, and P. HAGENMULLER, 'Characterization and electrical behavior of new lithium chalcoborate thin films', *Solid State Ion*, vol. 15, no. 2, pp. 163–169, Mar. 1985, doi: 10.1016/0167-2738(85)90096-7.

[95] S. Kondo, K. Takada, and Y. Yamamura, 'New lithium ion conductors based on Li2S-SiS2 system', *Solid State Ion*, vol. 53–56, pp. 1183–1186, Jul. 1992, doi: 10.1016/0167-2738(92)90310-L.

[96] F. Mizuno, A. Hayashi, K. Tadanaga, and M. Tatsumisago, 'New, Highly Ion-Conductive Crystals Precipitated from Li2S-P2S5 Glasses', *Advanced Materials*, vol. 17, no. 7, pp. 918–921, Apr. 2005, doi: 10.1002/adma.200401286.

[97] M. Tatsumisago, M. Nagao, and A. Hayashi, 'Recent development of sulfide solid electrolytes and interfacial modification for all-solid-state rechargeable lithium batteries', *Journal of Asian Ceramic Societies*, vol. 1, no. 1, pp. 17–25, Mar. 2013, doi: 10.1016/j.jascer.2013.03.005.

[98] A. Hayashi, K. Minami, S. Ujiie, and M. Tatsumisago, 'Preparation and ionic conductivity of Li7P3S11−z glass-ceramic electrolytes', *J Non Cryst Solids*, vol. 356, no. 44–49, pp. 2670–2673, Oct. 2010, doi: 10.1016/j.jnoncrysol.2010.04.048.

[99] A. Kato, M. Nose, M. Yamamoto, A. Sakuda, A. Hayashi, and M. Tatsumisago, 'Mechanical properties of sulfide glasses in all-solid-state batteries', *Journal of the Ceramic Society of Japan*, vol. 126, no. 9, pp. 719–727, Sep. 2018, doi: 10.2109/jcersj2.18022.

[100] A. Sakuda, A. Hayashi, and M. Tatsumisago, 'Recent progress on interface formation in all-solid-state batteries', *Curr Opin Electrochem*, vol. 6, no. 1, pp. 108–114, Dec. 2017, doi: 10.1016/j.coelec.2017.10.008.

[101] Y. Seino, T. Ota, K. Takada, A. Hayashi, and M. Tatsumisago, 'A sulphide lithium super ion conductor is superior to liquid ion conductors for use in rechargeable batteries', *Energy Environ. Sci.*, vol. 7, no. 2, pp. 627–631, 2014, doi: 10.1039/C3EE41655K.

[102] R. Kanno, T. Hata, Y. Kawamoto, and M. Irie, 'Synthesis of a new lithium ionic conductor, thio-LISICON–lithium germanium sulfide system', *Solid State Ion*, vol. 130, no. 1–2, pp. 97–104, May 2000, doi: 10.1016/S0167-2738(00)00277-0.

[103] M. Murayama *et al.*, 'Synthesis of New Lithium Ionic Conductor Thio-LISICON—Lithium Silicon Sulfides System', *J Solid State Chem*, vol. 168, no. 1, pp. 140–148, Oct. 2002, doi: 10.1006/jssc.2002.9701.

[104] R. Kanno and M. Murayama, 'Lithium Ionic Conductor Thio-LISICON: The Li[sub 2]S-GeS[sub 2]-P[sub 2]S[sub 5] System', *J Electrochem Soc*, vol. 148, no. 7, p. A742, 2001, doi: 10.1149/1.1379028.

[105] G. Sahu, Z. Lin, J. Li, Z. Liu, N. Dudney, and C. Liang, 'Air-stable, high-conduction solid electrolytes of arsenic-substituted Li $_4$ SnS $_4$', *Energy Environ. Sci.*, vol. 7, no. 3, pp. 1053–1058, 2014, doi: 10.1039/C3EE43357A.

[106] D. Lin, Y. Liu, and Y. Cui, 'Reviving the lithium metal anode for high-energy batteries', *Nat Nanotechnol*, vol. 12, no. 3, pp. 194–206, Mar. 2017, doi: 10.1038/nnano.2017.16.

[107] Y. Kato *et al.*, 'High-power all-solid-state batteries using sulfide superionic conductors', *Nat Energy*, vol. 1, no. 4, p. 16030, Mar. 2016, doi: 10.1038/nenergy.2016.30.

[108] Z.-Q. Wang, M. Wu, G. Liu, X. L. Lei, B. Xu, and C. Ouyang, 'Elastic Properties of New Solid State Electrolyte Material Li10GeP2S12: A Study from First-Principles Calculation', *Int. J. Electrochem. Sci* , vol. 9, no. 2, pp. 562–568, Feb. 2014.

[109] H.-J. Deiseroth *et al.*, 'Li6PS5X: A Class of Crystalline Li-Rich Solids With an Unusually High Li+ Mobility', *Angewandte Chemie International Edition*, vol. 47, no. 4, pp. 755–758, Jan. 2008, doi: 10.1002/anie.200703900.

[110] L. Zhou, A. Assoud, Q. Zhang, X. Wu, and L. F. Nazar, 'New Family of Argyrodite Thioantimonate Lithium Superionic Conductors', *J Am Chem Soc*, vol. 141, no. 48, pp. 19002–19013, Dec. 2019, doi: 10.1021/jacs.9b08357.

[111] H. Muramatsu, A. Hayashi, T. Ohtomo, S. Hama, and M. Tatsumisago, 'Structural change of Li2S–P2S5 sulfide solid electrolytes in the atmosphere', *Solid State Ion*, vol. 182, no. 1, pp. 116–119, Feb. 2011, doi: 10.1016/j.ssi.2010.10.013.

[112] Y. S. Jung, D. Y. Oh, Y. J. Nam, and K. H. Park, 'Issues and Challenges for Bulk-Type All-Solid-State Rechargeable Lithium Batteries using Sulfide Solid Electrolytes', *Isr J Chem*, vol. 55, no. 5, pp. 472–485, May 2015, doi: 10.1002/ijch.201400112.

[113] F. Han, Y. Zhu, X. He, Y. Mo, and C. Wang, 'Electrochemical Stability of Li $_{10}$ GeP $_{2}$ S $_{12}$ and Li $_{7}$ La $_{3}$ Zr $_{2}$ O $_{12}$ Solid Electrolytes', *Adv Energy Mater*, vol. 6, no. 8, p. 1501590, Apr. 2016, doi: 10.1002/aenm.201501590.

[114] B. R. Shin, Y. J. Nam, D. Y. Oh, D. H. Kim, J. W. Kim, and Y. S. Jung, 'Comparative Study of TiS 2 /Li-In All-Solid-State Lithium Batteries Using Glass-Ceramic Li 3 PS 4 and Li 10 GeP 2 S 12 Solid Electrolytes', *Electrochim Acta*, vol. 146, pp. 395–402, Nov. 2014, doi: 10.1016/j.electacta.2014.08.139.

[115] Y. Mo, S. P. Ong, and G. Ceder, 'First Principles Study of the Li $_{10}$ GeP $_{2}$ S $_{12}$ Lithium Super Ionic Conductor Material', *Chemistry of Materials*, vol. 24, no. 1, pp. 15–17, Jan. 2012, doi: 10.1021/cm203303y.

[116] F. Han, T. Gao, Y. Zhu, K. J. Gaskell, and C. Wang, 'A Battery Made from a Single Material', *Advanced Materials*, vol. 27, no. 23, pp. 3473–3483, Jun. 2015, doi: 10.1002/adma.201500180.

[117] S. Wenzel *et al.*, 'Direct Observation of the Interfacial Instability of the Fast Ionic Conductor Li $_{10}$ GeP $_{2}$ S $_{12}$ at the Lithium Metal Anode', *Chemistry of Materials*, vol. 28, no. 7, pp. 2400–2407, Apr. 2016, doi: 10.1021/acs.chemmater.6b00610.

[118] H. Eickhoff *et al.*, 'Lithium Phosphidogermanates α- and β-Li $_{8}$ GeP $_{4}$ —A Novel Compound Class with Mixed Li $^{+}$ Ionic and Electronic Conductivity', *Chemistry of Materials*, vol. 30, no. 18, pp. 6440–6448, Sep. 2018, doi: 10.1021/acs.chemmater.8b02759.

[119] S. Strangmüller *et al.*, 'Fast Ionic Conductivity in the Most Lithium-Rich Phosphidosilicate Li $_{14}$ SiP $_{6}$', *J Am Chem Soc*, vol. 141, no. 36, pp. 14200–14209, Sep. 2019, doi: 10.1021/jacs.9b05301.

[120] T. M. F. Restle *et al.*, 'Fast Lithium Ion Conduction in Lithium Phosphidoaluminates', *Angewandte Chemie*, vol. 132, no. 14, pp. 5714–5723, Mar. 2020, doi: 10.1002/ange.201914613.

[121] T. Asano, A. Sakai, S. Ouchi, M. Sakaida, A. Miyazaki, and S. Hasegawa, 'Solid Halide Electrolytes with High Lithium-Ion Conductivity for Application in 4 V Class Bulk-Type All-Solid-State Batteries', *Advanced Materials*, vol. 30, no. 44, p. 1803075, Nov. 2018, doi: 10.1002/adma.201803075.

[122] J. Liang, X. Li, K. R. Adair, and X. Sun, 'Metal Halide Superionic Conductors for All-Solid-State Batteries', *Acc Chem Res*, vol. 54, no. 4, pp. 1023–1033, Feb. 2021, doi: 10.1021/acs.accounts.0c00762.

[123] L. Zhou *et al.*, 'High areal capacity, long cycle life 4 V ceramic all-solid-state Li-ion batteries enabled by chloride solid electrolytes', *Nat Energy*, vol. 7, no. 1, pp. 83–93, Jan. 2022, doi: 10.1038/s41560-021-00952-0.

[124] D. C. Ginnings and T. E. Phipps, 'TEMPERATURE-CONDUCTANCE CURVES OF SOLID SALTS. III. HALIDES OF LITHIUM', *J Am Chem Soc*, vol. 52, no. 4, pp. 1340–1345, Apr. 1930, doi: 10.1021/ja01367a006.

[125] Z. Liu, S. Ma, J. Liu, S. Xiong, Y. Ma, and H. Chen, 'High Ionic Conductivity Achieved in Li $_3$ Y(Br $_3$ Cl $_3$) Mixed Halide Solid Electrolyte via Promoted Diffusion Pathways and Enhanced Grain Boundary', *ACS Energy Lett*, vol. 6, no. 1, pp. 298–304, Jan. 2021, doi: 10.1021/acsenergylett.0c01690.

[126] X. Li *et al.*, 'Air-stable Li $_3$ InCl $_6$ electrolyte with high voltage compatibility for all-solid-state batteries', *Energy Environ Sci*, vol. 12, no. 9, pp. 2665–2671, 2019, doi: 10.1039/C9EE02311A.

[127] X. Li *et al.*, 'Progress and perspectives on halide lithium conductors for all-solid-state lithium batteries', *Energy Environ Sci*, vol. 13, no. 5, pp. 1429–1461, 2020, doi: 10.1039/C9EE03828K.

[128] C. Wang, J. Liang, J. T. Kim, and X. Sun, 'Prospects of halide-based all-solid-state batteries: From material design to practical application', *Sci Adv*, vol. 8, no. 36, Sep. 2022, doi: 10.1126/sciadv.adc9516.

[129] Y. Liu *et al.*, 'Stabilizing the Interface of NASICON Solid Electrolyte against Li Metal with Atomic Layer Deposition', 2018, doi: 10.1021/acsami.8b06366.

[130] Z. Yang *et al.*, 'Facile interfacial adhesion enabled LATP-based solid-state lithium metal battery', *Chemical Engineering Journal*, vol. 392, p. 123650, Jul. 2020, doi: 10.1016/j.cej.2019.123650.

[131] L. Li *et al.*, 'Enhancing the interface stability of Li1.3Al0.3Ti1.7(PO4)3 and lithium metal by amorphous Li1.5Al0.5Ge1.5(PO4)3 modification', *Ionics (Kiel)*, vol. 26, no. 8, pp. 3815–3821, Aug. 2020, doi: 10.1007/s11581-020-03503-x.

[132] Z. Chen *et al.*, 'Highly Stable Quasi-Solid-State Lithium Metal Batteries: Reinforced Li $_{1.3}$ Al $_{0.3}$ Ti $_{1.7}$ (PO $_4$) $_3$ /Li Interface by a Protection Interlayer', *Adv Energy Mater*, vol. 11, no. 30, p. 2101339, Aug. 2021, doi: 10.1002/aenm.202101339.

[133] Q. Cheng *et al.*, 'Stabilizing Solid Electrolyte-Anode Interface in Li-Metal Batteries by Boron Nitride-Based Nanocomposite Coating', *Joule*, vol. 3, no. 6, pp. 1510–1522, Jun. 2019, doi: 10.1016/j.joule.2019.03.022.

[134] 'https://alum.kuleuven.be/alumni-ingenieurs/nieuws-activiteiten/activiteiten/forumavonden/forumavonden-2017-2018/batterijen/forumavond-batterijen-thomas-leysen.pdf'.

[135] N. Boaretto *et al.*, 'Lithium solid-state batteries: State-of-the-art and challenges for materials, interfaces and processing', *J Power Sources*, vol. 502, p. 229919, Aug. 2021, doi: 10.1016/J.JPOWSOUR.2021.229919.

[136] T. Chartier and A. Bruneau, 'Aqueous tape casting of alumina substrates', *J Eur Ceram Soc*, vol. 12, no. 4, pp. 243–247, Jan. 1993, doi: 10.1016/0955-2219(93)90098-C.

[137] D. Hotza and P. Greil, 'Review: aqueous tape casting of ceramic powders', *Materials Science and Engineering: A*, vol. 202, no. 1–2, pp. 206–217, Nov. 1995, doi: 10.1016/0921-5093(95)09785-6.

[138] L. Wang, G. Tang, and Z.-K. Xu, 'Preparation and electrical properties of multilayer ZnO varistors with water-based tape casting', *Ceram Int*, vol. 35, no. 1, pp. 487–492, Jan. 2009, doi: 10.1016/j.ceramint.2008.01.011.

[139] J. Marie, J. Bourret, P.-M. Geffroy, A. Smith, V. Chaleix, and T. Chartier, 'Eco-friendly alumina suspensions for tape-casting process', *J Eur Ceram Soc*, vol. 37, no. 16, pp. 5239–5248, Dec. 2017, doi: 10.1016/j.jeurceramsoc.2017.04.033.

[140] R. K. Nishihora, P. L. Rachadel, M. G. N. Quadri, and D. Hotza, 'Manufacturing porous ceramic materials by tape casting—A review', *J Eur Ceram Soc*, vol. 38, no. 4, pp. 988–1001, Apr. 2018, doi: 10.1016/j.jeurceramsoc.2017.11.047.

[141] D. Hotza, R. K. Nishihora, R. A. F. Machado, P. Geffroy, T. Chartier, and S. Bernard, 'Tape casting of preceramic polymers toward advanced ceramics: A review', *International Journal of Ceramic Engineering & Science*, vol. 1, no. 1, pp. 21–41, May 2019, doi: 10.1002/ces2.10009.

[142] D. Y. Oh, D. H. Kim, S. H. Jung, J.-G. Han, N.-S. Choi, and Y. S. Jung, 'Single-step wet-chemical fabrication of sheet-type electrodes from solid-electrolyte precursors for all-solid-state lithium-ion batteries', *J. Mater. Chem. A*, vol. 5, no. 39, pp. 20771–20779, 2017, doi: 10.1039/C7TA06873E.

[143] G. Piana, F. Bella, F. Geobaldo, G. Meligrana, and C. Gerbaldi, 'PEO/LAGP hybrid solid polymer electrolytes for ambient temperature lithium batteries by solvent-free, "one pot" preparation', *J Energy Storage*, vol. 26, p. 100947, Dec. 2019, doi: 10.1016/j.est.2019.100947.

[144] Á. Miguel, F. González, V. Gregorio, N. García, and P. Tiemblo, 'Solvent-Free Procedure for the Preparation under Controlled Atmosphere Conditions of Phase-Segregated Thermoplastic Polymer Electrolytes', *Polymers (Basel)*, vol. 11, no. 3, p. 406, Mar. 2019, doi: 10.3390/polym11030406.

[145] P.-A. Lavoie, R. Laliberté, J. Dubé, and Y. Gagnon, 'Co-extrusion manufacturing process of thin film electrochemical cell for lithium polymer batteries and apparatus therefor', 7,700,019, Apr. 20, 2010

[146] K.-H. Choi, D. B. Ahn, and S.-Y. Lee, 'Current Status and Challenges in Printed Batteries: Toward Form Factor-Free, Monolithic Integrated Power Sources', *ACS Energy Lett*, vol. 3, no. 1, pp. 220–236, Jan. 2018, doi: 10.1021/acsenergylett.7b01086.

[147] C. M. Costa, R. Gonçalves, and S. Lanceros-Méndez, 'Recent advances and future challenges in printed batteries', *Energy Storage Mater*, vol. 28, pp. 216–234, Jun. 2020, doi: 10.1016/j.ensm.2020.03.012.

[148] S. Yu, A. Mertens, H. Tempel, R. Schierholz, H. Kungl, and R.-A. Eichel, 'Monolithic All-Phosphate Solid-State Lithium-Ion Battery with Improved Interfacial Compatibility', *ACS Appl Mater Interfaces*, vol. 10, no. 26, pp. 22264–22277, Jul. 2018, doi: 10.1021/acsami.8b05902.

[149] S. Zekoll *et al.*, 'Hybrid electrolytes with 3D bicontinuous ordered ceramic and polymer microchannels for all-solid-state batteries', *Energy Environ Sci*, vol. 11, no. 1, pp. 185–201, 2018, doi: 10.1039/C7EE02723K.

[150] D. W. McOwen *et al.*, '3D-Printing Electrolytes for Solid-State Batteries', *Advanced Materials*, vol. 30, no. 18, p. 1707132, May 2018, doi: 10.1002/adma.201707132.

[151] J. Bates, 'Thin-film lithium and lithium-ion batteries', *Solid State Ion*, vol. 135, no. 1–4, pp. 33–45, Nov. 2000, doi: 10.1016/S0167-2738(00)00327-1.

[152] C. M. Julien and A. Mauger, 'Pulsed Laser Deposited Films for Microbatteries', *Coatings*, vol. 9, no. 6, p. 386, Jun. 2019, doi: 10.3390/coatings9060386.

[153] A. Rambabu, S. B. Krupanidhi, and P. Barpanda, 'An Overview of Nanostructured Li-based Thin Film Micro-batteries', *Proceedings of the Indian National Science Academy*, vol. 98, no. 0, Aug. 2018, doi: 10.16943/ptinsa/2018/49472.

[154] R. Xu *et al.*, 'Artificial Interphases for Highly Stable Lithium Metal Anode', *Matter*, vol. 1, no. 2, pp. 317–344, Aug. 2019, doi: 10.1016/j.matt.2019.05.016.

[155] J. BATES, 'Electrical properties of amorphous lithium electrolyte thin films', *Solid State Ion*, vol. 53–56, pp. 647–654, Jul. 1992, doi: 10.1016/0167-2738(92)90442-R.

[156] R. Pfenninger, M. Struzik, I. Garbayo, E. Stilp, and J. L. M. Rupp, 'A low ride on processing temperature for fast lithium conduction in garnet solid-state battery films', *Nat Energy*, vol. 4, no. 6, pp. 475–483, May 2019, doi: 10.1038/s41560-019-0384-4.

[157] F. Aguesse *et al.*, 'Microstructure and ionic conductivity of LLTO thin films: Influence of different substrates and excess lithium in the target', *Solid State Ion*, vol. 272, no. 0, pp. 1–8, 2015, doi: http://dx.doi.org/10.1016/j.ssi.2014.12.005.

[158] Z. Fan *et al.*, 'Solid/Solid Interfacial Architecturing of Solid Polymer Electrolyte–Based All-Solid-State Lithium–Sulfur Batteries by Atomic Layer Deposition', *Small*, vol. 15, no. 46, p. 1903952, Nov. 2019, doi: 10.1002/smll.201903952.

[159] C.-L. Tsai *et al.*, 'Li 7 La 3 Zr 2 O 12 Interface Modification for Li Dendrite Prevention', *ACS Appl Mater Interfaces*, vol. 8, no. 16, pp. 10617–10626, Apr. 2016, doi: 10.1021/acsami.6b00831.

[160] J. Wakasugi, H. Munakata, and K. Kanamura, ' Effect of Gold Layer on Interface Resistance between Lithium Metal Anode and Li 6.25 Al 0.25 La 3 Zr 2 O 12 Solid Electrolyte ', *J Electrochem Soc*, vol. 164, no. 6, pp. A1022–A1025, Jan. 2017, doi: 10.1149/2.0471706jes.

[161] K. K. Fu *et al.*, 'Transient Behavior of the Metal Interface in Lithium Metal–Garnet Batteries', *Angewandte Chemie - International Edition*, vol. 56, no. 47, pp. 14942–14947, Nov. 2017, doi: 10.1002/anie.201708637.

[162] L. Wang *et al.*, 'Long lifespan lithium metal anodes enabled by Al2O3 sputter coating', *Energy Storage Mater*, vol. 10, pp. 16–23, Jan. 2018, doi: 10.1016/J.ENSM.2017.08.001.

[163] M. Rawlence *et al.*, 'Effect of Gallium Substitution on Lithium-Ion Conductivity and Phase Evolution in Sputtered Li 7–3 x Ga x La 3 Zr 2 O 12 Thin Films', *ACS Appl Mater Interfaces*, vol. 10, no. 16, pp. 13720–13728, Apr. 2018, doi: 10.1021/acsami.8b03163.

[164] L. Indrizzi, N. Ohannessian, D. Pergolesi, T. Lippert, and E. Gilardi, 'Pulsed Laser Deposition as a Tool for the Development of All Solid-State Microbatteries', *Helv Chim Acta*, vol. 104, no. 2, Feb. 2021, doi: 10.1002/hlca.202000203.

[165] K. (Kelvin) Fu *et al.*, 'Toward garnet electrolyte–based Li metal batteries: An ultrathin, highly effective, artificial solid-state electrolyte/metallic Li interface', *Sci Adv*, vol. 3, no. 4, p. e1601659, Apr. 2017, doi: 10.1126/sciadv.1601659.

[166] M. NAGAO, A. HAYASHI, and M. TATSUMISAGO, 'Bulk-Type Lithium Metal Secondary Battery with Indium Thin Layer at Interface between Li Electrode and Li2S-P2S5 Solid Electrolyte', *Electrochemistry*, vol. 80, no. 10, pp. 734–736, 2012, doi: 10.5796/electrochemistry.80.734.

[167] H. C. M. Knoops, M. E. Donders, M. C. M. van de Sanden, P. H. L. Notten, and W. M. M. Kessels, 'Atomic layer deposition for nanostructured Li-ion batteries', *Journal of Vacuum Science & Technology A: Vacuum, Surfaces, and Films*, vol. 30, no. 1, p. 010801, Jan. 2012, doi: 10.1116/1.3660699.

[168] J. Liu *et al.*, 'Rational Design of Atomic-Layer-Deposited LiFePO 4 as a High-Performance Cathode for Lithium-Ion Batteries', *Advanced Materials*, vol. 26, no. 37, pp. 6472–6477, Oct. 2014, doi: 10.1002/adma.201401805.

[169] G. Wang *et al.*, 'Toward ultrafast lithium ion capacitors: A novel atomic layer deposition seeded preparation of Li4Ti5O12/graphene anode', *Nano Energy*, vol. 36, pp. 46–57, Jun. 2017, doi: 10.1016/j.nanoen.2017.04.020.

[170] M. Nisula, Y. Shindo, H. Koga, and M. Karppinen, 'Atomic Layer Deposition of Lithium Phosphorus Oxynitride', *Chemistry of Materials*, vol. 27, no. 20, pp. 6987–6993, Oct. 2015, doi: 10.1021/acs.chemmater.5b02199.

[171] A. C. Kozen, A. J. Pearse, C. F. Lin, M. Noked, and G. W. Rubloff, 'Atomic Layer Deposition of the Solid Electrolyte LiPON', *Chemistry of Materials*, vol. 27, no. 15, pp. 5324–5331, Jul. 2015, doi: 10.1021/acs.chemmater.5b01654.

[172] E. Kazyak *et al.*, 'Atomic Layer Deposition of the Solid Electrolyte Garnet Li 7 La 3 Zr 2 O 12', *Chemistry of Materials*, vol. 29, no. 8, pp. 3785–3792, Apr. 2017, doi: 10.1021/acs.chemmater.7b00944.

[173] H. Liu, X. Cheng, Y. Chong, H. Yuan, J.-Q. Huang, and Q. Zhang, 'Advanced electrode processing of lithium ion batteries: A review of powder technology in battery fabrication', *Particuology*, vol. 57, pp. 56–71, Aug. 2021, doi: 10.1016/j.partic.2020.12.003.

[174] Z. Lyu *et al.*, 'Design and Manufacture of 3D-Printed Batteries', *Joule*, vol. 5, no. 1, pp. 89–114, Jan. 2021, doi: 10.1016/j.joule.2020.11.010.

[175] 'https://emsliegroup.mcmaster.ca/orf-re/ald'.

[176] H. A. Kuhn and B. L. Ferguson, 'Pseudo-Isostatic Powder Metallurgy Densification Process', Feb. 1983. doi: 10.4271/830362.

[177] S. Hans, 'Cold-pressing process and apparatus', 3,280,613, Oct. 25, 1966

[178] C. Meyer, H. Bockholt, W. Haselrieder, and A. Kwade, 'Characterization of the calendering process for compaction of electrodes for lithium-ion batteries', *J Mater Process Technol*, vol. 249, pp. 172–178, Nov. 2017, doi: 10.1016/j.jmatprotec.2017.05.031.

[179] G. B. Appetecchi, J. Hassoun, B. Scrosati, F. Croce, F. Cassel, and M. Salomon, 'Hot-pressed, solvent-free, nanocomposite, PEO-based electrolyte membranes', *J Power Sources*, vol. 124, no. 1, pp. 246–253, Oct. 2003, doi: 10.1016/S0378-7753(03)00611-6.

[180] T. Okumura *et al.*, 'LISICON-Based Amorphous Oxide for Bulk-Type All-Solid-State Lithium-Ion Battery', *ACS Appl Energy Mater*, vol. 3, no. 4, pp. 3220–3229, Apr. 2020, doi: 10.1021/acsaem.9b01949.

[181] X. Kuang, G. Carotenuto, and L. Nicolais, 'A Review of Ceramic Sintering and Suggestions on Reducing Sintering Temperatures', *Advanced Performance Materials 1997 4:3*, vol. 4, no. 3, pp. 257–274, Jul. 1997, doi: 10.1023/A:1008621020555.

[182] L. Miara *et al.*, 'About the Compatibility between High Voltage Spinel Cathode Materials and Solid Oxide Electrolytes as a Function of Temperature', *ACS Appl Mater Interfaces*, vol. 8, no. 40, pp. 26842–26850, Oct. 2016, doi: 10.1021/ACSAMI.6B09059/SUPPL_FILE/AM6B09059_SI_001.PDF.

[183] J. L. Allen, J. Wolfenstine, E. Rangasamy, and J. Sakamoto, 'Effect of substitution (Ta, Al, Ga) on the conductivity of Li7La3Zr2O12', *J Power Sources*, vol. 206, pp. 315–319, May 2012, doi: 10.1016/J.JPOWSOUR.2012.01.131.

[184] A. Paolella *et al.*, 'Toward an All-Ceramic Cathode–Electrolyte Interface with Low-Temperature Pressed NASICON Li1.5Al0.5Ge1.5(PO4)3 Electrolyte', *Adv Mater Interfaces*, vol. 7, no. 12, p. 2000164, Jun. 2020, doi: 10.1002/ADMI.202000164.

[185] Y. Suzuki *et al.*, 'Transparent cubic garnet-type solid electrolyte of Al2O3-doped Li7La3Zr2O12', *Solid State Ion*, vol. 278, pp. 172–176, Oct. 2015, doi: 10.1016/J.SSI.2015.06.009.

[186] I. Lisenker and C. R. Stoldt, 'Improving NASICON sinterability through crystallization under high-frequency electrical fields', *Front Energy Res*, vol. 4, no. MAR, p. 13, 2016, doi: 10.3389/FENRG.2016.00013/BIBTEX.

[187] M. Oghbaei and O. Mirzaee, 'Microwave versus conventional sintering: A review of fundamentals, advantages and applications', *J Alloys Compd*, vol. 494, no. 1–2, pp. 175–189, Apr. 2010, doi: 10.1016/J.JALLCOM.2010.01.068.

[188] L. Hallopeau *et al.*, 'Microwave-assisted reactive sintering and lithium ion conductivity of Li1.3Al0.3Ti1.7(PO4)3 solid electrolyte', *J Power Sources*, vol. 378, pp. 48–52, Feb. 2018, doi: 10.1016/J.JPOWSOUR.2017.12.021.

[189] H. X. Geng, A. Mei, C. Dong, Y. H. Lin, and C. W. Nan, 'Investigation of structure and electrical properties of Li0.5La0.5TiO3 ceramics via microwave sintering', *J Alloys Compd*, vol. 481, no. 1–2, pp. 555–558, Jul. 2009, doi: 10.1016/J.JALLCOM.2009.03.038.

[190] J. P. Maria *et al.*, 'Cold sintering: Current status and prospects', *J Mater Res*, vol. 32, no. 17, pp. 3205–3218, Sep. 2017, doi: 10.1557/JMR.2017.262/FIGURES/10.

[191] H. Guo, A. Baker, J. Guo, and C. A. Randall, 'Cold Sintering Process: A Novel Technique for Low-Temperature Ceramic Processing of Ferroelectrics', *Journal of the American Ceramic Society*, vol. 99, no. 11, pp. 3489–3507, Nov. 2016, doi: 10.1111/JACE.14554.

[192] S. W. Baek, J. M. Lee, T. Y. Kim, M. S. Song, and Y. Park, 'Garnet related lithium ion conductor processed by spark plasma sintering for all solid state batteries', *J Power Sources*, vol. 249, pp. 197–206, Mar. 2014, doi: 10.1016/J.JPOWSOUR.2013.10.089.

[193] E. C. Bucharsky, K. G. Schell, A. Hintennach, and M. J. Hoffmann, 'Preparation and characterization of sol–gel derived high lithium ion conductive NZP-type ceramics Li1 + x AlxTi2 − x(PO4)3', *Solid State Ion*, vol. 274, pp. 77–82, Jun. 2015, doi: 10.1016/J.SSI.2015.03.009.

[194] T. Okumura *et al.*, 'LISICON-Based Amorphous Oxide for Bulk-Type All-Solid-State Lithium-Ion Battery', *ACS Appl Energy Mater*, vol. 3, no. 4, pp. 3220–3229, Apr. 2020, doi: 10.1021/ACSAEM.9B01949/SUPPL_FILE/AE9B01949_SI_001.PDF.

[195] A. Aboulaich *et al.*, 'A New Approach to Develop Safe All-Inorganic Monolithic Li-Ion Batteries', *Adv Energy Mater*, vol. 1, no. 2, pp. 179–183, Mar. 2011, doi: 10.1002/AENM.201000050.

[196] X. Wei, J. Rechtin, and E. A. Olevsky, 'The Fabrication of All-Solid-State Lithium-Ion Batteries via Spark Plasma Sintering', *Metals 2017, Vol. 7, Page 372*, vol. 7, no. 9, p. 372, Sep. 2017, doi: 10.3390/MET7090372.

[197] A. M. Laptev, H. Zheng, M. Bram, M. Finsterbusch, and O. Guillon, 'High-pressure field assisted sintering of half-cell for all-solid-state battery', *Mater Lett*, vol. 247, pp. 155–158, Jul. 2019, doi: 10.1016/J.MATLET.2019.03.109.

[198] S. S. Berbano, J. Guo, H. Guo, M. T. Lanagan, and C. A. Randall, 'Cold sintering process of Li1.5Al0.5Ge1.5(PO4)3 solid electrolyte', *Journal of the*

American Ceramic Society, vol. 100, no. 5, pp. 2123–2135, May 2017, doi: 10.1111/JACE.14727.

[199] M. Vinnichenko *et al.*, 'Li-Ion Conductive Li1.3Al0.3Ti1.7(PO4)3 (LATP) Solid Electrolyte Prepared by Cold Sintering Process with Various Sintering Additives', *Nanomaterials*, vol. 12, no. 18, p. 3178, Sep. 2022, doi: 10.3390/nano12183178.

[200] H. Nakaya, M. Iwasaki, and C. A. Randall, 'Thermal-assisted cold sintering study of a lithium electrolyte: Li13.9Sr0.1Zn(GeO4)4', *J Electroceram*, vol. 44, no. 1–2, pp. 16–22, Apr. 2020, doi: 10.1007/S10832-019-00196-1/TABLES/3.

[201] J. H. Seo *et al.*, 'Cold sintering of a Li-ion cathode: LiFePO4-composite with high volumetric capacity', *Ceram Int*, vol. 43, no. 17, pp. 15370–15374, Dec. 2017, doi: 10.1016/J.CERAMINT.2017.08.077.

[202] J. H. Seo, K. Verlinde, R. Rajagopalan, E. D. Gomez, T. E. Mallouk, and C. A. Randall, 'Cold sintering process for fabrication of a high volumetric capacity Li4Ti5O12 anode', *Materials Science and Engineering: B*, vol. 250, p. 114435, Nov. 2019, doi: 10.1016/J.MSEB.2019.114435.

[203] Y. Huang, Y. Jiang, Y. Zhou, Z. Hu, and X. Zhu, 'Influence of Liquid Solutions on the Ionic Conductivity of $Li_{1.3}Al_{0.3}Ti_{1.7}(PO_4)_3$ Solid Electrolytes', *ChemElectroChem*, vol. 6, no. 24, pp. 6016–6026, Dec. 2019, doi: 10.1002/celc.201901687.

[204] J.-H. Seo *et al.*, 'Cold sintering, enabling a route to co-sinter an all-solid-state lithium-ion battery', *Jpn J Appl Phys*, vol. 60, no. 3, p. 037001, Mar. 2021, doi: 10.35848/1347-4065/abdd4c.

[205] P. Jiang *et al.*, 'Solid-state Li metal battery enabled by cold sintering at 120 °C', *Materials Today Physics*, vol. 20, p. 100476, Sep. 2021, doi: 10.1016/j.mtphys.2021.100476.

[206] E. Yi *et al.*, 'All-Solid-State Batteries Using Rationally Designed Garnet Electrolyte Frameworks', *ACS Appl Energy Mater*, vol. 3, no. 1, pp. 170–175, Jan. 2020, doi: 10.1021/acsaem.9b02101.

[207] Y. Xiao, L. J. Miara, Y. Wang, and G. Ceder, 'Computational Screening of Cathode Coatings for Solid-State Batteries', *Joule*, vol. 3, no. 5, pp. 1252–1275, May 2019, doi: 10.1016/j.joule.2019.02.006.

[208] Y. Tian *et al.*, 'Compatibility issues between electrodes and electrolytes in solid-state batteries', *Energy Environ Sci*, vol. 10, no. 5, pp. 1150–1166, 2017, doi: 10.1039/C7EE00534B.

[209] S. Kaboli *et al.*, 'Behavior of Solid Electrolyte in Li-Polymer Battery with NMC Cathode via in-Situ Scanning Electron Microscopy', *Nano Lett*, vol. 20, no. 3, pp. 1607–1613, Mar. 2020, doi: 10.1021/acs.nanolett.9b04452.

[210] K. Nie *et al.*, 'Increasing Poly(ethylene oxide) Stability to 4.5 V by Surface Coating of the Cathode', *ACS Energy Lett*, vol. 5, no. 3, pp. 826–832, Mar. 2020, doi: 10.1021/acsenergylett.9b02739.

[211] H. Visbal, S. Fujiki, Y. Aihara, T. Watanabe, Y. Park, and S. Doo, 'The influence of the carbonate species on LiNi0.8Co0.15Al0.05O2 surfaces for all-solid-state lithium ion battery performance', *J Power Sources*, vol. 269, pp. 396–402, Dec. 2014, doi: 10.1016/j.jpowsour.2014.07.021.

[212] Y. Xiao, Y. Wang, S.-H. Bo, J. C. Kim, L. J. Miara, and G. Ceder, 'Understanding interface stability in solid-state batteries', *Nat Rev Mater*, vol. 5, no. 2, pp. 105–126, Dec. 2019, doi: 10.1038/s41578-019-0157-5.

[213] G.-L. Xu *et al.*, 'Building ultraconformal protective layers on both secondary and primary particles of layered lithium transition metal oxide cathodes', *Nat Energy*, vol. 4, no. 6, pp. 484–494, May 2019, doi: 10.1038/s41560-019-0387-1.

[214] K. Takahashi *et al.*, 'All-solid-state lithium battery with LiBH4 solid electrolyte', *J Power Sources*, vol. 226, pp. 61–64, Mar. 2013, doi: 10.1016/j.jpowsour.2012.10.079.

[215] N. Ohta *et al.*, 'LiNbO3-coated LiCoO2 as cathode material for all solid-state lithium secondary batteries', *Electrochem commun*, vol. 9, no. 7, pp. 1486–1490, Jul. 2007, doi: 10.1016/j.elecom.2007.02.008.

[216] M. Du, K. Liao, Q. Lu, and Z. Shao, 'Recent advances in the interface engineering of solid-state Li-ion batteries with artificial buffer layers: challenges, materials, construction, and characterization', *Energy Environ Sci*, vol. 12, no. 6, pp. 1780–1804, 2019, doi: 10.1039/C9EE00515C.

[217] X. Li *et al.*, 'Constructing double buffer layers to boost electrochemical performances of NCA cathode for ASSLB', *Energy Storage Mater*, vol. 18, pp. 100–106, Mar. 2019, doi: 10.1016/j.ensm.2018.10.003.

[218] S. Wang, S. Li, B. Wei, and X. Lu, 'Interfacial Engineering at Cathode/LATP Interface for High-Performance Solid-State Batteries', *J Electrochem Soc*, vol. 167, no. 10, p. 100528, Jun. 2020, doi: 10.1149/1945-7111/ab9a00.

[219] Z. Bi *et al.*, 'Surface coating of $LiMn_2O_4$ cathodes with garnet electrolytes for improving cycling stability of solid lithium batteries', *J Mater Chem A Mater*, vol. 8, no. 8, pp. 4252–4256, 2020, doi: 10.1039/C9TA11203K.

[220] Q. Zhao, P. Chen, S. Li, X. Liu, and L. A. Archer, 'Solid-state polymer electrolytes stabilized by task-specific salt additives', *J Mater Chem A Mater*, vol. 7, no. 13, pp. 7823–7830, 2019, doi: 10.1039/C8TA12008K.

[221] C. Zhao *et al.*, 'Rechargeable Lithium Metal Batteries with an In-Built Solid-State Polymer Electrolyte and a High Voltage/Loading Ni-Rich Layered Cathode', *Advanced Materials*, vol. 32, no. 12, p. 1905629, Mar. 2020, doi: 10.1002/adma.201905629.

[222] Z. Li *et al.*, 'Interfacial engineering for stabilizing polymer electrolytes with 4V cathodes in lithium metal batteries at elevated temperature', *Nano Energy*, vol. 72, p. 104655, Jun. 2020, doi: 10.1016/j.nanoen.2020.104655.

[223] S.-T. Myung, Y. Hitoshi, and Y.-K. Sun, 'Electrochemical behavior and passivation of current collectors in lithium-ion batteries', *J Mater Chem*, vol. 21, no. 27, p. 9891, 2011, doi: 10.1039/c0jm04353b.

[224] R. Koerver *et al.*, 'Redox-active cathode interphases in solid-state batteries', *J Mater Chem A Mater*, vol. 5, no. 43, pp. 22750–22760, 2017, doi: 10.1039/C7TA07641J.

[225] S. Choi, J. Kim, M. Eom, X. Meng, and D. Shin, 'Application of a carbon nanotube (CNT) sheet as a current collector for all-solid-state lithium batteries', *J Power Sources*, vol. 299, pp. 70–75, Dec. 2015, doi: 10.1016/j.jpowsour.2015.08.081.

[226] B. De, A. Yadav, S. Khan, and K. K. Kar, 'A Facile Methodology for the Development of a Printable and Flexible All-Solid-State Rechargeable Battery', *ACS Appl Mater Interfaces*, vol. 9, no. 23, pp. 19870–19880, Jun. 2017, doi: 10.1021/acsami.7b04112.

[227] X. Chen, H. Huang, L. Pan, T. Liu, and M. Niederberger, 'Fully Integrated Design of a Stretchable Solid-State Lithium-Ion Full Battery', *Advanced Materials*, vol. 31, no. 43, p. 1904648, Oct. 2019, doi: 10.1002/adma.201904648.

[228] A. N. Filippin *et al.*, 'Chromium nitride as a stable cathode current collector for all-solid-state thin film Li-ion batteries', *RSC Adv*, vol. 7, no. 43, pp. 26960–26967, 2017, doi: 10.1039/C7RA03580B.

[229] A. N. Filippin *et al.*, 'Ni–Al–Cr superalloy as high temperature cathode current collector for advanced thin film Li batteries', *RSC Adv*, vol. 8, no. 36, pp. 20304–20313, 2018, doi: 10.1039/C8RA02461H.

[230] G. Oh, M. Hirayama, O. Kwon, K. Suzuki, and R. Kanno, 'Bulk-Type All Solid-State Batteries with 5 V Class $LiNi_{0.5}Mn_{1.5}O_4$ Cathode and $Li_{10}GeP_2S_{12}$ Solid Electrolyte', *Chemistry of Materials*, vol. 28, no. 8, pp. 2634–2640, Apr. 2016, doi: 10.1021/acs.chemmater.5b04940.

[231] R. Koerver *et al.*, 'Capacity Fade in Solid-State Batteries: Interphase Formation and Chemomechanical Processes in Nickel-Rich Layered Oxide Cathodes and Lithium Thiophosphate Solid Electrolytes', *Chemistry of Materials*, vol. 29, no. 13, pp. 5574–5582, Jul. 2017, doi: 10.1021/acs.chemmater.7b00931.

[232] X. Li *et al.*, 'Atomic layer deposition of solid-state electrolyte coated cathode materials with superior high-voltage cycling behavior for lithium ion battery application', *Energy Environ. Sci.*, vol. 7, no. 2, pp. 768–778, 2014, doi: 10.1039/C3EE42704H.

[233] J. Lau, R. H. DeBlock, D. M. Butts, D. S. Ashby, C. S. Choi, and B. S. Dunn, 'Sulfide Solid Electrolytes for Lithium Battery Applications', *Adv Energy Mater*, vol. 8, no. 27, p. 1800933, Sep. 2018, doi: 10.1002/aenm.201800933.

[234] J. B. Goodenough and K.-S. Park, 'The Li-Ion Rechargeable Battery: A Perspective', *J Am Chem Soc*, vol. 135, no. 4, pp. 1167–1176, Jan. 2013, doi: 10.1021/ja3091438.

[235] N. Ohta, K. Takada, L. Zhang, R. Ma, M. Osada, and T. Sasaki, 'Enhancement of the High-Rate Capability of Solid-State Lithium Batteries by Nanoscale Interfacial Modification', *Advanced Materials*, vol. 18, no. 17, pp. 2226–2229, Sep. 2006, doi: 10.1002/adma.200502604.

[236] F. Mizuno, A. Hayashi, K. Tadanaga, and M. Tatsumisago, 'Effects of Conductive Additives in Composite Positive Electrodes on Charge-Discharge Behaviors of All-Solid-State Lithium Secondary Batteries', *J Electrochem Soc*, vol. 152, no. 8, p. A1499, 2005, doi: 10.1149/1.1939633.

[237] K. Borzutzki, M. Winter, and G. Brunklaus, 'Improving the NMC111|Polymer Electrolyte Interface by Cathode Composition and Processing', *J Electrochem Soc*, vol. 167, no. 7, p. 070546, Jan. 2020, doi: 10.1149/1945-7111/ab7fb5.

[238] J. Sakamoto, 'More pressure needed', *Nat Energy*, vol. 4, no. 10, pp. 827–828, Oct. 2019, doi: 10.1038/s41560-019-0478-z.

[239] X. Zhang, Q. J. Wang, K. L. Harrison, S. A. Roberts, and S. J. Harris, 'Pressure-Driven Interface Evolution in Solid-State Lithium Metal Batteries', *Cell Rep Phys Sci*, vol. 1, no. 2, p. 100012, Feb. 2020, doi: 10.1016/j.xcrp.2019.100012.

[240] X.-Q. Zhang, X.-B. Cheng, and Q. Zhang, 'Advances in Interfaces between Li Metal Anode and Electrolyte', *Adv Mater Interfaces*, vol. 5, no. 2, p. 1701097, Jan. 2018, doi: 10.1002/admi.201701097.

[241] S. Wang, H. Xu, W. Li, A. Dolocan, and A. Manthiram, 'Interfacial Chemistry in Solid-State Batteries: Formation of Interphase and Its Consequences', *J Am Chem Soc*, vol. 140, no. 1, pp. 250–257, Jan. 2018, doi: 10.1021/jacs.7b09531.

[242] P. Barai, A. T. Ngo, B. Narayanan, K. Higa, L. A. Curtiss, and V. Srinivasan, 'The Role of Local Inhomogeneities on Dendrite Growth in LLZO-Based Solid Electrolytes', *J Electrochem Soc*, vol. 167, no. 10, p. 100537, Jan. 2020, doi: 10.1149/1945-7111/ab9b08.

[243] W. Manalastas *et al.*, 'Mechanical failure of garnet electrolytes during Li electrodeposition observed by in-operando microscopy', *J Power Sources*, vol. 412, pp. 287–293, Feb. 2019, doi: 10.1016/j.jpowsour.2018.11.041.

[244] X. Ke, Y. Wang, L. Dai, and C. Yuan, 'Cell failures of all-solid-state lithium metal batteries with inorganic solid electrolytes: Lithium dendrites', *Energy Storage Mater*, vol. 33, pp. 309–328, Dec. 2020, doi: 10.1016/j.ensm.2020.07.024.

[245] K. TAKADA, 'Solid state batteries with sulfide-based solid electrolytes', *Solid State Ion*, vol. 172, no. 1–4, pp. 25–30, Aug. 2004, doi: 10.1016/j.ssi.2004.02.027.

[246] Z. Jiang, Q. Han, S. Wang, and H. Wang, 'Reducing the Interfacial Resistance in All-Solid-State Lithium Batteries Based on Oxide Ceramic Electrolytes',

ChemElectroChem, vol. 6, no. 12, pp. 2970–2983, Jun. 2019, doi: 10.1002/celc.201801898.

[247] X. Yang *et al.*, 'Suppressed dendrite formation realized by selective Li deposition in all-solid-state lithium batteries', *Energy Storage Mater*, vol. 27, pp. 198–204, May 2020, doi: 10.1016/j.ensm.2020.01.031.

[248] Y. Liu *et al.*, 'Transforming from planar to three-dimensional lithium with flowable interphase for solid lithium metal batteries', *Sci Adv*, vol. 3, no. 10, Oct. 2017, doi: 10.1126/sciadv.aao0713.

[249] M. Liu *et al.*, 'Controlling the Lithium-Metal Growth To Enable Low-Lithium-Metal-Excess All-Solid-State Lithium-Metal Batteries', *ACS Mater Lett*, vol. 2, no. 7, pp. 665–670, Jul. 2020, doi: 10.1021/acsmaterialslett.0c00152.

[250] X. Han *et al.*, 'Negating interfacial impedance in garnet-based solid-state Li metal batteries', *Nat Mater*, vol. 16, no. 5, pp. 572–579, May 2017, doi: 10.1038/nmat4821.

[251] W. E. Tenhaeff, X. Yu, K. Hong, K. A. Perry, and N. J. Dudney, 'Ionic Transport Across Interfaces of Solid Glass and Polymer Electrolytes for Lithium Ion Batteries', *J Electrochem Soc*, vol. 158, no. 10, p. A1143, 2011, doi: 10.1149/1.3625281.

[252] Y. Kim *et al.*, 'Electrochemical Stability of Li6.5La3Zr1.5M0.5O12 (M = Nb or Ta) against Metallic Lithium', *Front Energy Res*, vol. 4, May 2016, doi: 10.3389/fenrg.2016.00020.

[253] Y. Zhu *et al.*, 'Dopant-Dependent Stability of Garnet Solid Electrolyte Interfaces with Lithium Metal', *Adv Energy Mater*, vol. 9, no. 12, p. 1803440, Mar. 2019, doi: 10.1002/aenm.201803440.

[254] R. H. Brugge *et al.*, 'The origin of chemical inhomogeneity in garnet electrolytes and its impact on the electrochemical performance', *J Mater Chem A Mater*, vol. 8, no. 28, pp. 14265–14276, 2020, doi: 10.1039/D0TA04974C.

[255] A. Paolella *et al.*, 'Understanding the Reactivity of a Thin $Li_{1.5}Al_{0.5}Ge_{1.5}(PO_4)_3$ Solid-State Electrolyte toward Metallic Lithium Anode', *Adv Energy Mater*, vol. 10, no. 32, p. 2001497, Aug. 2020, doi: 10.1002/aenm.202001497.

[256] Y. Liu *et al.*, 'Germanium Thin Film Protected Lithium Aluminum Germanium Phosphate for Solid-State Li Batteries', *Adv Energy Mater*, vol. 8, no. 16, p. 1702374, Jun. 2018, doi: 10.1002/aenm.201702374.

[257] Q. Yu *et al.*, 'Constructing Effective Interfaces for $Li_{1.5}Al_{0.5}Ge_{1.5}(PO_4)_3$ Pellets To Achieve Room-Temperature Hybrid Solid-State Lithium Metal Batteries', *ACS Appl Mater Interfaces*, vol. 11, no. 10, pp. 9911–9918, Mar. 2019, doi: 10.1021/acsami.8b20413.

[258] Q. Liu *et al.*, 'Self-Healing Janus Interfaces for High-Performance LAGP-Based Lithium Metal Batteries', *ACS Energy Lett*, vol. 5, no. 5, pp. 1456–1464, May 2020, doi: 10.1021/acsenergylett.0c00542.

[259] Z. Zhang *et al.*, 'Stable cycling of all-solid-state lithium battery with surface amorphized Li1.5Al0.5Ge1.5(PO4)3 electrolyte and lithium anode', *Electrochim Acta*, vol. 297, pp. 281–287, Feb. 2019, doi: 10.1016/j.electacta.2018.11.206.

[260] S. Sicolo, M. Fingerle, R. Hausbrand, and K. Albe, 'Interfacial instability of amorphous LiPON against lithium: A combined Density Functional Theory and spectroscopic study', *J Power Sources*, vol. 354, pp. 124–133, Jun. 2017, doi: 10.1016/j.jpowsour.2017.04.005.

[261] M. Sakuma, K. Suzuki, M. Hirayama, and R. Kanno, 'Reactions at the electrode/electrolyte interface of all-solid-state lithium batteries incorporating Li–M (M = Sn, Si) alloy electrodes and sulfide-based solid electrolytes', *Solid State Ion*, vol. 285, pp. 101–105, Feb. 2016, doi: 10.1016/j.ssi.2015.07.010.

[262] J. M. Whiteley, J. H. Woo, E. Hu, K.-W. Nam, and S.-H. Lee, 'Empowering the Lithium Metal Battery through a Silicon-Based Superionic Conductor', *J Electrochem Soc*, vol. 161, no. 12, pp. A1812–A1817, Aug. 2014, doi: 10.1149/2.0501412jes.

[263] S. Yubuchi *et al.*, 'All-solid-state cells with Li4Ti5O12/carbon nanotube composite electrodes prepared by infiltration with argyrodite sulfide-based solid electrolytes via liquid-phase processing', *J Power Sources*, vol. 417, pp. 125–131, Mar. 2019, doi: 10.1016/j.jpowsour.2019.01.070.

[264] S. Yubuchi, M. Uematsu, C. Hotehama, A. Sakuda, A. Hayashi, and M. Tatsumisago, 'An argyrodite sulfide-based superionic conductor synthesized by a liquid-phase technique with tetrahydrofuran and ethanol', *J Mater Chem A Mater*, vol. 7, no. 2, pp. 558–566, 2019, doi: 10.1039/C8TA09477B.

[265] T. Ates, M. Keller, J. Kulisch, T. Adermann, and S. Passerini, 'Development of an all-solid-state lithium battery by slurry-coating procedures using a sulfidic electrolyte', *Energy Storage Mater*, vol. 17, pp. 204–210, Feb. 2019, doi: 10.1016/j.ensm.2018.11.011.

[266] C. Y. Yu, J. Choi, V. Anandan, and J. H. Kim, 'High-Temperature Chemical Stability of Li1.4Al0.4Ti1.6(PO4)3Solid Electrolyte with Various Cathode Materials for Solid-State Batteries', *Journal of Physical Chemistry C*, vol. 124, no. 28, pp. 14963–14971, Jul. 2020, doi: 10.1021/ACS.JPCC.0C01698/ASSET/IMAGES/ACS.JPCC.0C01698.SOCIAL.JPEG_V03.

[267] S. Wang, M. Yan, Y. Li, C. Vinado, and J. Yang, 'Separating electronic and ionic conductivity in mix-conducting layered lithium transition-metal oxides', *J Power Sources*, vol. 393, pp. 75–82, Jul. 2018, doi: 10.1016/j.jpowsour.2018.05.005.

[268] Q. Zhang, Z. Yu, P. Du, and C. Su, 'Carbon Nanomaterials Used as Conductive Additives in Lithium Ion Batteries', *Recent Pat Nanotechnol*, vol. 4, no. 2, pp. 100–110, May 2010, doi: 10.2174/187221010791208803.

[269] M. Sakakura and Y. Iriyama, 'Development of oxide-based all-solid-state batteries using aerosol deposition', *Journal of Asian Ceramic Societies*, pp. 1–10, Dec. 2022, doi: 10.1080/21870764.2022.2163080.

[270] X. Kuang, G. Carotenuto, and L. Nicolais, 'Review of ceramic sintering and suggestions on reducing sintering temperatures', *Advanced Performance Materials*, vol. 4, no. 3, pp. 257–274, Jul. 1997, doi: 10.1023/A:1008621020555.

[271] L. Miara *et al.*, 'About the Compatibility between High Voltage Spinel Cathode Materials and Solid Oxide Electrolytes as a Function of Temperature', *ACS Appl Mater Interfaces*, vol. 8, no. 40, pp. 26842–26850, Oct. 2016, doi: 10.1021/acsami.6b09059.

[272] C. Y. Yu, J. Choi, V. Anandan, and J. H. Kim, 'High-Temperature Chemical Stability of Li1.4Al0.4Ti1.6(PO4)3Solid Electrolyte with Various Cathode Materials for Solid-State Batteries', *Journal of Physical Chemistry C*, vol. 124, no. 28, pp. 14963–14971, Jul. 2020, doi: 10.1021/acs.jpcc.0c01698.

[273] S. Sharifi-Asl, J. Lu, K. Amine, and R. Shahbazian-Yassar, 'Oxygen Release Degradation in Li-Ion Battery Cathode Materials: Mechanisms and Mitigating Approaches', *Adv Energy Mater*, vol. 9, no. 22, p. 1900551, Jun. 2019, doi: 10.1002/aenm.201900551.

[274] G. Lombardo, B. Ebin, M. R. J. St Foreman, B. M. Steenari, and M. Petranikova, 'Chemical Transformations in Li-Ion Battery Electrode Materials by Carbothermic Reduction', *ACS Sustain Chem Eng*, vol. 7, no. 16, pp. 13668–13679, Aug. 2019, doi: 10.1021/acssuschemeng.8b06540.

[275] J. P. Beaupain *et al.*, 'Reaction of Li1.3Al0.3Ti1.7(PO4)3 and LiNi0.6Co0.2Mn0.2O2 in Co-Sintered Composite Cathodes for Solid-State Batteries', *ACS Appl Mater Interfaces*, 2021, doi: 10.1021/ACSAMI.1C11750.

[276] L. Miara *et al.*, 'About the Compatibility between High Voltage Spinel Cathode Materials and Solid Oxide Electrolytes as a Function of Temperature', *ACS Appl Mater Interfaces*, vol. 8, no. 40, pp. 26842–26850, Oct. 2016, doi: 10.1021/acsami.6b09059.

[277] 'Oxygen Release and Its Effect on the Cycling Stability of LiNi x Mn y Co z O 2 (NMC) Cathode Materials for Li-Ion Batteries', doi: 10.1149/2.0021707jes.

[278] T. Li, X.-Z. Yuan, L. Zhang, D. Song, K. Shi, and C. Bock, 'Degradation Mechanisms and Mitigation Strategies of Nickel-Rich NMC-Based Lithium-Ion Batteries', *Electrochemical Energy Reviews*, vol. 3, no. 1, pp. 43–80, Mar. 2020, doi: 10.1007/s41918-019-00053-3.

[279] L. D. Prayogi, M. Faisal, E. Kartini, W. Honggowiranto, and Supardi, 'Morphology and conductivity study of solid electrolyte Li3PO4', in *AIP Conference Proceedings*, Feb. 2016, vol. 1710, no. 1, p. 030047. doi: 10.1063/1.4941513.

[280] M. C. Biesinger, B. P. Payne, A. P. Grosvenor, L. W. M. Lau, A. R. Gerson, and R. S. C. Smart, 'Resolving surface chemical states in XPS analysis of first row transition metals, oxides and hydroxides: Cr, Mn, Fe, Co and Ni', *Appl Surf Sci*, vol. 257, no. 7, pp. 2717–2730, Jan. 2011, doi: 10.1016/j.apsusc.2010.10.051.

[281] S. Suzer, 'Differential Charging in X-ray Photoelectron Spectroscopy: A Nuisance or a Useful Tool?', *Anal Chem*, vol. 75, no. 24, pp. 7026–7029, Dec. 2003, doi: 10.1021/AC034823T.

[282] Y. Wei, K. W. Nam, K. B. Kim, and G. Chen, 'Spectroscopic studies of the structural properties of Ni substituted spinel LiMn2O4', *Solid State Ion*, vol. 177, no. 1–2, pp. 29–35, Jan. 2006, doi: 10.1016/j.ssi.2005.10.015.

[283] D. Fa, B. Yu, and Y. Miao, 'Synthesis of ultra-long nanowires of nickel phosphate by a template-free hydrothermal method for electrocatalytic oxidation of glucose', *Colloids Surf A Physicochem Eng Asp*, vol. 564, pp. 31–38, Mar. 2019, doi: 10.1016/j.colsurfa.2018.12.035.

[284] M. Hassel and H.-J. Freund, 'High Resolution XPS Study of a Thin CoO(111) Film Grown on Co(0001)', *Surface Science Spectra*, vol. 4, no. 3, pp. 273–278, Jul. 1996, doi: 10.1116/1.1247797.

[285] J. C. Dupin, D. Gonbeau, H. Benqlilou-Moudden, P. Vinatier, and A. Levasseur, 'XPS analysis of new lithium cobalt oxide thin-films before and after lithium deintercalation', *Thin Solid Films*, vol. 384, no. 1, pp. 23–32, Mar. 2001, doi: 10.1016/S0040-6090(00)01802-2.

[286] L. Dahéron *et al.*, 'Electron transfer mechanisms upon lithium deintercalation from LiCoO 2 to CoO2 investigated by XPS', *Chemistry of Materials*, vol. 20, no. 2, pp. 583–590, Jan. 2008, doi: 10.1021/cm702546s.

[287] T. Hanawa and M. Ota, 'Calcium phosphate naturally formed on titanium in electrolyte solution', *Biomaterials*, vol. 12, no. 8, pp. 767–774, Oct. 1991, doi: 10.1016/0142-9612(91)90028-9.

[288] R. Franke, T. Chassé, P. Streubel, and A. Meisel, 'Auger parameters and relaxation energies of phosphorus in solid compounds', *J Electron Spectros Relat Phenomena*, vol. 56, no. 4, pp. 381–388, Jul. 1991, doi: 10.1016/0368-2048(91)85035-R.

[289] B. Wu *et al.*, 'The role of the solid electrolyte interphase layer in preventing Li dendrite growth in solid-state batteries', *Energy Environ Sci*, vol. 11, no. 7, pp. 1803–1810, Jul. 2018, doi: 10.1039/c8ee00540k.

[290] M. C. Biesinger, L. W. M. Lau, A. R. Gerson, and R. S. C. Smart, 'Resolving surface chemical states in XPS analysis of first row transition metals, oxides and hydroxides: Sc, Ti, V, Cu and Zn', *Appl Surf Sci*, vol. 257, no. 3, pp. 887–898, Nov. 2010, doi: 10.1016/j.apsusc.2010.07.086.

[291] G. Assat, D. Foix, C. Delacourt, A. Iadecola, R. Dedryvère, and J. M. Tarascon, 'Fundamental interplay between anionic/cationic redox governing the kinetics

and thermodynamics of lithium-rich cathodes', *Nat Commun*, vol. 8, no. 1, pp. 1–12, Dec. 2017, doi: 10.1038/s41467-017-02291-9.

[292] A. J. Naylor *et al.*, 'Depth-dependent oxygen redox activity in lithium-rich layered oxide cathodes', *J Mater Chem A Mater*, vol. 7, no. 44, pp. 25355–25368, Nov. 2019, doi: 10.1039/c9ta09019c.

[293] H. Ronduda *et al.*, 'On the Sensitivity of the Ni-rich Layered Cathode Materials for Li-ion Batteries to the Different Calcination Conditions', *Nanomaterials*, vol. 10, no. 10, p. 2018, Oct. 2020, doi: 10.3390/nano10102018.

[294] S. Wang, Y. Ding, G. Zhou, G. Yu, and A. Manthiram, 'Durability of the Li1+xTi2-xAlx(PO4)3 Solid Electrolyte in Lithium-Sulfur Batteries', *ACS Energy Lett*, vol. 1, no. 6, pp. 1080–1085, Dec. 2016, doi: 10.1021/acsenergylett.6b00481.

[295] J. Li, Z. R. Zhang, X. J. Guo, and Y. Yang, 'The studies on structural and thermal properties of delithiated LixNi1/3Co1/3Mn1/3O2 ($0 < x \leq 1$) as a cathode material in lithium ion batteries', *Solid State Ion*, vol. 177, no. 17–18, pp. 1509–1516, Jul. 2006, doi: 10.1016/j.ssi.2006.03.055.

[296] I. Belharouak, W. Lu, D. Vissers, and K. Amine, 'Safety characteristics of Li(Ni0.8Co0.15Al 0.05)O2 and Li(Ni1/3Co1/3Mn 1/3)O2', *Electrochem commun*, vol. 8, no. 2, pp. 329–335, Feb. 2006, doi: 10.1016/j.elecom.2005.12.007.

[297] S. K. Jung *et al.*, 'Understanding the degradation mechanisms of LiNi0.5Co 0.2Mn0.3O2 cathode material in lithium ion batteries', *Adv Energy Mater*, vol. 4, no. 1, Jan. 2014, doi: 10.1002/aenm.201300787.

[298] S. Hwang *et al.*, 'Investigation of changes in the surface structure of LixNi 0.8Co0.15Al0.05O2 cathode materials induced by the initial charge', *Chemistry of Materials*, vol. 26, no. 2, pp. 1084–1092, Jan. 2014, doi: 10.1021/cm403332s.

[299] F. Lin *et al.*, 'Surface reconstruction and chemical evolution of stoichiometric layered cathode materials for lithium-ion batteries', *Nat Commun*, vol. 5, no. 1, p. 3529, Mar. 2014, doi: 10.1038/ncomms4529.

[300] X. Xiong *et al.*, 'Washing effects on electrochemical performance and storage characteristics of LiNi0.8Co0.1Mn0.1O2 as cathode material for lithium-ion batteries', *J Power Sources*, vol. 222, pp. 318–325, Jan. 2013, doi: 10.1016/j.jpowsour.2012.08.029.

[301] B. Han *et al.*, 'From Coating to Dopant: How the Transition Metal Composition Affects Alumina Coatings on Ni-Rich Cathodes', *ACS Appl Mater Interfaces*, vol. 9, no. 47, pp. 41291–41302, Nov. 2017, doi: 10.1021/ACSAMI.7B13597/SUPPL_FILE/AM7B13597_SI_001.PDF.

[302] B. Han *et al.*, 'Understanding the Role of Temperature and Cathode Composition on Interface and Bulk: Optimizing Aluminum Oxide Coatings for Li-Ion Cathodes', *ACS Appl Mater Interfaces*, vol. 9, no. 17, pp. 14769–14778,

May 2017, doi: 10.1021/ACSAMI.7B00595/SUPPL_FILE/AM7B00595_SI_001.PDF.

[303] O. Tiurin, N. Solomatin, M. Auinat, and Y. Ein-Eli, 'Atomic layer deposition (ALD) of lithium fluoride (LiF) protective film on Li-ion battery LiMn1.5Ni0.5O4 cathode powder material', *J Power Sources*, vol. 448, p. 227373, Feb. 2020, doi: 10.1016/j.jpowsour.2019.227373.

[304] J. P. Beaupain *et al.*, 'Reaction of Li1.3Al0.3Ti1.7(PO4)3and LiNi0.6Co0.2Mn0.2O2in Co-Sintered Composite Cathodes for Solid-State Batteries', *ACS Appl Mater Interfaces*, vol. 13, no. 40, pp. 47488–47498, Oct. 2021, doi: 10.1021/ACSAMI.1C11750/SUPPL_FILE/AM1C11750_SI_001.PDF.

[305] S. Valiyaveettil-SobhanRaj *et al.*, 'High temperature thermal reactivity and interface evolution of NMC-LATP-carbon composite cathode (Under revision)', *ACS Appl Mater Interface*.

[306] Q. Zhang, Z. Yu, P. Du, and C. Su, 'Carbon Nanomaterials Used as Conductive Additives in Lithium Ion Batteries', *Recent Pat Nanotechnol*, vol. 4, no. 2, pp. 100–110, Jun. 2010, doi: 10.2174/187221010791208803.

[307] X. Dou *et al.*, 'Hard carbons for sodium-ion batteries: Structure, analysis, sustainability, and electrochemistry', *Materials Today*, vol. 23, pp. 87–104, Mar. 2019, doi: 10.1016/J.MATTOD.2018.12.040.

[308] R. E. Franklin and IUCr, 'The interpretation of diffuse X-ray diagrams of carbon', *urn:issn:0365-110X*, vol. 3, no. 2, pp. 107–121, Mar. 1950, doi: 10.1107/S0365110X50000264.

[309] D. Saurel *et al.*, 'A SAXS outlook on disordered carbonaceous materials for electrochemical energy storage', *Energy Storage Mater*, vol. 21, pp. 162–173, Sep. 2019, doi: 10.1016/J.ENSM.2019.05.007.

[310] L. Bokobza, J. L. Bruneel, and M. Couzi, 'Raman spectroscopy as a tool for the analysis of carbon-based materials (highly oriented pyrolitic graphite, multilayer graphene and multiwall carbon nanotubes) and of some of their elastomeric composites', *Vib Spectrosc*, vol. 74, pp. 57–63, Sep. 2014, doi: 10.1016/J.VIBSPEC.2014.07.009.

[311] J. Hodkiewicz, 'Characterizing Carbon Materials with Raman Spectroscopy'.

[312] A. C. Ferrari *et al.*, 'Raman spectrum of graphene and graphene layers', *Phys Rev Lett*, vol. 97, no. 18, p. 187401, Oct. 2006, doi: 10.1103/PHYSREVLETT.97.187401/FIGURES/3/MEDIUM.

[313] M. A. Worsley *et al.*, 'Synthesis and characterization of highly crystalline graphene aerogels', *ACS Nano*, vol. 8, no. 10, pp. 11013–11022, Oct. 2014, doi: 10.1021/NN505335U/SUPPL_FILE/NN505335U_SI_001.PDF.

[314] B. V. Peshnev, V. K. Nguen, N. N. Gavrilova, A. S. Filimonov, and A. I. Nikolaev, 'Influence of the Surface Area of a Carbon Material on Pore

Formation upon Its Oxidation', *Solid Fuel Chemistry 2022 56:1*, vol. 56, no. 1, pp. 15–20, Mar. 2022, doi: 10.3103/S0361521922010062.

[315] F. H. Abdulrazzak, S. K. Esmail, H. A. Dawod, A. M. Abbas, and M. K. K. Almaliki, 'X-ray Analysis for Purification Process of Synthesized Multi-Walled Carbon Nanotubes by Chemical Vapor Deposition', *Article in International Journal of Basic & Applied Sciences*, 2016.

[316] C. S. Johnson, N. Li, C. Lefief, J. T. Vaughey, and M. M. Thackeray, 'Synthesis, Characterization and Electrochemistry of Lithium Battery Electrodes: xLi2MnO3·(1 − x)LiMn0.333Ni0.333Co0.333O2 (0 ≤ x ≤ 0.7)', *Chemistry of Materials*, vol. 20, no. 19, pp. 6095–6106, Oct. 2008, doi: 10.1021/CM801245R.

[317] X. J. Guo *et al.*, 'Structural and electrochemical characterization of xLi[Li1/3Mn2/3]O2·(1 − x)Li[Ni1/3Mn1/3Co1/3]O2 (0 ≤ x ≤ 0.9) as cathode materials for lithium ion batteries', *J Power Sources*, vol. 184, no. 2, pp. 414–419, Oct. 2008, doi: 10.1016/J.JPOWSOUR.2008.04.013.

[318] M. N. Ates, S. Mukerjee, and K. M. Abraham, 'A Li-Rich Layered Cathode Material with Enhanced Structural Stability and Rate Capability for Li-on Batteries', *J Electrochem Soc*, vol. 161, no. 3, pp. A355–A363, Jan. 2014, doi: 10.1149/2.070403JES/XML.

[319] M. Latifatu *et al.*, 'Structural Effect of Conductive Carbons on the Adhesion and Electrochemical Behavior of $LiNi_{0.4}Mn_{0.4}Co_{0.2}O_2$ Cathode for Lithium Ion Batteries', *Journal of Electrochemical Science and Technology*, vol. 9, no. 4, pp. 330–338, Dec. 2018, doi: 10.5229/JECST.2018.9.4.330.

[320] H. J. Noh, S. Youn, C. S. Yoon, and Y. K. Sun, 'Comparison of the structural and electrochemical properties of layered Li[NixCoyMnz]O2 (x = 1/3, 0.5, 0.6, 0.7, 0.8 and 0.85) cathode material for lithium-ion batteries', *J Power Sources*, vol. 233, pp. 121–130, Jul. 2013, doi: 10.1016/J.JPOWSOUR.2013.01.063.

[321] R. Jung, M. Metzger, F. Maglia, C. Stinner, and H. A. Gasteiger, 'Oxygen Release and Its Effect on the Cycling Stability of $LiNi_x Mn_y Co_z O_2$ (NMC) Cathode Materials for Li-Ion Batteries', *J Electrochem Soc*, vol. 164, no. 7, pp. A1361–A1377, May 2017, doi: 10.1149/2.0021707jes.

[322] M. N. Ates, S. Mukerjee, and K. M. Abraham, 'A Li-Rich Layered Cathode Material with Enhanced Structural Stability and Rate Capability for Li-on Batteries', *J Electrochem Soc*, vol. 161, no. 3, pp. A355–A363, Jan. 2014, doi: 10.1149/2.070403JES/XML.

[323] H. Yu *et al.*, 'High-energy "composite" layered manganese-rich cathode materials via controlling Li2MnO3 phase activation for lithium-ion batteries', *Physical Chemistry Chemical Physics*, vol. 14, no. 18, pp. 6584–6595, Apr. 2012, doi: 10.1039/C2CP40745K.

[324] D. Asakura *et al.*, 'Material/element-dependent fluorescence-yield modes on soft X-ray absorption spectroscopy of cathode materials for Li-ion batteries', *AIP Adv*, vol. 6, no. 3, p. 035105, Mar. 2016, doi: 10.1063/1.4943673.

[325] K. Yang, L. Chen, J. Ma, Y. He, and F. Kang, ‘ Progress and perspective of Li 1 + x Al x Ti 2 -x (PO 4) 3 ceramic electrolyte in lithium batteries ’, *InfoMat*, vol. 3, no. 11, pp. 1195–1217, Nov. 2021, doi: 10.1002/INF2.12222.

[326] H. Aono, E. Sugimoto, … Y. S.-J. of the, and undefined 1990, ‘Ionic conductivity of solid electrolytes based on lithium titanium phosphate’, *The Electrochemical Society*.

[327] J. Narváez-Semanate, A. R.-S. S. Ionics, and undefined 2010, ‘Microstructure and ionic conductivity of Li1+ xAlxTi2− x (PO4) 3 NASICON glass-ceramics’, *Elsevier*.

[328] T. Yoshinari, R. Koerver, P. Hofmann, Y. Uchimoto, W. G. Zeier, and J. Janek, ‘Interfacial Stability of Phosphate-NASICON Solid Electrolytes in Ni-Rich NCM Cathode-Based Solid-State Batteries’, *ACS Appl Mater Interfaces*, vol. 11, no. 26, pp. 23244–23253, Jul. 2019, doi: 10.1021/acsami.9b05995.

[329] Y. Zhu, X. He, and Y. Mo, ‘Origin of Outstanding Stability in the Lithium Solid Electrolyte Materials: Insights from Thermodynamic Analyses Based on First-Principles Calculations’, 2015, doi: 10.1021/acsami.5b07517.

[330] T. K. Schwietert, A. Vasileiadis, and M. Wagemaker, ‘First-Principles Prediction of the Electrochemical Stability and Reaction Mechanisms of Solid-State Electrolytes’, vol. 1, pp. 1488–1496, 2021, doi: 10.1021/jacsau.1c00228.

[331] X. Xu, Z. Wen, X. Yang, J. Zhang, and Z. Gu, ‘High lithium ion conductivity glass-ceramics in Li2O–Al2O3–TiO2–P2O5 from nanoscaled glassy powders by mechanical milling’, *Solid State Ion*, vol. 177, no. 26–32, pp. 2611–2615, Oct. 2006, doi: 10.1016/J.SSI.2006.04.010.

[332] K. Waetzig *et al.*, ‘Synthesis and sintering of Li1.3Al0.3Ti1.7(PO4)3 (LATP) electrolyte for ceramics with improved Li+ conductivity’, *J Alloys Compd*, vol. 818, p. 153237, Mar. 2020, doi: 10.1016/j.jallcom.2019.153237.

[333] K. Waetzig, A. Rost, U. Langklotz, and J. Schilm, ‘Lithium Loss Indicated Formation of Microcracks in LATP Ceramics’, *Ceramic Engineering and Science Proceedings*, vol. 37, no. 6, pp. 143–150, 2017, doi: 10.1002/9781119321774.CH15.

[334] S. D. Jackman and R. A. Cutler, ‘Effect of microcracking on ionic conductivity in LATP’, *J Power Sources*, vol. 218, pp. 65–72, Nov. 2012, doi: 10.1016/J.JPOWSOUR.2012.06.081.

[335] B. Davaasuren, F. T.-S. S. Ionics, and undefined 2019, ‘Impact of sintering temperature on phase formation, microstructure, crystallinity and ionic conductivity of Li1. 5Al0. 5Ti1. 5 (PO4) 3’, *Elsevier*.

[336] D. Milligan, U. Engstrom, and S. Smith, ‘High-Temperature Sintering-a Cost-Effective Way to Future High-Performance Materials. , 1, 5.’, *ADVANCES IN POWDER METALLURGY AND PARTICULATE MATERIALS*, vol. 1, no. 5, 2005.

[337] A. M. Laptev, H. Zheng, M. Bram, M. Finsterbusch, and O. Guillon, 'High-pressure field assisted sintering of half-cell for all-solid-state battery', *Mater Lett*, vol. 247, pp. 155–158, Jul. 2019, doi: 10.1016/J.MATLET.2019.03.109.

[338] R. Ramaraghavulu and S. Buddhudu, 'Analysis of structural, thermal and dielectric properties of LiTi2(PO4)3 ceramic powders', *Ceram Int*, vol. 37, no. 8, pp. 3651–3656, Dec. 2011, doi: 10.1016/J.CERAMINT.2011.06.025.

[339] K. N. Kudin, B. Ozbas, H. C. Schniepp, R. K. Prud'homme, I. A. Aksay, and R. Car, 'Raman Spectra of Graphite Oxide and Functionalized Graphene Sheets', 2008, doi: 10.1021/nl071822y.

[340] F. Rosenburg, E. Ionescu, N. Nicoloso, and R. Riedel, 'High-Temperature Raman Spectroscopy of Nano-Crystalline Carbon in Silicon Oxycarbide', *Materials 2018, Vol. 11, Page 93*, vol. 11, no. 1, p. 93, Jan. 2018, doi: 10.3390/MA11010093.

[341] S. Yu *et al.*, 'Influence of microstructure and AlPO4 secondary-phase on the ionic conductivity of Li1.3Al0.3Ti1.7(PO4)3 solid-state electrolyte', *http://dx.doi.org/10.1142/S1793604716500661*, vol. 9, no. 5, Oct. 2016, doi: 10.1142/S1793604716500661.

[342] F. Jülich, R. Schierholz, S. Yu, and H. Kungl, 'Combined quantitative microscopy on the microstructure and Combined quantitative microscopy on the microstructure and phase evolution in Li phase evolution in Li 1.3 1.3 Al Al 0.3 0.3 Ti Ti 1.7 1.7 (PO (PO 4 4)) 3 3 ceramics ceramics Deniz Cihan GUNDUZ', *Journal of Advanced Ceramics*, vol. 9, doi: 10.1007/s40145-019-0354-0.

[343] S. Wang, Y. Ding, G. Zhou, G. Yu, and A. Manthiram, 'Durability of the Li 1+x Ti 2−x Al x (PO 4) 3 Solid Electrolyte in Lithium−Sulfur Batteries', vol. 1, 2016, doi: 10.1021/acsenergylett.6b00481.

[344] J. Wolfenstine, J. L. Allen, J. Sakamoto, D. J. Siegel, and H. Choe, 'Mechanical behavior of Li-ion-conducting crystalline oxide-based solid electrolytes: a brief review', *Ionics (Kiel)*, vol. 24, no. 5, pp. 1271–1276, May 2018, doi: 10.1007/S11581-017-2314-4/TABLES/3.

[345] J. Zhu *et al.*, 'Insights into the local structure, microstructure and ionic conductivity of silicon doped NASICON-type solid electrolyte Li1.3Al0.3Ti1.7P3O12', *Energy Storage Mater*, vol. 44, pp. 190–196, Jan. 2022, doi: 10.1016/j.ensm.2021.10.003.

[346] M. Rumpel, L. Appold, J. Baber, W. Stracke, A. Flegler, and G. Sextl, 'Impact of the sintering additive Li3PO4 on the sintering behaviour, microstructure and electrical properties of a ceramic LATP electrolyte', *Mater Adv*, 2022, doi: 10.1039/D2MA00655C.

[347] H. Bai *et al.*, 'Influence of LiBO2 addition on the microstructure and lithium-ion conductivity of Li1+xAlxTi2−x(PO4)3(x = 0.3) ceramic electrolyte', *Ceram Int*, vol. 44, no. 6, pp. 6558–6563, Apr. 2018, doi: 10.1016/J.CERAMINT.2018.01.058.

[348] Q. Xu *et al.*, 'Insights into the reactive sintering and separated specific grain/grain boundary conductivities of Li1.3Al0.3Ti1.7(PO4)3', *J Power Sources*, vol. 492, p. 229631, Apr. 2021, doi: 10.1016/J.JPOWSOUR.2021.229631.

[349] B. Davaasuren and F. Tietz, 'Impact of sintering temperature on phase formation, microstructure, crystallinity and ionic conductivity of Li1.5Al0.5Ti1.5(PO4)3', *Solid State Ion*, vol. 338, pp. 144–152, Oct. 2019, doi: 10.1016/J.SSI.2019.05.016.

[350] L. Dai, J. Wang, Z. Shi, L. Yu, and J. Shi, 'Influence of LiBF4 sintering aid on the microstructure and conductivity of LATP solid electrolyte', *Ceram Int*, vol. 47, no. 8, pp. 11662–11667, Apr. 2021, doi: 10.1016/J.CERAMINT.2021.01.004.

[351] S. Duan *et al.*, 'Non-equilibrium microstructure of Li1.4Al0.4Ti1.6(PO4)3 superionic conductor by spark plasma sintering for enhanced ionic conductivity', *Nano Energy*, vol. 51, pp. 19–25, Sep. 2018, doi: 10.1016/J.NANOEN.2018.06.050.

[352] Y. Liu *et al.*, 'Insight into the Microstructure and Ionic Conductivity of Cold Sintered NASICON Solid Electrolyte for Solid-State Batteries', *ACS Appl Mater Interfaces*, vol. 11, no. 31, pp. 27890–27896, Aug. 2019, doi: 10.1021/ACSAMI.9B08132/SUPPL_FILE/AM9B08132_SI_001.PDF.

[353] N. Sharma, D. Meng, X. Wu, L. S. de Vasconcelos, L. Li, and K. Zhao, 'Nanoindentation measurements of anisotropic mechanical properties of single crystalline NMC cathodes for Li-ion batteries', *Extreme Mech Lett*, vol. 58, p. 101920, Jan. 2023, doi: 10.1016/j.eml.2022.101920.

[354] E. J. Cheng, K. Hong, N. J. Taylor, H. Choe, J. Wolfenstine, and J. Sakamoto, 'Mechanical and physical properties of LiNi0.33Mn0.33Co0.33O2 (NMC)', *J Eur Ceram Soc*, vol. 37, no. 9, pp. 3213–3217, Aug. 2017, doi: 10.1016/j.jeurceramsoc.2017.03.048.

[355] J. Rodríguez-Carvajal, 'Recent advances in magnetic structure determination by neutron powder diffraction', *Physica B Condens Matter*, vol. 192, no. 1–2, pp. 55–69, Oct. 1993, doi: 10.1016/0921-4526(93)90108-I.

[356] J. H. Scofield, 'Theoretical photoionization cross sections from 1 to 1500 keV.', Jan. 1973, doi: 10.2172/4545040.

[357] M. P. Seah, 'Simple universal curve for the energy-dependent electron attenuation length for all materials', *Surface and Interface Analysis*, vol. 44, no. 10, pp. 1353–1359, Oct. 2012, doi: 10.1002/SIA.5033.

[358] M. P. Seah and W. A. Dench, 'Quantitative electron spectroscopy of surfaces: A standard data base for electron inelastic mean free paths in solids', *Surface and Interface Analysis*, vol. 1, no. 1, pp. 2–11, Feb. 1979, doi: 10.1002/SIA.740010103.

[359] A. Barla *et al.*, 'Design and performance of BOREAS, the beamline for resonant X-ray absorption and scattering experiments at the ALBA synchrotron light source', *urn:issn:1600-5775*, vol. 23, no. 6, pp. 1507–1517, Oct. 2016, doi: 10.1107/S1600577516013461.

[360] M. Dierick, B. Masschaele, and L. Van Hoorebeke, 'Octopus, a fast and user-friendly tomographic reconstruction package developed in LabView®', *Meas Sci Technol*, vol. 15, no. 7, p. 1366, Jun. 2004, doi: 10.1088/0957-0233/15/7/020.

[361] A. Limaye, 'Drishti: a volume exploration and presentation tool', *https://doi.org/10.1117/12.935640*, vol. 8506, pp. 191–199, Oct. 2012, doi: 10.1117/12.935640.

[362] Z. Fu, J. Hu, W. Hu, S. Yang, and Y. Luo, 'Quantitative analysis of Ni 2+ /Ni 3+ in Li[Ni x Mn y Co z]O 2 cathode materials: Non-linear least-squares fitting of XPS spectra', *Appl Surf Sci*, vol. 441, pp. 1048–1056, May 2018, doi: 10.1016/j.apsusc.2018.02.114.

[363] A. N. Mansour, 'Characterization of NiO by XPS', *Surface Science Spectra*, vol. 3, no. 3, pp. 231–238, Jul. 1994, doi: 10.1116/1.1247751.

[364] A. N. Mansour, ' Characterization of LiNiO 2 by XPS ', *Surface Science Spectra*, vol. 3, no. 3, pp. 279–286, Jul. 1994, doi: 10.1116/1.1247757.

[365] L. Dahéron *et al.*, 'Surface properties of LiCoO2investigated by XPS analyses and theoretical calculations', *Journal of Physical Chemistry C*, vol. 113, no. 14, pp. 5843–5852, Apr. 2009, doi: 10.1021/jp803266w.

[366] R. C. Reynolds, 'The Lorentz-Polarization Factor and Preferred Orientation in Oriented Clay Aggregates', *Clays and Clay Minerals 1986 34:4*, vol. 34, no. 4, pp. 359–367, Aug. 1986, doi: 10.1346/CCMN.1986.0340402.

[367] H. Lipson, J. I. Langford, and H.-C. Hu, 'Trigonometric intensity factors', *International Tables for Crystallography*, pp. 596–598, Oct. 2006, doi: 10.1107/97809553602060000601.

[368] E. C. Self *et al.*, 'Synthesis and Electrochemical and Structural Investigations of Oxidatively Stable Li2MoO3 and xLi2MoO3·(1 - X)LiMO2 Composite Cathodes', *Chemistry of Materials*, vol. 30, no. 15, pp. 5061–5068, Aug. 2018, doi: 10.1021/acs.chemmater.8b01408.

[369] J. Pires *et al.*, 'Tris(2,2,2-trifluoroethyl) phosphite as an electrolyte additive for high-voltage lithium-ion batteries using lithium-rich layered oxide cathode', *J Power Sources*, vol. 296, pp. 413–425, Aug. 2015, doi: 10.1016/j.jpowsour.2015.07.065.

[370] W. S. Yoon, K. Y. Chung, J. McBreen, D. A. Fischer, and X. Q. Yang, 'Changes in electronic structure of the electrochemically Li-ion deintercalated LiNiO2 system investigated by soft X-ray absorption spectroscopy', *J Power Sources*, vol. 163, no. 1, pp. 234–237, Dec. 2006, doi: 10.1016/J.JPOWSOUR.2006.02.013.

[371] L. Mu *et al.*, 'Structural and Electrochemical Impacts of Mg/Mn Dual Dopants on the LiNiO2 Cathode in Li-Metal Batteries', *ACS Appl Mater Interfaces*, vol. 12, no. 11, pp. 12874–12882, Mar. 2020, doi: 10.1021/ACSAMI.0C00111/SUPPL_FILE/AM0C00111_SI_001.PDF.

[372] F. M. F. De Groot, J. C. Fuggle, B. T. Thole, and G. A. Sawatzky, '2*p* x-ray absorption of 3*d* transition-metal compounds: An atomic multiplet description including the crystal field', *Phys Rev B*, vol. 42, no. 9, p. 5459, Sep. 1990, doi: 10.1103/PhysRevB.42.5459.

[373] S. C. Das, R. J. Green, J. Podder, T. Z. Regier, G. S. Chang, and A. Moewes, 'Band Gap Tuning in ZnO Through Ni Doping via Spray Pyrolysis', *Journal of Physical Chemistry C*, vol. 117, no. 24, pp. 12745–12753, Jun. 2013, doi: 10.1021/JP3126329.

[374] H. Wang *et al.*, 'L-edge sum rule analysis on 3d transition metal sites: from d10 to d0 and towards application to extremely dilute metallo-enzymes', *Physical Chemistry Chemical Physics*, vol. 20, no. 12, pp. 8166–8176, Mar. 2018, doi: 10.1039/C7CP06624D.

[375] S. Baskar *et al.*, 'Ionic valences and spin structure of Co0.6Fe0.9Mn1.5O4 investigated by NMR and XAS', *New J Phys*, vol. 11, no. 4, p. 043008, Apr. 2009, doi: 10.1088/1367-2630/11/4/043008.

[376] R. Qiao *et al.*, 'Revealing and suppressing surface Mn(II) formation of Na0.44MnO2 electrodes for Na-ion batteries', *Nano Energy*, vol. 16, pp. 186–195, Sep. 2015, doi: 10.1016/J.NANOEN.2015.06.024.

[377] S. Baskar *et al.*, 'Ionic valences and spin structure of Co0.6Fe0.9Mn1.5O4 investigated by NMR and XAS', *New J Phys*, vol. 11, no. 4, p. 043008, Apr. 2009, doi: 10.1088/1367-2630/11/4/043008.

[378] D. K. Bora, X. Cheng, M. Kapilashrami, P. A. Glans, Y. Luo, and J. H. Guo, 'Influence of crystal structure, ligand environment and morphology on Co L-edge XAS spectral characteristics in cobalt compounds', *J Synchrotron Radiat*, vol. 22, no. 6, pp. 1450–1458, Nov. 2015, doi: 10.1107/S1600577515017178/RV5036SUP1.PDF.

[379] C. H. Chuang *et al.*, 'The Effect of Thermal Reduction on the Photoluminescence and Electronic Structures of Graphene Oxides', *Scientific Reports 2014 4:1*, vol. 4, no. 1, pp. 1–7, Apr. 2014, doi: 10.1038/srep04525.

[380] N. A. Vinogradov *et al.*, 'Impact of Atomic Oxygen on the Structure of Graphene Formed on Ir(111) and Pt(111)', *Journal of Physical Chemistry C*, vol. 115, no. 19, pp. 9568–9577, May 2011, doi: 10.1021/JP111962K.

[381] W. Hua, B. Gao, S. Li, H. Ågren, and Y. Luo, 'X-ray absorption spectra of graphene from first-principles simulations', *Phys Rev B Condens Matter Mater Phys*, vol. 82, no. 15, p. 155433, Oct. 2010, doi: 10.1103/PHYSREVB.82.155433/FIGURES/6/MEDIUM.

[382] K. G. Latham, M. I. Simone, W. M. Dose, J. A. Allen, and S. W. Donne, 'Synchrotron based NEXAFS study on nitrogen doped hydrothermal carbon: Insights into surface functionalities and formation mechanisms', *Carbon N Y*, vol. 114, pp. 566–578, Apr. 2017, doi: 10.1016/J.CARBON.2016.12.057.

[383] M. K. Rabchinskii *et al.*, 'Graphene oxide conversion into controllably carboxylated graphene layers via photoreduction process in the inert atmosphere', *https://doi.org/10.1080/1536383X.2019.1686625*, vol. 28, no. 3, pp. 221–225, Mar. 2019, doi: 10.1080/1536383X.2019.1686625.

[384] B. Singh, Y. Fang, B. C. C. Cowie, and L. Thomsen, 'NEXAFS and XPS characterisation of carbon functional groups of fresh and aged biochars', *Org Geochem*, vol. 77, pp. 1–10, Dec. 2014, doi: 10.1016/J.ORGGEOCHEM.2014.09.006.

[385] E. Boulard *et al.*, 'Experimental investigation of the stability of Fe-rich carbonates in the lower mantle', *J Geophys Res Solid Earth*, vol. 117, no. B2, Feb. 2012, doi: 10.1029/2011JB008733.

eman ta zabal zazu

Universidad del País Vasco

Euskal Herriko Unibertsitatea

All inorganic solid-state batteries (SSBs) are considered the batteries of the future because of their superior energy density and safety. Their commercialization is in its infancy since a further understanding of the materials and processing aspects is still required. Here we propose an oxide-based SSB model comprising NMC+LATP+carbon composite cathode, LATP solid electrolyte, and Li metal anode able to potentially convey an energy density of >300 Wh/kg and >700 Wh/l. A review of existing processing techniques of the selected materials indicates the necessity of very high densification temperatures to assure sufficient ionic conductivity and mechanical stability. The electrode and electrolyte need to be co-densified to avoid interfacial contact resistance, but the components of the composite cathode react at these elevated temperatures. In this work, the composite cathode thermal compatibility is first studied to determine the tolerance of the system under temperature, considering also the heating atmosphere and the decomposition reaction mechanism. In the second step, mitigation strategies to overcome the threshold limits identified have been examined, such as the selection of the carbon conducting additive and the impact of other additives. On the other hand, the realization that the threshold temperature is much lower than the conventional processing temperature requires the exploration of alternative low-temperature densification techniques. Hence a high-pressure low-temperature (HPLT) technique has been identified and initially investigated for oxide-based ceramic solid electrolyte densification. Our results show that this technique enables a significant reduction of the processing temperature and time compared to conventional sintering. Finally, preliminary investigations indicate that with further exploration of the HPLT technique, the realization of the proposed SSB model should be possible, resulting in significant gains in processing consumed energy.